Multi-scale imaging of the North Anatolian Fault Zone using seismic interferometry

David George Taylor

Submitted in accordance with the requirements for the degree of
Doctor of Philosophy

The University of Leeds
School of Earth and Environment

June 2018

The candidate confirms that the work submitted is his own, except where work which has formed part of jointly authored publications has been included. The contribution of the candidate and the other authors to this work has been explicitly indicated below. The candidate confirms that appropriate credit has been given within the thesis where reference has been made to the work of others.

The work in Chapter 2 of the thesis has appeared in publication as follows:
Taylor, G., S. Rost, and G. Houseman (2016), *Crustal imaging across the North Anatolian Fault Zone from the autocorrelation of ambient seismic noise*, Geophysical Research Letters, 43, doi:10.1002/2016GL067715.

I developed the ideas and methodology in this manuscript, in particular the application of the phase correlation algorithm for autocorrelating ambient noise. I performed the data processing and analysis. I wrote the manuscript and created all of the figures, which were improved with comments and suggestions from the co-authors.

The work in Chapter 3 of the thesis has been accepted for publication pending major revisions under the following title:
Taylor, G., S. Rost, G. Houseman and G. Hillers (2018), *Near surface structure of the North Anatolian Fault Zone from Rayleigh and Love wave tomography using ambient seismic noise*, Journal of Geophysical Research: Solid Earth.

I developed the ideas for this paper, including applying the established methodology of ambient noise tomography to our seismic data set. The raw cross-correlation functions were calculated by Gregor Hillers. I performed the remaining analysis, including the phase velocity picking, the tomographic inversion, and the analysis of azimuthal anisotropy. I wrote the manuscript, which was improved by suggestions and comments of the co-authors. Gregor Hillers produced Figures A.1 and A.2. I produced all the remaining figures, which were improved by comments from the co-authors.

The work in Chapter 4 of the thesis is a manuscript about to be submitted under the following title:
Taylor, G., S. Rost, G. Houseman (in prep), *P-wave reflectivity structure of the North Anatolian Fault from the auto-correlation of teleseismic coda waves.*

I developed the ideas and methodology in this manuscript, and performed all the data processing and analysis. I wrote the manuscript and created all of the figures, which were improved with comments and suggestions from the co-authors.

Acknowledgements

Firstly, to get the official part out of the way, this work has been generously supported by the Leeds-York Doctoral Training Programme of the Natural Environment Research Council.

Now, what I'd really like to say. The past 3 years and 9 months, though tough at times, has been truly rewarding. I am proud of how much I have improved, and of what I have managed to accomplish in the past few years. First of all, I must thank my supervisors Sebastian Rost and Greg Houseman for all of their help and support, who were always there when I needed them, no matter how busy they were. I can't remember a time when they weren't on hand to help solve my problems. Without their encouragement and ever-helpful suggestions, I don't think I would have made it very far at all. I'd also like to thank Gregor Hillers for stepping in just as we were about to give up trying to make the ambient noise cross-correlations work. I'm very much looking forward to working with you in Helsinki for the next couple of years.

I'd also like to thank the rest of the Institute of Geophysics and Tectonics at Leeds for providing the perfect work environment in which to carry out this work, and I am very happy I chose to spend the past few years here. Richard Rigby provided IT support without which, I could not have produced many results at all. He even recovered this thesis after I accidentally deleted it a few weeks ago. The thoughtful suggestions from many wonderful colleagues here greatly improved the work in this thesis, and helped me through multiple conference presentations. My office mates all deserve mention, but in particular, joking with Huw Goodall, Patrick Sugden, Dave Price, Charlie Dunham and Matt Gaddes definitely made writing up in the last few months more bearable. I couldn't have asked for better friends to share this experience with than Ruth Amey, Tom Ingleby and Ben Todd. Special thanks to Josh Williams for the laughs over many years, and for always being willing to (heavily) criticise my writing.

Finally, I would like to thank my family for all of their support since I left home to begin this career nearly 7 years ago. Mum, Dad, Liddy and Charlie: thank you for providing a permanent home and special place for me in Devon. I always looked forward to coming back, and now I can't wait to come and take a much longer break there. Gemma, thank you for being by my side whilst we both went through this together. I can't wait to see what the future holds for us. A special mention is reserved

for my great uncle Paul. Without your urging, I would never have come to Leeds to study Geophysics at all. I know you would have loved to read this thesis yourself, and it is my great regret that you missed this moment by only a couple of weeks, but I'm sure you are proud all the same.

Abstract

Seismic imaging allows us to examine the subsurface structure of fault zones. Accurate knowledge of the structure of fault zones is critical for our understanding of earthquake hazard, and the processes of strain accumulation within the crust and upper mantle. The North Anatolian Fault Zone is a $\sim$ 1200 km long continental strike-slip fault zone located in northern Turkey. In the 20th century, the North Anatolian Fault has accommodated a westward propagating sequence of twelve $M_w > 6.5$ earthquakes. The most recent of these earthquakes occurred at İzmit and Düzce in 1999, 86 km south-east of Istanbul. In this thesis I use techniques from seismic interferometry to create seismic images of the crustal and upper mantle structure along the Izmit-Adapazari section of the North Anatolian Fault, in the vicinity of the 1999 İzmit rupture.

I develop methods for observing P-wave reverberations from the free surface that are contained within the ambient seismic noise field and the P-wave coda of teleseismic earthquakes. By autocorrelating the seismic records from a dense seismic array in north-western Turkey, I use these reverberations to create high resolution seismic reflection images of the crust and upper mantle beneath the North Anatolian Fault Zone. In addition, I calculate inter-station cross-correlations to observe Rayleigh and Love waves propagating between stations in the Izmit-Adapazari region. I then use Rayleigh and Love wave phase velocity measurements to perform surface wave tomography and construct an S-wave velocity model of the top 10 km of the crust in the Izmit-Adapazari region.

In the reflection images, I observe a clear arrival associated with a Moho reflected P-wave ($PPmP$). A $\sim$ 3 s variation in travel time of the $PPmP$ arrival suggests that the Moho is vertically offset beneath the northern branch of the North Anatolian Fault Zone. The vertical offset in the Moho occurs over a region less than 7 km wide approximately 16 km north of the surface trace of the North Anatolian Fault. The location of the vertical offsets indicates that the North Anatolian Fault is a localised structure that dips at an angle between 60° and 70° through the entire crust and enters the upper mantle as a narrow shear zone. I also note a reduction in the amplitude of the $PPmP$ phase beneath both the northern and southern branches of the North Anatolian Fault Zone. This amplitude reduction could result from the presence of fluids and serpentinite minerals in the upper mantle which reduce Moho reflectivity beneath the North

Anatolian Fault.

The surface wave tomography shows that the North Anatolian Fault Zone is a vertical zone of low S-wave velocity (2.8 – 3.0 km s^{-1}) in the top 10 km of the crust. I also detect further low velocity anomalies (1.2 – 1.6 km s^{-1}) associated with $\sim$ 3 km deep pull-apart sedimentary basins along both branches of the North Anatolian Fault Zone. Both branches of the North Anatolian Fault appear to skirt the edges of the Armutlu Block, a tectonic unit of crystalline rocks that exhibits high S-wave velocity (3.2 – 3.6 km s^{-1}). It is likely that the Armutlu Block has a strong rheology, and localises strain along the faults at its northern and southern edges. I also measure the azimuthal anisotropy of the phase velocity observations, which displays an average magnitude of $\sim$ 2.5% with a fast direction of 70° from north. The 70° fast direction aligns parallel with the direction of maximum extension in the Izmit-Adapazari region, and indicates that deformation-aligned mineral fabrics may dominate the anisotropy signal in the top 10 km of the crust.

Contents

List of Figures

Nomenclature

List of acronyms

DANA	Dense Array for Northern Anatolia
GEOSCOPE	Global Network of Broad Band Seismic Stations
KOERI	Kandilli Observatory and Earthquake Research Institute
NAFZ	North Anatolian Fault Zone
NNAF	Northern branch of the North Anatolian Fault
PKIKP	Seismic phase that travels as an P-wave in the mantle, P-wave in the outer core, P-wave in the inner core, a further P-wave in the outer core, and finally further P-wave in the mantle
PKiKP	Seismic phase that travels as an P-wave in the mantle, P-wave in the outer core, reflects from the inner core boundary, travels as a further P-wave in the outer core, and finally further P-wave in the mantle
PKP	Seismic phase that travels as an P-wave in the mantle, P-wave in the outer core, and a further P-wave in the mantle
PPmp	Seismic phase that travels as an P-wave in the mantle, reflects of the free surface as a P-wave and reflects once more from the Moho as a P-wave
SKS	Seismic phase that travels as an S-wave in the mantle, P-wave in the outer core, and a further S-wave in the mantle
SmS	Seismic phase that travels as an S-wave in the mantle, and reflects off the Moho as an S-wave
SNAF	Southern branch of the North Anatolian Fault

List of symbols

$\boldsymbol{d_{obs}}$	Observed surface wave travel times	[s]
$\boldsymbol{g(m)}$	Modelled surface wave travel times	[s]
$\boldsymbol{m_0}$	Starting phase velocity model	[km s^{-1}]
$\boldsymbol{m}$	Phase velocity model	[km s^{-1}]
$\dagger$	Complex conjugate	
δ	Kronecker delta	
ϵ	Damping parameter for phase velocity tomography	[s^4 km^{-2}]
μ	Tuning parameter for phase-weighted stacking	
$\phi(t)$, $\psi(t)$	Instantaneous phase of a signal	[rad]
ϕ_2	Fast propagation azimuth of the 2θ component of anisotropy	[°]
ϕ_4	Fast propagation azimuth of the 4θ component of anisotropy	[°]
ϕ_m	Data misfit of the neighbourhood algorithm	
τ	Correlation lag time	[s]
θ	Wave propagation azimuth	[°]
$*$	Convolution	
A	Amplitude of the 2θ component of anisotropy	[km s^{-1}]
B	Amplitude of the 4θ component of anisotropy	[km s^{-1}]
c	Surface wave phase velocity	[km s^{-1}]
C_{pac}	Phase autocorrelation	
D	Recorded down-going wavefield within a medium	
$H(s(t))$	Hilbert transform of the signal $s(t)$	
M_w	Moment magnitude	
N	Number of seismic records	
n_f	Number of frequencies in dispersion curve	
R	Recorded wavefield containing seismic reflections from within a medium	
$s(t)$	A seismic record	

S_n	Source time function of a seismic source	
T	Recorded wavefield transmitted into a medium from a distance source	
U	Recorded up-going wavefield within a medium	
$u(t)$	Actual ground motion recorded at a seismogram	[m s^{-1}]
u_0	Average (isotropic) phase velocity	[km s^{-1}]
v_{di}	Observed phase velocity in neighbourhood algorithm	[km s^{-1}]
v_{mi}	Predicted phase velocity in neighbourhood algorithm	[km s^{-1}]

Chapter 1

Introduction

Earthquakes in the continental interiors pose a hazard to society that is often underestimated and poorly understood (*England and Jackson*, 2011). Whilst the theory of plate tectonics provides a basis for a large leap forward in our understanding of earthquake processes and seismic risk, the complex composition and structure of the continental crust often means that deformation processes are not simple, and are difficult to predict (*Bürgmann and Dresen*, 2008). The structure of fault zones and plate boundaries is difficult to observe beneath the surface, and yet this structure can often have a profound impact on the spatial distribution of strain accumulation, and earthquake rupture patterns (*Fagereng et al.*, 2011, *Biasi and Wesnousky*, 2016, *Bonini et al.*, 2014).

Knowledge of fault zone structure allows us to infer important information about the fault, such as the strength of the rocks, areas of likely strain accumulation, and regions at particular risk of large ground motions during an earthquake (*Yang*, 2015). Seismic imaging techniques are the best tool that we have to investigate the physical properties of rocks at depth, and they are an invaluable tool for investigating the structure of fault zones. This thesis will focus on using seismic interferometry to image the crustal structure of the North Anatolian Fault in north western Turkey.

First proposed by *Claerbout* (1968), the true potential of seismic interferometry for fault zone imaging was realised just after the turn of the century (*Shapiro et al.*, 2004, 2005). By removing the reliance of seismologists on favourable distributions of seismic sources such as earthquakes, seismic interferometry opened up an almost unprecedented number of opportunities for seismic imaging. In particular, the ability to use the ambient seismic noise field as a source for techniques such as seismic tomography has removed the limitations imposed by the irregular distribution of seismic sources across the planet. Freedom from the constraint of source positions means it is now feasible to deploy dense arrays of seismometers across any desired target, such as a fault, to obtain a precise image of the subsurface.

In this Chapter I will present background information on the tectonic and geological structure of the North Anatolian Fault, and in particular the Izmit-Adapazari region.

Figure 1.1: Tectonic units of Turkey and the eastern Mediterranean from *Okay and Tüysüz* (1999). Each tectonic unit is colour coded and annotated. Major suture zones are denoted by the black lines marked with triangles. Figure from *Tüysüz* (2017).

This information is pertinent to the discussion and interpretation of a surface wave tomography of the region in Chapter 3. I will also describe the seismic data set that will be used throughout this thesis. I will then review some of the results provided to us by previous seismic imaging of continental fault zones, and I will highlight previous experiments that have focused on the North Anatolian Fault. Finally, I will introduce seismic interferometry and detail some of the procedures necessary for properly implementing it in seismic imaging. This information is important for understanding the methods and approach taken in Chapters 2, 3 and 4. I will end by setting out my principle aims, and describing the layout of this thesis.

1.1 Tectonic setting of the North Anatolian Fault

1.1.1 The Izmit-Adapazari region

This study will focus on the section of the North Anatolian Fault within the Izmit-Adapazari region of north western Turkey, located approximately 150 km south east of Istanbul. Turkey is comprised of three main tectonic units: the Pontides, the Anatolides-Taurides and the Arabian platform (*Okay*, 2008), each separated by major continental suture zones (Fig. 1.1). The Izmit-Adapazari region is located at the northern edge of most northern tectonic unit, the Pontides.

The Izmit-Adapazari region consists of three tectonic units: the Istanbul Zone, the Sakarya Terrane and the Armutlu-Almacik Block. Between the Triassic (250 Ma)

and the Lower Cretaceous (100 Ma) the Istanbul Zone and the Sakarya Terrane were separated by the Intra-Pontide Ocean (*Akbayram et al.*, 2013). The subduction of the Intra-Pontide Ocean along its northern edge initiated back-arc spreading during the Cretaceous, which separated the Sakarya Terrane from the Eastern European Platform and the Istanbul Zone from the Odessa Shelf (Fig. 1.1), opening the Black Sea. The final closure of the Intra-Pontide Ocean was marked by the Cretaceous collision of the Istanbul Zone with the Sakarya Terrane, forming what is now known as the Intra-Pontide Suture. The Istanbul Zone and Sakarya Terrane are continental fragments, and their geological and tectonic histories are relatively well constrained (*Okay et al.*, 1994, *Okay*, 2008, *Yılmaz et al.*, 1995). On the other hand the origins of the Armutlu-Almacik Block, which separates the Istanbul Zone and Sakarya Terrane and contains the Intra-Pontide Suture in the Izmit-Adapazari region, are controversial and the age and origin of many of the rock units are poorly understood (*Yılmaz et al.*, 1995, *Okay and Tüysüz*, 1999, *Okay et al.*, 2008, *Akbayram et al.*, 2013). The geology of each of these units will be briefly summarised below.

1.1.2 Geology of the Istanbul Zone

The Istanbul Zone is a cratonic fragment of the Eurasian continent, and of exotic origin compared to the surrounding tectonic units. The Istanbul Zone is 400 km east–west, and 50 km north–south, and was rifted from Eurasia and transported south during the subduction of the Intra-Pontide Ocean and the subsequent period of back-arc extension that opened the Black Sea (*Okay et al.*, 1994). As a result, the Istanbul Zone collided with the Sakarya Terrane during the Upper Cretaceous (66 – 100 Ma) (*Yılmaz et al.*, 1995). The boundary between these two units is known as the Intra-Pontide Suture.

The Istanbul Zone has a Precambrian crystalline basement of metamorphic rocks (*Chen et al.*, 2002). In the west (Fig. 1.2), the basement is overlain by a Paleozoic – Triassic sedimentary sequence, which is in turn overlain by a Cretaceous – Paleogene sequence of clastic marine and volcanic rocks (*Özacan et al.*, 2012, *Akbayram et al.*, 2013). Notably, the Istanbul Zone lacks evidence of deformation or metamorphism (aside from volcanism) that could be attributed to its southward motion during the Cretaceous and subsequent the collision with the Sakarya Terrane.

Since the upper Pliocene (3.6 Ma) and the formation of the North Anatolian Fault, flooding of the Sakarya River has deposited a deep sedimentary basin within the Izmit-Adapazari region, known as the Adapazarı basin (*Ünay et al.*, 2001). The basin was formed due to extension along normal faults striking northwest–southeast through the region, though right lateral strike slip faults in an east–west orientation are also present (*Şengör et al.*, 2005). Using findings from a gravity survey and observation of micro-seisms *Komazawa et al.* (2002) estimated the depth to bedrock beneath the Adapazarı basin to be between 1.0 km and 1.5 km. Conversely, *Frederiksen et al.* (2015) used seismic transfer functions to estimate the sedimentary thickness within the Adapazarı

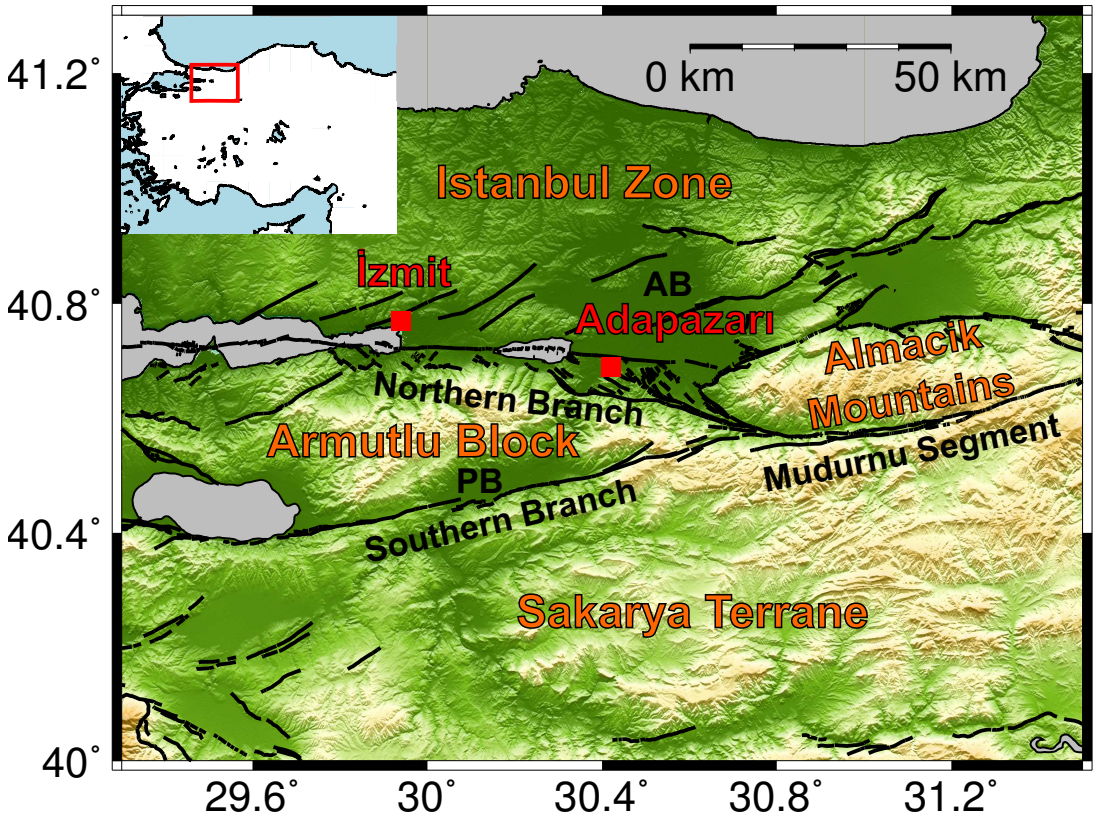

Figure 1.2: Overview of the Izmit-Adapazari region. Mapped faults are indicated by the thick black lines (*Emre et al.*, 2016), and important fault segments are annotated in black. Important population centres are marked with a red square and annotated in red. The four major tectonic units separated by the fault zone are annotated in orange. The top left shows a map of Turkey, with the red box indicating the Izmit-Adapazari region shown in the main figure. AB and PB indicate the location of the Adapazari and Pamukova sedimentary basins, respectively. Topography data were acquired by the Shuttle Radar Topography Mission (*USGS*, 2006).

basin to be greater than 3.5 km. However, *Frederiksen et al.* (2015) assumed a seismic velocity (5 km/s) that is greater than would be expected for Quaternary sedimentary deposits, so it is likely that the quoted sedimentary thickness reflects older, more consolidated material. Geodetic observations show that the Adapazarı basin is subsiding at a rate of about 6 mm/yr, though it is not clear if this subsidence is tectonic in nature, or due to human factors such as water pumping for agriculture (*Hussain et al.*, 2016a).

1.1.3 Geology of the Sakarya Terrane

The Sakarya Terrane lies to the south of the Istanbul Zone, and south of the North Anatolian Fault. The basement of the Sakarya Terrane, known as the Karakaya Complex, is highly metamorphosed and consists of a mix of shallow marine carbonates and volcanic deposits interpreted as a Permian – Triassic subduction accretionary complex (*Şengör and Yılmaz*, 1981). The Karakaya Complex is heavily deformed, likely a result

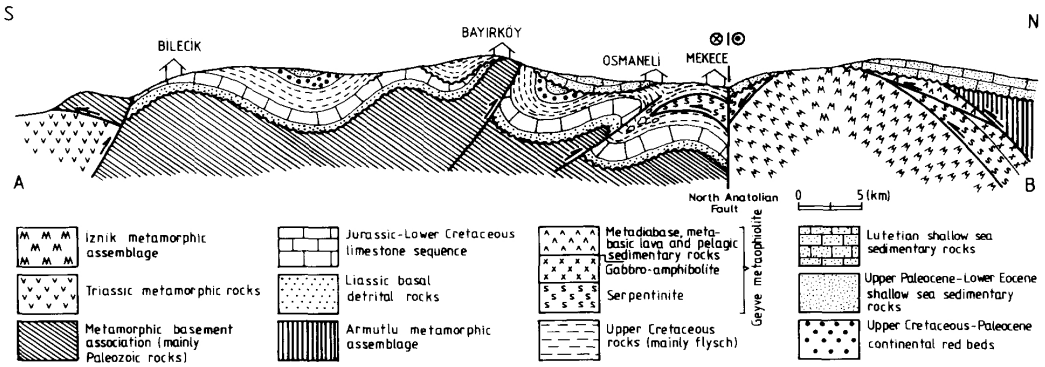

Figure 1.3: Geological cross-section of the Sakarya Terrane and the Armutlu Block by *Yılmaz et al.* (1995). The cross-section is a north-south profile located at 30° east. Significant towns are annotated at the surface. Jagged black lines indicate geological unconformities. Smooth black lines represent faults, with the half-arrows displaying the sense of motion along the fault. Figure from *Yılmaz et al.* (1995).

of the northwards motion of Sakarya Terrane during the closure of the Intra-Pontide Ocean and the subsequent collision with the Istanbul Zone in the Upper Cretaceous (*Okay et al.*, 1994).

The sedimentary sequence overlying the metamorphic basement contains no rocks older than the Upper Triassic (210 – 230 Ma) (*Okay et al.*, 1994) (Fig. 1.3). The main geological unit overlying the basement of the Sakarya Terrane is a Jurassic – Paleogene sedimentary succession (*Okay*, 2008, *Okay and Tüysüz*, 1999). The boundary between the Istanbul Zone and the Sakarya Terrane is known as the Intra-Pontide Suture, and is located within the Armutlu-Almacik Block (described in Sec. 1.1.4) (*Yılmaz et al.*, 1995, *Akbayram et al.*, 2013). During the collision of the Istanbul Zone and Sakarya Terrane during the Cretaceous, the Istanbul Zone may have been thrust on top of the Sakarya Terrane (*Yılmaz et al.*, 1995).

1.1.4 Geology of the Armutlu Block

Located between the Istanbul Zone and the Sakarya Terrane is the Armutlu-Almacik Block. Once a contiguous tectonic unit, the Armutlu Block has been separated from the Almacik Block due to right lateral motion along the North Anatolian Fault since the Pliocene epoch (3 Ma) with a total offset of 52 km (*Akbayram et al.*, 2016). This offset has placed the Armutlu Block within the Izmit-Adapazari region. The Armutlu Block is an east–west trending chain of mountains, although the cause of this high topography is unclear. Possible explanations include the collision of the Istanbul Zone and the Sakarya Terrane (*Yılmaz et al.*, 1995) or the classification of the Armutlu-Almacik Block as push-up structures due to strike-slip motion on the North Anatolian Fault (*Yıldırım and Tüysüz*, 2017).

The geology of the Armutlu Block is dominated by assemblages of metamorphosed

sedimentary rocks (*Akbayram et al.*, 2013). In the south eastern portion of the Armutlu Block, the Geyve metaophiolite contains layers of ultramafic rocks and basaltic lavas, along with metamorphosed deep marine sediments. The Geyve metaophiolite likely represents the remnants of the Intra-Pontide Ocean sandwiched between the Istanbul Zone and Sakarya Terrane, and could represent the Intra-Pontide Suture (*Yılmaz et al.*, 1995). A geological cross-section of the Sakarya Terrane and the Armutlu Block, showing the Geyve metaophiolite, is shown in Fig. 1.3. The crystalline basement of the Istanbul Zone is also close to the surface, and outcrops at the eastern end of the Armutlu Block (*Akbayram et al.*, 2013).

On the southern edge of the Armutlu Block, at the contact with the southern branch of the North Anatolian Fault, is the Pamukova sedimentary basin. The Pamukova basin is an elongate structure (30 km long and 6 km wide) filled with Quaternary sedimentary rocks likely deposited by the Sakarya river that flows through the basin (*Şengör et al.*, 2005). Stress analysis of striations and slickenlines along the southern branch of the North Anatolian Fault within the Pamukova basin indicate it likely opened due to extension in the NE–SW direction related to strike slip motion along the North Anatolian Fault (*Doğan et al.*, 2014). The thickness of the sediment within the Pamukova basin is generally unknown, but it is thought to be less than within the Adapazarı basin (*Şengör et al.*, 2005). *Frederiksen et al.* (2015) estimate the thickness of the consolidated sedimentary cover to be greater than 3.5 km, similar to the Adapazarı basin (Sec. 1.1.2).

1.1.5 Neotectonics and the North Anatolian Fault

The North Anatolian Fault Zone (NAFZ) is a large right lateral strike-slip fault system that delineates the boundary between the Anatolian block (modern day Turkey) and the continent of Eurasia. Part of the Alpine-Himalayan system, the NAFZ began to localise at the Karliova Triple Junction in eastern Turkey during the early Miocene epoch (16 – 20 Ma) and tracks approximately 1200 km across northern Turkey to the Sea of Marmara at İzmit (*Şengör*, 1979), and then into the Marmara Sea (*Koukouvelas and Aydin*, 2002).

The Anatolian peninsula has experienced an anti-clockwise rotation as the result of a gradient in gravitational potential energy (*England et al.*, 2016) that is sustained by the collision of the Arabian and Eurasian plates in the east, and the roll-back of the Hellenic subduction zone to the south west of the peninsula. As described in sections 1.1.2, 1.1.3 and 1.1.4 most of the geology of the Izmit-Adapazari region pre-dates the formation of the North Anatolian Fault Zone by roughly 70 million years. As such, modern day strike slip motion along the NAFZ is overprinting geological structures that formed as a result of continental collision during the Upper Cretaceous.

Major seismic activity on the North Anatolian Fault

Initially believed to be the suture zone between Gondwana and Eurasia in Anatolia following the Alpine orogen, the NAFZ's true nature as a strike slip fault was revealed after a devastating earthquake (M_w 7.8) at Erzincan in 1939 (*Şengör*, 1979). Since 1939 a sequence of westward propagating large earthquakes ($M_w > 6.7$) has followed the Erzincan event (*Ambraseys*, 1970). Each subsequent earthquake in this sequence appears to trigger the next towards the west, with a mean period of 10 years between the events (*Stein et al.*, 1997). Coulomb stress calculations by *Stein et al.* (1997) show that each large event that has occurred along the North Anatolian Fault since 1939 has increased stress significantly in the region of the earthquake that strikes next, and that particularly large events have the potential to permanently alter the stress state of the region. *Hubert-Ferrari et al.* (2000) used similar modelling techniques to show that the entire length of the North Anatolian Fault likely ruptured in a similar cascading sequence of earthquakes between the years 1668 and 1766 A.D., and that the recent M_w 7.6 İzmit earthquake in 1999 has greatly increased the likelihood of a large earthquake occurring beneath the Marmara Sea in the near future. The 1999 İzmit earthquake was particularly devastating (*Barka*, 1999). This event ruptured a 145 km long section of pre-existing faults between the Hersek delta near İzmit, and the town of Akyazi (*Barka et al.*, 2002). The highest level of strike-slip displacement was 5.2 m, recorded between Lake Sapanca and Akyazi, near the town of Adapazarı (Fig. 1.2), though there was also a component of normal faulting (2.3 m), particularly between İzmit and Lake Sapanca (*Barka et al.*, 2002).

Aseismic creep on the North Anatolian Fault

Following the 1999 event, geodetic observations by *Hussain et al.* (2016a) observed a degree of aseismic creep along the İzmit section of the fault in the Izmit-Adapazari region. The average creep rate between 2002 and 2010 was 11 ± 2 mm/yr, though there was a rapid deceleration within the first 5 years following the İzmit earthquake to a rate of approximately 5 mm/yr. *Hussain et al.* (2016a) calculated that the moment released by this aseismic creep is small compared to that of the İzmit earthquake, and amounts to a maximum of 40% of the moment accumulation from plate loading. It is therefore likely that the North Anatolian Fault remains mostly locked and is accumulating strain in the Izmit-Adapazari region. The rapid deceleration of this creep following the 1999 İzmit earthquake suggests that it is likely a transient effect associated with afterslip following the main event. The only section of the North Anatolian Fault currently known to undergo aseismic creep during the interseismic period is a 130 km long section near the town of Ismetpasa in the central part of the fault zone to the east of Izmit-Adapazari (*Ambraseys*, 1970, *Hussain et al.*, 2016b). Geodetic measurements by *Hussain et al.* (2016b) found an average creep rate of 8 ± 2 mm/yr along this section,

which would only reduce the rate of interseismic strain accumulation by a maximum of 40% compared to a fully locked fault. These observations show that all sections of the North Anatolian Fault are currently accumulating strain, and remain capable of producing large earthquakes.

Geometry the North Anatolian Fault in the Izmit-Adapazari region

The ages of the pull-apart sedimentary basins on the Izmit-Adapazari section of the North Anatolian Fault indicate that it is relatively young compared to the fault further east, likely becoming active within the past 2 million years (*Şengör et al.*, 2005). In the Izmit-Adapazari region, the North Anatolian Fault bifurcates into two strands: a northern branch and a southern branch. The northern branch ruptured during the 1999 İzmit earthquake. The northern branch of the North Anatolian Fault appears to exploit the boundary between the Istanbul Zone (1.1.2) and the Armutlu Block (1.1.4), and the southern branch marks the boundary between the Armutlu Block and the Sakarya Terrane (1.1.3).

This bifurcation of the fault zone is likely due to the general westward broadening of the zone of deformation associated with the North Anatolian Fault (*Şengör et al.*, 2005), which is accompanied by a reduction in fault slip rate in the west (*Hussain et al.*, 2016b). The northern branch appears to have formed a well connected, through-going fault, whilst the southern branch appears to be much more fragmented (*Şengör et al.*, 1985, *Le Pichon et al.*, 2003). Stress modelling utilising paleostress orientations and local earthquake focal mechanisms done by *Karimi et al.* (2014) show that the northern and southern branch of the North Anatolian Fault are likely linked by another fault that separates the Armutlu Block from the Almacik Mountains.

Of the two fault branches, the northern branch is more active, although considerable seismicity also occurs along the southern branch (*Altuncu Poyraz et al.*, 2015). Whilst the major ($M_w > 6.7$) earthquakes seem to be localised to the main fault branches (*Barka et al.*, 2002), *Altuncu Poyraz et al.* (2015) also note that the micro-seismicity is not very well localised to the main structures of the North Anatolian Fault, and a significant amount of deformation occurs off of the mapped faults. The focal mechanisms of the seismicity show predominantly right-lateral strike-slip faulting, especially along the northern and southern branches of the North Anatolian Fault. Within the Adapazarı basin, there is a large amount of normal faulting (*Altuncu Poyraz et al.*, 2015).

1.1.6 The Dense Array for Northern Anatolia (DANA)

Between May 2012 and October 2013 the University of Leeds and Turkish partners including Kandilli Observatory and Earthquake Research Institute and Sakarya University deployed a network of seismometers throughout the Izmit-Adapazari region,

across both the northern and southern branches of the North Anatolian Fault Zone (*DANA*, 2012). The array was known as the Dense Array for Northern Anatolia, or DANA, and was specifically deployed across the rupture zone of the 1999 İzmit earthquake.

DANA consisted of a main body of 66 three component seismometers deployed in 6 north–south oriented lines to build a rectangular array with an aperture approximately 70 km north–south, and 35 km east–west. The stations that comprise this part of the array are referred to as D[A–F][01–11]. A–F indicates the longitudinal position of the station, with A being the most western line, and F the most eastern. [01–11] indicates the latitudinal position, with 01 in the south, and 11 in the north. The majority of the instruments are broad-band Guralp CMG-6TD's (maximum period 30 s), but some stations (DA01, DA07, DA11, DD02, DF01, DF06, DF11) are CMG-3T's (maximum period 120 s). The main rectangular array was supplemented by 7 stations positioned to the east in a semi-circular pattern. These stations were named KO0[1–7], with KO01 being the most southern station and KO07 being the most northern. These instruments were all Guralp CMG-6TD's.

DANA was designed to provide optimal resolution for seismic images of the crust, and the data set has been used for a variety of applications including transfer functions (*Frederiksen et al.*, 2015), receiver functions (*Kahraman et al.*, 2015) and teleseismic tomography (*Papaleo et al.*, 2017, 2018). The results of these studies will be introduced in Sec. 1.2. In this thesis I will use the DANA dataset for imaging using techniques from seismic interferometry (Sec. 1.3) in Chapters 2, 3 and 4.

1.2 The structure of fault zones

Knowledge of the geological structure of fault zones plays an important role in understanding the physical processes that control them. In particular, imaging structural changes within the lithosphere in the vicinity of fault zones allows insights into the mechanisms of strain localisation and lithospheric rheology and has important implications for our understanding of the earthquake cycle and seismic hazard. Seismic imaging allows us to directly observe the physical properties of the rocks within and around a fault zone. This section will briefly summarise the seismic methods that are relevant to the discussion in this thesis, and I will highlight some important results of studies that have utilised these techniques to image fault zones.

1.2.1 Seismic tomography and the seismic velocity structure of fault zones

Seismic tomography

Seismic tomography is the general term given to the technique of using seismic observations to construct a model of the distribution of seismic velocities within the earth. Generally, seismic tomography requires solving a large non-linear inverse problem that relates our observations to seismic velocity. The problem is non-linear due to the fact that the path taken by seismic waves through the Earth is a function of the velocity structure through which it passes. However, the number of model parameters required to satisfactorily describe an Earth model also mean that fully non-linear approaches are often too computationally intensive to attempt. The most common set of observations that are inverted in seismic tomography are travel time observations of particular seismic phases, such as the direct P-wave. Good overviews of travel time tomography are given by *Phillips and Fehler* (1991), *Rawlinson and Sambridge* (2003) and *Rawlinson et al.* (2010). Recent advances in computing infrastructure have also created opportunities for techniques that model the entire seismic waveform, rather than being limited to travel times. Full waveform tomography is the process of obtaining a seismic image by modelling the interaction between structure and the shape of seismic waveforms. The principle is the same as with travel time tomography, although the forward problem that must be modelled is different. Instead of computing theoretical travel times to compare to the data, synthetic seismograms must be calculated at each iteration of the inversion. Further details of full waveform tomography can be found in *Virieux and Operto* (2009), *Liu and Gu* (2012) and the references contained therein.

There are two principle wave types that can be utilised in a tomography study: body waves and surface waves. In body wave tomography, the travel times of first arrivals of a particular seismic phase (usually the direct P-wave) from a particular seismic source are recorded at a set of receivers that overlie the target region of the Earth. In body wave tomography studies that utilise teleseismic earthquakes as the source, it is necessary to overcome errors in the origin time of the earthquake and uncertainties associated with the long path the wave takes outside of the target region. these uncertainties are normally resolved by removing the mean travel time residual with respect to some reference velocity model on a source-by-source basis. Removing the mean travel time comes at the expense of information relating to absolute seismic velocity of the target region, and the velocity relative to the reference model is often the parameter that is quoted instead. When the sources are in closer proximity to the receivers, such as in local earthquake tomography, the path uncertainties are smaller, and this process is often unnecessary. It is often difficult to constrain near surface structure using body wave tomography as the rays will arrive at the stations on the surface with similar (near vertical) angles of incidence. The lateral resolution at shallow depths is controlled by

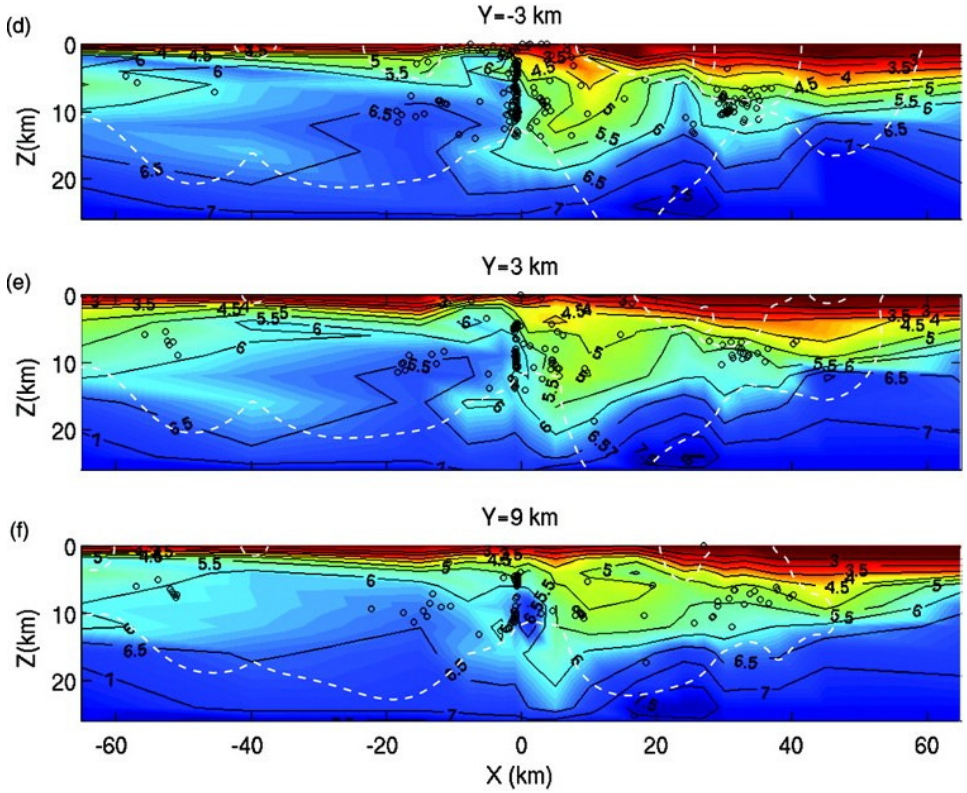

Figure 1.4: Selected fault perpendicular profiles of the 3-D velocity model of the San Andreas Fault in the Parkfield region from *Thurber et al.* (2006). The black contours and colours from red (slow) to blue (fast) indicate P-wave velocity. The white dashed contour encloses the region believed to be well-resolved by *Thurber et al.* (2006). Black circles indicate the hypocentres of earthquakes used in the tomographic inversion. X = 0 km indicates the location of the San Andreas Fault trace, and the Y variable indicates the along-strike distance of the profile. Figure modified from *Thurber et al.* (2006).

the geographical separation of receivers on the surface.

Surface wave tomography exploits the dispersive property of surface waves in order to image seismic velocities as a function of depth. Longer period surface waves will arrive at a receiver earlier than short period surface waves from the same source. This is due to the fact that longer period surface waves are sensitive to deeper structure within the Earth, and seismic velocity tends to increase with increasing depth. Surface waves are overwhelmingly sensitive to the S-wave velocity structure of a medium, and as such are normally restricted to producing models of S-wave velocity. The amplitudes of surface waves decay exponentially with depth, and so they are best suited for constraining relatively shallow structure within the Earth. The depth resolution of a surface wave study is controlled by the period of the waves that can be measured.

Examples of fault zone imaging with seismic tomography

A great deal of modern seismic tomography studies that focus on the imaging of fault zones within the crust use the San Andreas Fault Zone in California as their target.

The San Andreas Fault is heavily instrumented with many permanent and temporary networks of seismometers. This is primarily due to the San Andreas Fault's location within, and hazard it poses to, one of the most economically developed regions of the United States. One of the earliest earthquake body wave tomography studies of the San Andreas Fault was carried out by *Eberhart-Phillips and Michael* (1993) and *Michael and Eberhart-Phillips* (1991), who studied the 3-D structure of the top 15 km of the Parkfield region in central California. The most important result of *Eberhart-Phillips and Michael* (1993) was the observation of a sharp change in seismic velocity across the San Andreas Fault. This sharp contrast in seismic velocity is well correlated with the transition to the north eastern section of the San Andreas that is known to exhibit significant aseismic creep (32 ± 3 mm/yr (*Thatcher*, 1979)). *Eberhart-Phillips and Michael* (1993) hypothesise that this creep may be encouraged in this region due to the simple structure and uniform contrast in physical properties across the fault. Another observation made by *Eberhart-Phillips and Michael* (1993) is that despite the complexity of the geology near the surface along the San Andreas Fault, at depth the fault appears to be a narrow, vertical structure up to a depth of at least 15 km.

Thurber et al. (2006) took advantage of an increase in the quantity of seismic observations to improve upon the 3-D model of the Parkfield region of *Eberhart-Phillips and Michael* (1993). The results of *Thurber et al.* (2006) supported the existence of a sharp velocity contrast across the San Andreas Fault (Fig. 1.4), and relocated earthquake hypocentres also show a narrow, simple structure for the fault through the upper crust. A large seismic velocity contrast was also observed across the Denali Fault in Alaska by *Allam et al.* (2017). This velocity contrast appears to be pervasive throughout the crust into the upper mantle (>35 km depth). *Allam et al.* (2017) interpret that the Totschunda fault segment of the Denali Fault zone likely exploits an old suture zone, and in turn appears to be far more tectonically active than the main eastern branch of the Denali Fault, including rupturing during the 2002 M_w 7.9 Denali earthquake (*Eberhart-Phillips et al.*, 2003).

Seismic tomography has also been carried out on the southern section of the San Andreas Fault Zone in the vicinity of the San Jacinto Fault, south east of Los Angeles. *Zigone et al.* (2015) carried out a surface wave tomographic study to construct an S-wave velocity model of the top 7 km of the crust. This tomography model is shown in Fig. 1.5. An interesting feature of the model of *Zigone et al.* (2015) is that, near the surface, both the San Andreas Fault and San Jacinto Fault are associated with areas of low S-wave velocity. These low velocity zones are particularly prominent in regions of potentially complicated geological structure, such as the junction between the San Andreas and San Jacinto Fault. *Zigone et al.* (2015) note that the low velocity zones associated with the faults appear to decrease in width at depth, which suggests that the low seismic velocities could be the result of a deformation zone which narrows with depth, typically referred to as a 'flower structure' (*Sylvester*, 1988). Flower structures

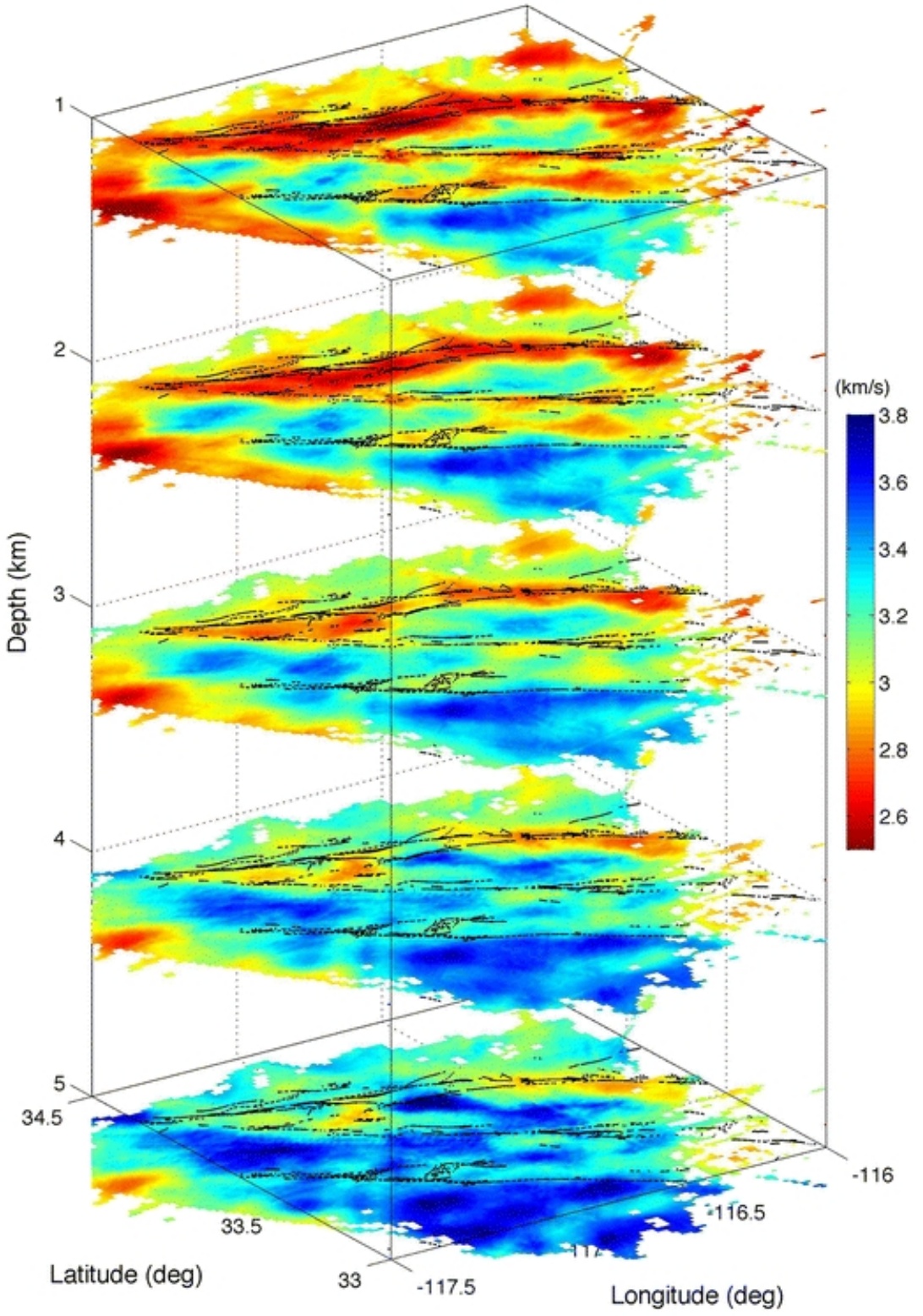

Figure 1.5: Depth slices through the tomographic image of *Zigone et al.* (2015) showing the San Jacinto Fault and the surrounding region. The colours in the image show S-wave velocity as derived from an inversion of Rayleigh wave group velocities. The mapped faults from closest to farthest in the figure are: Elsinore Fault, San Jacinto Fault and San Andreas Fault. Figure from *Zigone et al.* (2015)

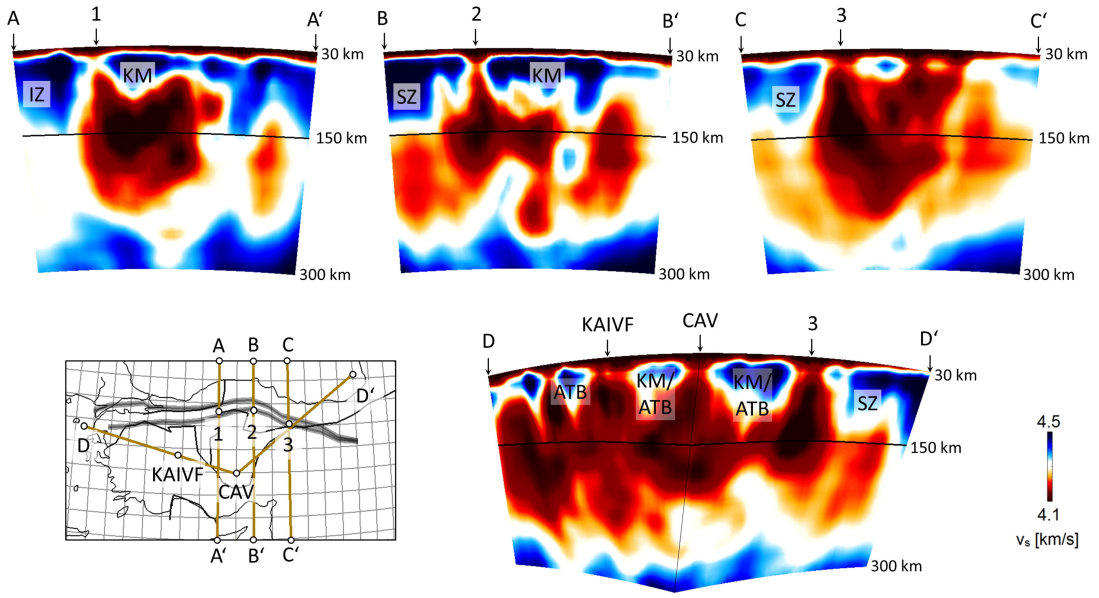

Figure 1.6: S-wave velocity model of the lower crust and upper mantle beneath the North Anatolian Fault. The locations of the four profiles are shown on the map of Turkey in the lower left. Major tectonic units of Turkey are labelled: IZ = Istanbul Zone (Sec. 1.1.2), SZ = Sakarya Zone (Sec. 1.1.3), km = Kırşehir Massif, ATB = Anatolide-Tauride Block and CAV = Central Anatolian Volcanics. Figure from *Fichtner et al.* (2013).

in the vicinity of the San Jacinto Fault were also interpreted in a larger scale body wave tomography of southern California (*Allam and Ben-Zion*, 2012). Broad damage zones are typically features of relatively young faults, and are the result of the early organisational stage of fault formation, before deformation can localise onto a single narrow fault plane (*Ben-Zion and Sammis*, 2003).

Low velocity zones are also associated with other continental transform faults. *Eberhart-Phillips and Bannister* (2002) used body wave tomography to construct a velocity model of the Alpine Fault, located on the South Island of New Zealand. *Eberhart-Phillips and Bannister* (2002) observed a narrow (<20 km wide) low velocity zone associated with the entire fault down to a depth of at least 15 km. Along the south-eastern portion of the Alpine Fault, where the sense of motion is primarily strike slip, this low velocity zone cuts vertically through the crust. In sections where there is a significant component of dip slip the low velocity zone transitions to become a dipping structure (*Norris and Cooper*, 2001).

Seismic tomography studies of the North Anatolian Fault Zone

The North Anatolian Fault Zone has been imaged at depth by *Fichtner et al.* (2013), who constructed an isotropic S-wave velocity model using full waveform tomography of earthquake sources. Crucially, *Fichtner et al.* (2013) observe that the structure of the North Anatolian Fault is not confined to the crust, and appears to be associated with a low velocity anomaly that penetrates far into the upper mantle, at least until

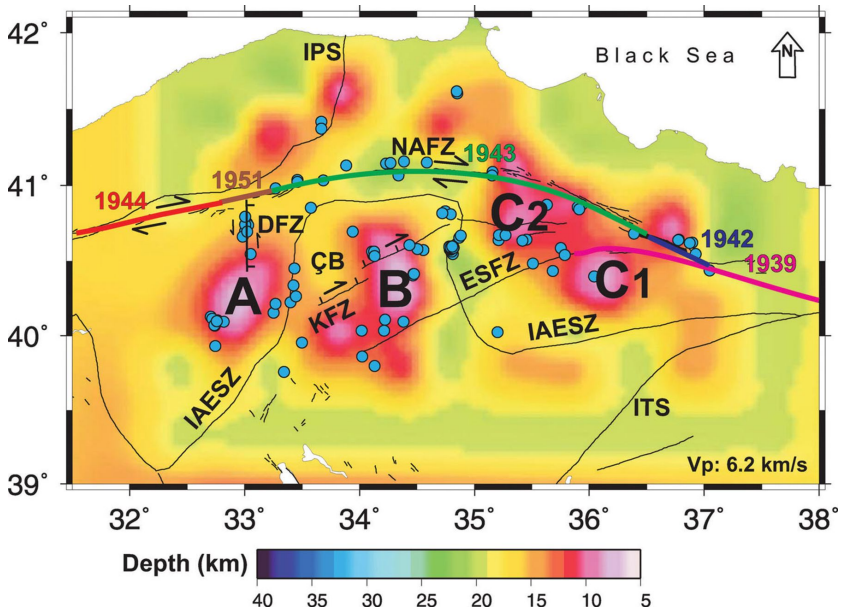

Figure 1.7: Map of the central section of the North Anatolian Fault and the depth to high velocity material. The colours indicate the depth to material with a P-wave velocity exceeding 6.2 km s^{-1}. The velocity anomalies A, B, C_1 and C_2 are interpreted as continental fragments accreted onto Anatolia during the closure of the Neo-Tethys Ocean. Thin black lines represent important faults and suture zones: IAESZ = Izmir-Ankara-Erzincan Suture Zone, DFZ = Dodurga Fault Zone, ESFZ = Ezine Pazari-Sungurlu Fault Zone, ÇB = Çankiri Basin, KFZ = Kizilirmak Fault Zone, NAFZ = North Anatolian Fault Zone, IPS = Intra-Pontide Suture and ITS = Intra-Tauride Suture. The coloured sections of the North Anatolian Fault Zone represent the rupture zones of the historical earthquakes and their corresponding year of occurrence. The Erzincan earthquake occurred in 1939. Figure from *Yosal-Çevikbilen et al.* (2012)

200 km depth. Within the crust, the model of *Fichtner et al.* (2013) shows that the North Anatolian Fault is often bounded by regions of high seismic velocity, such as the Istanbul Zone and Sakarya Terrane, whilst the fault itself appears to exploit the areas between these blocks (Fig. 1.6). The narrow signature of the fault between the Istanbul Zone and Sakarya Terrane is evidence that the development of the North Anatolian Fault in the crust was guided by pre-existing structures such as suture zones (*Fichtner et al.*, 2013).

Yosal-Çevikbilen et al. (2012) used local earthquake tomography to image the crustal structure of the central section of the North Anatolian Fault Zone in the region of the Izmir - Ankara - Erzincan suture zone. They detect several regions of high P-wave velocity (>6.0 km/s) close to the surface, which they interpret as crystalline basement rocks that were accreted during the subduction of the Neo-Tethys Ocean (Sec. 1.1). *Yosal-Çevikbilen et al.* (2012) also note that the fault zone appears to cut through the zones of high seismic velocity in regions where the dominant stress regime is transtensional, but does not in regions of transpression. *Yosal-Çevikbilen et al.* (2012) also hypothesized that these high velocity blocks could have a role in terminating the ruptures of large earthquakes along the North Anatolian Fault (Fig. 1.7). In particular,

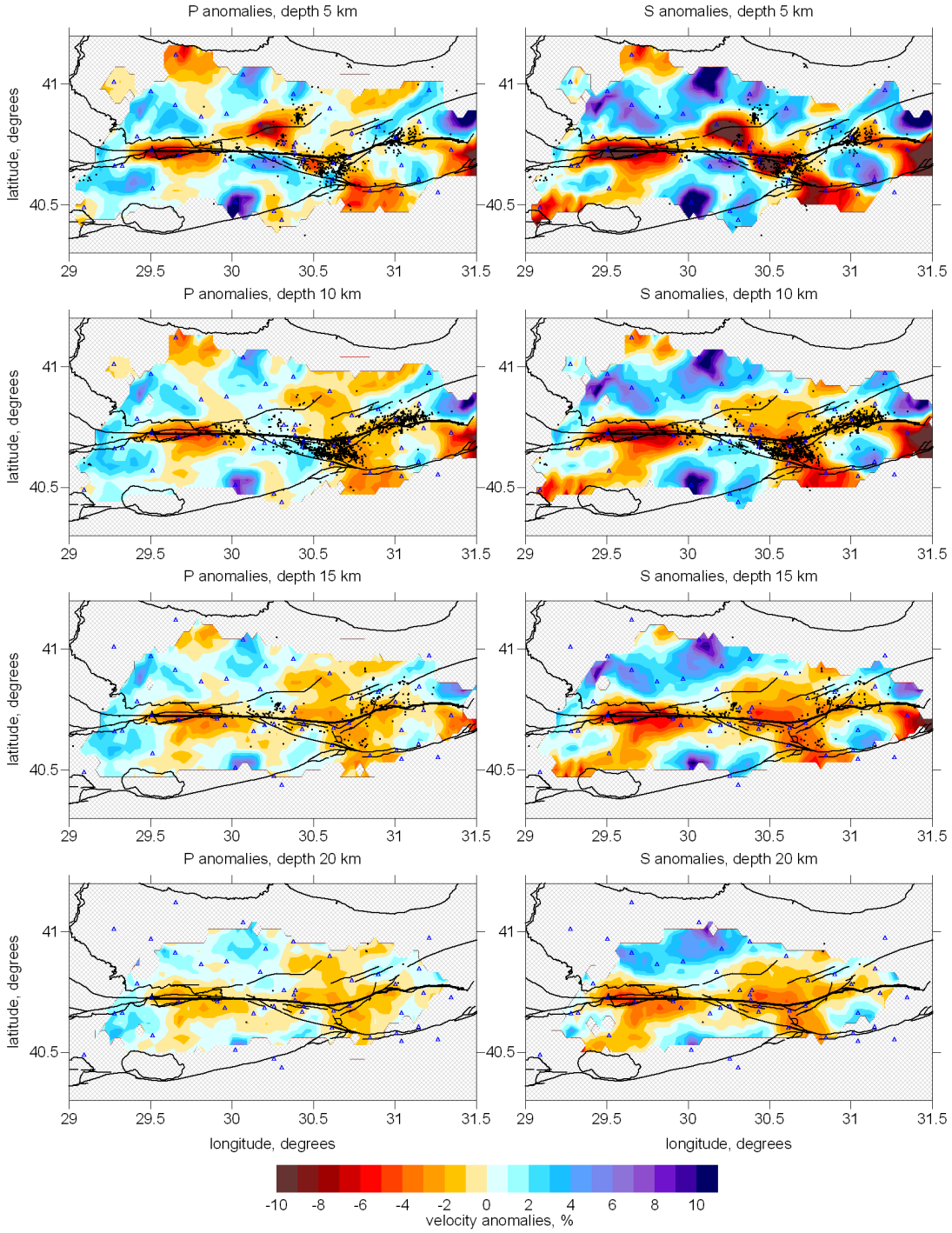

Figure 1.8: P and S-wave velocity anomalies of the Izmit-Adapazari region, derived from local earthquake body wave tomography. Red colours represent low velocities,blue colours represent high velocities. Mapped faults in the area are marked by black lines. Figure from *Koulakov et al.* (2010)

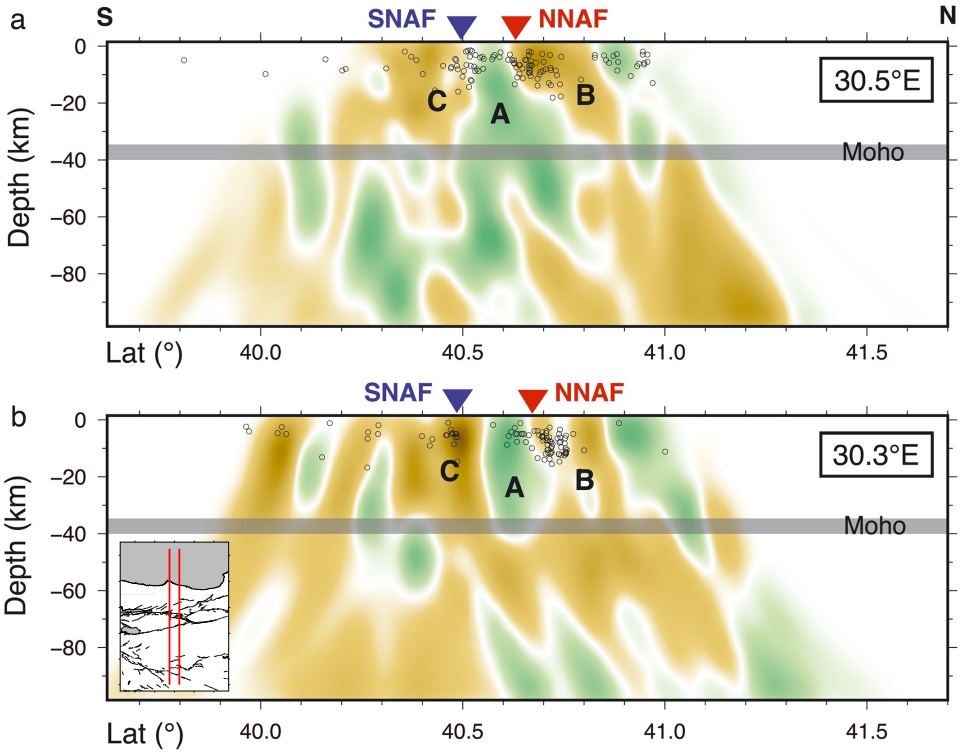

Figure 1.9: P-wave velocity anomalies of the Izmit-Adapazari region. Brown colours represent low velocities, green colours represent high velocities. The locations of the surface traces of the northern and southern branches of the North Anatolian Fault are labelled NNAF and SNAF, respectively (Fig. 1.2). A, B and C refer to anomalies discussed by *Papaleo et al.* (2017). The inset map in the lower left shows the location of the two vertical profiles in the Izmit-Adapazari region with thick red lines. Figure modified from *Papaleo et al.* (2017)

it appears that the rupture of the 1939 Erzincan earthquake was arrested at the edge of one of the high seismic velocity anomalies imaged by *Yosal-Çevikbilen et al.* (2012).

The crustal structure of the Izmit-Adapazari region (Sec. 1.1), which will be the region under investigation in this thesis, has been imaged by local earthquake tomography in the past. *Koulakov et al.* (2010) created P and S-wave velocity models of the Istanbul Zone (Sec. 1.1.2) and Armutlu Block (Sec. 1.1.4), which is shown in Fig. 1.8. *Koulakov et al.* (2010) imaged low seismic velocities associated with Adapazarı Basin and the faulted sediments near İzmit, as well as high seismic velocities for the Armutlu Block. *Koulakov et al.* (2010) also recognised the lack of seismicity within the Armutlu Block, indicating an apparent resistance to strain, and commented that it appears that strain is typically localised to regions of sharp contrasts in seismic velocity structure.

Most recently, the P- and S-wave velocity structure of the Izmit-Adapazari region has been imaged using teleseismic tomography by *Papaleo et al.* (2017) (P-wave) and *Papaleo et al.* (2018) (S-wave). The data set used by *Papaleo et al.* (2017) and *Papaleo et al.* (2018) is the same as that used in this thesis, and is described later in section 1.1.6. The P-wave velocity model is shown in Fig. 1.9. Both of these studies observe a strong velocity contrast over the fault zone, and a low velocity zone that appears to

be strongly associated with the northern branch (Sec. 1.1.5) of the North Anatolian Fault. The velocity contrast likely represents the Intra-Pontide Suture (Sec. 1.1) that has been exploited by the North Anatolian Fault. The models of both *Papaleo et al.* (2017) and *Papaleo et al.* (2018) show that this low velocity zone is at most 12 km wide throughout the crust, but broadens considerably to a width of approximately 50 km below the Moho. *Papaleo et al.* (2017) also note that both the southern and northern branches of the North Anatolian Fault are localised at the edges of the Armutlu Block (Sec. 1.1.4), a region of high seismic velocity, and suggest that the Armutlu Block is a barrier to strain.

1.2.2 Receiver functions and the deep structure of faults

Receiver functions are a seismic technique useful for detecting discontinuities in physical properties beneath seismic stations. Receiver functions will be briefly discussed here as there are considerable parallels that can be drawn between receiver functions and the autocorrelation methods that will be presented in chapters 2 and 4. P-wave receiver functions are primarily sensitive to discontinuities in velocity structure beneath a seismometer. They are usually calculated by deconvolving the P-wave coda recorded on the vertical component of a seismogram from one of the horizontal components (e.g. *Langston* (1979), *Ligorria and Ammon* (1999)). In theory, this process removes the main P-wave and its coda, leaving S-waves produced by P-to-S conversions at velocity discontinuities encountered by the P-wave.

Receiver function studies of fault zones

The San Andreas Fault in California has been a common target for receiver function studies. *Zhu* (2000) constructed a profile of receiver functions that spanned the San Andreas Fault and the East California Shear Zone in southern California, north of Los Angeles. His results (Fig. 1.10) show a clear P-to-S conversion from the Moho at roughly 30 km depth throughout the profile. Beneath the surface trace of the San Andreas Fault, the Moho appears to be offset by as much as 5 km within 20 km of the fault, and the amplitude of the conversion is much reduced. *Zhu* (2000) attributes this offset in the Moho to right-lateral motion of the crust that has juxtaposed two crustal blocks of different thickness, and concludes that the San Andreas Fault remains a narrow (<10 km wide) zone of deformation into the upper mantle. The amplitude of the Moho conversion beneath the East California Shear Zone is also reduced, suggesting that this structure also penetrates the upper mantle in a zone that is 10 – 20 km wide.

A further receiver function study of the entire San Andreas Fault System was carried out by *Ford et al.* (2014), who found that a shear zone up to 50 kim wide associated with the San Andreas Fault may even extend into the asthenosphere. *Ford et al.* (2014) detected an abrupt change in depth of a discontinuity that they interpret to be

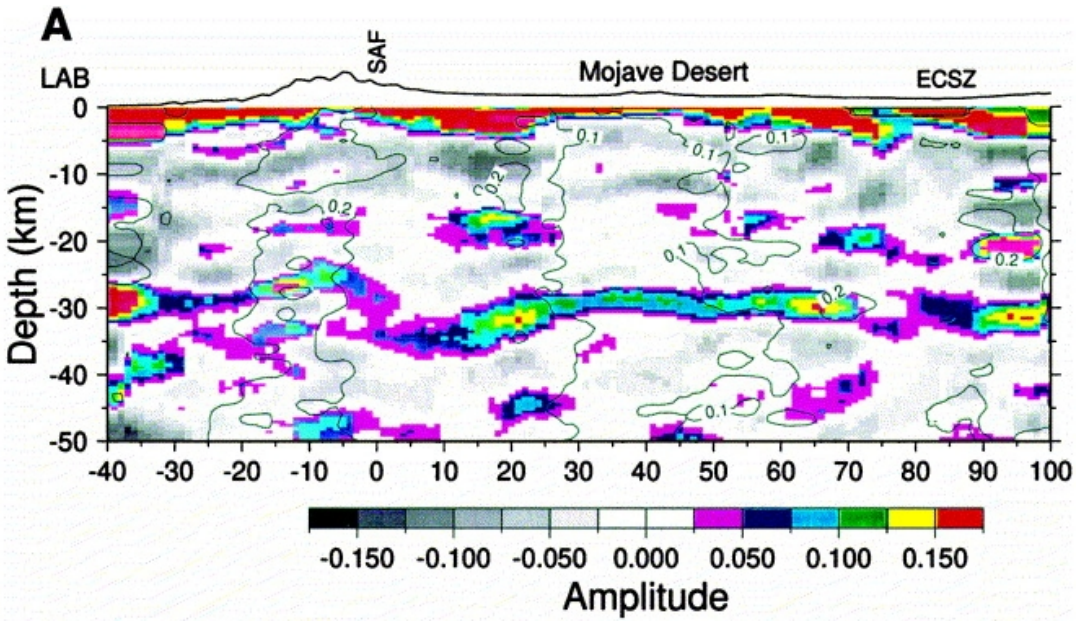

Figure 1.10: Receiver function image of the San Andreas Fault and East California Shear Zone from *Zhu* (2000). The colour scale indicates the amplitude of P-to-S conversions beneath the seismometers. The most prominent arrival is from the Moho, typically at about 30 km depth. The contours are annotated with the variance of the stack for the common conversion point receiver functions. The features labelled in the figure are: LAB = Los Angeles Basin, SAF = San Andreas Fault and ECSZ = East California Shear Zone.

the lithosphere-asthenosphere boundary. This offset of the lithosphere-asthenosphere boundary correlates spatially with the surface trace of the San Andreas Fault, occurs over a region less than 50 km wide, and suggests that strain localisation is possible throughout the lithosphere (*Ford et al.*, 2014).

Evidence for the localisation of strain at depth is not restricted to the San Andreas Fault, or indeed to continental transform faults. *Zhang et al.* (2014) calculated receiver functions for a profile of seismometers across western Tibet. The images (Fig. 1.11) produced by *Zhang et al.* (2014) clearly show several discontinuities in P-to-S conversions from the lower crust and the Moho that are associated with steeply dipping thrust faults. This deflection of the Moho below a thrust fault implies significant stress that appears to be concentrated over a relatively narrow region (*Zhang et al.*, 2014), and has been noted in other receiver function and wide-angle reflection studies of the Tibetan Plateau (*Hirn et al.*, 1984, *Vergne et al.*, 2002). There is also evidence of a strong P-to-S conversion from a discontinuity at around 50 km depth in the lower crust (Fig. 1.11). *Zhang et al.* (2014) interpret this observation as the top of an eclogitised layer, which would require fluid present within the lower crust where eclogitisation reactions occur.

Distortion of the Moho is not always observed beneath major faults. A receiver function image of the Marlborough Fault Zone produced by *Wilson et al.* (2004) shows a continuous Moho that is not disrupted in the vicinity of the fault system. A large

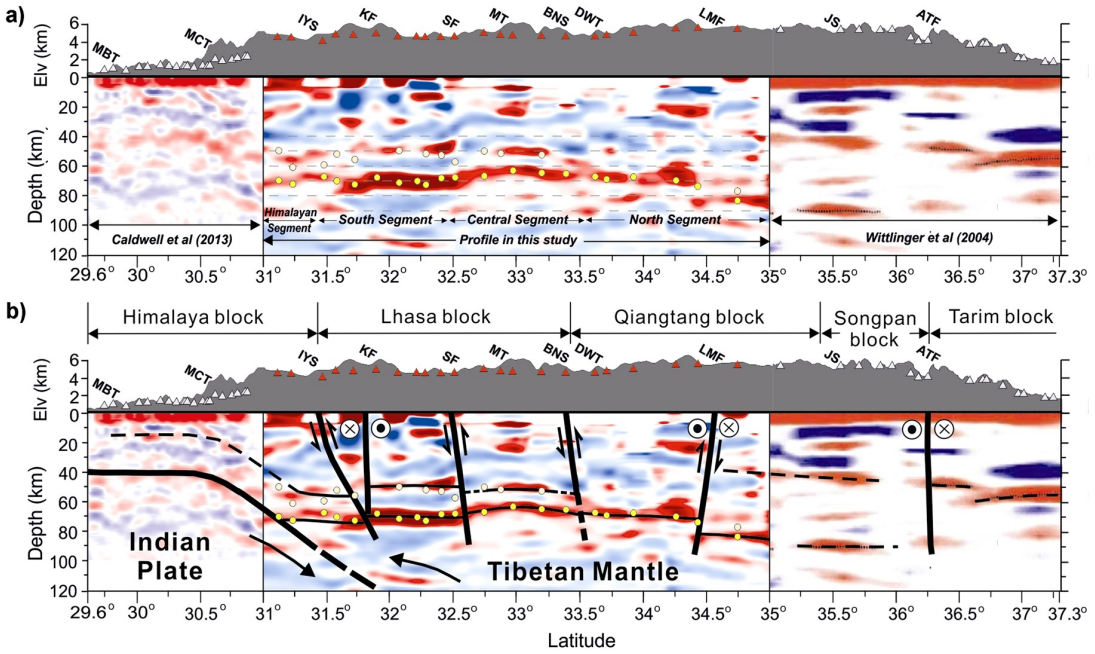

Figure 1.11: Receiver function image from a line of receivers through western Tibet at 80^circ east from *Zhang et al.* (2014). Red colours indicate positive amplitude P-to-S conversions, blue colours indicate negative conversions. a) Raw receiver function image. Topography is shown in grey, and station locations are shown as red triangles. Yellow circles indicate Moho depths. Structural features annotated on the section are: MBT = Main Boundary Thrust, MCT = Main Central Thrust, IYS = Indus-Yarlung Suture, KF = Karakorum Fault, SF = Shiquanhe Fault, MT = MandongCuobei Thrust, BNS = BangongNujiang Suture, DWT = DomarWuijiang Thrust, LMF = Longmucuo Fault, JS = Jinsha Suture and ATF = Altyn Tagh Fault. b) Receiver function profile shown in a), but annotated with the major thrust faults shown by thick black lines. The two other profiles shown are from *Caldwell et al.* (2013) and *Wittlinger et al.* (2004). Figure from *Zhang et al.* (2014)

variation in conversion amplitude as a function of azimuth has been interpreted in terms of a degree of seismic anisotropy in the lower crust beneath the Marlborough Fault Zone. *Wilson et al.* (2004) interpret both these observations as evidence that the surface faulting transitions into a zone of more diffuse (>60 km wide) deformation below approximately 15 km depth, rather than forming a discrete shear zone that cuts through the entire crust.

Receiver function study of the Izmit-Adapazari region

Kahraman et al. (2015) carried out a receiver function study of the Izmit-Adapazari region using the same data set that will be used for the work presented in this thesis (Sec. 1.1.6). North–South and East–West profiles from *Kahraman et al.* (2015) are shown in Fig. 1.12. The Moho is observed at approximately 38 km depth. Localised deformation associated with the northern branch of the North Anatolian Fault was found to penetrate into the upper mantle to a depth of at least 50 km, and the P-to-S conversion from the Moho beneath the fault has a reduced amplitude (*Kahraman*

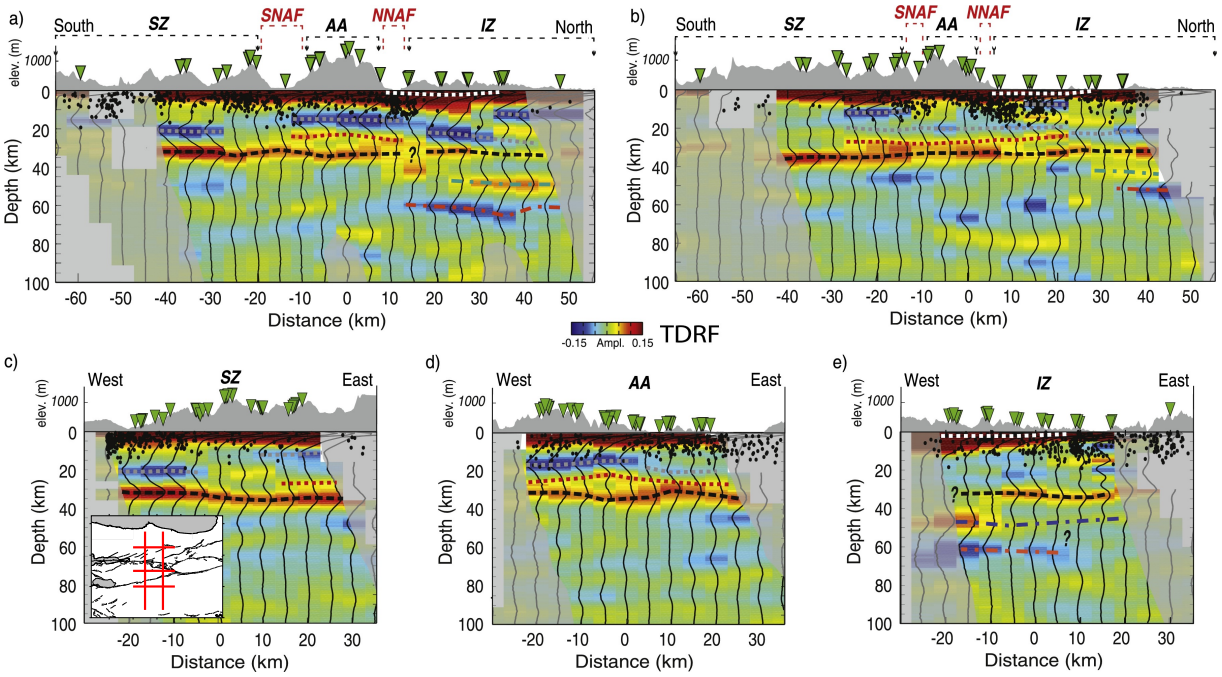

Figure 1.12: Receiver function image of the Izmit-Adapazari region from *Kahraman et al.* (2015). Red colours indicate positive amplitude P-to-S conversions, blue colours indicate negative conversions. a) Raw receiver function image. Topography is shown in grey, and station locations are shown as green triangles. Structural features are annotated as: SZ = Sakarya Zone (Sec. 1.1.3), AA = Armutlu Block (Sec. 1.1.4), IZ = Istanbul Zone (Sec. 1.1.2), NNAF = Northern branch of the North Anatolian Fault and SNAF = Southern branch of the North Anatolian Fault. The thick red lines on the inset map shows the location of the profiles within the Izmit-Adapazari region. Figure modified from *Kahraman et al.* (2015)

et al., 2015). In addition, it appears as if the northern branch of the North Anatolian Fault dips towards the north, although the steepness of this dip is variable, and the dip reduces to the east. On the other hand, the southern branch of the North Anatolian Fault does not seem to be associated with an offset in the Moho, though it appears that there may be two conversions in the lower crust (one positive and one negative) that are truncated by the southern branch (Fig 1.12). As such it is difficult to conclude how the southern branch is interacting with the deep structure of the fault zone, and whether strain is significantly localised in the upper mantle (*Kahraman et al.*, 2015). In addition, there are several conversions with negative amplitude in the lower crust of the Izmit-Adapazari region, particularly beneath the Armutlu Block (Sec. 1.1.4). Negative amplitudes in P-to-S receiver function images are normally interpreted to represent the top of zones of low P-wave velocity.

1.2.3 Azimuthal anisotropy and the mechanisms for deformation in fault zones

Seismic anisotropy, the variation of seismic velocity through a material as a function of the direction of travel, is a useful tool in fault zone imaging. In particular, mea-

surements of anisotropy can be used to determine patterns of deformation within the Earth. This is due to the fact that the crystal structure of many common minerals such as olivine (e.g. *Hess* (1964), *Ismaïl and Mainprice* (1998)), amphibole and micas (e.g. *Mainprice and Nicolas* (1989), *Kern and Wenk* (1990), *Sherrington et al.* (2004)) are inherently anisotropic. These minerals tend to form cleavage planes, or have a preferred crystallographic orientation that aligns with the dominant strain field. In a bulk rock, where minerals are typically randomly oriented, this anisotropy will tend to cancel out on average, leading to a material that is isotropic overall. However, once a rock undergoes deformation, crystallographic axes can align in a preferred orientation. If this occurs, the bulk rock will become anisotropic just like the minerals it is composed of (e.g. *Savage* (1999), *Tommasi et al.* (2000)).

Several studies have shown that micas, amphiboles and clay minerals such as sillimanite will often dominate the anisotropy of a bulk rock, even if they are not the most abundant mineral (*Mainprice and Nicolas*, 1989, *Kern and Wenk*, 1990, *Ji and Salisbury*, 1993, *Barruol and Kern*, 1996). Quartz and feldspar, whilst common in crustal rocks and anisotropic in single crystal form, typically do not form a preferred orientation that causes significant anisotropy (*Kern and Wenk*, 1990, *Ji and Salisbury*, 1993, *Barruol and Kern*, 1996). Experiments performed by *Kern and Wenk* (1990) showed that fast directions of both P and S-waves is usually parallel to the foliations formed in mid and lower crustal rocks that have undergone deformation.

Another cause of seismic anisotropy, particularly in the upper crust, is the presence of aligned cracks (e.g. *Crampin et al.* (1980), *Crampin* (1981)). Aligned fractures are an important source of anisotropy when the confining pressure is low (*Kern and Wenk*, 1990). This anisotropy can be significant, particularly for fluid filled cracks (*Crampin*, 1987), which can have an especially strong effect on S-wave velocity. *Kendall et al.* (2006) found that the uppermost 75 km of the East African Rift System is highly anisotropic for surface wave phase velocities, with the fast direction oriented parallel to the major fault systems and melt bodies. If cracks are the dominant source of anisotropy within a rock, the seismic fast direction will usually align with the direction of maximum compressive stress (*Lin and Schmandt*, 2014). This is due to the fact that cracks will preferentially be closed in the direction of maximum compressive stress, leading to an increase in seismic velocity (*Crampin and Lovell*, 1991).

Seismic observations thus allow us to discern the nature of anisotropy within a region, and infer characteristics about deformation, including the dominant strain field.

Observations of seismic anisotropy in fault zones

The anisotropic parameters of the crust can be measured using surface wave observations, as these waves are most sensitive to shallow structure. Other common methods for measuring seismic anisotropy include receiver functions and shear wave splitting. Surface wave observations are sensitive to the P and S-wave velocity of a medium

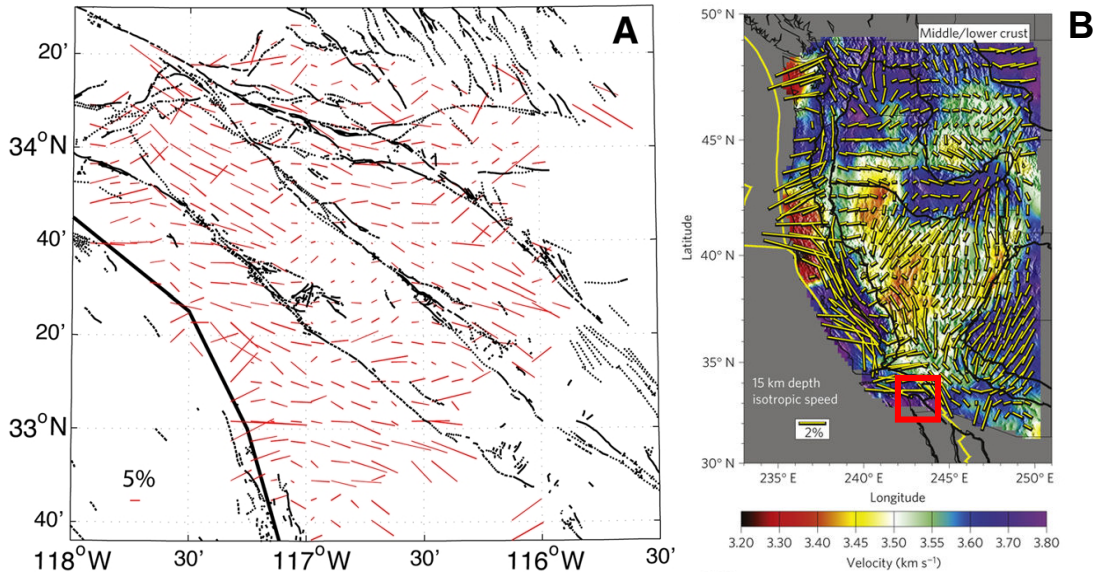

Figure 1.13: A) 2θ component of azimuthal anisotropy in 7 s period Rayleigh wave group velocities across the San Jacinto Fault Zone from *Zigone et al.* (2015). The direction of the red lines indicates the fast direction at that location, the length of the line indicates the amplitude of the anisotropy. The thick black line shows the coast of the United States. The thin black line indicates the mapped faults of the region. South west: Elsinore Fault, centre: San Jacinto Fault, north east: San Andreas Fault. B) 2θ component of azimuthal anisotropy in Rayleigh wave phase velocities at 15 km depth across the western United States from *Lin et al.* (2011). The colours show the phase velocity tomography model of *Lin et al.* (2011), with red indicating slow velocities and blue indicating fast velocities. The yellow lines indicate the direction and amplitude of anisotropy, as in A). The red box indicates the approximate study region shown in A). Figures modified from *Zigone et al.* (2015) and *Lin et al.* (2011).

in the propagation direction. Receiver functions and shear wave splitting provide us with observations of the fast and slow polarisation directions of S-waves in a material. Azimuthal anisotropy of surface wave velocities is typically modelled as:

$$c(\theta) = u_0 + A\cos(2(\theta - \phi_2)) + B\cos(4(\theta - \phi_4)). \tag{1.1}$$

This equation is a truncated fourier expansion first introduced by *Smith and Dahlen* (1973) that describes the variation of surface wave phase (or group) velocity c as a function of azimuth, θ. u_0 represents the average (isotropic) velocity. The 2θ represents variations with azimuth that have a period of 180°, the 4θ terms represents a periods of 90°. ϕ_2 and ϕ_4 give the corresponding fast directions for the 2θ and 4θ terms. A and B are amplitudes of the 2θ and 4θ terms, respectively.

Zigone et al. (2015) measured the distribution of the 2θ component of azimuthal anisotropy in Rayleigh and Love wave group velocities throughout the San Jacinto fault zone in southern California (Fig. 1.13). The 4θ term was found to have a negligible amplitude. The fast direction is generally perpendicular to fault strike in the immediate vicinity (within a couple of kilometres) of the major faults.(Fig. 1.5). In regions of

complex structure, and in particular areas where *Zigone et al.* (2015) observe low seismic velocity (Fig. 1.5), the fast direction is predominantly oriented parallel to the strike of the faults. Away from the fault zone, the fast direction is generally perpendicular to the California coast. *Zigone et al.* (2015) found that the magnitude of anisotropy varied on average between 6 – 10%, though this magnitude was reduced in areas that have a more uniform seismic velocity structure. The observations of *Zigone et al.* (2015) agree with those of *Lin et al.* (2011), who studied the entire western United States. *Lin et al.* (2011) found a general pattern of coast perpendicular fast directions for Rayleigh wave phase velocities throughout the crust (Fig. 1.13). However, in the vicinity of the San Andreas Fault Zone, the fast directions strongly align with the strike of the fault (*Lin et al.*, 2011).

Measurements of anisotropy in the lower crust and upper mantle show that the deformation field can have a large impact on faulting and mineral fabric and alignment at depth. A study of Rayleigh wave anisotropy by *Endrun et al.* (2011) shows that in the northern Aegean the seismic fast direction is parallel to the strike of the fault zones at the surface throughout the crust (Fig. 1.14). *Endrun et al.* (2011) suggest that in areas of the Aegean that are currently experiencing only a small amount of strain, the seismic fast direction may be aligned with the direction of paleo-strain associated with the last major deformation event, in this case the NE–SW extension during the Miocene (Sec. 1.1). Within the mantle lithosphere beneath the Aegean, the fast direction is aligned almost directly north–south, which *Endrun et al.* (2011) interpret as representing the current extensional strain field within the Aegean due to roll-back of the Hellenic Trench (*Reilinger et al.*, 2010). *Evangelidis et al.* (2011) observed that the fast polarisation direction of SKS splitting measurements in the Aegean is also parallel to the direction of maximum extension since the Miocene.

Sherrington et al. (2004) modelled the amplitudes of radial and transverse receiver functions recorded at stations across the Tibetan Plateau in order to invert for the best fitting anisotropic parameters in the crust for vertically propagating shear waves. *Sherrington et al.* (2004) found significant anisotropy in the shallow crust (<5 km), with magnitudes in the region of 14 ± 1%. The fast S-wave polarisation direction of this anisotropy was oriented east–west, parallel to the strike of the major thrust and strike-slip faults and suture zones in the region, and perpendicular to the direction of maximum compressive stress. This pattern of anisotropy is consistent throughout the crust, and is interpreted by *Sherrington et al.* (2004) to likely be caused by the alignment of anisotropic mineral grains that have undergone deformation in the past. Further measurements of SKS splitting by *Li et al.* (2011) confirm that the fast polarisation direction in north–eastern Tibet is aligned parallel to the strike of major lithospheric strike-slip faults, such as the Kunlun Fault.

Despite the apparent link between seismic fast directions in the upper crust, lower crust and upper mantle and the observed faulting patterns at the surface, the style of

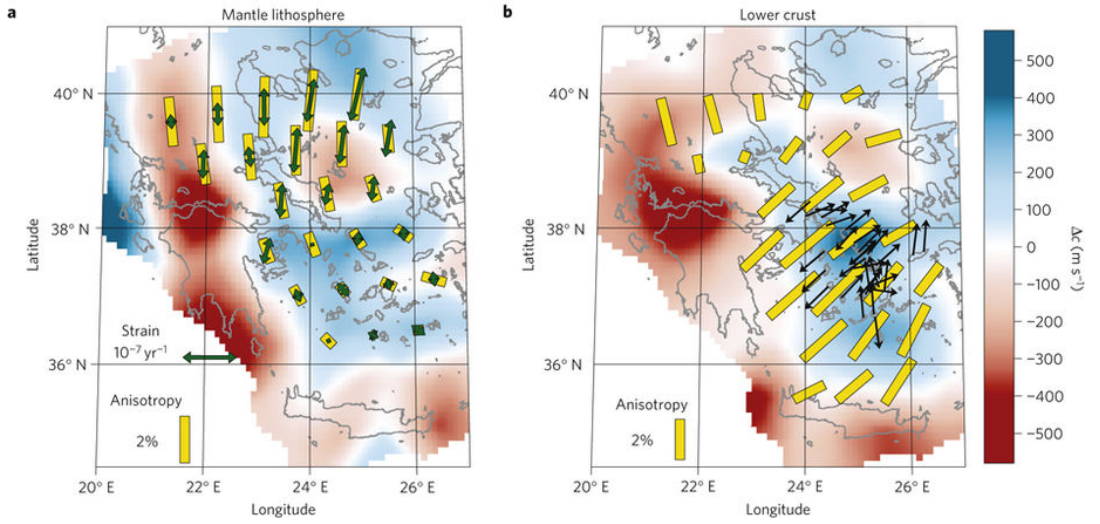

Figure 1.14: Distribution of azimuthal anisotropy in the Aegean Sea, measured by *Endrun et al.* (2011). a) Azimuthal anisotropy in the upper mantle, from 30 s period Rayleigh wave observations. The direction of the yellow bars indicates the fast direction measured by *Endrun et al.* (2011), whilst the length of the bar represents the magnitude of anisotropy. Green arrows show the extensional component of the current strain field from the Global Strain Rate Map Project (*Kreemer et al.*, 2003). The colours represent the phase velocity tomography of *Endrun et al.* (2011) at 30 s period. b) Distribution of azimuthal anisotropy within the lower crust from Rayleigh wave observations at 15 s period. The black arrows indicate Miocene stretching lineations that represent the direction of paleo-extension (*Tirel et al.*, 2009).

deformation that is causing the anisotropy is affected by the transition from brittle to ductile flow at depth (*Bourne et al.*, 1998). *Wilson et al.* (2004) observed a variation in the amplitude of P-to-S conversions as a function of back-azimuth from a discontinuity at 16 – 20 km depth beneath the Marlborough Fault Zone in New Zealand. This observation suggests anisotropy within the lower crust. *Balfour et al.* (2005) utilised shear wave splitting observations from local earthquakes to constrain the polarisation anisotropy in the top 16 km to be oriented at 65°±50° from north, which matches the average strike of the surface faulting within the Marlborough Fault Zone, whilst being 60° out of alignment with the direction of maximum compressive stress.

1.3 Overview of seismic interferometry

Seismic interferometry is the practice of exploiting the interference of seismic waves generated by a source, or distributed sources, to represent a new seismic response at detector A from a virtual source at detector B. Interferometry can be performed with both controlled seismic sources (*Bakulin and Calvert*, 2004, *Schuster et al.*, 2004), or passive sources (such as the ambient noise field, or earthquakes) (e.g. *Wapenaar* (2004)). The interferometric process normally involves the cross-correlation of recordings of different seismic wavefields, but can also include autocorrelation, or deconvolution. After a summation over all recorded sources, when the source distribution is sufficiently isotropic,

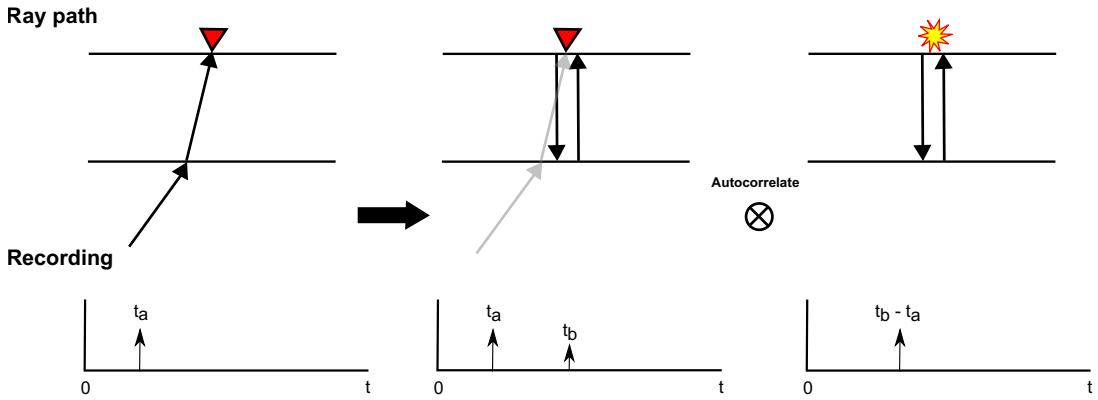

Figure 1.15: Illustration of reflection interferometry. The top row shows and example ray path of the waves in the medium. The black arrows show the ray paths, horizontal black lines indicate discontinuities in the medium. The grey arrows indicate the ray path of the previous panel. The yellow explosion is the synthetic source created by the autocorrelation process. The bottom row shows a simplified seismic recording for each ray path at a station indicated by the red triangle. t_a is the arrival of the initial upcoming wave. t_b is the arrival of the surface multiple reflection from an interior discontinuity. $\otimes$ indicates autocorrelation of the record from the middle panel. Autocorrelation produces the arrival $t_b - t_a$, which has the travel time of a zero offset reflection with a co-located source and receiver. Note that only the positive lag times of the autocorrelation function are shown in the figure.

the result of the cross-correlation is ideally the response of the system to a point source located at one of the receivers, often called a Green's function (*Green*, 1828). This section will outline the theory of seismic interferometry in 1-D media, with a focus on the retrieval of body wave reflections, and give examples of its past application. I will also detail different approaches for applying seismic interferometry, such as data pre-processing and methods used to enhance signal-to-noise ratio. I will focus on the retrieval of body waves from noise and earthquake coda waves, but many of the techniques discussed are equally applicable to the retrieval of surface waves and the use of active source data.

1.3.1 Theory of Green's function retrieval

The first clear derivation of a seismic interferometric method was provided by *Claerbout* (1968). *Claerbout* (1968) showed that by autocorrelating the transmission response of a layered medium (the incoming waves that enter the medium and are recorded at the surface), one can obtain the reflection response of said medium as if there had been an impulsive point source co-located with the receiver at the surface. An intuitive explanation of this concept is shown in Fig. 1.15. Autocorrelating the record of the initial arrival and the free surface multiple reflection, the path taken by the wave prior to the reflection at the free surface is cancelled out. This leaves only the recording that would be observed if there was a co-located source and receiver at the surface.

There is mathematical basis for the process in Fig. 1.15 (*Claerbout*, 1968, *Wapenaar*, 2003), and the following explanation follows that of *Wapenaar* (2003). We denote the

down-going wave after the reflection at the free surface (left panel in Fig. 1.15), as having an amplitude of 1. This represents the fact that all of the incident energy is reflected at the free surface. Assuming a medium that doesn't attenuate, the receiver will record an up-going series of waves reflected from interfaces within the medium, $R(\omega)$. There will also be a set of down-going waves reflected from the same interfaces, $-R(\omega)$. The total down-going wavefield will be: $D(\omega) = 1 - R(\omega)$ and the up-going wavefield is: $U(\omega) = R(\omega)$. $D(\omega)$ and $U(\omega)$ represent the wavefields in the frequency domain. For the following derivation, the dependence on ω is implied and the symbol omitted. If a wavefield has components in a given frequency range, then the power spectrum of the integrated wavefield is the frequency-domain autocorrelation $D^\dagger D$ and $U^\dagger U$, where † represents the complex conjugate. We can thus calculate the total power flux at the bottom of a layered medium is:

$$D^\dagger D - U^\dagger U = (1 - R^\dagger)(1 - R) - R^\dagger R = 1 - R - R^\dagger. \tag{1.2}$$

At the lowest boundary of the medium we denote the transmitted down-going wavefield as T. If we assume that the medium is homogeneous below the lowest boundary, there will be no up-going reflected waves at this interface ($U^\dagger U = 0$), the down-going power flux is:

$$D^\dagger D - U^\dagger U = D^\dagger D = T^\dagger T. \tag{1.3}$$

The power flux must be conserved, so the right-hand side of equations 1.2 and 1.3 must equal, and can be arranged as:

$$R + R^\dagger = 1 - T^\dagger T. \tag{1.4}$$

Using reciprocity, we know that the down-going transmitted wavefield at the lowest boundary will be equal to the initial up-going transmitted wavefield, so we can use the recording of the transmitted wave (left panel in Fig. 1.15) in Eq. 1.4. In the time domain this will become:

$$T(t) * T(-t) = \delta(t) - R(t) - R(-t). \tag{1.5}$$

The * denotes convolution. $T(t)$ and $T(-t)$ represent the transmission response, and time-reverse transmission response, respectively. $\delta(t)$ is the impulse of the autocorrelation function at zero lag time. $R(t)$ and $R(-t)$ are the positive and negative lag times of the autocorrelation function, which represents the reflection response of the medium. In the case where the sources are not impulsive and transient (such as noise) *Claerbout* (1968) showed that Eq. 1.5 can be modified to:

$$\{R(t) * R(-t)\} * S_n(t) = S_n(t) - \langle u(t) * u(-t) \rangle. \tag{1.6}$$

$S_n(t)$ is the autocorrelation of the noise source time function. $\langle\rangle$ denotes averaging over many source recordings. $u(t)$ is the actual recorded wavefield at the receiver: the convolution of the transmission response and the noise source time function.

Eq. 1.6 shows that it is possible to retrieve the reflection response of a medium by autocorrelating seismic records of waves transmitted through that medium. A similar approach could be taken for horizontally travelling waves to extend the analogy to direct body wave or surface wave retrieval (e.g. *Wapenaar et al.* (2010a)). The caveat that is apparent in Eq. 1.6 is that this reflection response is convolved with the source time function, which is normally unknown. When using ambient noise, $S_n(t)$ is complex and difficult to estimate, so the raw noise auto-correlation functions are interpreted in the knowledge that some signature of the source time function remains within the data. In coda wave interferometry, removing the imprint of the source is still difficult, though some studies attempt to remove its influence by subtracting the average auto-correlation function from the entire data set (*Ruigrok and Wapenaar*, 2012). *Claerbout* (1968) showed that Eq. 1.6 will hold for arbitrarily layered media, and also conjectured that the theory could be applied to 3-D structure. More than one station can be included in the interferometric process, in which case autocorrelation is replaced with cross-correlation, and the retrieved Green's function represents the response that would be recorded at one station, if an impulsive source were placed at another.

A mathematical proof of the application of seismic interferometry to 3-D structure was provided by *Wapenaar* (2004) through the use of representation theorems. For more mathematical background to the proof of seismic interferometry by correlation in 3-D media, the reader is referred to publications such as *Wapenaar and Fokkema* (2006), *Snieder et al.* (2007) and the references contained therein.

1.3.2 Pre-processing for seismic interferometry

The procedure of seismic interferometry can be summarised in three phases: 1. preparation of seismic records, 2. correlation and summation over sources (averaging of the correlation functions), 3. analysis of the retrieved Green's functions (e.g. surface wave dispersion measurements). There are several preparation steps required in seismic interferometry that go beyond regular seismic processing such as band-pass filtering and tapering. These steps are described in detail by *Bensen et al.* (2007), and will be briefly introduced here, alongside justification for each processing step. Pre-processing is often required for noise datasets, but in some cases can be skipped when using active source recordings, or records of energetic sources such as earthquakes.

Temporal normalisation of ambient noise records

Amplitude normalisation is a procedure designed to reduce the effect of high energy signals on the seismic record. These signals can include ballistic signals from earth-

quakes or other large seismic sources, instrumental glitches, or high amplitude noise sources local to the seismic station. If high amplitude signals are present during the correlation process, they will produce spurious non-physical arrivals, which will obscure the target waves contained within the noise. Earthquakes are a particular problem due to their random distribution in time, and the fact that earthquake catalogues are often incomplete, making any *a priori* exclusion of noise windows based on the presence of earthquake signals difficult and time consuming.

The simplest way to normalise the amplitude of seismic records is to disregard amplitude completely. This method, known as one-bit normalisation, was popular in early noise studies (*Shapiro et al.*, 2004, 2005, *Campillo and Paul*, 2003). For one-bit normalisation only the sign of the signal is retained, and the amplitude is either 1 or -1. Another method of time domain normalisation is to clip or mute any samples of the data window that have an amplitude much higher than some average of the entire data window. *Bensen et al.* (2007) advocate a data adaptive method of normalisation that involves down-weighting high amplitude signals by the running-average of a variable data window. However, *Bensen et al.* (2007) found that the signal-to-noise ratio of the final Green's function produced after the running-average normalisation is not significantly different to simple one-bit normalisation.

In the appendix (Figs. A.1 and A.2), I present the results of tests that were performed during the pre-processing steps of ambient noise surface wave tomography. We tested the effect of one-bit normalisation versus amplitude clipping on the signal-to-noise ratio of the final Green's function. Figs. A.1 and A.2 show that, whilst there is little difference between the processing schemes, amplitude clipping has slight advantages in terms of improved signal-to-noise ratio and frequency domain coherency, when compared with one-bit normalisation.

Spectral normalisation ambient noise records

Prior to cross-correlation, the frequency spectrum of each recording must also be balanced in order to ensure that it is not dominated by a single seismic noise source. If the frequency spectrum is not balanced, persistent noise at a particular frequency can result in Green's functions that 'ring' at that frequency (panel a) in Fig. 1.16). Spectral balancing is usually achieved by dividing the frequency spectrum of a signal with a smoothed version of itself. The level of applied smoothing controls how strong the balancing in the frequency domain is. Too much spectral balancing can result in the introduction of incoherent noise to the signal, and a degradation of the resultant Green's function.

The ambient noise field of the Earth is dominated by two sources known as the primary and secondary microseisms. The primary microseism, which generates seismic waves around 15 s period, is likely caused by the direct interaction of ocean waves with the sea floor (*Haubrich et al.*, 1963). The secondary microseism produces seismic waves

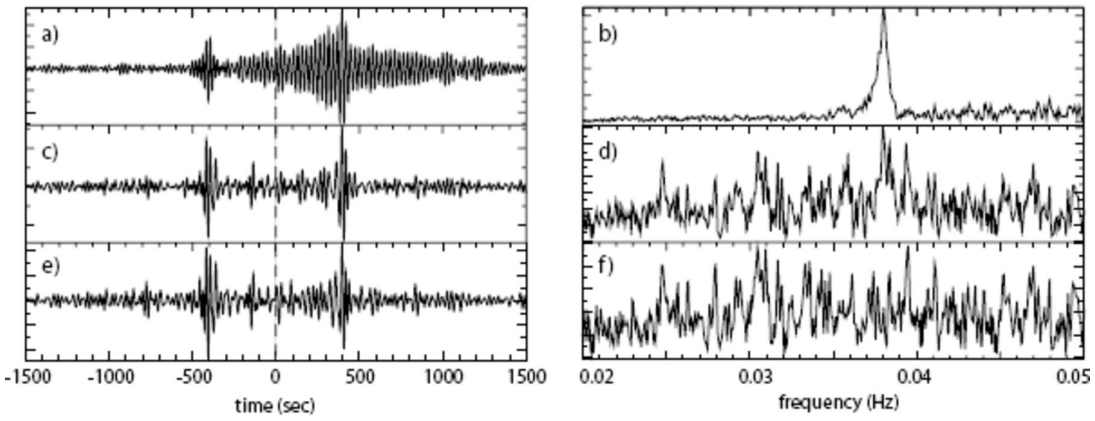

Figure 1.16: The effect of the 26 s period microseismic peak on Green's function retrieval. The left hand column shows the time domain signals when a) spectral balancing is not applied, c) Spectral balancing has been applied and e) spectral balancing has been applied, and a notch filter centred at 26 s period has been implemented. The right hand column b), d) and f) are the corresponding frequency spectra. Figure from *Bensen et al.* (2007).

near 7.5 s period, and is caused by pressure changes on the sea floor as a result of non-linear interactions between standing waves in the deep oceans (*Longuet-Higgins*, 1950). Higher frequency noise (>1 Hz) is typically found in the coda of large earthquakes (*Seriff et al.*, 1965, *Gupta*, 1965). Other, more exotic noise sources can also cause issues for seismic interferometry. *Shapiro et al.* (2006) located a persistent, monochromatic noise source with a period of 26 s in the Gulf of Guinea off the west African coast. This source was recorded at seismic stations around the planet, and is likely the result of interactions between oceanic waves and the African continental shelf (*Shapiro et al.*, 2006).

Correlation and stacking procedure

After pre-processing the seismic waveforms, the correlation and stacking process can be performed. The length of the time window selected for correlation is flexible, but the decision is normally driven by factors such as the expected frequency and speed of the target waves, and the inter-station distance. Low frequency waves with slow apparent velocity that are recorded at stations with a large separation will normally require a long correlation time window, which is usually related to the travel time of the target waves. The correlation window length used in different studies can range from 1 day (e.g., *Bensen et al.*, 2007), to a few hours (e.g., *Poli et al.*, 2012), to a matter of minutes (e.g., *Nakata et al.*, 2014). After the correlation functions have been obtained, they must be averaged (stacked) in order to mimic the integration over all sources required for interferometry (Eq. 1.6). The amount of data that is required in the stack depends on the spatial distribution of the sources available (Fig. 1.17). Longer periods of data may be required in instances of inhomogeneous noise distribution. One year

of seismic records is normally sufficient for most regional scale studies, although some studies have utilised as little as one day of recording (*Draganov et al.*, 2013, *Nakata et al.*, 2015).

As with any cross-correlation, the estimated Green's function will be a two-sided function with both positive and negative lag times. The positive lag times, often termed the causal signal represent waves travelling from the virtual source to the second receiver. The negative, or acausal, lag times represent waves that travel from the receiver to the virtual source. In the case of homogeneous distribution of noise sources Fig. 1.17), the causal and acausal parts of the Green's function can be expected to be identical. In most cases, the noise source distribution is not homogeneous, and there can be considerable asymmetry between the causal and acausal components. For this reason, it is common practice to average the causal and acausal parts of the Green's function.

1.3.3 Absence of body waves from ambient noise studies

Eq. 1.6 shows that the reflection response of a medium can be obtained by averaging the autocorrelations of recordings of ambient seismic noise at a receiver. One limitation to this approach is the apparent weak amplitude of body waves within the noise field that consists predominantly of surface waves (*Campillo and Paul*, 2003, *Shapiro et al.*, 2004). Body wave phases have been identified in some early noise studies (*Roux et al.*, 2005, *Draganov et al.*, 2009), but their presence seems to be heavily reliant on the background incoherent noise field being low amplitude, such as within continental interiors (*Poli et al.*, 2012). The lack of body waves in the noise field can probably be explained by the fact that most sources of seismic noise are located at the surface, rather than at depth. Thus, the majority of energy in the noise field propagates as surface waves.

The retrieval of the full Green's function between two receivers of a 3-D medium requires an ideal source distribution that forms a closed surface surrounding the receivers (*Wapenaar et al.*, 2010b) (Fig. 1.17). The lack of body waves in ambient noise cross correlations can therefore be attributed to imperfections in this source distribution. *Forghani and Snieder* (2010) show that in order to retrieve a direct surface wave by cross correlating a wavefield recorded at two receivers, it is only necessary to record a source in line with a receiver pair, so long as the source is not located between the receivers. To retrieve a body wave, the source must be located in the appropriate stationary phase region (*Snieder*, 2004), which usually forms an elliptical region with the major axis parallel to the receiver line (Fig. 1.17). During the cross-correlation process, spurious arrivals can appear due to the correlation of body waves and surface waves. These spurious arrivals are known as cross-terms. These cross-terms are much higher amplitude than the correlation of the body waves with themselves (*Forghani and Snieder*, 2010). If the noise source distribution within the stationary phase region (Fig. 1.17) is sufficiently isotropic, these cross terms will integrate to zero, and the result-

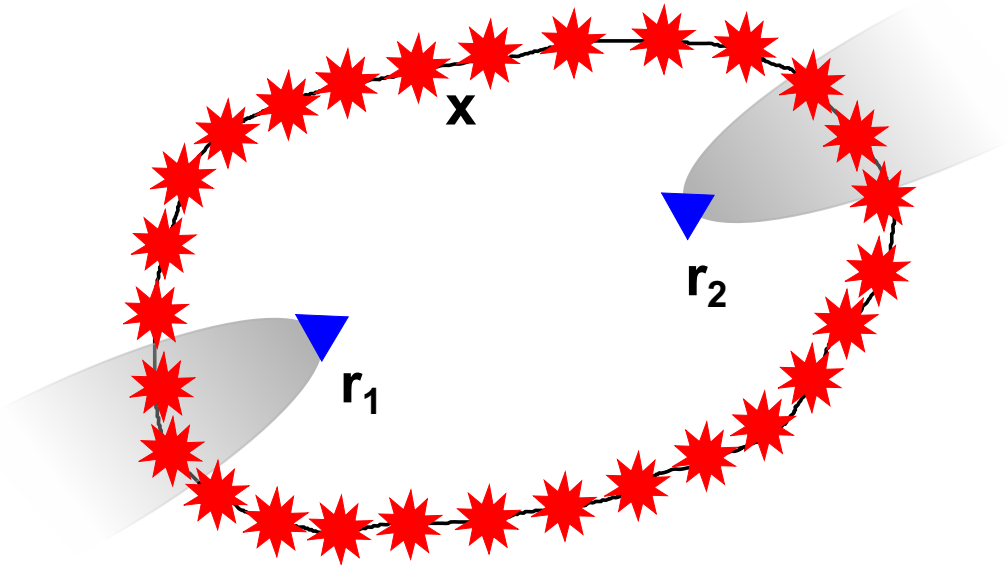

Figure 1.17: The ideal source distribution for Green's function retrieval with seismic interferometry. The sources (red stars) should form a closed surface, $\mathbf{x}$, around the receivers r_1 and r_2. The shaded grey regions represent the approximate stationary phase regions. Sources falling within the stationary phase region will provide the greatest contribution to the retrieved Green's function following correlation and summation over sources (*Snieder*, 2004).

ing Green's Function should be a faithful representation of the true impulse response (*Snieder*, 2004).

1.3.4 Methods for retrieving reflections from ambient noise

Given the challenges laid out in Sec. 1.3.3, special effort often has to be made in order to retrieve reflections from ambient noise. *Draganov et al.* (2009)performed one of the first studies to specifically target reflections in the ambient noise field for exploration purposes. Using a dense seismic array in Libya *Draganov et al.* (2009) were able to employ frequency-wavenumber analysis to filter out the surface wave arrivals prior to cross-correlation. This method is possible with dense arrays that have sufficiently dense spatial sampling for a high wavenumber resolution. *Draganov et al.* (2013) extended this methodology with the same data set by visually inspecting each noise window, and selecting windows that contained a significant portion of vertically travelling energy for cross-correlation. *Ruigrok et al.* (2011) took a similar approach and discarded noise windows that were found to contain energy arriving at a slowness inconsistent with vertically travelling body waves prior to cross-correlation.

Very dense seismic networks (with station spacing on the order of metres) appear to have greater efficacy at retrieving body waves from ambient noise. This is likely due to the higher frequency content of body waves in the noise field (>1 Hz) (*Seriff et al.*, 1965, *Gupta*, 1965) and the corresponding increase in attenuation over long distances. *Nakata et al.* (2011) were able to use high frequency traffic noise (12 – 16 Hz) recorded

at a dense array of geophones to produce a reflection image. A similar approach was taken by *Nakata et al.* (2015) using an array deployed at Long Beach, California. Despite the density of instruments at Long Beach, *Nakata et al.* (2015) had to design a selection filter for the recorded noise windows that discarded those recordings that were not likely to contain body wave energy. This selection filter compared each individual cross-correlation function to the overall stack. If the correlation coefficient between the cross-correlation function and the overall stack is > 0.5, it is accepted. The logic behind this filter is that the low amplitude body waves will be more prominent in the overall stack, which can be used to select individual cross-correlation functions that contain body wave energy. It is clear that without employing amplitude independent techniques, careful data selection is required for the extraction of body waves from ambient noise.

Phase correlation and stacking methods

One way to extract low amplitude signals from a wavefield is to use techniques that are sensitive to instantaneous phase rather than amplitude. Whilst body wave reflections are low amplitude when compared with surface waves, they remain in-phase with any multiples that arrive at a later time. *Schimmel and Paulssen* (1997) devised an amplitude-independent method that exploits this property to enhance the detection of weak yet coherent signals in the seismic wavefield. This approach is known as phase weighted stacking. In phase weighted stacking, each sample of a linear stack of seismic traces is multiplied with a weighting function. The weighting function, known as the phase stack, is calculated as (*Schimmel and Paulssen*, 1997):

$$c(t) = \left| \frac{1}{N} \sum_{j=1}^{N} \exp[i\phi_j(t)] \right|, \tag{1.7}$$

where N is the number of seismic records in the stack, $\phi_j(t)$ is the instantaneous phase of the j_{th} trace, and i is the imaginary unit. The instantaneous phase is the unwrapped angle (argument) of the series of complex numbers given by the analytic signal of the seismic record which is defined as:

$$S(t) = s(t) + iH(s(t)) = A(t)\exp[i\phi(t)], \tag{1.8}$$

where $s(t)$ is the seismic record, $H(s(t))$ is the Hilbert transform of $s(t)$ (*Bracewell*, 1965). $A(t)$ is the envelope of the seismic record. The phase weighted stack has amplitudes between 0 and 1 as a function of time. The full phase weighted stack can

be calculated by (*Schimmel and Paulssen*, 1997):

$$g(t) = \frac{1}{N}\sum_{j=1}^{N} s_j(t) \left| \frac{1}{N}\sum_{k=1}^{N} \exp[i\phi_k(t)] \right|^{\nu}, \tag{1.9}$$

where ν represents an optional tuning parameter. The higher this tuning parameter is set, the heavier the weighting will be towards coherent energy. Note that the phase weighted stack is a non-linear process that will distort the waveform of the final stacked record, and should be avoided for studies that utilise waveform modelling. *Schimmel and Paulssen* (1997) applied the phase weighted stacking technique to the detection of weak P-to-S conversions from the mantle. In this thesis, phase weighted stacking will be employed to retrieve weak multiple reflections from the P-wave coda of teleseismic earthquakes in Chapter 4.

Schimmel (1999) expanded the use of the instantaneous phase to derive an amplitude-independent measure of similarity between two seismic traces. Termed phase correlation, it is defined as:

$$c_{pc}(t) = \frac{1}{2N}\sum_{\tau=\tau_0}^{\tau_0+T} \left\{ \left| e^{i\phi(t+\tau)} + e^{i\psi(\tau)} \right| - \left| e^{i\phi(t+\tau)} - e^{i\psi(\tau)} \right| \right\}. \tag{1.10}$$

τ is the time shift for which the level of similarity between the signals is being computed, The total length of the correlation time window is given by T. $\psi(\tau)$ represents the instantaneous phase of a second signal. The substitution of sine and cosine functions gives:

$$C_{pc}(t) = \frac{1}{N}\sum_{\tau=\tau_0}^{\tau_0+T} \left\{ \left| \cos\left(\frac{\phi(t+\tau) - \psi(\tau)}{2} \right) \right| - \left| \sin\left(\frac{\phi(t+\tau) - \psi(\tau)}{2} \right) \right| \right\}. \tag{1.11}$$

Like a regular correlation function, the phase correlation will output a result between -1 and 1 for each time shift τ. 1 indicates perfect correlation, and -1 indicates perfect anti-correlation. Initially implemented by *Schimmel* (1999) with the purpose of detecting P-to-S wave conversions from the mantle transition zone discontinuities, *Schimmel et al.* (2011) demonstrated that phase correlation can replace the correlation process in seismic interferometry. *Schimmel et al.* (2011) performed seismic interferometry on data recorded at an array in southern Spain, showing that Green's functions produced by phase correlation were more robust to the addition of white noise, and enhanced the detection of low amplitude phases such as the direct P-wave when compared with regular cross correlation (Fig. 1.18).

For this thesis, I have used the phase autocorrelation process as defined in Eq. 1.10 to retrieve P-wave Moho reflections from the ambient noise field in Chapter 2.

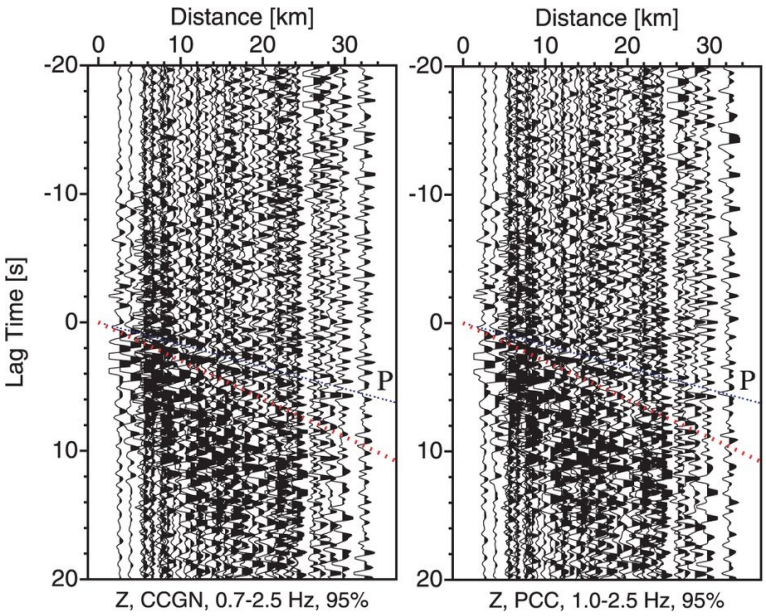

Figure 1.18: Comparison between amplitude correlation and phase correlation by *Schimmel et al.* (2011). The left panel shows Green's functions produced by regular, amplitude based correlation. The right panel shows the same Green's functions produced by phase correlation (eq 1.10). Both panels shows the vertical component of ground motion, and the filter applied is shown at the bottom of the panel. The dotted black line indicates the theoretical travel time of a direct P-wave, the red dotted line indicates the travel time of the direct S-wave. Modified after *Schimmel et al.* (2011).

1.3.5 Previous studies using the autocorrelation of seismic noise

The first successful attempt to retrieve reflections from ambient noise using an autocorrelation approach was a study by *Tibuleac and von Seggern* (2012). Using data from stations located in the continental interior of the United States (Nevada) *Tibuleac and von Seggern* (2012) autocorrelated continuous records of ambient noise that were filtered between 0.5 and 1 Hz. Two clear arrivals can be identified on all three components of motion (north–south, east–west and vertical): one arriving at 10 s, and another at 17 s (Fig. 1.19). These arrivals have the opposite polarity to the autocorrelation maximum at t = 0 due to the interaction with the free surface (Fig. 1.15). *Tibuleac and von Seggern* (2012) interpret the arrival at 10 s as a P-wave reflection from a Moho that is located at approximately 30 km depth, and the 17 s arrival as an S-wave reflection from the same interface. Whilst it is surprising that an S-wave arrival is so prominent on the vertical component, simple analysis by *Nakata et al.* (2014) shows that the correlation interferometry will produce cross-terms between P- and S-waves. *Tibuleac and von Seggern* (2012) point out that the use of ambient noise will likely mean that some amount of non-horizontally polarised S-wave energy will be present on the vertical component recordings.

Following the work of *Tibuleac and von Seggern* (2012), several studies attempted to retrieve P-wave reflections from the Moho from noise recorded across the continent

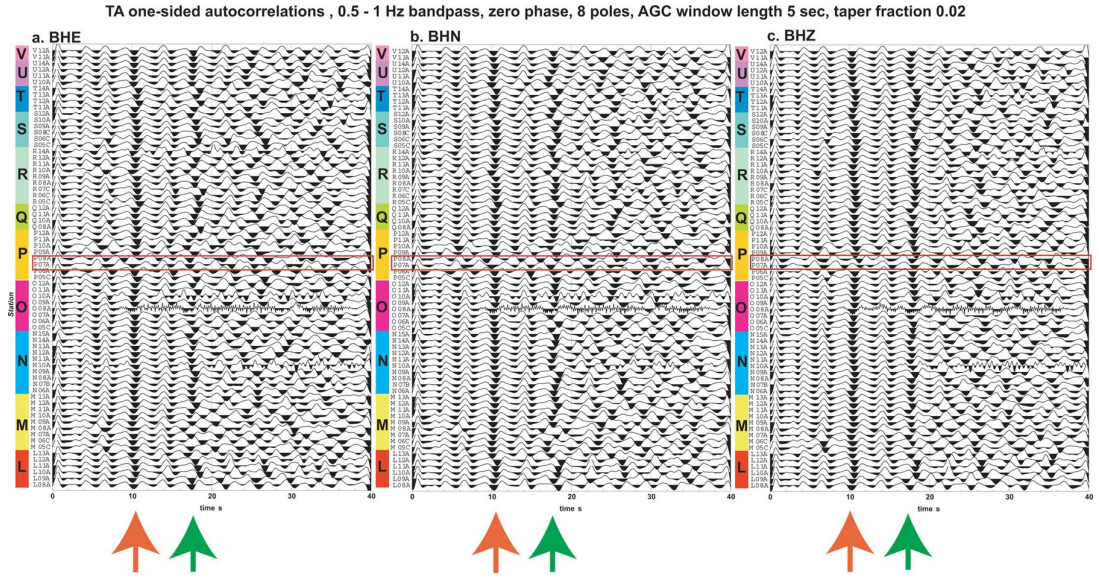

Figure 1.19: Autocorrelation functions of *Tibuleac and von Seggern* (2012), filtered between 0.5 and 1 Hz. a), b) and c) show autocorrelations of the east, north and vertical components, respectively. The orange arrow indicates the arrival of a reflection at 10 s, the green arrow shows a later reflection at 17 s. The coloured boxes containing letters indicate stations of a constant latitude. Figure from *Tibuleac and von Seggern* (2012)

of Australia (*Gorbatov et al.*, 2013, *Kennett*, 2015, *Kennett et al.*, 2015). *Gorbatov et al.* (2013) detected coherent arrivals at autocorrelation lag time between 8 and 16 s at many of these stations. These arrivals where detected in a frequency range between 1.5 and 4.0 Hz, and were interpreted as P-wave reflections from the Moho. No pre-processing was applied to the noise records (Sec. 1.3.2), aside from the rejection of data windows containing high amplitude glitches (*Gorbatov et al.*, 2013). *Gorbatov et al.* (2013) note that the arrival time of a multiple reflection will be a function of the wave slowness. The ambient noise field will inherently result in incoming waves with a range of slowness, which may result in a 'smearing' in the arrival times of the reflections, rather than a time-localised pulse.

Kennett et al. (2015) and *Kennett* (2015) take the same approach as *Gorbatov et al.* (2013), but advocate the observation of a general change in the level of reflectivity in order to detect the lithospheric discontinuities, rather than a coherent arrival from a sharp interface. *Kennett et al.* (2015) and *Kennett* (2015) use previous seismological evidence for Moho depth in conjunction with the observation of a general reduction in amplitude, or change in frequency content, in the autocorrelation functions to pick lag times that could represent seismic discontinuities (Fig. 1.20).

Following the work of *Taylor et al.* (2016) (chapter 2), *Saygin et al.* (2017) used the autocorrelation method to retrievec 2 – 4 Hz reflections from the noise field within the Jakarta Basin. In order to mitigate the effect of spectral holes in the frequency content of the noise field (Sec. 1.3.2), *Saygin et al.* (2017) employ a regularised water level de-

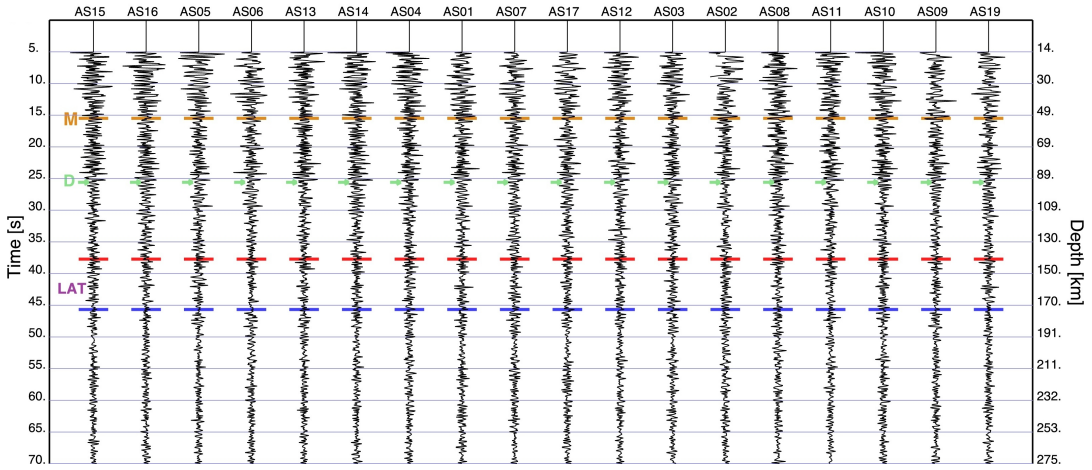

Figure 1.20: Autocorrelation functions from *Kennett* (2015), filtered between 0.5 and 4.0 Hz. The x-axis represents different stations. The orange ticks marked 'M' mark the Moho depth of *Salmon et al.* (2013). The red and blue ticks indicate the upper and lower bounds placed on the depth lithosphere-asthenosphere transition by *Yoshizawa* (2014), respectively. The green tick marks labelled D mark portions of the autocorrelation functions that display a systematic change in amplitude and frequency content, identified by (*Kennett*, 2015). Figure modified after *Kennett* (2015).

convolution technique (*Helmberger and Wiggins*, 1971) rather than an autocorrelation function. Additionally, *Saygin et al.* (2017) use the phase weighted stacking technique of *Schimmel and Paulssen* (1997) (Sec. 1.3.4) when averaging the autocorrelation functions in order to increase the signal-to-noise ratio. *Saygin et al.* (2017) found that this approach improved the signal-to-noise ratio of reflections from the crystalline basement beneath the Jakarta Basin, and also note that a sedimentary environment would likely cause issues for the receiver function method in the form of multiple reverberations from the top of the bedrock, that would make a receiver function difficult to interpret. The fact that the autocorrelation method specifically exploits these reverberations likely makes it more reliable imaging technique in this environment.

Oren and Nowack (2017) applied a more traditional ambient noise pre-processing scheme (Sec. 1.3.2) in their autocorrelation study at stations in the United States. In particular, *Oren and Nowack* (2017) apply one-bit normalisation prior to autocorrelation, and then whiten the spectrum of each auto-correlation function before stacking. This spectral whitening procedure was designed to limit the impact of the ocean microseisms in the period band 0.3 – 0.55 Hz, though *Oren and Nowack* (2017) note that care should be taken not to over-whiten the spectrum, as this may destroy the low amplitude body wave information contained within the noise waveform. *Oren and Nowack* (2017) give an example from one station also used by *Tibuleac and von Seggern* (2012) (Fig. 1.21), and obtain very similar waveforms to the previous study. Synthetic modelling indicates that the arrival observed at approximately 25 s is indeed likely to be the SmS phase (*Oren and Nowack*, 2017). It is interesting to note that the P-wave reflection

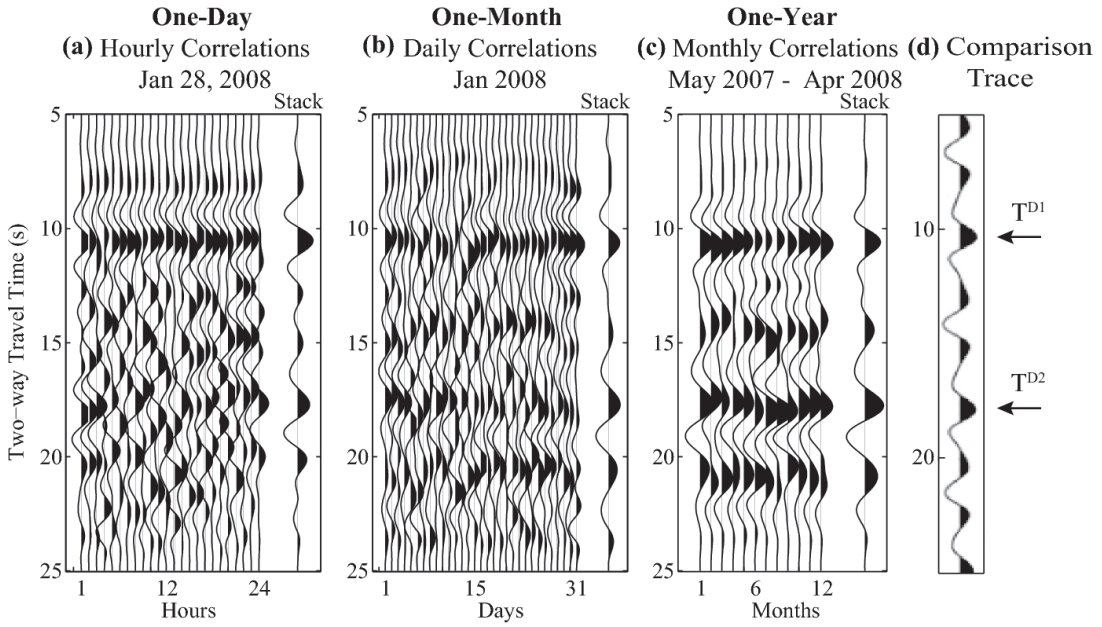

Figure 1.21: Noise autocorrelations from the study of *Oren and Nowack* (2017). Panels a), b) and c) show autocorrelation functions with hourly, daily, and monthly stacks, respectively. The average of the traces is shown in the right of each panel. Panel d) shows the results of *Tibuleac and von Seggern* (2012) for this station, V12A. The arrival time of PmP and SmS estimated by *Tibuleac and von Seggern* (2012) are shown as T^{D1} and T^{D2} respectively. Modified after *Oren and Nowack* (2017).

from the Moho at $\sim$ 15 s in Fig. 1.21 is apparent after stacking only one day of noise, whereas a month's worth of recording is required in order to produce a coherent S-wave reflection.

Becker and Knapmeyer-Endrun (2017) follow the same approach as *Kennett et al.* (2015) and *Kennett* (2015) by interpreting changes in amplitude and frequency content of auto-correlation functions as evidence for seismic discontinuities beneath eastern Europe. *Becker and Knapmeyer-Endrun* (2017) employ the phase auto-correlation algorithm of *Schimmel* (1999) (Eq. 1.10). The presence of narrow-band, incoherent noise at a frequency of $\sim$ 2.0 Hz across Germany (*Bokelmann and Baisch*, 1999) complicates the interpretation of the auto-correlation functions from stations in this region. As a result, *Becker and Knapmeyer-Endrun* (2017) had to apply a spectral smoothing process to the auto-correlation functions similar to *Oren and Nowack* (2017) in order to avoid ringing as a result of the 2 Hz signal.

Most recently, the noise auto-correlation method was used by *Heath et al.* (2018) to detect reflections from the interior of Newberry volcano in central Oregon. The study of *Heath et al.* (2018) is an attempt to observe reflections contained within the noise from an interface that may not represent a large contrast in physical properties, such as the Moho or crystalline rocks that underlie sediments. *Heath et al.* (2018) observe a reflection from an interface at roughly 2.5 km depth within the volcano, which they interpret to be the top of a magma body. *Heath et al.* (2018) also posit that the

vicinity around an active volcano may be the ideal location for seismic interferometry, given the abundance of natural seismic sources, and the complex subsurface structure that could facilitate the scattering of seismic waves. These features mean that the underlying assumption of a diffuse seismic wavefield could be well satisfied in a volcanic environment,

1.3.6 Previous studies using the autocorrelation of coda waves

Seismic interferometry can also be performed on ballistic waves, such as earthquake sources. Autocorrelation of earthquake waveforms can be used to retrieve the free surface multiple reflections contained in the coda waves (Sec. 1.3.1). *Ruigrok and Wapenaar* (2012) apply this theory to the Hi-CLIMB linear seismic array deployed across the Tibetan Plateau (84°E). By targeting global seismic phases that travel near-vertically in the lithosphere (such as PKP, PKIKP and PKiKP) *Ruigrok and Wapenaar* (2012) constructed a P-wave reflection image of the crust and upper mantle. One issue created by using earthquake waveforms is the potential for spurious, non-physical arrivals to appear in the autocorrelation functions. These spurious terms are the result of the correlation between the direct phase and other arrivals within the coda that are not the target reverberations. *Ruigrok and Wapenaar* (2012) often observe strong amplitudes related to both PKIKP and PKP within the same time window, and as a result decide to reject any window which will likely be contaminated by the spurious signals arising from cross correlations between these two phases.

Much like noise autocorrelations, using earthquake coda signals will result in the estimate of reflectivity being convolved with the average source time function of each earthquake. *Ruigrok and Wapenaar* (2012) propose a potential solution to this problem, though it is dependent on having recorded data over a large spatial area. They assume the heterogeneous structure beneath the array will result in the reflectivity term vanishing in an average of all the auto-correlation functions. On the other hand, the convolution of the source time functions will sum coherently. As such, the average of all the auto-correlation functions can be assumed to represent the $S_n(t)$ term in Eq. 1.6, which can then be subtracted from each individual auto-correlation function to leave just the reflectivity term remaining (Fig. 1.22).

Sun and Kennett (2016) expanded the single station autocorrelation technique to include cross correlation of multiple components of ground motion recorded at a receiver. From recordings of teleseismic earthquakes made throughout Australia, *Sun and Kennett* (2016) used S-waves recorded on the radial component in addition to P-waves from the vertical component, and autocorrelated each component pair station-by-station (ZZ, RR, ZR, RZ). The ZZ and RR components represent the P-wave and S-wave reflection response, respectively, whilst the ZR and RZ cross-correlations will contain P-to-S (ZR) and S-to-P (RZ) conversions, in analogy with classical receiver functions (*Galetti and Curtis*, 2012). The interpretation of S-wave reflectivity is complicated by the fact that

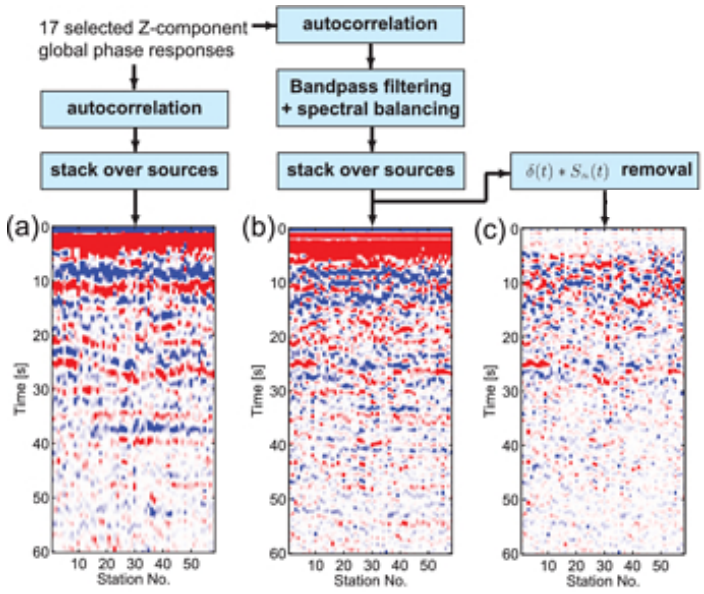

Figure 1.22: P-wave reflectivity beneath the Tibetan Plateau from *Ruigrok and Wapenaar* (2012). Panel a) shows the effect of simply autocorrelating and stacking the P-wave coda of the 17 selected earthquakes. b) The auto-correlation function following spectral balancing (Sec. 1.3.2) to enhance the high frequency content of the waveforms. c) Auto-correlation functions following the subtraction of the average of all the autocorrelations in order to remove the effect of the earthquake source time functions. Modified from *Ruigrok and Wapenaar* (2012)

the S-wave coda typically contains a large variety of different phases which increases the noise on the correlation functions (*Ruigrok and Wapenaar*, 2012). *Sun and Kennett* (2016) achieve higher resolution images than *Gorbatov et al.* (2013) and *Kennett* (2015) obtained by autocorrelating noise. *Sun and Kennett* (2017) attribute this to the fact that teleseismic coda waves contain much more energetic arrivals and subsequent reverberations at near-vertical incidence.

Pham and Tkalčić (2017) further demonstrated the applicability of coda wave auto-correlations, giving examples of retrieving the reflection response of both an Antarctic glacier, and the crust beneath southern Africa. Using synthetic data, *Pham and Tkalčić* (2017) show that spectral balancing (Sec. 1.3.2) is an important processing step to improve the retrieval of the target reflections. However, *Pham and Tkalčić* (2017) also note that when applied to real data, the level of incoherent noise can often be so great that spectral balancing may degrade the waveforms to such an extent that no reflections are visible. However, in all cases, phase weighted stacking (*Schimmel*, 1999) is sufficient to raise the amplitude of the reflections above the noise level in the final stack.

Over the past two decades, significant progress has been made in the field of seismic interferometry. The method has progressed from primarily targeting surface waves (e.g. *Shapiro et al.* (2004)) to the providing the ability to extract body waves (e.g. *Nakata et al.* (2011), *Nakata et al.* (2015)). The development of auto-correlation methods and phase-based approaches to correlation and stacking have increased the potential for

seismic interferometry to produce high resolution seismic reflection images. Furthermore, established imaging techniques such as receiver functions could be combined with auto-correlation methods (*Galetti and Curtis*, 2012) to provide better constraints on Earth structure beneath seismic arrays, and create more accurate seismic models.

1.4 Aims and objectives

The overall aim of my thesis is to produce seismic images of the North Anatolian Fault Zone in the Izmit-Adapazari region in order to better understand the geological structure of the fault, and how this structure impacts on the tectonics of the area. In addition, I also aim to test and develop upon the autocorrelation methods of seismic interferometry described in Sec. 1.3. To achieve these aims, the specific objectives are:

1. Implement a phase correlation algorithm (Sec. 1.3.4) and use this algorithm to autocorrelate ambient noise recorded at the DANA network (Sec. 1.1.6) to produce a seismic reflection image of the crust and upper mantle of the Izmit-Adapazari region. The intent is to see if taking the phase correlation approach produces a clear seismic image than an amplitude based approach.

2. Apply the autocorrelation method to the P-wave coda of teleseismic earthquake recordings at DANA, and determine if using earthquake coda can achieve a higher resolution reflection image than the noise based approach.

3. Interpret these reflection images to determine if the fault zone off-sets any crustal or upper mantle discontinuities, which could indicate that strain is localised in a narrow region beneath the North Anatolian Fault.

4. Extract both Rayleigh and Love waves from the ambient noise field recorded at the DANA network, and perform ambient noise surface wave tomography to produce an S-wave velocity model of the crustal structure in the Izmit-Adapazari region.

5. Interpret the tomographic model to determine how the geological structure of the Izmit-Adapazari region interacts with the North Anatolian Fault. In particular, I will try to determine if the internal structure Armutlu-Almacik Block could be related to the bifurcation of the fault zone, and the occurrence of large earthquakes at its edges.

6. Investigate the azimuthal anisotropy of Rayleigh and Love wave phase velocities within the top 10 km of the crust in the Izmit-Adapazari region. Determine if the distribution of anisotropy is consistent with fractures or mineral orientations that may be expected to result from deformation associated with the North Anatolian Fault, or regional tectonic forces.

1.5 Thesis Road Map

In **Chapter** 2 I apply the phase correlation algorithm of *Schimmel* (1999) to the autocorrelation of ambient seismic noise recorded at DANA (Sec. 1.1.6). This work was published in *Taylor et al.* (2016). This study marks the first application of phase correlation to ambient noise autocorrelations that I am aware of. In this investigation, I was able to extract P-wave reflections from the Moho, and identify other possible reflections from the mid-to-lower crust and upper mantle. My interpretation of the reflection images is that these reflectors appear to terminate in the vicinity of the surface location of the North Anatolian Fault. This behaviour could indicate that the North Anatolian Fault has penetrated into the upper mantle as a narrow shear zone that is off-setting these structural discontinuities. I also speculate as to the cause of reduced Moho reflectivity beneath the North Anatolian Fault, which could be linked to serpentinisation of the upper mantle, and the presence of fluids. This study supports the first and third objective of this thesis (Sec. 1.4).

In **Chapter** 3 I perform ambient noise surface wave tomography, again with the seismic noise field recorded at DANA. This work has been accepted for publication pending major revisions as *Taylor et al.* (2018, accepted, in revision). In this study I extracted both Rayleigh and Love waves within the noise field propagating between the stations at DANA. From these observations, I measured phase velocities for waves with periods between 1.5 s and 10 s and then jointly inverted these phase velocities to create an isotropic S-wave velocity model of the top 10 km of the Izmit-Adapazari region. I show that the Armutlu Block that is located between the two branches of the North Anatolian Fault is characterised by high S-wave velocities, likely due to the presence of large amounts of metamorphic rocks. This result could indicate that the Armtulu Block is rigid and resistant to strain. Other features, such as the Adapazarı and Pamukova Basins are clear in the images, and appear to extend to depths of up to 4 km. This work supports objectives four and five of the thesis. I also analyse the azimuthal anisotropy of both Rayleigh and Love waves, and conclude that the fast direction for Rayleigh waves aligns parallel to the direction of maximum extension in the Izmit-Adapazari region.

In **Chapter** 4 I continue with efforts to produce reflection images through seismic interferometry by autocorrelating records of teleseimic earthquakes recorded at DANA. This study will build upon previous work (Sec. 1.3.6) to extract coherent reflections from the Moho beneath the Izmit-Adapazari region. These reflection images are then used to determine the nature of the North Anatolian Fault throughout the crust and upper mantle, the results of which are compared to the receiver function analysis of *Kahraman et al.* (2015). The potential for the northern branch of the North Anatolian Fault to be a northwards dipping structure, rather than near-vertical, is also discussed. The results are also compared to the ambient noise autocorrelations of **Chapter** 2

in terms of structural resolution, and clarity of the reflection images. The work in **Chapter** 4 is presented as a draft paper that is ready for submission to Earth and Planetary Science Letters, and supports objectives two and three.

In **Chapter** 5 I discuss the implications for the findings presented in this thesis, and provide context for the results that are obtained. In particular, I draw comparisons between the crustal structure of the North Anatolian Fault and the San Andreas Fault, and compare my observations to previous seismic results obtained in the Izmit-Adapazari region from the DANA dataset. I also discuss the evidence for the presence of serpentinite in the upper mantle beneath continental strike-slip faults, especially below the North Anatolian and San Andreas faults. Finally, I discuss the development of the autocorrelation method in recent years, along with the advantages and disadvantages provided by the variety of pre-processing schemes that are associated with the autocorrelation approach. I end the chapter by summarising the key findings that are presented in this thesis.

References

Akbayram, K., A. L. Okay, and M. Satır (2013), Early Cretaceous closure of the Intra-Pontide Ocean in western Pontides (northwestern Turkey), *J. Geodyn.*, *65*, doi:10.1016/j.jog.2012.05.003. 1.1.1, 1.1.2, 1.1.3, 1.1.4

Akbayram, K., C. C. Sorlien, and A. L. Okay (2016), Evidence for a minimum 52 ± 1 km of total offset along the northern branch of the North Anatolian Fault in northwest Turkey, *Tectonophys.*, *668*, doi:10.1016/j.tecto.2015.11.026. 1.1.4

Allam, A. A., and Y. Ben-Zion (2012), Seismic velocity structures in the southern California plate-boundary environment from double-difference tomography, *Geophys. J. Int.*, *190*, doi:10.1111/j.1365-246X.2012.05544.x. 1.2.1

Allam, A. A., V. Schulte-Pelkum, Y. Ben-Zion, C. Tape, N. Ruppert, and Z. E. Ross (2017), Ten kilometer vertical Moho offset and shallow velocity contrast along the Denali fault zone from double-difference tomography, receiver functions, and fault zone head waves, *Tectonophys.*, *721*, doi:10.1016/j.tecto.2017.09.003. 1.2.1

Altuncu Poyraz, S., M. U. Teoman, N. Türkelli, M. Kahraman, D. Cambaz, A. Mutlu, S. Rost, G. A. Houseman, D. A. Thompson, D. Cornwell, M. Utkucu, and L. Gülen (2015), New constraints on micro-seismicity and stress state in the western part of the North Anatolian Fault Zone: Observations from a dense seismic array, *Tectonophys.*, *656*, doi:10.1016/j.tecto.2014.03.015. 1.1.5

Ambraseys, N. N. (1970), Some characteristic features of the Anatolian fault zone, *Tectonophys.*, *9*, doi:10.1016/0040-1951(70)90014-4. 1.1.5, 1.1.5

Bakulin, A., and R. Calvert (2004), Virtual source: New method for imaging and 4D below complex overburden, *74th Annual International Meeting, SEG, Expanded Abstracts*. 1.3

Balfour, N. J., M. K. Savage, and J. Townend (2005), Stress and crustal anisotropy in Marlborough, New Zealand: evidence for low fault strength and structure-controlled anisotropy, *Geophys. J. Int.*, *163*, doi:10.1111/j.1365-246X.2005.02783.x. 1.2.3

Barka, A. (1999), The 17 August 1999 Izmit Earthquake, *Science*, *285*, doi:10.1126/science.285.5435.1858. 1.1.5

Barka, A., H. S. Akyüz, E. Altunel, G. Sunel, Z. Çakir, A. Dikbas, B. Yerli, R. Armijo, B. Meyer, J. B. de Chabalier, T. Rockwell, J. Dolan, R. Hartleb, T. Dawson, S. Christofferson, A. Tucker, T. Fumal, R. Langridge, R. Stenner, W. Lettis, J. Bachhuber, and W. Page (2002), The Surface Rupture and Slip Distribution of the 17 August 1999 Izmit Earthquake (M 7.4), North Anatolian Fault, *Bull. Seismol. Soc. Am.*, *92*, doi:10.1785/0120000841. 1.1.5, 1.1.5

Barruol, G., and H. Kern (1996), Seismic anisotropy and shearwave splitting in lowercrustal and uppermantle rocks from the Ivrea Zone-experimental and calculated data, *Phys. Earth Planet. Inter.*, *95*, doi:10.1016/0031-9201(95)03124-3. 1.2.3

Becker, G., and B. Knapmeyer-Endrun (2017), Crustal thickness across the Trans-European Suture Zone from ambient noise autocorrelations, *Geophys. J. Int.*, *212*, doi:10.1093/gji/ggx485. 1.3.5

Ben-Zion, Y., and C. G. Sammis (2003), Characterization of fault zones, *Pure Appl. Geophys.*, *160*, doi:10.1007/978-3-0348-8010-7_11. 1.2.1

Bensen, G. D., M. H. Ritzwoller, M. P. Barmin, A. L. Levshin, F. Lin, M. P. Moschetti, N. M. Shapiro, and Y. Yang (2007), Processing seismic ambient noise data to obtain reliable broad-band surface wave dispersion measurements, *Geophys. J. Int.*, *169*, doi:10.1111/j.1365-246X.2007.03374.x. 1.3.2, 1.3.2, 1.16, 1.3.2

Biasi, G. P., and S. G. Wesnousky (2016), Steps and Gaps in Ground Ruptures: Empirical Bounds on Rupture Propagation, *Bull. Seismol. Soc. Am.*, *106*, doi:10.1785/0120150175. 1

Bokelmann, G. H. R., and S. Baisch (1999), Nature of narrow-band signals at 2.083 Hz, *Bull. Seismol. Soc. Am.*, *89*. 1.3.5

Bonini, L., G. Toscani, and S. Seno (2014), Three-dimensional segmentation and different rupture behavior during the 2012 Emilia seismic sequence (Northern Italy), *Tectonophys.*, *630*, doi:10.1016/j.tecto.2014.05.006. 1

Bourne, S. J., P. C. England, and B. Parsons (1998), The motion of crustal blocks driven by flow of the lower lithosphere and implications for slip rates of continental strike-slip faults, *Nature*, *391*, doi:10.1144/SP311.10. 1.2.3

Bracewell, R. N. (1965), *The Fourier transform and its applications*, Mcgraw-Hill, New York, NY. 1.3.4

Bürgmann, R., and G. Dresen (2008), Rheology of the lower crust and upper mantle: Evidence from rock mechanics, geodesy, and field observations, *Annu. Rev. Earth Planet. Sci.*, *36*, doi:10.1146/annurev.earth.36.031207.124326. 1

Caldwell, W. B., S. L. Klemperer, J. F. Lawrence, S. S. Rai, and I. A. Parvez (2013), Characterizing the Main Himalayan Thrust in the Garhwal Himalaya, India with receiver function CCP stacking, *Earth Planet. Sci. Lett.*, *367*, doi:10.1016/j.epsl.2013.02.009. 1.11

Campillo, M., and A. Paul (2003), Long-range correlations in the diffuse seismic coda, *Science*, *299*, doi:10.1126/science.1078551. 1.3.2, 1.3.3

Chen, F., W. Siebel, M. Satir, M. N. Terzioğlu, and K. Saka (2002), Geochronology of the Karadere basement (NW Turkey) and implications for the geological evolution of the Istanbul zone , *Int. J. Earth Sci.*, *91*, doi:10.1007/s00531-001-0239-6. 1.1.2

Claerbout, J. F. (1968), Synthesis of a layered medium from its acoustic transmission response, *Geophysics*, *33*, doi:10.1190/1.1439927. 1, 1.3.1, 1.3.1, 1.3.1, 1.3.1

Crampin, S. (1981), A review of wave motion in anisotropic and cracked elastic-media, *Wave Motion*, *3*, doi:10.1016/0165-2125(81)90026-3. 1.2.3

Crampin, S. (1987), Geological and industrial implications of extensive-dilatancy anisotropy, *Nature*, *328*, doi:10.1038/328491a0. 1.2.3

Crampin, S., and J. H. Lovell (1991), A decade of shear-wave splitting in the Earth's crust: what does it mean? What use can we make of it? And what should we do next?, *J. Geophys. Int.*, *107*, doi:10.1111/j.1365-246X.1991.tb01401.x. 1.2.3

Crampin, S., R. McGonigle, and D. Bamford (1980), Estimating crack parameters from observations of Pwave velocity anisotropy, *Geophysics*, *45*, doi:10.1190/1.1441086. 1.2.3

Şengör, A. M. C., and Y. Yılmaz (1981), Tethyan evolution of Turkey: A plate tectonic approach, *Tectonophys.*, *75*, doi:10.1016/0040-1951(81)90275-4. 1.1.3

Şengör, A. M. C., O. Tüysüz, C. İmren, M. Sakınç, H. Eyidoğan, N. Görür, X. L. Pichon, and C. Rangin (2005), The North Anatolian Fault: A New Look, *Annu. Rev. Earth Planet. Sci.*, *33*, doi:10.1146/annurev.earth.32.101802.120415. 1.1.2, 1.1.4, 1.1.5

DANA (2012), Dense Array for Northern Anatolia, *Int. Fed. of Digital Seismograph Networks, Other/Seismic Network, Seattle, Wash.*, doi:10.7914/SN/YH_2012. 1.1.6

Doğan, B., O. Tüysüz, and F. B. Sanli (2014), Tectonostratigraphic evolution of the basins on the southern branch of the North Anatolian Fault System in the SE Marmara Region, Turkey, *Int. J. Earth Sci.*, *104*, doi:10.1007/s00531-014-1083-9. 1.1.4

Draganov, D., X. Campman, J. Thorbecke, A. Verdel, and K. Wapenaar (2009), Reflection images from ambient seismic noise, *Geophysics*, *74*, doi:10.1190/1.3193529. 1.3.3, 1.3.4

Draganov, D., X. Campman, J. Thorbecke, A. Verdel, and K. Wapenaar (2013), Seismic exploration-scale velocities and structure from ambient seismic noise (¿ 1 Hz), *J. Geophys. Res. Solid Earth*, *118*, doi:10.1002/jgrb.50339. 1.3.2, 1.3.4

Eberhart-Phillips, D., and S. Bannister (2002), Three-dimensional crustal structure in the Southern Alps region of New Zealand from inversion of local earthquake and active source data, *J. Geophys. Res. Solid Earth*, *107*, doi:10.1029/2001JB000567. 1.2.1

Eberhart-Phillips, D., and A. J. Michael (1993), Three-dimensional velocity structure, seismicity, and fault structure in the Parkfield Region, Central California, *J. Geophys. Res.*, *98*, doi:10.1029/93JB01029. 1.2.1

Eberhart-Phillips, D., P. J. Haeussler, J. T. Freymueller, A. D. Frankel, C. M. Rubin, P. Craw, N. A. Ratchovski, G. Anderson, G. A. Carver, A. J. Crone, T. E. Dawson, H. Fletcher, R. Hansen, E. L. Harp, R. A. Harris, D. P. Hill, o. S. Hreinsd R. W. Jibson, L. M. Jones, R. Kayen, D. K. Keefer, C. F. Larsen, S. C. Moran, S. F. Personius, G. Plafker, B. Sherrod, K. Sieh, N. Sitar, and W. K. Wallace (2003), The 2002 Denali Fault Earthquake, Alaska: A Large Magnitude, Slip-Partitioned Event, *Science*, *300*, doi:10.1126/science.1082703. 1.2.1

Emre, Ö., T. Y. Duman, S. Özalp, F. Şaroğlu, Ş. Olgun, H. Elmacı, and T. Çan (2016), Active fault database of Turkey, *Bull. Earthquake Eng.*, doi:10.1007/s10518-016-0041-2. 1.2

Endrun, B., S. Lebedev, T. Meier, C. Tirel, and W. Friederich (2011), Complex layered deformation within the Aegean crust and mantle revealed by seismic anisotropy, *Nature Geosci.*, *4*, doi:10.1038/ngeo1065. 1.2.3, 1.14

England, P., and J. Jackson (2011), Uncharted seismic risk, *Nature Geosci.*, *4*, doi:10.1038/ngeo1168. 1

England, P., G. Houseman, and J. Nocquet (2016), Constraints from GPS measurements on the dynamics of deformation in Anatolia and the Aegean, *J. Geophys. Res. Solid Earth*, *121*, doi:10.1002/2016JB013382. 1.1.5

Evangelidis, C. P., W. Liang, N. S. Melis, and K. I. Konstantinou (2011), Shear wave anisotropy beneath the Aegean inferred from SKS splitting observations, *J. Geophys. Res. Solid Earth*, *116*, doi:10.1029/2010JB007884. 1.2.3

Fagereng, A., V. Toy, and J. V. Rowland (eds) (2011), Geology of the Earthquake Source: A Volume in Honour of Rick Sibson, *Geol. Soc. Lond. Spec. Pub.*, *359*, doi:10.1144/SP359.1. 1

Fichtner, A., E. Saygin, T. Taymaz, P. Cupillard, Y. Capdeville, and J. Trampert (2013), The deep structure of the North Anatolian Fault Zone, *Earth Planet. Sci. Lett.*, *373*, doi:10.1016/j.epsl.2013.04.027. 1.6, 1.2.1

Ford, H. A., K. M. Fischer, and V. Lekic (2014), Localized shear in the deep lithosphere beneath the San Andreas fault system, *Geology*, *42*, doi:10.1130/G35128.1. 1.2.2

Forghani, F., and R. Snieder (2010), Underestimation of body waves and feasibility of surface-wave reconstruction by seismic interferometry, *The Leading Edge*, *29*, doi:10.1190/1.3462779. 1.3.3

Frederiksen, A. W., D. A. Thompson, S. Rost, D. G. Cornwell, L. Gülen, G. A. Houseman, M. Kahraman, S. Altuncu Poyraz, U. M. Teoman, N. Türkelli, and M. Utkucu (2015), Crustal thickness variations and isostatic disequilibrium across the North Anatolian Fault, western Turkey, *Geophys. Res. Lett.*, *42*, doi:10.1002/2014GL062401. 1.1.2, 1.1.4, 1.1.6

Galetti, E., and A. Curtis (2012), Generalised receiver functions and seismic interferometry, *Tectonophys.*, *532-535*, doi:10.1016/j.tecto.2011.12.004. 1.3.6

Gorbatov, A., E. Saygin, and B. L. N. Kennett (2013), Crustal properties from seismic station autocorrelograms, *Geophys. J. Int.*, *192*, doi:10.1093/gji/ggs064. 1.3.5, 1.3.6

Green, G. (1828), *An essay on the application of mathematical analysis to the theories of electricity and magnetism*, Privately Published. 1.3

Gupta, I. N. (1965), Standing-wave phenomena in short-period seismic noise, *Geophysics*, *30*, doi:10.1190/1.1439707. 1.3.2, 1.3.4

Haubrich, R. A., W. H. Munk, and F. E. Snodgrass (1963), Comparative spectra of microseisms and swell, *Bull. Seismol. Soc. Am.*, *53*. 1.3.2

Heath, B. A., E. E. E. Hooft, and D. R. Toomey (2018), Autocorrelation of the Seismic Wavefield at Newberry Volcano: Reflections From the Magmatic and Geothermal Systems, *Geophys. Res. Lett.*, *45*, doi:10.1002/2017GL076706. 1.3.5

Helmberger, D., and R. A. Wiggins (1971), Retrieval of the P wave reflectivity response from autocorrelation of seismic noise: Jakarta Basin, Indonesia, *J. Geophys. Res.*, *76*, doi:10.1029/JB076i014p03229. 1.3.5

Hess, H. H. (1964), Seismic Anisotropy of the Uppermost Mantle under Oceans, *Nature*, *203*, doi:10.1038/203629a0. 1.2.3

Hirn, A., J. Lepine, G. Jobert, M. Spain, G. Wittlinger, Z. X. Xu, E. Y. Gao, X. J. Wang, J. W. Teng, S. B. Xiong, M. R. Pandey, and J. M. Tater (1984), Crustal structure and variability of the Himalayan border of Tibet, *Nature*, *307*, doi:10.1038/307023a0. 1.2.2

Hubert-Ferrari, A., A. Barka, E. Jacques, S. S. Nalbant, B. Meyer, R. Armijo, P. Tapponier, and G. C. P. King (2000), Seismic hazard in the Marmara Sea region following the 17 August 1999 Izmit earthquake, *Nature*, *404*, doi:10.1038/35005054. 1.1.5

Hussain, E., T. J. Wright, R. J. Walters, D. Bekaert, A. Hooper, and G. A. Houseman (2016a), Geodetic observations of postseismic creep in the decade after the 1999 Izmit earthquake, Turkey: Implications for a shallow slip decit, *J. Geophys. Res. Solid Earth*, *121*, doi:10.1002/2015JB012737. 1.1.2, 1.1.5

Hussain, E., A. Hooper, T. J. Wright, R. J. Walters, and D. Bekaert (2016b), Interseismic strain accumulation across the central North Anatolian Fault from iteratively unwrapped InSAR measurements, *J. Geophys. Res. Solid Earth*, *121*, doi:10.1002/2016JB013108. 1.1.5, 1.1.5

Ismaïl, W. B., and D. Mainprice (1998), An olivine fabric database: an overview of upper mantle fabrics and seismic anisotropy, *Tectonophys.*, *296*, doi:10.1016/S0040-1951(98)00141-3. 1.2.3

Ji, S., and M. H. Salisbury (1993), Shearwave velocities, anisotropy and splitting in highgrade mylonites, *Tectonophys.*, *221*, doi:10.1016/0040-1951(93)90173-H. 1.2.3

Kahraman, M., D. G. Cornwell, D. A. Thompson, S. Rost, G. A. Houseman, N. Türkelli, U. Teoman, S. Altuncu Poyraz, M. Utkucu, and L. Gülen (2015), Crustal-scale shear zones and heterogeneous structure beneath the North Anatolian Fault Zone, Turkey, revealed by a high-density seismometer array, *Earth Planet. Sci. Lett.*, *430*, doi:10.1016/j.epsl.2015.08.014. 1.1.6, 1.2.2, 1.12, 1.5

Karimi, B., N. McQuarrie, J. Lin, and W. Harbert (2014), Determining the geometry of the North Anatolian Fault East of the Marmara Sea through integrated stress modeling and remote sensing techniques, *Tectonophys.*, *623*, doi:10.1016/j.tecto.2014.03.015. 1.1.5

Kendall, J. M., S. Pilidou, D. Keir, I. D. Bastow, G. W. Stuart, and A. Ayele (2006), Mantle upwellings, melt migration and the rifting of Africa: insights from seismic anisotropy, *Geol. Soc. London Spec. Pubs.*, *259*, doi:10.1144/GSL.SP.2006.259.01.06. 1.2.3

Kennett, B. L. N. (2015), Lithosphere–asthenosphere P-wave reflectivity across Australia, *Earth Planet. Sci. Lett.*, *431*, doi:10.1016/j.epsl.2015.09.039. 1.3.5, 1.20, 1.3.5, 1.3.6

Kennett, B. L. N., E. Saygin, and M. Salmon (2015), Stacking autocorrelograms to map Moho depth with high spatial resolution in southeastern Australia, *Geophys. Res. Lett.*, *42*, doi:10.1002/2015GL065345. 1.3.5, 1.3.5

Kern, H., and H. R. Wenk (1990), Fabricrelated velocity anisotropy and shear wave splitting in rocks from the Santa Rosa Mylonite Zone, California, *J. Geophys. Res. Solid Earth*, *95*, doi:10.1029/JB095iB07p11213. 1.2.3

Komazawa, M., H. Morikawa, K. Nakamura, J. Akamatsu, K. Nishimura, S. Sawada, A. Erken, and A. Onalp (2002), Bedrock structure in Adapazari, Turkey: a possible cause of severe damage by the 1999 Kocaeli earthquake, *Soil Dyn. Earthquake Eng.*, *22*, doi:10.1016/S0267-7261(02)00105-7. 1.1.2

Koukouvelas, I. K., and A. Aydin (2002), Fault structure and related basins of the North Aegean Sea and its surroundings, *Tectonics*, *21*, doi:10.1029/2001TC901037. 1.1.5

Koulakov, I., D. Bindi, S. Parolai, H. Grosser, and C. Milkereit (2010), Distribution of Seismic Velocities and Attenuation in the Crust beneath the North Anatolian Fault (Turkey) from Local Earthquake Tomography, *Bull. Seismol. Soc. Am.*, *100*, doi:10.1785/0120090105. 1.8, 1.2.1

Kreemer, C., W. E. Holt, and A. J. Haines (2003), An integrated global model of present-day plate motions and plate boundary deformation, *Geophys. J. Int.*, *154*, doi:10.1046/j.1365-246X.2003.01917.x. 1.14

Langston, C. (1979), Structure Under Mount Rainier, Washington, Inferred From Teleseismic Body Waves, *J. Geophys. Res.*, *84*, doi:10.1029/JB084iB09p04749. 1.2.2

Le Pichon, X., N. Chamot-Rooke, C. Rangin, and A. M. C. Şengör (2003), The North Anatolian Fault in the Sea of Marmara, *J. Geophys. Res.*, *108*, doi:10.1029/2002JB001862. 1.1.5

Li, Y., Q. Wu, F. Zhang, Q. Feng, and R. Zhang (2011), Seismic anisotropy of the Northeastern Tibetan Plateau from shear wave splitting analysis, *Earth Planet. Sci. Lett.*, *304*, doi:10.1016/j.epsl.2011.01.026. 1.2.3

Ligorria, J. P., and C. J. Ammon (1999), Iterative deconvolution and receiver-function estimation, *Bull. Seismol. Soc. Am.*, *89*. 1.2.2

Lin, F., M. H. Ritzwoller, Y. Yang, M. P. Moschetti, and M. J. Fouch (2011), Complex and variable crustal and uppermost mantle seismic anisotropy in the western United States, *Nature Geosci.*, *4*, doi:10.1038/ngeo1036. 1.13, 1.2.3

Lin, F. C., and B. Schmandt (2014), Upper crustal azimuthal anisotropy across the contiguous U.S. determined by Rayleigh wave ellipticity, *Geophys. Res. Lett.*, *41*, doi:10.1002/2014GL062362. 1.2.3

Liu, Q., and Y. J. Gu (2012), Seismic imaging: From classical to adjoint tomography, *Tectonophys.*, *566-567*, doi:10.1016/j.tecto.2012.07.006. 1.2.1

Longuet-Higgins, M. S. (1950), A theory of the origin of microseisms, *Philos. Trans. R. Soc. London*, *243*, doi:10.1098/rsta.1950.0012. 1.3.2

Mainprice, D., and A. Nicolas (1989), Development of shape and lattice preferred orientations: application to the seismic anisotropy of the lower crust, *J. Struct. Geol.*, *11*, doi:10.1016/0191-8141(89)90042-4. 1.2.3

Michael, A. J., and D. Eberhart-Phillips (1991), Relations Among Fault Behavior, Subsurface Geology, and Three-Dimensional Velocity Models, *Science*, *253*, doi:10.1126/science.253.5020.651. 1.2.1

Nakata, N., R. Snieder, T. Tsuji, K. Larner, and T. Matsuoka (2011), Shear wave imaging from traffic noise using seismic interferometry by cross-coherence, *Geophysics*, *76*, doi:10.1190/geo2010-0188.1. 1.3.4, 1.3.6

Nakata, N., R. Snieder, and M. Behm (2014), Body-wave interferometry using regional earthquakes with multidimensional deconvolution after wavefield decomposition at the free surface, *Geophys. J. Int.*, *199*, doi:10.1093/gji/ggu316. 1.3.2, 1.3.5

Nakata, N., J. P. Chang, J. F. Lawrence, and P. Boué (2015), Body wave extraction and tomography at Long Beach, California, with ambientnoise interferometry , *J. Geophys. Res. Solid Earth*, *120*, doi:10.1002/2015JB011870. 1.3.2, 1.3.4, 1.3.6

Norris, R. J., and A. F. Cooper (2001), Late Quaternary slip rates and slip partitioning on the Alpine Fault, New Zealand, *J. Struct. Geol.*, *23*, doi:10.1016/S0191-8141(00)00122-X. 1.2.1

Okay, A. I., A. M. C. Şengör, and N. Görür (1994), Kinematic history of the opening of the Black Sea and its effect on the surrounding regions, *Geology*, *22*, doi:10.1130/0091-7613(1994)022¡0267:KHOTOO¿2.3.CO;2. 1.1.1, 1.1.2, 1.1.3

Okay, A. L. (2008), Geology of Turkey: A Synopsis, *Anschnitt*, *21*. 1.1.1, 1.1.1, 1.1.3

Okay, A. L., and O. Tüysüz (1999), Tethyan sutures of northern Turkey, *Geological Society, London, Special Publications*, *156*, doi:10.1144/GSL.SP.1999.156.01.22. 1.1, 1.1.1, 1.1.3

Okay, A. L., E. Bozkurt, M. Satır, E. Yiğitbaş, Q. G. Crowley, and C. K. Shang (2008), Defining the southern margin of Avalonia in the Pontides: Geochronological data from the Late Proterozoic and Ordovician granitoids from NW Turkey, *Tectonophys.*, *461*, doi:10.1016/j.tecto.2008.02.004. 1.1.1

Oren, C., and R. L. Nowack (2017), Seismic body-wave interferometry using noise autocorrelations for crustal structure, *Geophys. J. Int.*, *208*, doi:10.1093/gji/ggw394. 1.3.5, 1.21, 1.3.5

Özacan, Z., A. I. Okay, E. Özacan, A. Hakyemez, and S. Özacan-Altıner (2012), Late CretaceousEocene Geological Evolution of the Pontides Based on New Stratigraphic and Palaeontologic Data Between the Black Sea Coast and Bursa (NW Turkey), *Turkish J. Earth Sci.*, *21*, doi:10.3906/yer-1102-8. 1.1.2

Papaleo, E., D. G. Cornwell, and N. Rawlinson (2017), Seismic tomography of the North Anatolian Fault: New insights into structural heterogeneity along a continental strikeslip fault, *Geophys. Res. Lett.*, *44*, doi:10.1002/2017GL072726. 1.1.6, 1.9, 1.2.1

Papaleo, E., D. G. Cornwell, and N. Rawlinson (2018), Constraints on North Anatolian Fault zone width in the crust and upper mantle from Swave teleseismic tomography, *J. Geophys. Res. Solid Earth*, doi:10.1002/2017JB015386. 1.1.6, 1.2.1

Pham, T., and H. Tkalčić (2017), On the feasibility and use of teleseismic P wave coda autocorrelation for mapping shallow seismic discontinuities, *J. Geophys. Res. Solid Earth*, *122*, doi:10.1002/2017JB013975. 1.3.6

Phillips, W. S., and M. C. Fehler (1991), Traveltime tomography: A comparison of popular methods, *Geophysics*, *56*, doi:10.1190/1.1442974. 1.2.1

Poli, P., H. A. Pedersen, M. Campillo, and the POLENET/LAPNET Working Group (2012), Emergence of body waves from crosscorrelation of short period seismic noise, *Geophys. J. Int.*, *188*, doi:10.1111/j.1365-246X.2011.05271.x. 1.3.2, 1.3.3

Rawlinson, N., and M. Sambridge (2003), Seismic traveltime tomography of the crust and lithosphere, *Adv. Geophys.*, *46*, doi:10.1016/S0065-2687(03)46002-0. 1.2.1

Rawlinson, N., S. Pozgay, and S. Fishwick (2010), Seismic tomography: A window into deep Earth, *Phys. Earth Planet. Int.*, *178*, doi:10.1016/j.pepi.2009.10.002. 1.2.1

Reilinger, R., S. McClusky, D. Paradissis, S. Ergintav, and P. Vernant (2010), Geodetic constraints on the tectonic evolution of the aegean region and strain accumulation along the hellenic subduction zone, *Tectonophys.*, *488*, doi:10.1016/j.tecto.2009.05.027. 1.2.3

Roux, P., K. Sabra, P. Gerstoft, W. A. Kuperman, and M. C. Fehler (2005), P-wave from cross-correlation of seismic noise, *Geophys. Res. Lett.*, *32*, doi:10.1029/2005GL023803. 1.3.3

Ruigrok, E., and K. Wapenaar (2012), Globalphase seismic interferometry unveils Pwave reflectivity below the Himalayas and Tibet, *Geophys. Res. Lett.*, *39*, doi:10.1029/2012GL051672. 1.3.1, 1.3.6, 1.3.6, 1.22

Ruigrok, E., X. Campman, and K. Wapenaar (2011), Extraction of P-wave reflections from microseisms, *CR. Geosci.*, *343*, doi:10.1016/j.crte.2011.02.006. 1.3.4

Salmon, M., B. L. N. Kennett, T. Stern, , and A. R. A. Aitken (2013), The Moho in Australia and New Zealand, *Tectonophys.*, *609*, doi:10.1016/j.tecto.2012.07.009. 1.20

Savage, M. K. (1999), Seismic anisotropy and mantle deformation: What have we learned from shear wave splitting?, *Rev. Geophys.*, *37*, doi:10.1029/98RG02075. 1.2.3

Saygin, E., P. R. Cummins, and D. Lumley (2017), Retrieval of the P wave reflectivity response from autocorrelation of seismic noise: Jakarta Basin, Indonesia, *Geophys. Res. Lett.*, *44*, doi:10.1002/2016GL071363. 1.3.5

Schimmel, M. (1999), Phase cross-correlations: Design, comparisons, and applications, *Bull. Seismol. Soc. Am.*, *89*. 1.3.4, 1.3.4, 1.3.5, 1.3.6, 1.5

Schimmel, M., and H. Paulssen (1997), Noise reduction and detection of weak, coherent signals through phase-weighted stacks, *Geophys. J. Int.*, *130*, doi:10.1111/j.1365-246X.1997.tb05664.x. 1.3.4, 1.3.4, 1.3.4, 1.3.5

Schimmel, M., E. Stutzmann, and J. Gallart (2011), Using instantaneous phase coherence for signal extraction from ambient noise data at a local to a global scale, *Geophys. J. Int.*, *184*, doi:10.1111/j.1365-246X.2010.04861.x. 1.3.4, 1.18

Schuster, G. T., J. Yu, J. Sheng, and J. Rickett (2004), Interferometric/daylight seismic imaging, *Geophys. J. Int.*, *157*, doi:10.1111/j.1365-246X.2004.02251.x. 1.3

Şengör, A. M. C. (1979), The North Anatolian transform fault: its age, offset and tectonic significance, *J. Geol. Soc.*, *136*, doi:10.1144/gsjgs.136.3.0269. 1.1.5, 1.1.5

Şengör, A. M. C., N. Görür, and F. Şaroğlu (1985), *Strike-Slip Deformation, Basin Formation, and Sedimentation*, doi:10.2110/pec.85.37.0227. 1.1.5

Seriff, A. J., C. Velzeboer, and R. Haase (1965), Possible P-wave observations in short-period seismic noise, *Geophysics*, *30*, doi:10.1190/1.1439709. 1.3.2, 1.3.4

Shapiro, N. M., M. H. Ritzwoller, P. Molnar, and V. Levin (2004), Thinning and Flow of Tibetan Crust Constrained by Seismic Anisotropy, *Science*, *305*, doi:10.1126/science.1098276. 1, 1.3.2, 1.3.3, 1.3.6

Shapiro, N. M., M. Campillo, L. STehly, and M. H. Ritzwoller (2005), High resolution surface wave tomography from ambient seismic noise, *Science*, *307*, doi:10.1126/science.1108339. 1, 1.3.2

Shapiro, N. M., M. H. Ritzwoller, and G. D. Bensen (2006), Source location of the 26 sec microseism from crosscorrelations of ambient seismic noise, *Geophys. Res. Lett.*, *33*, doi:10.1029/2006GL027010. 1.3.2

Sherrington, H. F., G. Zandt, and A. Frederiksen (2004), Crustal fabric in the Tibetan Plateau based on waveform inversions for seismic anisotropy parameters, *J. Geophys. Res. Solid Earth*, *109*, doi:10.1029/2002JB002345. 1.2.3, 1.2.3

Smith, M. L., and A. F. Dahlen (1973), The azimuthal dependence of Love and Rayleigh wave propagation in a slightly anisotropic medium, *J. Geophys. Res.*, *78*, doi:10.1029/JB078i017p03321. 1.2.3

Snieder, R. (2004), Extracting the Greens function from the correlation of coda waves: A derivation based on stationary phase, *Phys. Rev. E*, *69*, doi:10.1103/PhysRevE.69.046610. 1.3.3, 1.17

Snieder, R., K. Wapenaar, and U. Wegler (2007), Unified Green's function retrieval by cross-correlation; connection with energy principles, *Phys. Rev. E*, *75*, doi:10.1103/PhysRevE.75.036103. 1.3.1

Stein, R. S., A. A. Barka, and J. H. Dieterich (1997), Progressive failure on the North Anatolian fault since 1939 by earthquake stress triggering, *Geophys. J. Int.*, *128*, doi:10.1111/j.1365-246X.1997.tb05321.x. 1.1.5

Sun, W., and B. Kennett (2017), Midlithosphere discontinuities beneath the western and central North China Craton, *Geophys. Res. Lett*, *44*, doi:10.1002/2016GL071840. 1.3.6

Sun, W., and B. L. N. Kennett (2016), Receiver structure from teleseisms: Autocorrelation and cross correlation, *Geophys. Res. Lett.*, *43*, doi:10.1002/2016GL069564. 1.3.6

Sylvester, A. G. (1988), Strike-slip faults, *Geol. Soc. Am. Bull.*, *100*, doi:10.1130/0016-7606(1988)100¡1666:SSF¿2.3.CO;2. 1.2.1

Taylor, G., S. Rost, and G. Houseman (2016), Crustal imaging across the North Anatolian Fault Zone from the autocorrelation of ambient seismic noise, *Geophys. Res. Lett.*, *43*, doi:10.1002/2016GL067715. 1.3.5, 1.5

Taylor, G., S. Rost, G. Houseman, and G. Hillers (2018, accepted, in revision), Near surface structure of the North Anatolian Fault Zone from Rayleigh and Love wave tomography using ambient seismic noise, *J. Geophys. Res. Solid Earth*. 1.5

Thatcher, W. (1979), Systematic inversion of geodetic data in Central California, *J. Geophys. Res.*, *84*, doi:10.1029/JB084iB05p02283. 1.2.1

Thurber, C. H., H. Zhang, F. Waldhauser, J. Hardebeck, A. Michael, and D. Eberhart-Phillips (2006), Three-dimensional compressional wavespeed model, earthquake relocations, and focal mechanisms for the Parkfield, California, region, *Bull. Seismol. Soc. Am.*, *96*, doi:10.1785/0120050825. 1.4, 1.2.1

Tibuleac, I. M., and D. von Seggern (2012), Crust-mantle boundary reflectors in Nevada from ambient seismic noise autocorrelations, *Geophys. J. Int.*, *189*, doi:10.1111/j.1365-246X.2011.05336.x. 1.3.5, 1.3.5, 1.19, 1.3.5, 1.21

Tirel, C., P. Gautier, D. . J. J. van Hinsbergen, and M. J. R. Wortel (2009), Collision and Collapse at the AfricaArabiaEurasia Subduction Zone, *Spec. Pub. Geol. Soc. Lond.*, *311*, doi:10.1144/SP311.10. 1.14

Tommasi, A., D. Mainprice, G. Canova, and Y. Chastel (2000), Viscoplastic selfconsistent and equilibriumbased modeling of olivine lattice preferred orientations: Implications for the upper mantle seismic anisotropy, *J. Geophys. Res. Solid Earth*, *105*, doi:10.1029/1999JB900411. 1.2.3

Tüysüz, O. (2017), Cretaceous geological evolution of the Pontides, *Geol. Soc. Lond. Spec. Pub.*, *464*, doi:10.1144/SP464.9. 1.1

Ünay, E., Ö. Emre, T. Erkal, and M. Keçer (2001), The rodent fauna from the Adapazarı pull-apart basin (NW Anatolia): its bearings on the age of the North Anatolian fault, *Geodin. Acta*, *14*, doi:10.1080/09853111.2001.11432442. 1.1.2

USGS (2006), Shuttle Radar Topography Mission, *Global Land Cover Facility, University of Maryland*. 1.2

Vergne, J., G. Wittlinger, Q. Hui, P. Tapponnier, G. Poupinet, J. Mei, G. Herquel, and A. Paul (2002), Seismic evidence for stepwise thickening of the crust across the NE Tibetan Plateau, *Earth Planet. Sci. Lett.*, *203*, doi:10.1016/S0012-821X(02)00853-1. 1.2.2

Virieux, J., and S. Operto (2009), An overview of full-waveform inversion in exploration geophysics, *Geophysics*, *74*, doi:10.1190/1.3238367. 1.2.1

Wapenaar, K. (2003), Synthesis of an inhomogeneous medium from its acoustic transmission response, *Geophysics*, *68*, doi:10.1190/1.1620649. 1.3.1

Wapenaar, K. (2004), Retrieving the Elastodynamic Green's Function of an Arbitrary Inhomogeneous Medium by Cross Correlation, *Phys. Rev. Lett.*, *93*, doi:10.1103/PhysRevLett.93.254301. 1.3, 1.3.1

Wapenaar, K., and J. Fokkema (2006), Green's function representations for seismic interferometry, *Geophysics*, *71*, doi:10.1190/1.2213955. 1.3.1

Wapenaar, K., D. Draganov, R. Snieder, X. Campman, and A. Verdel (2010a), Tutorial on seismic interferometry: Part 1 Basic principles and applications, *Geophysics*, *75*, doi:10.1190/1.3457445. 1.3.1

Wapenaar, K., E. Slob, and R. Snieder (2010b), On seismic interferometry, the generalized optical theorem, and the scattering matrix of a point scatterer, *Geophysics*, *75*, doi:10.1190/1.3374359. 1.3.3

Wilson, C. K., C. H. Jones, P. Molnar, A. F. Sheehan, and O. S. Boyd (2004), Distributed deformation in the lower crust and upper mantle beneath a continental strike-slip fault zone: Marlborough fault system, South Island, New Zealand, *Geology*, *32*, doi:10.1130/G20657.1. 1.2.2, 1.2.3

Wittlinger, G., J. Vergne, P. Tapponnier, V. Farra, G. Poupinet, M. Jiang, H. Su, G. Herquel, and A. Paul (2004), Teleseismic imaging of subducting lithosphere and Moho offsets beneath western Tibet, *Earth Planet. Sci. Lett.*, *221*, doi:10.1016/S0012-821X(03)00723-4. 1.11

Yang, H. (2015), Recent advances in imaging crustal fault zones: a review, *Earthq. Sci.*, *28*, doi:10.1007/s11589-015-0114-3. 1

Yıldırım, C., and O. Tüysüz (2017), Estimation of the long-term slip, surface uplift and block rotation along the northern strand of the North Anatolian Fault Zone: Inferences from geomorphology of the Almacik Block, *Geomorphology*, *297*, doi:10.1016/j.geomorph.2017.08.038. 1.1.4

Yılmaz, Y., Ş. C. Genç, E. Yiğitbaş, M. Bozcu, and K. Yılmaz (1995), Geological evolution of the late Mesozoic continental margin of Northwestern Anatolia, *Tectonophys.*, *243*, doi:10.1016/0040-1951(94)00196-G. 1.1.1, 1.1.2, 1.3, 1.1.3, 1.1.4, 1.1.4

Yosal-Çevikbilen, S., C. B. Biryol, S. Beck, G. Zandt, T. Taymaz, H. E. Adıyaman, and A. A. Özacar (2012), 3-D crustal structure of the North Anatolian Fault Zone in north-central Anatolia revealed by local earthquake tomography, *Geophys. J. Int.*, *188*, doi:10.1111/j.1365-246X.2011.05313.x. 1.7, 1.2.1

Yoshizawa, K. (2014), Radially anisotropic 3-D shear wave structure of the Australian lithosphere and asthenosphere from multi-mode surface waves, *Phys. Earth Planet. Inter.*, *235*, doi:10.1016/j.pepi.2014.07.008. 1.20

Zhang, Z., Y. Wang, G. A. Houseman, T. Xu, Z. Wu, X. Yuan, Y. Chen, X. Tian, Z. Bai, and J. Teng (2014), The Moho beneath western Tibet: Shear zones and eclogitization in the lower crust, *Earth Planet. Sci. Lett.*, *408*, doi:10.1016/j.epsl.2014.10.022. 1.2.2, 1.11

Zhu, L. (2000), Crustal structure across the San Andreas Fault, southern California from teleseismic converted waves, *Earth Planet. Sci. Lett.*, *179*, doi:10.1016/S0012-821X(00)00101-1. 1.2.2, 1.10

Zigone, D., Y. Ben-Zion, M. Campillo, and P. Roux (2015), Seismic tomography of the Southern California plate boundary region from noise-based Rayleigh and Love waves, *Pure Appl. Geophys.*, *172*, doi:10.1007/s00024-014-0872-1. 1.2.1, 1.5, 1.13, 1.2.3

Chapter 2

Crustal imaging across the North Anatolian Fault Zone from the autocorrelation of ambient seismic noise

G. Taylor[1], S. Rost[1], and G. Houseman[1]

[1] *School of Earth and Environment, University of Leeds, Leeds, United Kingdom*

Abstract

Seismic images of active fault zones can be used to examine the structure of faults throughout the crust and upper mantle, and give clues as to whether the associated deformation occurs within a narrow shear zone, or is broadly distributed through the lower crust. Limitations on seismic resolution within the crust, and difficulties imaging shallow structures such as the crust-mantle boundary (Moho), place constraints on the interpretation of seismic images. In this study we retrieve body wave reflections from autocorrelations of ambient seismic noise. The instantaneous phase coherence autocorrelations allow unprecedented ambient noise images of the North Anatolian Fault Zone (NAFZ). Our reflection profiles show a Moho reflected P-wave, and additional structure within the crust and upper mantle. We image a distinct vertical offset of the Moho associated with the northern branch of the NAFZ indicating that deformation related to the fault remains narrow in the upper mantle.

2.1 Introduction

The behaviour of fault zones within continental settings is more complex than simple plate tectonics would predict. While deformation in oceanic environments is typically localised on plate boundaries, deformation within continents occurs across regions that can be thousands of kilometres wide (e.g. the Alpine-Himalayan Belt). It has been proposed that ductile flow within the lower crust causes distributed deformation that otherwise occurs within narrow shear zones in the continental upper crust and upper mantle (*Bürgmann and Dresen*, 2008). The formation and evolution of major continental transform faults, like the North Anatolian Fault, appears to be a delicate balance between accommodation of the dominant tectonic strain field, and the exploitation of weak pre-existing geological features such as suture zones.

In particular, understanding how structural changes throughout a fault zone can be used to infer the mechanism of strain localisation at lower crustal depths has important implications for our knowledge of lithospheric rheology, and our understanding of the earthquake cycle. Seismic imaging of active fault zones has provided two contrasting arguments: some authors, such as *Wilson et al.* (2004), argue that strain is more diffuse in the lower crust and upper mantle, forming a broad shear zone, and citing pervasive seismic anisotropy in the lower crust and, in the case of the Marlborough Fault Zone, the lack of visible offsets in the Moho discontinuity beneath the surface signature of the fault.

In contrast, other studies on continental strike slip faults (*Zhu* (2000), *Weber et al.* (2004)) argue that variations in crustal thickness, correlated with the location of active faults, show that the Moho has been offset during faulting therefore showing that strain may still be localised in a narrow band of ductile deformation to at least upper mantle depths. Receiver function analysis of the Tibetan Plateau (*Zhang et al.*, 2014) has also revealed apparent Moho depth offsets that correspond to surface traces of major faults and sutures, in the region of the Earth's thickest continental crust. Their images suggest that narrow zones of localised strain structures can reach to at least upper mantle depths, even though crustal thickening and anisotropy imply that diffuse strain is also important.

Here we aim to image the crustal structure of the North Anatolian Fault Zone (NAFZ) in Turkey in the region of the 1999 Izmit and Düzce earthquakes. The NAFZ is a ∼1500 km long right-lateral strike-slip system along which the Anatolian Block adjoins Eurasia. The NAFZ formed in the mid-Miocene and propagated westwards to reach the Sea of Marmara ∼ 200 ka ago (*Sengör et al.*, 2005), and extends now into the North Aegean trough. Since 1939 the NAFZ has displayed a westward migrating pattern of large earthquakes ($M_w \geq 7$), resulting most recently in the magnitude 7.6 and 7.2 Izmit and Düzce earthquakes of 1999 (*Barka et al.*, 2002), and continues to pose significant seismic hazard to the region.

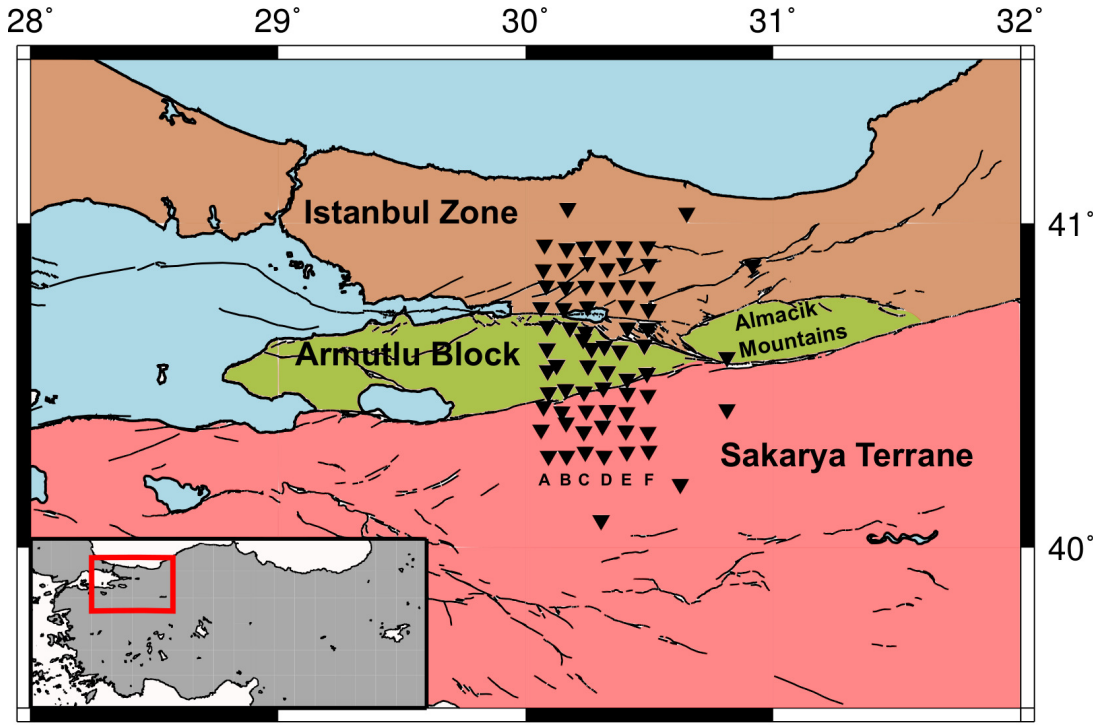

Figure 2.1: Overview of the tectonic region studied here. Stations of the DANA network are shown as black triangles. The letters beneath each vertical profile of receivers denote the labeling of the corresponding profile in Figure 2. All major geological units are color coded. Brown: Istanbul Zone. Green: Armutlu Block and Almacik Mountains. Pink: Sakarya Terrane. Black lines indicate mapped faults in the region (*MTA*, 2012). Inset: Map of Anatolia. Red box indicates the region of northwestern Anatolia, shown in the main map, which is the focus of this study.

In this region, the NAFZ divides into a northern and southern strand (*Karimi et al.*, 2014), with the northern strand showing more seismic activity (*Altuncu Poyraz et al.*, 2015). The NAFZ appears to follow the trend of accretionary complexes (Fig. 2.1) formed during the closing of the Tethys Ocean (*Sengör et al.*, 2005). The NAFZ roughly follows the Intra-Pontide Suture between the continental Istanbul Zone and the accretionary Sakarya Terrane in the south (*Okay*, 2008). In between the northern and southern strands of the NAFZ lies the Armutlu-Almacik block (Fig. 2.1), which formed in a similar fashion to the Sakarya Terrane, as a set of accretionary complexes during the closure of the Tethys Ocean (*Sengör et al.*, 2005, *Bekler and Gurbuz*, 2008).

Between May 2012 and October 2013, the University of Leeds, Kandilli Observatory and Earthquake Research Institute (KOERI) and Sakarya University installed a 66 station network of 3-component seismometers in a roughly rectangular grid (Fig. 2.1) with an approximate station spacing of $\sim$ 7 km known as the Dense Array for Northern Anatolia (*DANA*, 2012). DANA was supplemented by three permanent stations of the KOERI network (GULT, SAUV, and SPNC), and seven stations to the east of the array forming a semi-circle, with larger station spacing. The network was deployed across the rupture zone of the 1999 Izmit earthquake (*Barka et al.*, 2002), and crossed both

the northern and southern strands of the NAFZ to sample all three crustal terranes: the Istanbul Zone to the north, the Armutlu-Almacik block bounded by the two fault strands, and the Sakarya Terrane to the south (Fig. 2.1).

2.2 Data and Methods

In order to image the structure of the NAFZ throughout the entire crust and upper mantle, we constructed stacked autocorrelograms of continuous seismic records from DANA. It has been shown that the autocorrelation of surface displacement at a seismometer yields information on the reflection response of structure near the receiver, scaled by the spectrum of the sources exciting the ground motion and by amplitude of the waves arriving at the structure beneath the instrument (*Gorbatov et al.*, 2013). Thus, by autocorrelating continuous records of ground motion, it is possible to obtain Earth's reflection response at the seismometer location and to image crustal structure, including free surface reverberations, for a co-located source and receiver (*Claerbout*, 1968). This technique has been applied to image crustal structure beneath the continental United States (*Tibuleac and von Seggern*, 2012) and Australia (*Gorbatov et al.*, 2013, *Kennett et al.*, 2015, *Kennett*, 2015) and offers complementary information to the widely used receiver function technique. We constructed autocorrelograms for all stations of the DANA network by splitting the dataset into 1-hour long time windows of the vertical component of ground motion. In contrast to previous studies using autocorrelation interferometry (*Tibuleac and von Seggern*, 2012, *Gorbatov et al.*, 2013), here we employ a phase auto-correlation method to enhance the signal-to-noise ratio, and ensure that coherent signals such as body wave reflections are retrieved independent of amplitude (*Schimmel*, 1999).

Phase correlations have been rigorously compared with amplitude correlation methods by *Schimmel* (1999) and *Schimmel et al.* (2011). *Schimmel et al.* (2011) utilised phase correlations to obtain empirical Green's functions from seismic array data at a local array in southern Spain, as well as the GEOSCOPE global seismic network. *Schimmel et al.* (2011) noted close correspondence between the retrieved Green's functions obtained using phase and amplitude correlation, with those computed through phase correlation showing higher signal-to-noise ratio. The correspondence between phase and amplitude correlation implies that we can use phase autocorrelation to retrieve the reflection response of the Earth, even though the mathematical basis for this correspondence may be unclear. To calculate the phase correlograms, the 1 hour data segments are Hilbert transformed and the analytical signal (a complex valued time series in which the amplitude represents the envelope of the seismogram, and the argument the instantaneous phase) is calculated (*Bracewell*, 1965). From the analytical signal, the time series of instantaneous phase is extracted and these records are

autocorrelated using (*Schimmel*, 1999):

$$C_{pac}(t) = \frac{1}{N}\sum_{\tau=\tau_0}^{\tau_0+T} |\cos\left(\frac{\phi(t+\tau)-\phi(\tau)}{2}\right)| - |\sin\left(\frac{\phi(t+\tau)-\phi(\tau)}{2}\right)|, \quad (2.1)$$

where $C_{pac}(t)$ is the phase autocorrelation, ϕ is instantaneous phase and τ is the correlation lag time. The autocorrelation windows are then linearly stacked in order to enhance signal-to-noise ratio. Phase correlation has the advantage that it is amplitude independent and that coherent signals such as crustal reflections generated from the ambient seismic wavefield can be better retrieved than through an amplitude correlation, which is often dominated by high-amplitude surface waves (*Schimmel et al.*, 2011). The phase correlation also removes the need to remove coherent signals such as earthquake arrivals through e.g. temporal normalisation (*Bensen et al.*, 2007), as the instantaneous phase of arrivals from such sources is amplitude independent and of comparable magnitude to arrivals from transient low energy sources such as the ambient noise field. Thus, by stacking autocorrelations over a sufficiently long period of time, these transient energetic signals are rendered negligible in the final reflection image.

From the stacked phase autocorrelations it is possible to produce images consisting primarily of subsurface reflections, in contrast to many studies based on seismic interferometry that analyse the surface waves that dominate the ambient wavefield (e.g. *Shapiro et al.* (2005), *Ren et al.* (2013) and *Ekström* (2014)).

2.3 Results

It is only possible to retrieve reflections from interfaces representing relatively strong contrasts in material properties, due to the low amplitude of body wave reflections in the ambient noise field (*Gorbatov et al.*, 2013). Our autocorrelogram profiles show strong evidence for Moho reflections, and evidence for internal crustal reflectors (Fig. 2.2). We have visually interpreted the reflections seen in our autocorrelation profiles, and a sketch of Earth structure thus inferred beneath the DA and DF lines of DANA is shown in Fig. 2.3. All autocorrelograms are band-pass filtered between 0.2 and 0.4 Hz. Analysis of noise spectra show that this band contains high power from sources such as secondary ocean microseisms (*Stehly et al.*, 2006), and teleseismic earthquakes (*Seriff et al.*, 1965, *Gupta*, 1965). Higher frequency noise sources would be able to increase vertical resolution of this approach, but the ambient noise field recorded at DANA contains very little power at frequencies ≥ 1 Hz.

A coherent reflection is visible in all autocorrelograms at ~ 12 s, in close correspondence with the theoretical arrival time of a P-wave reflection from the Moho (PmP) at 39 km depth (12.53 s) as calculated for the crustal model of *Karahan et al.* (2001),

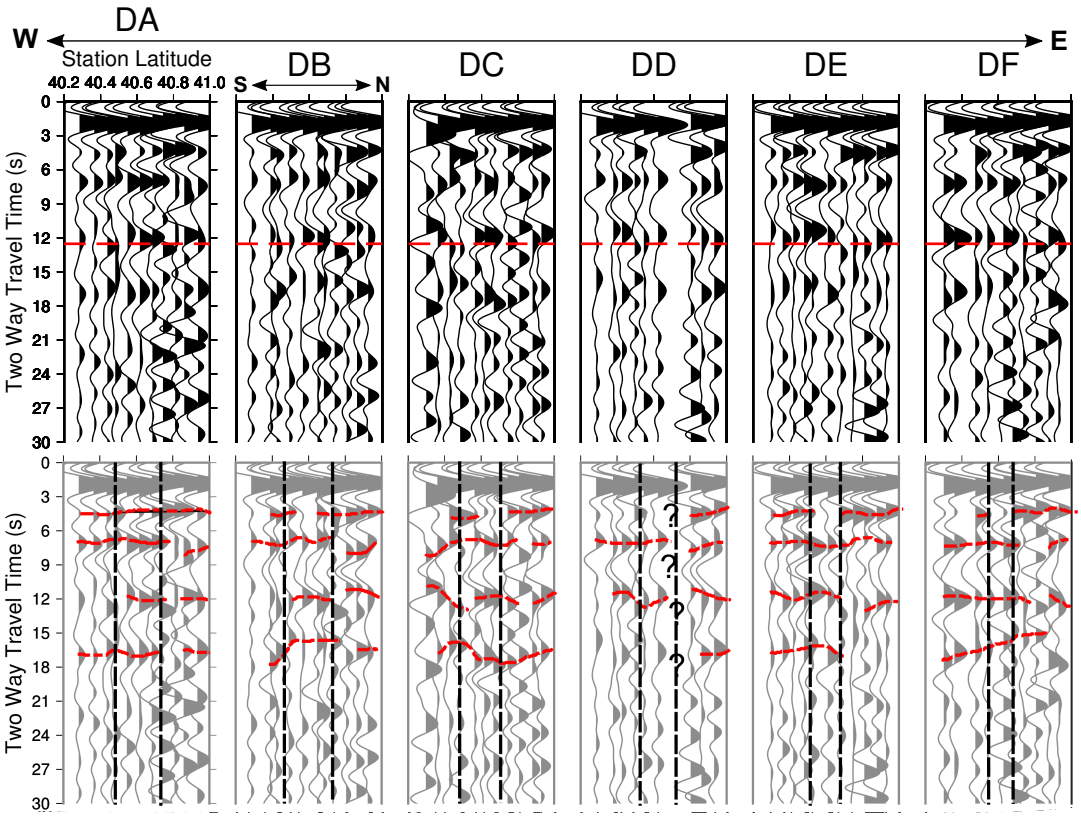

Figure 2.2: (top row) Profiles of autocorrelations for each receiver line of the DANA network. Each panel shows a northsouth profile of autocorrelations. Receivers and lines are separated by approximately 7 km, from DA line in the west to the DF line in the east. The profiles show twoway travel time of subsurface reflections, with positive reflections filled in black. The theoretical arrival time for the Moho reflection, PmP, at 39 km depth in the Anatolian crustal model of *Karahan et al.* (2001), is shown as the dashed red line. (bottom row) Interpreted autocorrelation profiles. Red dashed lines show the locations of interpreted reflections, while the vertical dashed black lines show the approximate location of the two branches of the NAFZ, projected vertically downward.

which we interpret as the Moho reflection. The arrival time of this reflection has a maximum variation between stations of ± 1 s, which is likely the combined result of variations in P-wave velocity structure in the crust, and topography on the Moho. *Kahraman et al.* (2015) and *Frederiksen et al.* (2015) utilised P-receiver functions and a transfer function method, respectively, to estimate crustal thickness across DANA as varying from 32 km in the Sakarya Terrane up to 45 km in the Istanbul Zone.

Evidence of shallower structure throughout the crust is also visible. Prominent arrivals are visible at ∼ 2.5 s and ∼ 7 s in all autocorrelations. Both of these arrivals display variation in arrival times on the order of 2 s. The arrival at ∼ 2.5 s may correspond to a reflection from a crystalline basement, that has been found beneath the Istanbul Zone (*Okay*, 2008), overlain by Tethyside accretionary complexes. An arrival is also apparent at ∼ 7 s, indicating a potential mid-crustal reflector. This reflector may correspond to an interface at 20 km depth also evident in receiver function images of structure beneath the DANA array (*Kahraman et al.*, 2015). The arrival at ∼ 7 s also appears to be systematically offset to a deeper location within the Istanbul Zone, particularly in profiles sampling the western half of the study area (DA, DB, DC).

A further arrival is visible at ∼ 5 s. This arrival is most prominent at stations located on the Istanbul Zone, however, it is also visible at some stations within the Sakarya Terrane, but not within the Armutlu Block. This arrival generally shallows towards the north of the array, arriving on average ∼ 1 s earlier in the Istanbul Zone than in the Sakarya Terrane. This northwards shallowing reflector could be indicative of a southwards dipping reflector, or of faster seismic velocities in the upper crust of the Istanbul Zone.

Finally, a coherent arrival is also seen below the Moho at ∼ 17.5 s. The arrival times of this phase vary by ± 1 s. A reflector at this depth has also been identified in wide-angle refraction studies in the continental United States (*Green and Hales*, 1968), as well as being identified in a previous reflection study using ambient noise in northern Africa (*Ruigrok et al.*, 2011). The autocorrelation method may have the potential to retrieve reflections from deeper upper mantle interfaces, but signal to noise ratio appears to decrease with depth.

2.4 Discussion

The clear P-wave Moho reflection in Fig. 2.2 shows the imaging potential of the autocorrelation technique. The Moho reflection is strong and coherent in the Sakarya Terrane and the Armutlu Block, but is less clear within the Istanbul Zone (e.g. lines DB and DF, north of latitude 40.7).

Our results show apparent topography on the Moho, though Moho depth variation may trade off against average crustal velocity. By varying the seismic velocities of the crustal model of north-western Anatolia derived from seismic refraction (*Karahan*

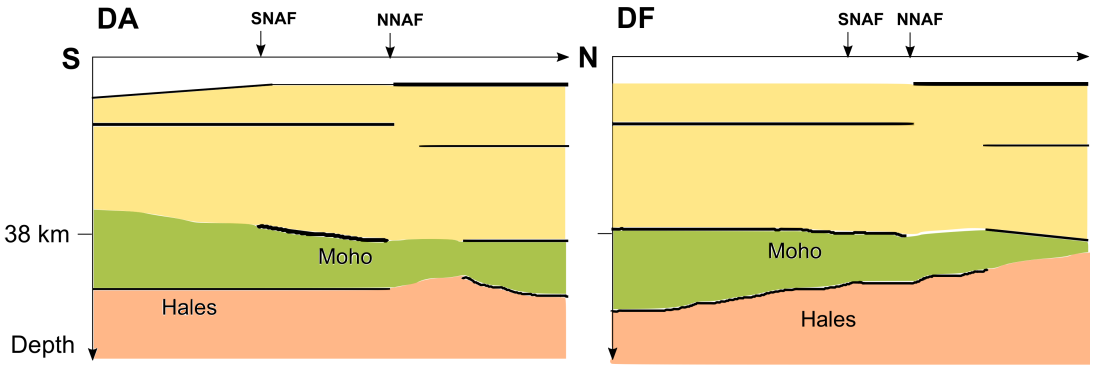

Figure 2.3: Sketch interpretations of Earth structure beneath the west (DA) and east (DF) lines of the DANA array. Reflectors are shown as black lines, and line thickness represents the strength of the reflection. Background colors represent layers within the Earth. White, upper crust; yellow, middle to lower crust; green, upper mantle; and brown, anisotropic upper mantle beneath Hales discontinuity. NNAF and SNAF denote the location of the northern and southern branch of the NAFZ, respectively. The average Moho depth of 38 km was calculated using the velocity model of *Karahan et al.* (2001)

et al., 2001) by ± 5 %, we calculate an upper limit of ± 0.6 s of travel time variation can be attributed to lateral variations in seismic velocities. This leaves ∼ 50 % of our observed travel time variations that could be attributed to topography on reflectors. Notably, *Kahraman et al.* (2015) detect a deepening of the Moho from West (DA, DB, DC) to East (DE, DF) within the Istanbul Zone. Fig. 2.2 shows that we also observe a delay in the Moho reflection in the northern part of profiles DE and DF, possibly indicating a deeper Moho towards the East.

We note a significant offset and disruption of the Moho reflection associated with the northern strand of the NAFZ, between the Istanbul Zone and Armutlu Block (station latitude north of ∼ 40.8). The Moho reflection is visible as a strong arrival in every autocorrelogram, but disappears for stations close (within 7 km) to the northern NAFZ (Fig. 2.2). The weak reflection in this region may indicate that deformation associated with the active fault has reduced the reflectivity of the crust-mantle boundary to the point that no reflections are generated. A potential mechanism for the reduced reflectivity of the upper mantle beneath the northern branch of the NAFZ is the serpentinization of the upper mantle, due to the percolation of fluids down through the shear zone. Serpentinization would reduce the seismic velocity of upper mantle rocks, causing the velocity contrast at the Moho to become more gradational, reducing the reflectivity. This process has been previously invoked to explain the absence of a Moho discontinuity beneath the Mid-Hungarian Shear Zone in a receiver function study of the Pannonian Basin (*Hetényi et al.*, 2015).

The autocorrelation images show a variety of crustal reflections of varying amplitude. The phase correlation technique is sensitive to coherence, so a lower amplitude arrival (e.g. the Moho arrival within the Istanbul Zone) is indicative of reduced reflection coherence. The loss of coherence could be due to a loss of reflectivity, but could also

be due to the existence of small scale structure at the reflector. A further consequence is that the Moho, which would be expected to be the most prominent discontinuity within the crust and upper mantle, is not higher in amplitude than any other reflector, in our profiles. This phenomenon can be attributed to the amplitude independence of phase correlation.

We note that the region of absent Moho reflections is narrow, suggesting fault-related strain in the lower crust may be localized to within 10 km of the NAFZ. The diminished strength of the reflected signal is consistent with receiver function analysis of the DANA dataset (*Kahraman et al.*, 2015) that shows a clear reduction in amplitude of P-to-S conversions at the Moho in the vicinity of the northern strand of the NAFZ. The receiver functions also show a somewhat less clear Moho amplitude reduction near the southern strand that is not observed in our study. We therefore infer that the damage zone of the northern branch of the NAFZ at least reaches the Moho and P-wave reflections from the boundary, as well as P-to-S conversions, are suppressed by a more gradual increase of velocity with depth across the Moho. The restricted spatial extent of the effect supports the contention that localized strain is occurring at lower crustal depths (*Weber et al.*, 2004). Below the crust, full-waveform inversion of the velocity field by *Fichtner et al.* (2013) has also shown that the mantle lithosphere beneath the NAFZ is generally marked by a relatively narrow band of low shear velocity that extends down to the asthenosphere and presumably defines a locus for more focussed deformation at crustal levels.

Our observation of offsets in Moho depth associated with the northern branch of the NAFZ indicates that it is likely that localized shear associated with the NAFZ has reached the upper mantle. Narrow shear zones that extend into the continental mantle have also been inferred at other large continental fault systems, such as the Dead Sea Transform (*Weber et al.*, 2004), and within the Tibetan Plateau (*Zhang et al.*, 2014). The apparent continuity of the Moho reflection across the southern strand of the NAFZ (Fig. 2.2) might then be interpreted as implying less strain accumulated on this structure.

Below the Moho, the autocorrelograms show a further coherent arrival at $\sim$ 17 s for most stations, with travel time variations on the order of 1 s. A similar arrival has been detected in autocorrelograms by *Tibuleac and von Seggern* (2012) in Nevada and has been interpreted as an S-wave arrival from the Moho (SmS). Vertical component autocorrelograms, however, should not be sensitive to vertically travelling S-waves, so we interpret this arrival as a P-wave reflection off an upper mantle discontinuity, likely the Hales discontinuity, which has previously been attributed as a phase transition from spinel to garnet in aluminous peridotite (*Hales*, 1969).

An alternative explanation for the Hales discontinuity is that it is the upper limit of a zone of enhanced seismic anisotropy due to mineral fabric beneath the lithospheric mantle lid that may appear as a seismic discontinuity to low frequency seismic waves

(*Levin and Park*, 2000). A potential mechanism for the formation of this fabric is the westward movement of Anatolia (*Reilinger et al.*, 2006, *Nocquet*, 2012) as it 'escapes' toward the Aegean Sea from the collision of Arabia with Eurasia (*Jackson and McKenzie*, 1984). The motion of the strong lithospheric lid over a weaker asthenosphere may have the potential to induce a coherent fabric in olivine crystals, forming the Hales discontinuity. Such continental escape processes have been invoked to explain the appearance of the Hales discontinuity in Arabia (*Levin and Park*, 2000), and the Basin and Range Province of the Sierra Nevada Mountains (*Jones and Phinney*, 1998).

Stations located in the Istanbul Zone show a strong reflector at $\sim$ 5 s. It appears to terminate at the location of the surface trace of the northern strand of the NAFZ. The Intra-Pontide Suture between the Istanbul Zone and Armutlu Block provides a simple explanation of discontinuous structure. This arrival is also visible at some stations within the Sakarya Terrane in the south but is not detected within the Armutlu Block. Receiver function analysis also reveals a strong discontinuity at a depth of 15 km within the Istanbul Zone, also terminating at the northern branch of the NAFZ (*Kahraman et al.*, 2015). It is likely that the reflection visible at $\sim$ 5 s corresponds to this discontinuity. Whilst this structure is observed in receiver functions to be stronger in the eastern part of the study region, our autocorrelograms show a reflector that is equally visible throughout the entire Istanbul Zone.

2.5 Conclusions

We have shown that it is possible to extract images of body wave reflections by constructing stacked autocorrelograms of ambient seismic noise. The dense station spacing of DANA enables high lateral resolution of the crustal structure in the vicinity of the NAFZ. Whilst these autocorrelograms are only sensitive to strong contrasts in physical properties in the subsurface, it is still possible to image crustal discontinuities such as the Moho using this technique. The dense station spacing of DANA greatly aids in identifying and interpreting coherent reflections from subsurface interfaces beneath the array. We have shown that it is possible to use microseismic noise sources in the frequency band 0.2 – 0.5 Hz in order to construct these autocorrelograms, negating the need for energetic sources such as earthquakes. Our reflection profiles show that, similar to receiver functions (*Kahraman et al.*, 2015), P-wave reflections from the Moho fade out beneath the northern NAFZ. In addition, offsets in Moho depth are visible within $\sim$ 10 km of the northern strand of the NAFZ, whilst the southern strand has a less clear effect on the Moho. We interpret that deformation associated with the northern branch of the NAFZ has at least reached the Moho, in the form of a narrow shear zone. These indications of localized Moho variation beneath the NAFZ are consistent with localized low velocity regions in the lithospheric mantle beneath (*Fichtner et al.*, 2013), as well as observations from other large continental fault zones, such as the Dead Sea

Transform (*Weber et al.*, 2004), San Andreas Fault (*Zhu*, 2000) and Tibetan Plateau (*Zhang et al.*, 2014), that show narrow bands of deformation associated with active faults which extend downward at least as far as the Moho. In contrast, the southern branch of the NAFZ either does not cut through the entirety of the crust, or, the deformation in the upper mantle likely occurs by a more diffuse shear zone, as interpreted for the Marlborough Fault System, New Zealand (*Wilson et al.*, 2004). Our observations demonstrate that the autocorrelation method may provide reliable estimates of important parameters such as crustal thickness, and the ability to map heterogeneity in the crust and upper mantle, independently of other established seismological techniques, such as receiver functions.

Acknowledgments

G.T. is supported by the Leeds-York Doctoral Training Partnership of the Natural Environment Research Council (NERC), UK. The DANA array was part of the Faultlab project, a collaborative effort by the University of Leeds, Kandilli Observatory and Earthquake Research Institute and Sakarya University. Major funding was provided by the UK NERC under grant NE/I028017/1. Equipment was provided and supported by the NERC Geophysical Equipment Facility (SEIS-UK) Loan 947. The facilities of Bogazici University Kandilli Observatory and Earthquake Research Institute Data Services (KOERI DS) were used for access to waveform and metadata required in this study. The KOERI DS is funded by the Ministry of Development of Turkey through the instrumentation and operation of the nationwide seismic network. The DANA dataset was collected by a team including: S. Rost, G. Houseman, D. Thompson, D. Cornwell, V. Lane, N. Turkelli, U. Teoman, M. Kahraman, S. Altuncu-Poyraz, L. Gulen, M. Utkucu. We thank Andreas Fichtner and one anonymous reviewer for their insightful comments, which aided in the improvement of this manuscript.

References

Altuncu Poyraz, S., M. U. Teoman, N. Türkelli, M. Kahraman, D. Cambaz, A. Mutlu, S. Rost, G. A. Houseman, D. A. Thompson, D. Cornwell, et al. (2015), New Constraints on Micro-Seismicity and Stress State in the Western Part of the North Anatolian Fault Zone: Observations from a Dense Seismic Array, *Tectonophys.*, *656*, 190–201, doi:doi:10.1016/j.tecto.2015.06.022. 2.1

Barka, A., H. Akyüz, E. Altunel, G. Sunal, Z. Cakir, A. Dikbas, B. Yerli, R. Armijo, B. Meyer, J. De Chabalier, et al. (2002), The Surface Rupture and Slip Distribution of the 17 August 1999 Izmit Earthquake (M 7.4), North Anatolian Fault, *Bull. Seismol. Soc. Am.*, *92*(1), 43–60, doi:10.1785/0120000841. 2.1, 2.1

Bekler, T., and C. Gurbuz (2008), Insight into the Crustal Structure of the Eastern Marmara Region, NW Turkey, *Pure Appl. Geophys.*, *165*(2), 295–309, doi:10.1007/s00024-008-0302-3. 2.1

Bensen, G., M. Ritzwoller, M. Barmin, A. Levshin, F. Lin, M. Moschetti, N. Shapiro, and Y. Yang (2007), Processing Seismic Ambient Noise Data to Obtain Reliable Broad-Band Surface Wave Dispersion Measurements, *Geophys. J. Int.*, *169*(3), 1239–1260, doi:10.1111/j.1365-246X.2007.03374.x. 2.2

Bracewell, R. (1965), *The Fourier Transform and its Applications*, McGraw-Hill, New York. 2.2

Bürgmann, R., and G. Dresen (2008), Rheology of the Lower Crust and Upper Mantle: Evidence from Rock Mechanics, Geodesy, and Field Observations, *Ann. Rev. Earth Planet. Sci.*, *36*(1), 531, doi:10.1146/annurev.earth.36.031207.124326. 2.1

Claerbout, J. F. (1968), Synthesis of a Layered Medium from its Acoustic Transmission Response, *Geophysics*, *33*(2), 264–269, doi:10.1190/1.1439927. 2.2

DANA (2012), *Dense Array for Northern Anatolia*, doi:10.7914/SN/YH_2012, Other/Seismic Network. 2.1

Ekström, G. (2014), Love and Rayleigh Phase-Velocity Maps, 5–40 s, of the Western and Central USA from USArray Data, *Earth Planet. Sci. Lett.*, *402*, 42–49, doi:10.1016/j.epsl.2013.11.022. 2.2

Fichtner, A., E. Saygin, T. Taymaz, P. Cupillard, Y. Capdeville, and J. Trampert (2013), The deep structure of the north anatolian fault zone, *Earth Planet. Sci. Lett.*, *373*, 109–117, doi:10.1016/j.epsl.2013.04.027. 2.4, 2.5

Frederiksen, A., D. Thompson, S. Rost, D. Cornwell, L. Gülen, G. Houseman, M. Kahraman, S. Poyraz, U. Teoman, N. Türkelli, et al. (2015), Crustal Thickness Variations and Isostatic Disequilibrium Across the North Anatolian Fault, Western Turkey, *Geophys. Res. Lett.*, *42*(3), 751–757, doi:10.1002/2014GL062401. 2.3

Gorbatov, A., E. Saygin, and B. Kennett (2013), Crustal Properties from Seismic Station Autocorrelograms, *Geophys. J. Int.*, *192*(2), 861–870, doi:10.1093/gji/ggs064. 2.2, 2.3

Green, R., and A. Hales (1968), The Travel Times of P waves to 30 in the Central United States and Upper Mantle Structure, *Bull. Seismol. Soc. Am.*, *58*(1), 267–289. 2.3

Gupta, I. N. (1965), Standing-Wave Phenomena in Short-Period Seismic Noise, *Geophysics*, *30*(6), 1179–1186, doi:10.1190/1.1439707. 2.3

Hales, A. (1969), A Seismic Discontinuity in the Lithosphere, *Earth Planet. Sci. Lett.*, *7*(1), 44–46, doi:10.1016/0012-821X(69)90009-0. 2.4

Hetényi, G., Y. Ren, B. Dando, G. W. Stuart, E. Hegedűs, A. C. Kovács, and G. A. Houseman (2015), Crustal Structure of the Pannonian Basin: The AlCaPa and Tisza Terrains and the Mid-Hungarian Zone, *Tectonophys.*, *646*, 106–116, doi:10.1016/j.tecto.2015.02.004. 2.4

Jackson, J., and D. McKenzie (1984), Active Tectonics of the Alpine-Himalayan Belt between Western Turkey and Pakistan, *Geophys. J. Int.*, *77*(1), 185–264, doi:10.1111/j.1365-246X.1984.tb01931. 2.4

Jones, C. H., and R. A. Phinney (1998), Seismic Structure of the Lithosphere from Teleseismic Converted Arrivals Observed at Small Arrays in the Southern Sierra Nevada and Vicinity, California, *J. Geophys. Res.*, *103*, 10–065, doi:10.1029/97JB03540. 2.4

Kahraman, M., D. G. Cornwell, D. A. Thompson, S. Rost, G. A. Houseman, N. Türkelli, U. Teoman, S. A. Poyraz, M. Utkucu, and L. Gülen (2015), Crustal-Scale Shear Zones and Heterogeneous Structure Beneath the North Anatolian Fault Zone, Turkey, Revealed by a High-Density Seismometer Array, *Earth Planet. Sc. Lett.*, *430*, 129–139, doi:10.1016/j.epsl.2015.08.014. 2.3, 2.4, 2.4, 2.5

Karahan, A. E., H. Berckhemer, and B. Baier (2001), Crustal Structure at the Western End of the North Anatolian Fault Zone from Deep Seismic Sounding, *Annali di Geofisica*. 2.3, 2.2, 2.4, 2.3

Karimi, B., N. McQuarrie, J.-S. Lin, and W. Harbert (2014), Determining the Geometry of the North Anatolian Fault East of the Marmara Sea Through Integrated Stress Modeling and Remote Sensing Techniques, *Tectonophys.*, *623*, 14–22, doi:doi:10.1016/j.tecto.2014.03.015. 2.1

Kennett, B. (2015), Lithosphere-Asthenosphere P-wave Reflectivity Across Australia, *Earth Planet. Sci. Lett.*, *431*, 225–235, doi:10.1016/j.epsl.2015.09.039. 2.2

Kennett, B., E. Saygin, and M. Salmon (2015), Stacking Autocorrelograms to Map Moho Depth with High Spatial Resolution in Southeastern Australia, *Geophys. Res. Lett.*, *42*(18), 7490–7497, doi:10.1002/2015GL065345. 2.2

Levin, V., and J. Park (2000), Shear Zones in the Proterozoic Lithosphere of the Arabian Shield and the Nature of the Hales Discontinuity, *Tectonophys.*, *323*(3), 131–148, doi:10.1016/S0040-1951(00)00105-0. 2.4

MTA (2012), *Active Fault Map of Turkey*, General Directorate of Mineral Research and Exploration. 2.1

Nocquet, J.-M. (2012), Present-Day Kinematics of the Mediterranean: A Comprehensive Overview of GPS results, *Tectonophys.*, *579*, 220–242, doi:10.1016/j.tecto.2012.03.037. 2.4

Okay, A. I. (2008), Geology of Turkey: A Synopsis, *Anschnitt*, *21*, 19–42. 2.1, 2.3

Reilinger, R., S. McClusky, P. Vernant, S. Lawrence, S. Ergintav, R. Cakmak, H. Ozener, F. Kadirov, I. Guliev, R. Stepanyan, et al. (2006), GPS Constraints on Continental Deformation in the Africa-Arabia-Eurasia Continental Collision Cone and Implications for the Dynamics of Plate Interactions, *J. Geophys. Res. Solid Earth*, *111*(B5), doi:10.1029/2005JB004051. 2.4

Ren, Y., B. Grecu, G. Stuart, G. Houseman, E. Hegedüs, S. C. P. W. Group, et al. (2013), Crustal Structure of the Carpathian–Pannonian Region from Ambient Noise Tomography, *Geophys. J. Int.*, p. ggt316, doi:10.1093/gji/ggt316. 2.2

Ruigrok, E., X. Campman, and K. Wapenaar (2011), Extraction of P-wave Reflections from Microseisms, *CR. Geosci.*, *343*(8), 512–525, doi:10.1016/j.crte.2011.02.006. 2.3

Schimmel, M. (1999), Phase Cross-Correlations: Design, Comparisons, and Applications, *Bull. Seismol. Soc. Am.*, *89*(5), 1366–1378, doi:10.1785/0120090105. 2.2

Schimmel, M., E. Stutzmann, and J. Gallart (2011), Using Instantaneous Phase Coherence for Signal Extraction from Ambient Noise Data at a Local to a Global Scale, *Geophys. J. Int.*, *184*(1), 494–506, doi:10.1111/j.1365-246X.2010.04861.x. 2.2, 2.2

Sengör, A., O. Tüysüz, C. Imren, M. Sakinç, H. Eyidogan, N. Görür, X. Le Pichon, and C. Rangin (2005), The North Anatolian Fault: A New Look, *Annu. Rev. Earth Planet. Sci.*, *33*, 37–112, doi:10.1146/annurev.earth.32.101802.120415. 2.1

Seriff, A., C. Velzeboer, and R. Haase (1965), Possible P-wave Observations in Short-Period Seismic Noise, *Geophysics*, *30*(6), 1187–1190, doi:10.1190/1.1439709. 2.3

Shapiro, N. M., M. Campillo, L. Stehly, and M. H. Ritzwoller (2005), High-Resolution Surface-Wave Tomography from Ambient Seismic Noise, *Science*, *307*(5715), 1615–1618, doi:10.1126/science.1108339. 2.2

Stehly, L., M. Campillo, and N. Shapiro (2006), A Study of the Seismic Noise from its Long-Range Correlation Properties, *J. Geophys. Res.*, *111*(B10), doi:10.1029/2005JB004237. 2.3

Tibuleac, I. M., and D. von Seggern (2012), Crust-Mantle Boundary Reflectors in Nevada from Ambient Seismic Noise Autocorrelations, *Geophys. J. Int.*, *189*(1), 493–500, doi:10.1111/j.1365-246X.2011.05336.x. 2.2, 2.4

Weber, M., K. Abu-Ayyash, A. Abueladas, A. Agnon, H. Al-Amoush, A. Babeyko, Y. Bartov, M. Baumann, Z. Ben-Avraham, G. Bock, et al. (2004), The Crustal Structure of the Dead Sea Transform, *Geophys. J. Int.*, *156*(3), 655–681, doi:10.1111/j.1365-246X.2004.02143. 2.1, 2.4, 2.5

Wilson, C. K., C. H. Jones, P. Molnar, A. F. Sheehan, and O. S. Boyd (2004), Distributed Deformation in the Lower Crust and Upper Mantle Beneath a Continental Strike-Slip Fault Zone: Marlborough Fault System, South Island, New Zealand, *Geology*, *32*, 837–840, doi:10.1130/G20657.1. 2.1, 2.5

Zhang, Z., Y. Wang, G. A. Houseman, T. Xu, Z. Wu, X. Yuan, Y. Chen, X. Tian, Z. Bai, and J. Teng (2014), The Moho Beneath Western Tibet: Shear Zones and Eclogitization in the Lower Crust, *Earth Planet. Sc. Lett.*, *408*, 370–377, doi:10.1016/j.epsl.2014.10.022. 2.1, 2.4, 2.5

Zhu, L. (2000), Crustal Structure Across the San Andreas Fault, Southern California from Teleseismic Converted Waves, *Earth Planet. Sc. Lett.*, *179*(1), 183–190, doi:10.1016/S0012-821X(00)00101-1. 2.1, 2.5

Chapter 3

Near surface structure of the North Anatolian Fault Zone from Rayleigh and Love wave tomography using ambient seismic noise

G. Taylor[1], S. Rost[1], G. Houseman[1] and G. Hillers[2,3]

[1] *School of Earth and Environment, University of Leeds, Leeds, United Kingdom*
[2] *Institut des Sciences de la Terre, Université Grenoble-Alpes, F- 38041, Grenoble, France*
[3] *Now at Institute of Seismology, University of Helsinki, Finland*

Abstract

We use observations of surface waves in the ambient noise field recorded at a dense seismic array to image the North Anatolian Fault Zone (NAFZ) in the region of the 1999 magnitude 7.6 Izmit earthquake in western Turkey. The NAFZ is a major strike slip fault system extending $\sim$ 1200 km across northern Turkey and poses a high level of seismic hazard, particularly to the city of Istanbul. Assuming isotropy, we obtain maps of phase velocity variation using surface wave tomography applied to Rayleigh and Love waves and construct high resolution images of S-wave velocity in the upper 10 km of a 70 km by 30 km region around Lake Sapanca. We observe low S-wave velocities (< 2.5 km s^{-1}) associated with the Adapazari and Pamukova sedimentary basins, as well as the northern branch of the NAFZ. In the Armutlu Block, between the two major branches of the NAFZ, we detect higher velocities (> 3.2 km s^{-1}) associated

with a shallow crystalline basement. We measure azimuthal anisotropy in our phase velocity observations, with the fast direction seeming to align with the direction of maximum extension for the region ($\sim 45°$). The signatures of both the northern and southern branches of the NAFZ are clearly associated with strong gradients in seismic velocity that also denote the boundaries of major tectonic units. Our results suggest that the development of the NAFZ has exploited this pre-existing contrast in physical properties.

3.1 Introduction

The formation of fault zones appears to be a balance between the accommodation of the tectonic strain field, and the exploitation of pre-existing weak zones such as tectonic suture zones or lithological boundaries (e.g. *Bercovici and Ricard* (2014), *Dayem et al.* (2009), *Gerbi et al.* (2016), *Tapponier et al.* (1982)). Studying how structural changes affect strain localisation in the upper crust is critical to understanding the earthquake cycle (*Bürgmann and Dresen*, 2008). Imaging the seismic velocity structure of fault zones provides information essential to understanding the long-term behaviour of faults and the earthquakes that occur on them.

Here we interpret images from ambient noise surface wave tomography of the upper 10 km of the North Anatolian Fault Zone (NAFZ), Turkey, in the rupture zone of the 1999 Izmit earthquake. This allows us to study the near surface structure of a recently ruptured fault. The NAFZ is a ~ 1200 km long strike slip fault that forms the boundary between the Anatolian block and the Eurasian continent. Progressively localized since the middle Miocene (~ 3 Ma), the NAFZ propagated westward from the Karliova Triple Junction, across northern Anatolia, and reached the Izmit-Adapazari region ~ 200 ka, although a more broad zone of shear deformation was present since the middle Miocene (*Şengör et al.*, 2005). The motion of Anatolia is driven by a gradient of lithospheric gravitational potential energy that extends across the Anatolian Peninsula (*England et al.*, 2016) and is sustained by the collision between the Arabian and Eurasian plate in the East, and the roll-back of the Hellenic trench to the southwest (*Flerit et al.*, 2004, *Reilinger et al.*, 1997). Since 1939 a westward propagating sequence of large earthquakes ($M_w > 7.0$) has occurred along the NAFZ (*Stein et al.*, 1997). The 1999 Izmit (M_w 7.6) and Düzce (M_w 7.2) earthquakes are the most recent in this sequence (*Barka et al.*, 2002), and the NAFZ continues to pose significant seismic hazard to the region.

In the Izmit-Adapazari region, the NAFZ is split into northern and southern branches (Fig. 3.1). The northern branch has seen more seismic activity historically, but micro-seismicity in this region does not appear to be strongly localised to the major fault strands (*Altuncu Poyraz et al.*, 2015). The northern branch of the fault appears to exploit the so-called Intra-Pontide Suture between the Eurasian continent and sedi-

mentary accretionary complexes formed during the closure of the Tethys Ocean (*Okay*, 2008). There are three major geological units delineated by the fault zone (Fig. 3.1). To the north of the northern branch of NAFZ is the Istanbul Zone, a cratonic fragment of the Eurasian continent. The Istanbul Zone includes the Adapazari Basin, a $\sim$ 2 km thick pull-apart sedimentary basin formed by right-lateral motion acting on a change in strike of the northern branch of the NAFZ (*Şengör et al.*, 2005).

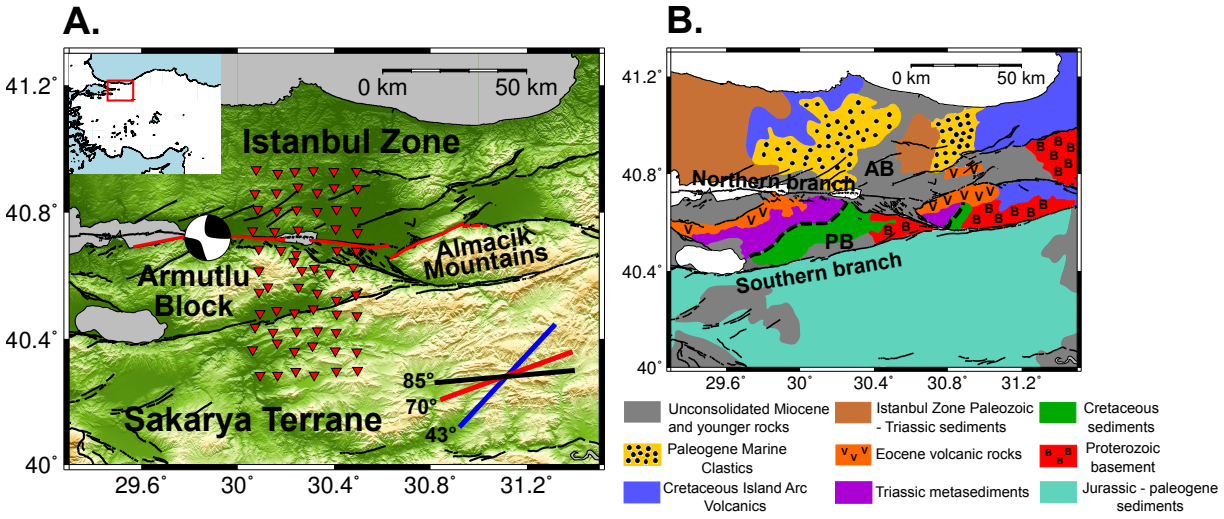

Figure 3.1: A.: Overview of the Izmit-Adapazari region and the DANA network. Stations of the DANA network are shown as red triangles; station names are of the form Dx01 to Dx11, where x is A through F from west to east and 01 is at the southern end of each line. Thick black lines identify mapped faults in the region (*Emre et al.*, 2016). The thick red line indicates the extent of the rupture of the 1999 Izmit earthquake (*Barka et al.*, 2002). The epicenter and focal mechanism for the Izmit earthquake provided by the GCMT catalogue (*Dziewonski et al.*, 1981, *Ekström et al.*, 2012) is shown. Topography data were acquired by the Shuttle Radar Topography Mission (*USGS*, 2006). The bottom right shows the approximate fast propagation direction described in section 3.3.6 for 1.5 – 4.0 s Rayleigh waves (85°, black line), 4.0 – 10.0 s Rayleigh waves (70°, red line). The 43° blue line is the fast S-wave polarisation direction for the upper mantle beneath the North Anatolian Fault as measured by SKS splitting from *Biryol et al.* (2010). B.: Geological map of the Izmit-Adapazari region, simpified from *Akbayram et al.* (2016). The location of the southern and northern branches of the North Anatolian Fault Zone are indicated. The black dashed line shows the location of the Intra-Pontide Suture within the Armutlu Block inferred by *Akbayram et al.* (2016). AB and PB show the location of the Adapazari and Pamukova Basin, respectively.

Located between the two fault branches are the Armutlu Block and the Almacik Mountains. The Armutlu Block is a section of the Almacik mountains that has migrated further westward with motion along the NAFZ. Both are areas of high topography, formed as an accretionary complex of upper cretaceous sediments overlying a metamorphic basement (*Yılmaz et al.*, 1995). The dominant feature of the Armutlu Block is an abundance of metamorphosed sediments and marbles of unknown age and provenance (*Okay and Tüysüz*, 1999). The Pamukova sedimentary basin is located in the southern part of the Armutlu Block. Striations and down dip motion on faults

observed along the southern branch of the NAFZ in the Pamukova basin indicate that extension in the NE – SW direction due to the right lateral motion is more dominant than shortening in the NW – SE. The resulting transtensional strain is believed to have caused the opening of the Pamukova basin (*Doğan et al.*, 2014). The total thickness of the sediments in the Pamukova basin is generally unknown, but it is thought to be thinner than in the Adapazari basin (*Şengör et al.*, 2005).

To the south of the NAFZ lies the Sakarya Terrane, an accretionary complex of sedimentary rocks from the Jurassic – lower Cretaceous, overlying a metamorphic basement of mainly Paleozoic rocks (*Yılmaz et al.*, 1995). The Sakarya Terrane also contains a number of ophiolitic melanges, including serpentinites close to the southern branch of the NAFZ that were probably produced by imbrication and thrust-stacking during the closure of the Neo-Tethys Ocean (*Şengör and Yılmaz*, 1981).

To study the structure of the NAFZ in the Izmit-Adapazari region the University of Leeds, Kandilli Observatory and Earthquake Research Institute (KOERI) and Sakarya University deployed a temporary array of seismometers across the rupture zone of the 1999 Izmit earthquake (*Kahraman et al.*, 2015). The array included 62 three-component seismometers in a 70 km x 35 km rectangular grid (Fig. 3.1), and an approximate station spacing of 7 km, known as the Dense Array for Northern Anatolia (*DANA*, 2012). Also included were three stations of the KOERI national network located within the main grid of the DANA array: GULT, SAUV and SPNC. DANA crossed both strands of the NAFZ in this region, with stations deployed on all three of the major crustal units described above (Fig. 3.1).

Short period surface waves from ambient noise have been used to study the upper crust in the vicinity of active fault zones in the past (e.g. *Lin et al.* (2013), *Zigone et al.* (2015)). In such studies low seismic velocities have been attributed to earthquake damage zones and pull-apart sedimentary basins. Here our analysis of the DANA data provides an image of the top 10 km of the NAFZ in the Izmit-Adapazari region with a lateral resolution dictated by the $\sim$ 7 km station spacing, to better constrain the relationship between the fault and its regional geological context.

3.2 Data and Methods

3.2.1 Calculation of the cross-correlation functions

To image the upper 10 km of the NAFZ we used ambient noise data recorded at DANA to construct cross-correlation functions and retrieve empirical estimates of the elastic Greens function of the Earth for all inter-station paths of the network (*Lobkis and Weaver*, 2001, *Wapenaar*, 2004). The instruments used for the DANA network were all three-component broadband sensors, the majority of which were Guralp CMG-6TDs (30 s maximum period). Some stations were equipped with CMG-3Ts or CMG-3ESPs

(120 s maximum period). From these cross-correlation functions we extract surface wave dispersion curves in order to perform seismic tomography and invert for S-wave velocity structure (*Shapiro et al.*, 2005). The data were first reduced to a 25 Hz sampling rate and corrected for the instrument response. An initial band-pass filter was applied between 0.02 and 10 Hz, and the frequency spectrum of each noise window was whitened between 0.05 and 2 Hz (*Bensen et al.*, 2007). We tested several pre-processing methods for producing the cross-correlation functions for this study. These included trialling the use of 4-hour and 1-hour long noise windows. In order to remove any data windows containing signals from large earthquakes, each window was split into three segments. If the amplitude of one of these segments has a significantly higher standard deviation (> 1.8 times) than the other two, the data window is discarded (*Poli et al.*, 2012). For amplitude normalisation (*Bensen et al.*, 2007), we tested 1-bit normalisation against clipping any data with an amplitude > 3.5 times the standard deviation of each data window. Supplementary Figs. A.1 and A.2 show the results of these tests. We found little difference between the processing schemes in terms of signal-to-noise ratio of the final cross-correlation functions. However, the approach of amplitude clipping for 4-hour long noise windows was found to produce correlation functions with slightly higher frequency domain coherence than the other schemes. As such, we proceed with this pre-processing method.

Following this pre-processing, each data window is cross correlated with the corresponding window at every other station in the network, and these cross correlations are then stacked over the entire duration of the array deployment (16 months of data). We calculated the correlations for all 9 possible combinations of the vertical, north and east components of ground motion, and then rotated the final stacked correlations into the relevant great circle path (station to station) to retrieve the vertical, radial and transverse correlation components (Fig. 3.2). The correlation functions in Fig. 3.2 are stacked in bins of 0.5 km interstation distance, and band-pass filtered between 0.05 and 2.0 Hz. The amplitudes are normalised within each bin.

3.2.2 Extraction of surface wave phase velocities

The record sections exhibit multiple features and arrivals. There are two explanations for the large-amplitude features around $t = 0$. Firstly, they may represent the signature of the overlapping converging and diverging surface waves that form high amplitude features near the origin in time-reversal experiments, known as the focal spot of the wave field (*Hillers et al.*, 2016). A second possible explanation is teleseismic body wave energy that arrives at the stations at a near-vertical incidence angle. When these arrivals are cross-correlated, the very small differential travel times of the energy result in a spike near the zero lag correlation time (*Hillers et al.*, 2013). The large amplitudes are particularly prominent on the ZZ component. This phenomenon has been observed in a previous ambient noise study in Turkey: *Warren et al.* (2013)

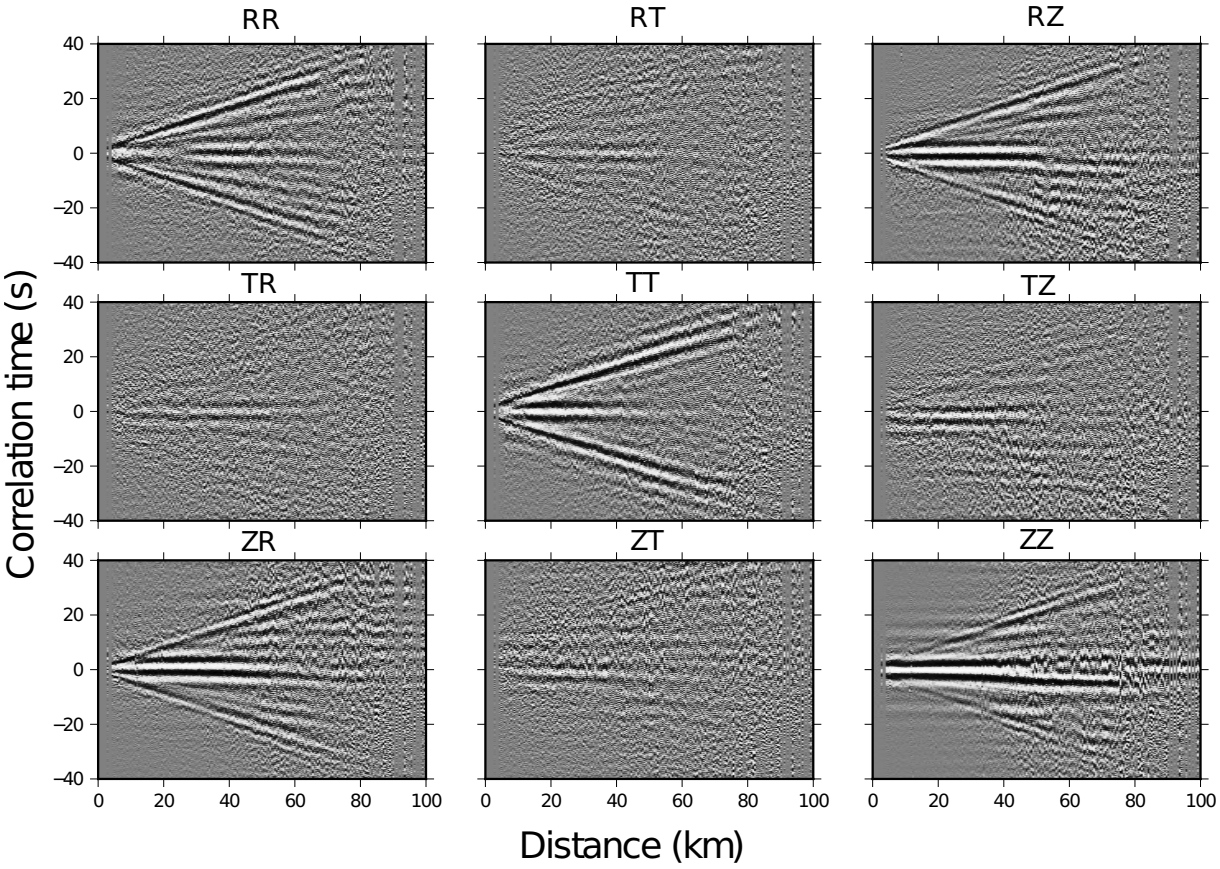

Figure 3.2: Record section of correlation functions calculated for inter-station paths of the DANA network. Correlation functions were filtered between 0.05 and 2.0 Hz and binned and stacked in 0.5 km distance bins, and the amplitude is normalized within each bin. Record sections for every combination of three component motion are labelled as follows: Z = vertical, R = radial, T = transverse. e.g. The ZR correlation (bottom left) represents the motion recorded on the radial component due to a vertical point source. ZZ, ZR, RR, RZ components show Rayleigh waves, and TT shows Love waves.

observe large zero-time amplitudes in their correlation functions up to a distance of 80 km. Additionally, large amplitude waveforms near $t = 0$ are often observed in ambient noise correlation studies (e.g. *Poli et al.* (2012), *Villaseñor et al.* (2007), *Zheng et al.* (2011)). While these waveforms can be used for imaging (e.g. *Hillers et al.* (2016), *Taylor et al.* (2016)), we focus here on the propagating surface waves that dominate the record sections. Correlations between the vertical and radial components (ZZ, ZR, RR and RZ) are predominantly produced by Rayleigh waves propagating between DANA stations, whilst the transverse (TT) correlations contain Love waves. Fig. 3.2 shows some evidence for cross talk between vertical and transverse components (ZT and TZ) in the form of low amplitude coherent waves, perhaps indicating the effects of anisotropy or the scattering of waves off 3D earth structure.

To obtain phase velocity dispersion measurements, we first created period - group velocity maps (*Levshin and Ritzwoller*, 2001) for each stacked correlation function be-

tween periods of 1.0 s and 10 s (supplementary Fig. A.3) using the program *do_mft* (*Herrmann*, 2013). We then pick the dispersion curve for each correlation function manually. Due to a poor signal to noise ratio on the ZZ component, Rayleigh wave dispersion measurements are picked from the RR component correlations, whilst Love wave measurements are picked from the TT component. Examples of period - group velocity maps used for picking the dispersion curves are shown in supplementary Fig. A.3. *Bensen et al.* (2007) suggest that in order for dispersion measurements to be considered reliable, the station separation must be greater than 3 wavelengths of the target wave. If we assume an average phase velocity of c = 3 km s^{-1} for the upper crust, our shortest period surface waves of 1.5 s will have a wavelength of 4.5 km. Thus, in order to satisfy the wavelength criterion, we discard all measurements with an interstation distance of 13.5 km or less as unreliable. For longer periods and distances, unreliable measurements are discarded based on visual inspection. This also ensures that the large amplitudes of the focal spot do not contaminate our measurements from the later arriving surface waves. We use 62 stations in this study, which amounts to a total of 1891 unique station pairs. As a result of the wavelength criterion, coupled with the visual inspection of each period - velocity map we retain measurements from 929 station pairs for Rayleigh waves (49% of the RR correlations), and 1173 station pairs for Love waves (62% of the TT correlations).

We then used *do_mft* (*Herrmann*, 2013) to produce a suite of possible phase velocity dispersion curves that correspond to the given group velocity curve. We use an a priori Earth model to construct an estimated phase velocity dispersion curve that can be compared with this suite of possible observed curves. The a priori model we chose is the upper crustal velocity model of *Karahan et al.* (2001), calculated from a seismic reflection and refraction survey of the Izmit-Adapazari region. We use this estimated dispersion curve as a guide to pick the correct phase velocity curve.

3.2.3 Phase velocity tomography

After picking phase velocity dispersion curves for all inter-station pairs for both Rayleigh and Love waves, we convert the phase velocity at each period into a travel time between the stations. We then use these travel time observations to invert for phase velocity as a function of position at each discrete period. We discretize each model as a 2D grid of phase velocity nodes with a spacing of 6.6 km in latitude and 7.6 km in longitude. The phase velocity tomography is carried out in a spherical co-ordinate system (*Rawlinson and Sambridge*, 2005), with the node spacing dictated by the average horizontal separation of the stations of the DANA network. We begin each inversion with a constant velocity model, with the velocity set to the average observed phase velocity at the given period. We then invert the travel times for periods between 1.5 s and 10.0 s using the method of *Rawlinson and Sambridge* (2005). This is an iterative inversion, with each step consisting of calculating travel times through the current phase velocity model

by wave front tracking using the Fast Marching Method (*Sethian and Popovici*, 1999). The inversion then seeks to minimise the objective function:

$$(\mathbf{g(m)} - \mathbf{d_{obs}})\mathbf{C_d^{-1}}(\mathbf{g(m)} - \mathbf{d_{obs}})^T + \epsilon \left((\mathbf{m} - \mathbf{m_0})^T \mathbf{C_m^{-1}} (\mathbf{m} - \mathbf{m_0}) \right) + \eta \left(\mathbf{m}^T \mathbf{D}^T \mathbf{Dm} \right), \tag{3.1}$$

where $\mathbf{g(m)}$ are the travel times through the current model, and $\mathbf{d_{obs}}$ are the observed travel times from our dispersion data. ϵ is a variable damping factor, η is the smoothing factor. $\mathbf{m}$ and $\mathbf{m_0}$ represent the current model and the starting model respectively. The data and model covariance matrices are represented by $\mathbf{C_d^{-1}}$ and $\mathbf{C_m^{-1}}$. The quantity $\mathbf{Dm}$ is an estimate of the spatial derivative of the current model. As we use an implicitly smooth parameterisation of the model through cubic splines, we neglect the smoothing term in Eq. 3.1 and set $\eta = 0$. In addition, due to the fact that the uncertainties on both the data and the model parameters are generally unknown, we set both $\mathbf{C_d^{-1}}$ and $\mathbf{C_m^{-1}}$ as diagonal matrices of constant values, which removes their effect on the inversion, which is instead controlled by the damping factor, ϵ. These adjustments result in the simplified misfit function

$$| \mathbf{g(m)} - \mathbf{d_{obs}} |^2 + \epsilon \left((\mathbf{m} - \mathbf{m_0})^T (\mathbf{m} - \mathbf{m_0}) \right). \tag{3.2}$$

The variable damping term is included in order to minimise unconstrained model parameters (phase velocities) by preventing them from straying too far from our initial constant velocity model. The choice of damping parameter, ϵ, is somewhat subjective, but should be selected with the aim of achieving a balance between the variance of the final phase velocity model (a high variance indicates unrealistic values for unconstrained model parameters) and obtaining a satisfactory misfit to the observed travel time data. We constructed trade-off curves (supplementary Fig. A.4) of final model variance vs. final data misfit for both the Rayleigh and Love wave inversions. We selected a damping factor of 40 s^4 km^{-2} for Rayleigh waves as it provided a 68% reduction in model variance (0.025 (km s^{-1})^2 to 0.008 (km s^{-1})^2) for only a 2% increase in data misfit (795 ms to 815 ms) at 4 s period. Likewise, for Love waves we choose a damping parameter of 60 s^4 km^{-2} which provides a 75% reduction in model variance (0.055 (km s^{-1})^2 to 0.014 (km s^{-1})^2) for an 8% increase in misfit (670 ms to 730 ms). Increasing the damping parameter above these values leads to an increase in misfit to the observed data which we find unacceptable. These constant damping factors are applied to the inversions at every period (Figs. 3.3 and 3.4).

We do not include a separate smoothing parameter in our inversion scheme, as a similar effect can be obtained by simply reducing the number of model parameters and controlling the inversion through a damping parameter as described above (*Rawlinson and Sambridge*, 2003). We have designed our model discretization so that our velocity node separation is comparable to our station separation, which should be a sufficiently

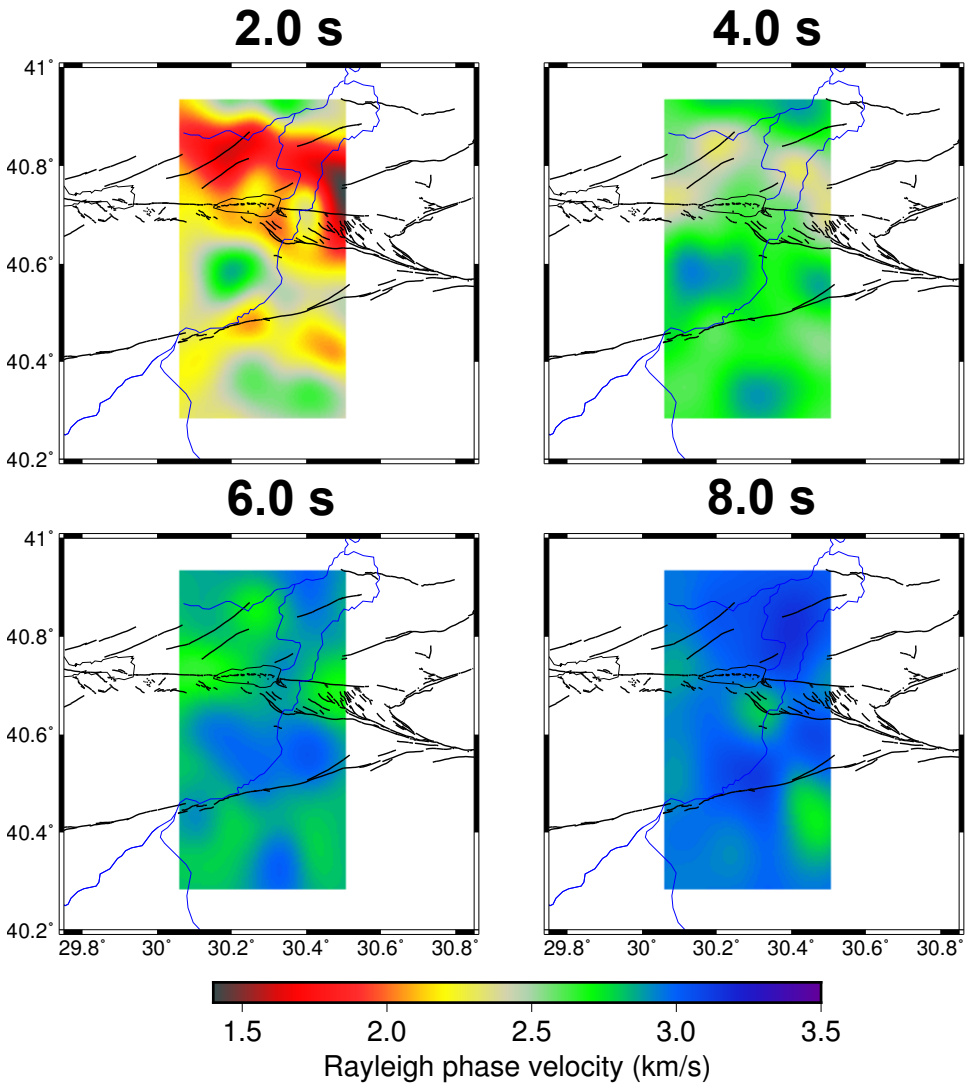

Figure 3.3: Rayleigh wave phase velocity maps at 2.0 to 8.0 s period. Black lines show the mapped faults. The blue line represents the Sakarya River, flowing towards the north.

coarse parameterization to constrain all our model parameters, and produce a smooth final model.

The minimization of the objective function is performed using an iterative subspace inversion approach (*Kennett et al.*, 1988), which projects the objective function on to a multi-dimensional subspace of the data and model parameters. After 10 iterations the data misfit does not improve appreciably with further iterations, and the inversion is judged to have converged. Stable solutions are shown in Fig. 3.3 and 3.4 for periods of 2.0, 4.0, 6.0 and 8.0 s.

3.2.4 S-wave velocity inversion

After obtaining 2D maps of phase velocity for all periods between 1.5 and 10.0 s, the resulting dispersion relation at each node on the same geographic grid was inverted to

obtain isotropic S-wave velocity as a function of depth at that location. Both Rayleigh and Love wave dispersion data are inverted together, with equal weighting, in order to obtain an S-wave velocity model that best satisfies both data sets. The initial inversion was performed using a neighbourhood algorithm (*Sambridge*, 1999, *Wathelet*, 2008) parameterised by a model consisting of 10 layers with variable layer thickness and S-wave velocity. The S-wave velocity of each layer is permitted to vary with a uniform distribution between 0.5 and 4.5 km s^{-1}, whilst layer thickness could vary between 0.5 and 1.5 km. An increase of S-wave velocity with layer depth is also prescribed. A total of 20050 different S-wave velocity models were generated by the algorithm for each node in the grid. Models that fit the dispersion curves extracted from the phase velocity tomography with $\phi_m < 0.25$ (Eq. 3.3) were used in a weighted average to construct an initial estimate for S-wave velocity vs. depth. The misfit parameter at each location is defined for the neighbourhood algorithm as:

$$\phi_m = \sqrt{\sum_{i=1}^{n_f} \frac{(v_{di} - v_{mi})^2}{v_{di}^2 n_f}}. \tag{3.3}$$

n_f is the number of frequencies in the dispersion curve, v_{di} is the observed phase velocity at frequency i from our tomographic model, and v_{mi} is the phase velocity at that frequency inferred from the inverted S-wave model. Examples of the distribution of models used in the weighted average at three grid points, one each in the Sakarya Terrane, Armutlu Block and Istanbul Zone, are shown in Fig. 3.5. The weighting of each model is the inverse of its misfit to the dispersion data as described in Eq. 3.3.

This average model was then used as the starting model for a linearised iterative inversion scheme as implemented in *surf96* (*Herrmann*, 2013). The inversion was judged to have converged once the root mean square change in the S-wave velocity model between iterations was negligible (< 0.1 km/s), usually within 6 iterations. The set of 1D models obtained from the linearised inversion represent our 3D S-wave velocity model for the region. By using a neighbourhood algorithm (*Sambridge*, 1999) to construct the initial S-wave velocity models we ensure that we gain a good sampling of the entire parameter space, and reduce the chance of falling into a local minimum for the data misfit during the final linearised inversion.

3.2.5 Measurement of azimuthal anisotropy

In order to quantify the level of azimuthal anisotropy in our phase velocity data set, we calculate phase velocity as a function of the azimuth of the propagation direction (from north). We bin these phase velocity measurements by azimuth, with a bin size of 5°. Rayleigh and Love wave observations are treated separately. Due to the presumed symmetry of propagation velocity in both directions between pairs of stations, our measurements are in an azimuth range of 0° to 180°. We attempt to fit the binned

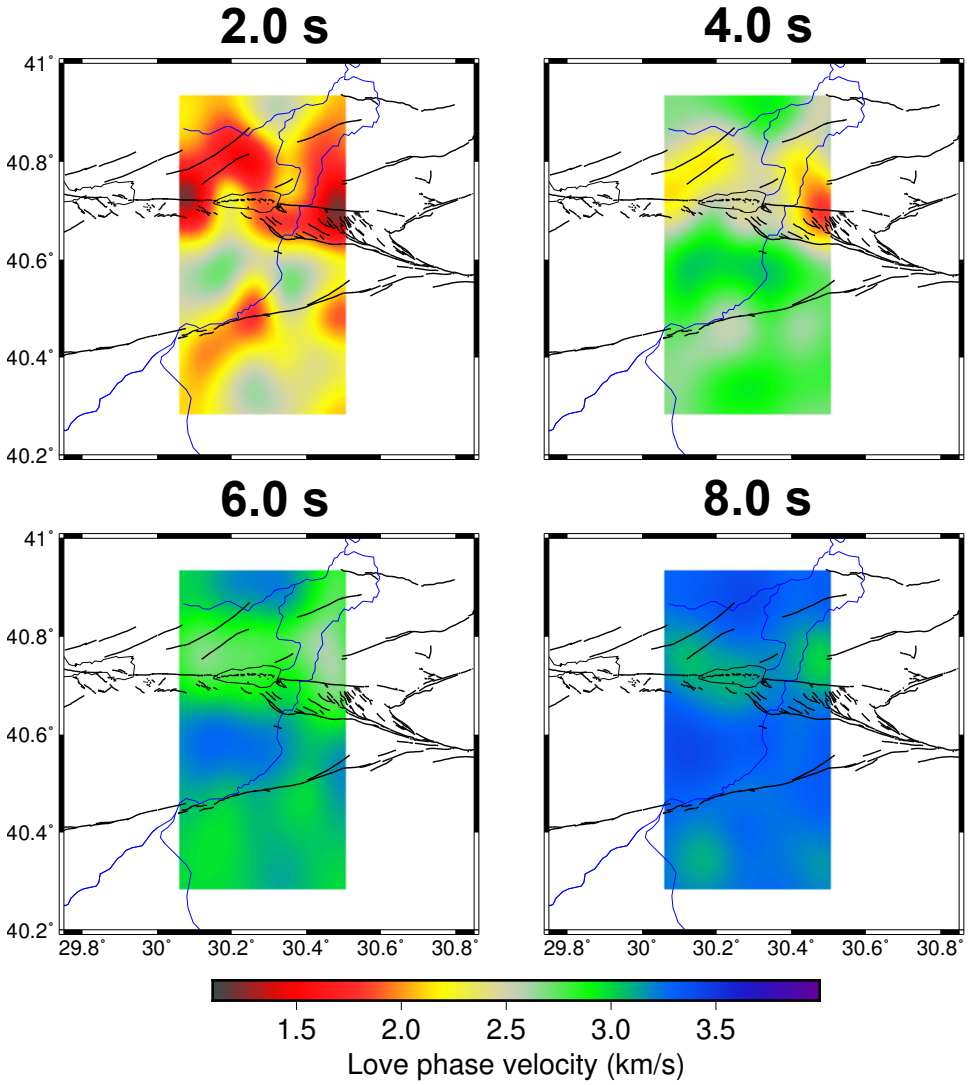

Figure 3.4: Love wave phase velocity maps at 2.0 to 8.0 s period. Black lines show the mapped faults. The blue line represents the Sakarya River, flowing towards the north.

data at each period with the following function to describe the azimuthal variation of phase velocity:

$$c(\theta) = u_0 + A\cos(2(\theta - \phi_2)) + B\cos(4(\theta - \phi_4)). \tag{3.4}$$

Eq. 3.4 uses the parameterisation of *Smith and Dahlen* (1973). u_0 is the average (isotropic) phase velocity. A is the amplitude of the 2θ term, which describes an azimuthal variation with 180° periodicity. ϕ_2 is the fast direction of the 2θ term. B is the amplitude of the 4θ term, which has 90° periodicity, and ϕ_4 is the corresponding fast direction.

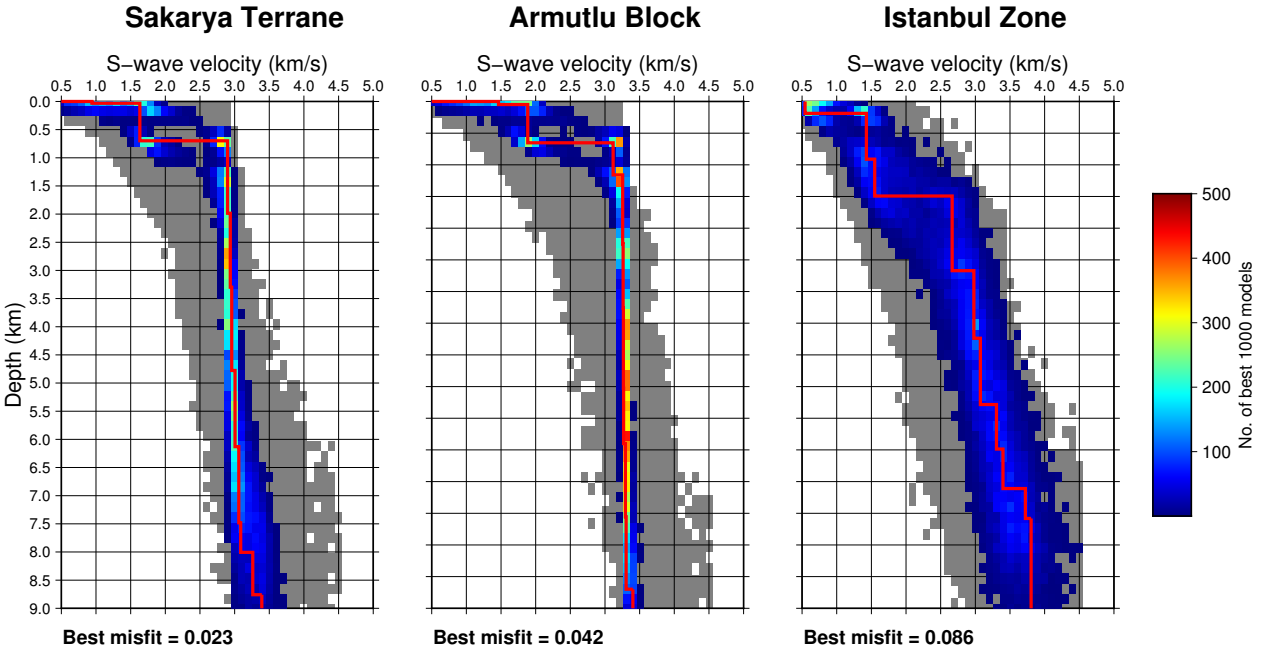

Figure 3.5: Results of the neighbourhood algorithm inversion for S-wave velocity at three nodes in the different geological units (Fig. 3.1). The grey region represents the range of accepted models with a misfit below 0.25 (Eq. 3.3). The coloured region shows the range of the 1000 models with the lowest misfit. Red colours indicate a higher number of the best 1000 models with a certain S-wave velocity at that depth. The solid red line shows the best fitting model, the misfit of which is shown at the bottom of each panel. The location of each of these nodes is shown in Fig. 3.6.

3.3 Results

In this section, we describe the phase velocity maps derived separately for Rayleigh and Love wave travel time data. Sensitivity kernels representing the vertical resolution for Rayleigh and Love waves within our period range can be found in the supplementary material (Fig. A.8), along with synthetic checker board recovery tests to illustrate the horizontal resolution of the inversion (Fig. A.9 and A.10). The initial and final data misfit of the tomography models for both Rayleigh and Love wave phase velocities are shown in supplementary Figs. A.5 and A.6. The significant reduction in the variance of the travel time residuals in the final models, on average about 50%, indicates that the final models better account for structural heterogeneity. Similarly, the higher variance of the final travel time residuals at shorter periods indicates stronger heterogeneity at shallow depths, or noisier phase velocity measurements at these periods.

3.3.1 Rayleigh wave phase velocity

Fig. 3.3 shows the results of the Rayleigh wave phase velocity tomography for periods between 2.0 s and 8.0 s. The most interesting features of the velocity model include the large low velocity (1.5 km s^{-1} - 2.0 km s^{-1}) anomalies located north of the northern

branch of the NAFZ. These low velocities are likely due to the deep sedimentary basin at Adapazari in the north eastern part of the model, and heavily faulted sediments near Izmit in the north western sector (*Şengör et al.*, 2005). In between the two fault strands, the Armutlu Block can be seen as a prominent region of high phase velocity ($\sim$ 3.0 km s^{-1}), likely associated with the metamorphic rocks and possible granitic intrusions that exist in this region (*Bekler and Gurbuz*, 2008, *Şengör et al.*, 2005). At 2.0 s and 4.0 s period, this high velocity region is particularly prominent in the western part of the Armutlu Block (Fig. 3.3). At 6.0 s period, the entire Armutlu Block consists of high velocities. At 2.0 s period, the sediments of the Pamukova basin can be seen along the southern branch of the NAFZ with velocities of approximately 2.0 km s^{-1}. To the south, in the Sakarya Terrane, a relatively high velocity anomaly (faster than 2.5 km s^{-1}) can be seen at all periods greater than 2.0 s. These velocities are in general higher than those observed in the part of the Istanbul Zone that bounds the fault, and they likely indicate the crystalline basement of the Sakarya Terrane at shallower depths, with thinner sedimentary cover. It is likely that the high phase velocities observed in the far north of the model correspond to the older sedimentary units and crystalline rocks of the Istanbul Zone that underlie the clastic sediments at Izmit and Adapazari (*Okay et al.*, 1994).

3.3.2 Love wave phase velocity

The Love wave phase velocity images (Fig. 3.4) show a very similar pattern to the Rayleigh wave images. To the north of the fault extremely low ($\sim$ 1.2 km s^{-1}) phase velocities are associated with the faulted sediments near Izmit, as well as the Adapazari Basin. Both of these features are visible for periods $<$ 6.0 s. Low velocities also seem to be strongly associated with the NW–SE striking faults just north of the rupture zone of the Izmit earthquake 40.7N and 30.45E. Focal mechanisms for earthquakes in this region show examples of normal faulting (*Altuncu Poyraz et al.*, 2015), indicating these low velocities could be associated with a releasing bend on the northern branch. The Armutlu Block in between the two fault strands shows high phase velocities exceeding 2.4 km s^{-1}, which is comparable with those of the Rayleigh wave images. The Pamukova basin can be seen for periods $<$ 4.0 s near the southern branch of the fault with velocities of 1.5 – 2.5 km s^{-1}. Above 4.0 s period, higher phase velocities ($>$ 3.0 km s^{-1}) are observed within the southern portion of the Sakarya Terrane, and the northern part of the Istanbul Zone. These high velocities are again interpreted to represent the crystalline basement of these tectonic units.

3.3.3 S-wave velocity model misfit

In order to construct an isotropic S-wave velocity velocity profile at each node a two-step inversion process was chosen, as described in Sec. 3.2.4. Examples of the results

of the neighbourhood algorithm from three locations in the Sakarya Terrane, Armutlu Block and Istanbul Zone, are shown in Fig. 3.5. The best 1000 models from the neighbourhood algorithm occupy a much smaller range for the Sakarya Terrane and Armutlu Block examples. The broader range for the Istanbul Zone example shows that the data here provide weaker or possibly conflicting constraints on the model velocity profile. In the final step of the inversion, the linearized approach using *surf96* (*Herrmann*, 2013) is used to find an optimum model. Supplementary Fig. A.7 shows the final fit of the dispersion curves calculated at each of the nodes shown in Fig. 3.5. The dispersion curves were calculated for the final S-wave velocity model, and compared to dispersion curves extracted from the Rayleigh and Love wave phase velocity tomography. Supplementary Fig. A.7 also summarises the improvement in the misfit to the dispersion data provided by employing the linearised inversion (*Herrmann*, 2013) after the neighbourhood algorithm. Each node has a significant improvement in misfit following the linearized inversion ($> 50\%$).

3.3.4 Isotropic S-wave velocity maps

Fig. 3.6 shows depth slices through the final S-wave velocity model at depths of 1.5 km, 3.5 km and 5.5 km. In the top 3 km of the crust we observe low S-wave velocities (1.6 – 2.0 km s^{-1}) on the north side of the northern fault strand, associated with the Adapazari basin and faulted sediments near Izmit. These low S-wave velocities are not observed at model depths of 3.5 km and below (Fig. 3.7), indicating that the Adapazari basin is likely not deeper than about 3.5 km. At 5.5 km depth, relatively low S-wave velocities (2.8 km s^{-1}) are clearly associated with the northern branch of the NAFZ, particularly within the zone of the Izmit rupture beneath Lake Sapanca at 40.7N and 30.2E. Faster S-wave velocities, up to 3.5 km s^{-1}, are observed within the Armutlu Block between the two strands of the NAFZ. As with the phase velocity maps, these high velocities are more prominent west of the Sakarya River to a depth of about 3.5 km. The slow velocities associated with the Pamukova basin along the southern branch of the NAFZ are much attenuated at 3.5 km depth, indicating that this basin is shallower than the Adapazari basin. We observe evidence in the southern part of the model for crystalline rocks below a depth of 1.5 km in the Sakarya Terrane, where S-wave velocities exceed 2.5 km s^{-1}. These high velocities are also observed in the far north of the model within the Istanbul Zone. Both the northern and southern branches of the NAFZ appear to exploit the regions where we observe high gradients in seismic S-wave velocity. Both branches of the main fault skirt the edges of the high velocity zone associated with the Armutlu Block.

3.3.5 Isotropic S-wave velocity vertical profiles

Fig. 3.7 shows two vertical sections through the S-wave velocity model along a North – South profile located at 30.2°E (profile A–B), and 30.4°E (profile A'–B'). In profile A–B the low velocity zone associated with the heavily faulted sediments near Izmit (40.82°N) can be observed to a depth of ∼ 3.5 km, as can the Adapazari basin along the profile A'–B'. In profile A–B the Armutlu Block is clearly distinguishable as a region of high velocity (∼ 2.8 km s^{-1}) extending towards the surface between 40.5°N and 40.6°N. It is clear that high velocity metamorphic rocks found in this region (*Yılmaz et al.*, 1995) are located closer to the surface than the basement rocks of the Sakarya Terrane and Istanbul Zone. In both profiles, a zone of low velocity (∼ 2.8 km s^{-1}) can be seen extending to a depth of at least 6 km beneath the location of the surface expression of the northern branch of the NAFZ. This low velocity zone appears to be on the order of 10 km wide (40.65°N to 40.75°N). Low velocities associated with the southern branch of the fault zone are less clear, particularly for the eastern profile A'–B', but are evident to 5 km depth beneath profile A–B. However, it is difficult to distinguish the southern branch of the fault from the surrounding sedimentary cover of the Sakarya Terrane and Pamukova basin.

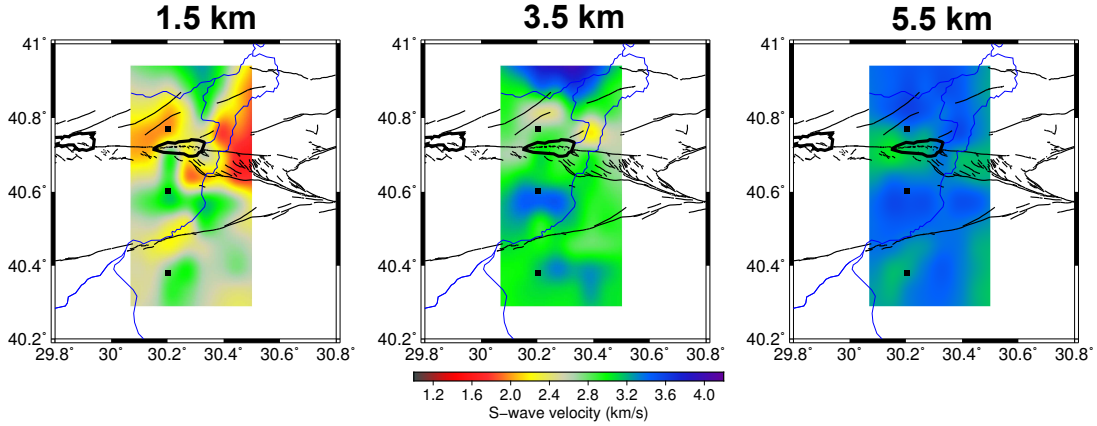

Figure 3.6: Isotropic S-wave velocity maps at 1.5, 3.5 and 5.5 km depth. Black lines show the mapped faults. The blue line represents the Sakarya River, flowing towards the north. The black squares represent the locations of the nodes shown in Fig. 3.5.

3.3.6 Azimuthal anisotropy

The azimuthal variation of Rayleigh wave phase velocities between 2.0 and 8.0 s period is shown in Fig. 3.8. It is clear that the fast direction for both the 2θ and 4θ terms varies between 60° and 75°. The amplitude of the 2θ component is variable, and generally increases at longer periods. The average amplitude of anisotropy for the measurements shown in Fig. 3.8 is 0.048 km s^{-1} or 1.7%. In general, the amplitude of the 4θ term is at least 50% lower than the 2θ term, which is to be expected for Rayleigh waves (*Smith and Dahlen*, 1973). The exception to these trends is at 2.0 s period. Here, the fast

directions do not align with those observed at longer periods, and the 4θ component has twice the amplitude of the 2θ component. However, both the RMS misfit and the variance of the residuals between the observed data and Eq. 3.4 are much greater at 2.0 s period, as is the case with the phase velocity tomography. In particular, the greater variance of the residuals implies a greater uncertainty in the data fit. Greater variance in the 2 s phase velocities is likely due to the fact that waves at 2.0 s period are more sensitive to short wavelength heterogeneities near the surface.

The azimuthal anisotropy of the Love wave phase velocities is shown in supplementary Fig. A.13. The Love wave anisotropy is less clear. In general, the 2θ fast direction lies between 25° and 40° from north. The 4θ fast direction is more variable, mostly lying between 85° and 120°. The average amplitude of the 2θ term is 0.036 km s^{-1}. Whilst the amplitude of the 4θ term is more comparable in amplitude to the 2θ term than for the Rayleigh waves, it is still consistently smaller, with an average of 0.024 km s^{-1}. The RMS misfit and variance of the residuals is again higher at the shorter periods of 2.0 s and 4.0, again indicating sensitivity to shorter wavelength structural complexities near the surface. The azimuthal distribution of ray paths used in this analysis is shown in supplementary Figs. A.14 and A.15.

Fig. 3.9 shows the variation in the 2θ fast direction and magnitude of anisotropy of Rayleigh wave phase velocities between 1.5 s and 9.5 s period. Fig. 3.9 shows a smooth variation in the fast direction with increasing period of the wave. At short periods (2 – 3 s) the fast direction is aligned close to 90° from north, but changes smoothly to $\sim$ 70° from north above 5 s period. Below 2 s period, the anisotropy has a magnitude greater than 1%, but this magnitude decreases substantially between 2 and 4 s period, before increasing again at periods greater than 4.0 s to a value of $\sim$ 3%.

3.4 Discussion

3.4.1 S-wave velocity model

The horizontal resolution of the S-wave velocity model at depth in Fig. 3.7 is limited by the wavelength of the surface waves used in this study. Receiver function and autocorrelation studies of the region show that the shear zone associated with the NAFZ is perhaps no wider than $\sim$ 7 km through the crust and into the upper mantle (*Kahraman et al.*, 2015, *Taylor et al.*, 2016). In the upper crust, the main fault strands are estimated to be no more than a few kilometres wide in this region (*Okay and Tüysüz*, 1999). Low S-wave velocities associated with the northern branch of the NAFZ are observable in our model down to a depth of 6 km. Below this depth, we rely on observations derived from Rayleigh waves with a period greater than 8.0 s (phase velocity sensitivity kernels in supplementary Fig. A.8). Assuming a phase velocity of 3 km s^{-1}, these waves have a wavelength of $\sim$ 24 km. Thus, we cannot expect to resolve

such a narrow structure at depth, unless it offsets rocks of differing seismic velocity. In this region it is clear that both the northern and southern branches of the NAFZ have exploited boundaries between major lithological units. In particular the metamorphic rocks of the Armutlu Block are clearly mapped due to the strong velocity contrast with rocks of the Istanbul Zone to the north and the Sakarya Terrane to the south (Figs. 3.3, 3.4 and 3.6).

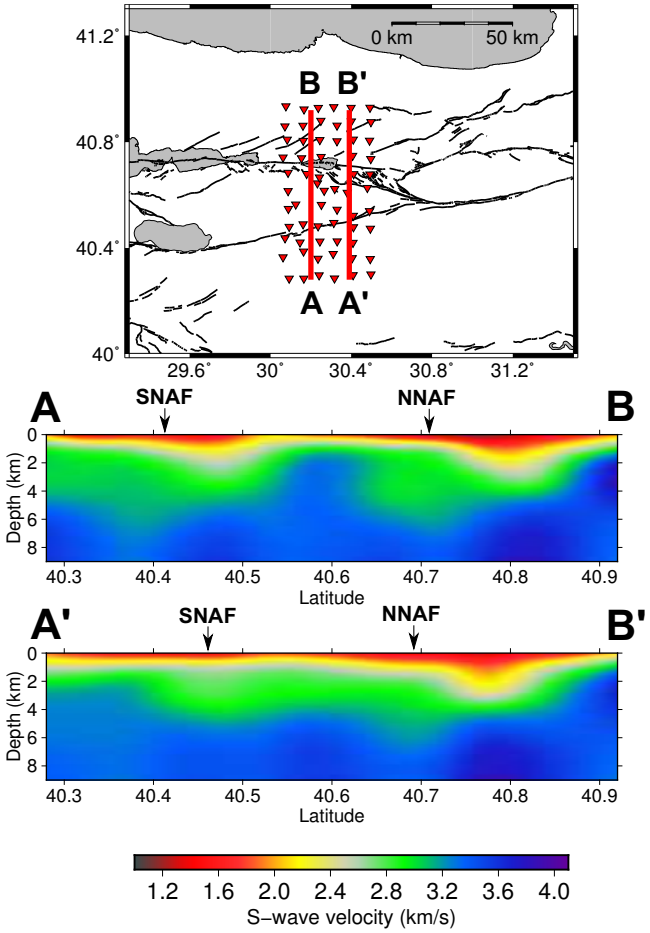

Figure 3.7: Top: Map of the Izmit-Adapazari region showing station locations of the DANA network as red triangles, and mapped faults as black lines. Thick red lines indicate the location of the vertical profiles taken through S-wave velocity model along lines A – B and A – B. Middle: Vertical S-wave velocity profile between A – B. Bottom: Vertical S-wave velocity profile between A – B. The profiles show S-wave velocity between the surface and 9 km depth. The approximate location of the surface traces of the northern and southern branches of the NAFZ are indicated by NNAF and SNAF, respectively.

P-wave velocity models of the crust in this region have also been constructed from teleseismic body wave tomography by *Papaleo et al.* (2017). They image depth averaged P velocity between the surface and 90 km depth, whilst maintaining sufficient resolution between 20 km depth and the surface to detect anomalies with sizes on the order of a few kilometres. While unable to resolve the sedimentary basins, they detect reduced crustal P-wave velocities immediately to the north of the NAFZ in the same regions

we observe low S-wave velocities associated with the Adapazari Basin, and heavily faulted sedimentary cover in the north western part of the array (Figs. 3.6, 3.7). Low P-wave velocities are also co-located with the low S-wave velocities detected in this study beneath the Pamukova basin. They also found relatively high P-wave velocity within the Armutlu Block, where we find high S-wave velocities that we attribute to the shallow metamorphic rocks reported in this region (*Yılmaz et al.*, 1995). We note that the relatively high seismic velocities we find in the upper crust of the Armutlu Block correspond to a region of relatively low electrical resistivity found by *Tank et al.* (2005) in the upper 10 km.

The depth of sedimentary cover of the Adapazari basin has been estimated to be at least 1.0 km in some locations (*Komazawa et al.*, 2002). These estimates were made by inverting Rayleigh wave phase velocity measurements from microseisms recorded at two arrays within the basin. Due to a lack of measurements below 0.6 Hz ($> \sim$ 1.6 s period) the inversion of *Komazawa et al.* (2002) assumed an S-wave velocity of 3.5 km s^{-1} below a depth of 500 m in the basin. Our velocity model, which incorporates Rayleigh wave observations up to 10.0 s period, indicates that S-wave velocity may be no greater than 3.0 km s^{-1} up to a depth of 2.5 km within the basin. Our measurements therefore imply that the Adapazari basin could have a depth of up to 2.5 km based on the observed increase in S-wave velocity at this depth. Similarly, the Pamukova basin may be as deep as 2.5 km, though it is difficult to accurately detect the depth to material interfaces using only surface wave observations.

Studies of the near surface structure of the San Jacinto fault zone in southern California (*Allam and Ben-Zion*, 2012, *Zigone et al.*, 2015) observe prominent flower structures associated with the fault. These structures are zones of low seismic velocity that are wide near the surface, become narrower with depth, and are interpreted to be a damage zone created during fault propagation through undeformed crust. The surface wave analysis does not enable us to observe a narrowing with depth of the low-velocity zone associated with the northern branch of the NAFZ in Fig. 3.7. Nonetheless the low velocity anomalies associated with the Adapazari and Izmit regions might be interpreted as crust that has been damaged by movement on and around the northern strand of the fault. It is clear that the strongest contrasts in seismic velocities in our model (Figs. 3.3, 3.4 and 3.6) are associated with boundaries between the three main tectonic units. The North Anatolian Fault Zone appears to have developed along pre-existing tectonic boundaries.

Such seismic velocity contrasts across an active strike-slip fault are also present in California on the creeping section of the San Andreas Fault to the north of Parkfield where the fault trace is located along a strong velocity contrast between the Great Valley sedimentary sequence and the granites of the Salinian terrane (*Eberhart-Phillips and Michael*, 1993, *Thurber et al.*, 2006). This phenomenon is also observed across the Hayward fault near San Francisco where there is a clear velocity contrast between the

Great Valley sequence and the Franciscan Complex (*Hardebeck et al.*, 2007, *Thurber et al.*, 2006). *Eberhart-Phillips and Michael* (1993) suggest that the San Andreas Fault is likely to creep in sections where this clear velocity contrast exists, whilst being locked and rupturing seismogenically where the velocity contrast across the fault is less defined. However, this association between a creeping fault segment and a clearly defined velocity contrast evidently does not hold for this section of the NAFZ where the 1999 Izmit and Düzce earthquakes occurred. Furthermore, a recent geodetic study found evidence of only low creep rates on this segment, probably related to earthquake after-slip at shallow depths (*Hussain et al.*, 2016).

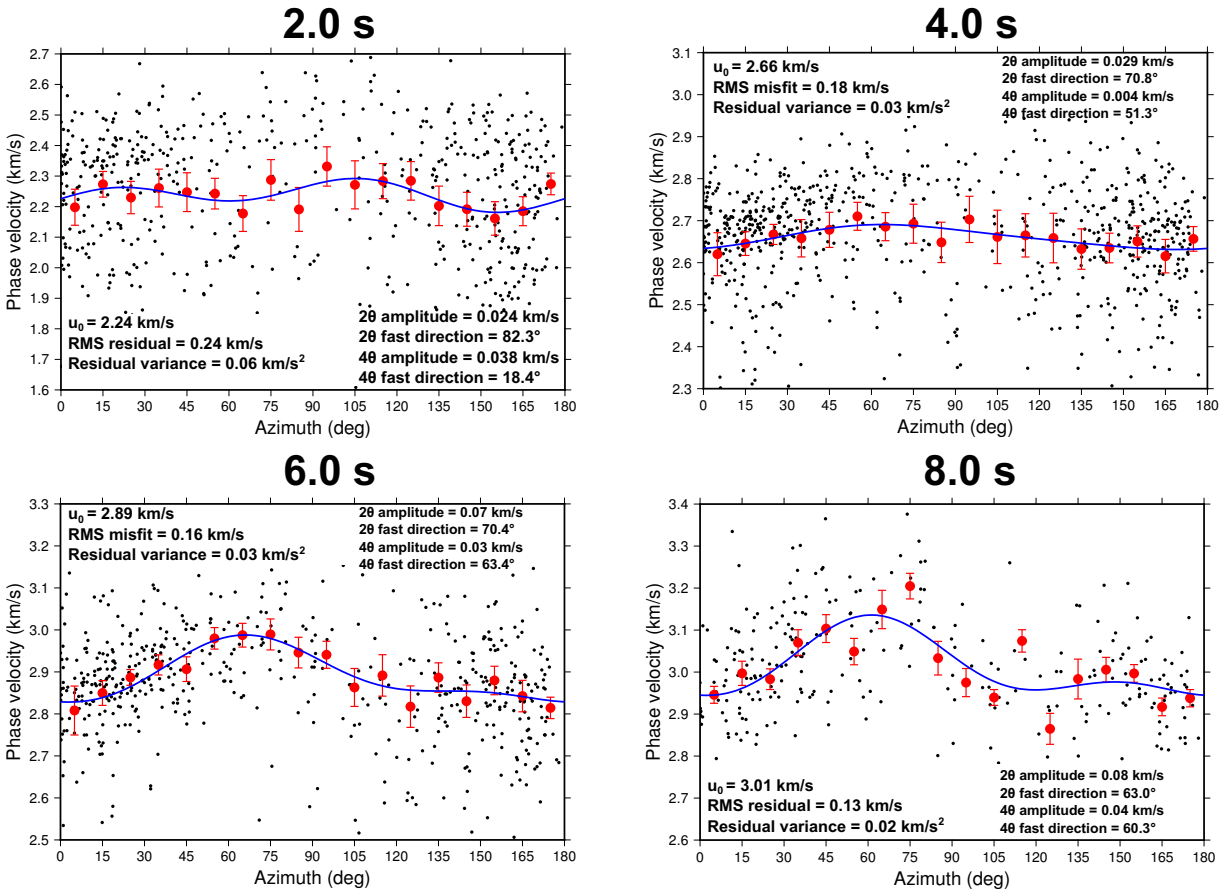

Figure 3.8: Azimuthal variation of Rayleigh wave phase velocities with propagation azimuth (from north). Black dots indicate the raw phase velocity measurements, large red dots show the average of the phase velocities within 5 degree azimuth bins, and the corresponding standard error of the mean for the bin. The blue line is the best fitting curve (Eq. 3.4) to the binned data (red dots). u_0 is the average (isotropic) phase velocity. We show the root mean square misfit of the blue curve to the phase velocity measurements, as well as the variance of the residuals. We indicate the 2θ and 4θ amplitudes and fast directions that correspond to the blue curve. The azimuthal distribution of ray paths used in this analysis is shown in supplementary Fig. A.14.

The relatively high S-wave velocities we observe within the Armutlu Block likely indicate metamorphic rocks and pre-Jurassic basement (*Akbayram et al.*, 2016) of which the surface outcrops are of unknown provenance and age (*Okay and Tüysüz*, 1999). This

metamorphic unit within the Armutlu Block is evidently resistant to strain, which is deflected onto the northern and southern branches of the NAFZ that bound this high S-wave velocity region. This behaviour is also observed in the near surface structure of the south eastern section of the Alpine Fault on South Island, New Zealand, where the fault trace is located at the edge of the metamorphic Haast Schist, and cuts through thick coastal sediments (*Eberhart-Phillips and Bannister*, 2002). *Fichtner et al.* (2013) image the S-wave velocity structure of the upper mantle beneath the NAFZ using full waveform inversion. At this much larger length and depth scale, they also note that the NAFZ appears to be bounded by tectonic blocks of high seismic velocity. They interpret this as evidence that the fault zone developed along the edges of high-rigidity blocks, analogous to our observations for the near-surface structure of the Armutlu Block.

3.4.2 Azimuthal anisotropy

The 2θ and 4θ fast directions for Rayleigh waves varies between 60° – 70° from north, whilst Love wave 2θ fast directions vary from 20° to 40° from north. These fast directions may be compared to the 45° direction of maximum extension for the Izmit-Adapazari region calculated from interseismic GPS data by *Allmendinger et al.* (2007). The Love wave 4θ fast direction is highly variable, with no distinct pattern that can be readily observed.

There are two possible explanations for crustal anisotropy: aligned cracks or mineral fabric. Some minerals in upper crustal rocks, such as micas and amphibole, typically have cleavage planes or crystallographic axes aligned with the dominant strain direction, and are the dominant source of anisotropy within the bulk rock (*Kern and Wenk*, 1990, *Mainprice and Nicolas*, 1989, *Sherrington et al.*, 2004). These minerals are particularly common in high grade metamorphic rocks such as slates and schists, and are likely abundant within the Armutlu Block. Analysis of samples of calcite and amphiboles taken from the Uludag Massif ($\sim$ 100 km south–west of Izmit-Adapazari) by *Farrell* (2017) show that the fast propagation for both P and S-waves aligns parallel to the foliation direction in these minerals. We therefore think it likely that the seismic fast directions we observe are determined by deformation fabrics aligned with the dominant shear regime.

Fig. 3.9 shows a 90° fast direction at 2 – 3 s period that aligns approximately with the strike of the North Anatolian Fault through the region. Above 3 s period, the fast direction smoothly transitions to an alignment closer to 70° from north (Fig. 3.9). Shear wave splitting measurements of the central portion of the North Anatolian Fault by *Biryol et al.* (2010) found a fast polarisation direction that varied between 35° and 60°. The shear wave splitting measurements are mainly sensitive to the lithospheric mantle, where mineral fabric is known to be the dominant source of seismic anisotropy *Christensen and Crosson* (1968). The average orientation of the fast direction of short

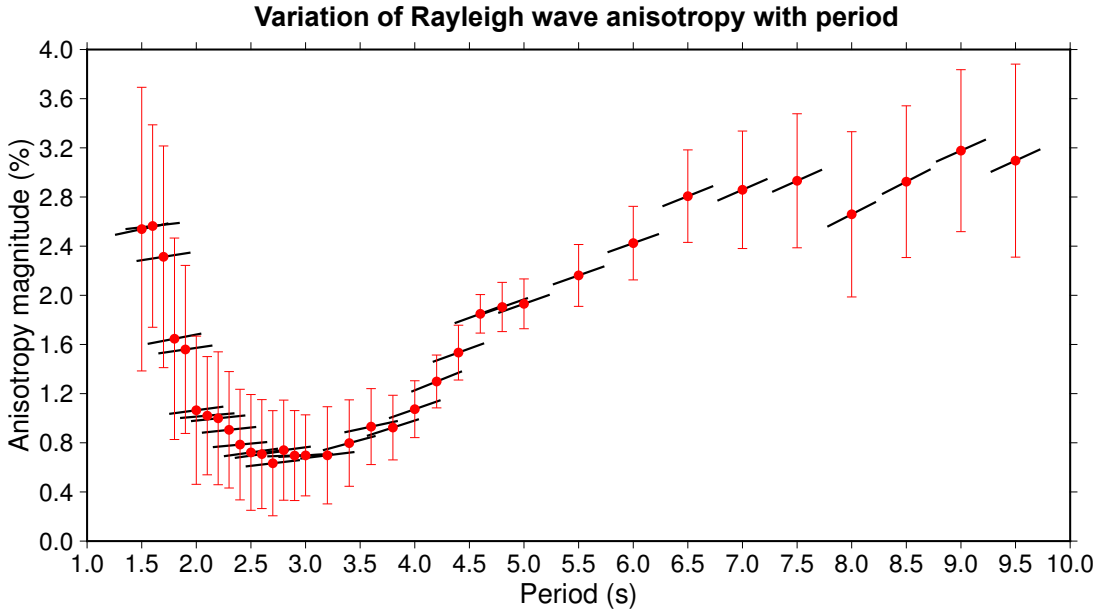

Figure 3.9: Variation of 2θ Rayleigh wave anisotropy with period in the Izmit-Adapazari region. The red dots are the measured magnitude of anisotropy at each period, and the corresponding uncertainty is the standard deviation of the anisotropy magnitude taken from the covariance matrix during the curve fitting process described in section 3.2.5. The black lines indicate the angle from north of the 2θ fast direction at each period, where the top of the plot represents north.

period (1.5 s – 4.0 s) and long period (4.0 s – 10.0 s) Rayleigh waves is shown on Fig. 3.1, alongside the average fast polarisation direction (43°) observed by *Biryol et al.* (2010). We observe a relatively smooth and monotonic of the fast anisotropy direction from alignment with the principle shear direction in the upper 2 – 3 km to an alignment with the principle extension direction for the lithosphere (*Biryol et al.*, 2010, *Allmendinger et al.*, 2007).

3.5 Conclusions

We utilised the ambient noise field recorded at a temporary network in the Izmit-Adapazari region of north western Turkey to retrieve Rayleigh and Love waves propagating between the stations of the array. We performed surface wave phase velocity tomography, followed by an inversion for S-wave velocity structure, with waves of periods from 1.5 to 10.0 s to image the shear wave velocity in the top 10 km of the North Anatolian Fault Zone.

Our model shows low S-wave velocity to the north of the NAFZ, associated with faulted marine clastic sediments near Izmit (*Akbayram et al.*, 2016) and with the Adapazari sedimentary basin, which we estimate to have a thickness of at least 2.5 km. In between the two branches of the NAFZ, we observe a high velocity region linked to metamorphic and igneous rocks in the Armutlu Block. It is likely that this high S-wave

velocity in the upper crust is indicative of a rheologically strong region that preferentially localises strain at the boundaries of the Armutlu Block, particularly along its northern boundary which has been identified as the Intra-Pontide Suture Zone. We also image the Pamukova basin as a region of low S-wave velocity to a depth of about 2.5 km, associated with the southern branch of the NAFZ. Both basins are likely related to pull-apart motion along the northern and southern branches of the NAFZ, where they are oblique to the principal shear direction.

To the south of the NAFZ, we image the Sakarya Terrane as a region of moderate to high S-wave velocity, consistent with the Sakarya Terrane being an accretionary complex of sedimentary rocks overlying a metamorphic crystalline basement (*Yılmaz et al.*, 1995). We find that both Rayleigh and Love waves have a fast direction which varies smoothly from the maximum shear direction in the upper few kilometres of the crust towards the principle extension direction of the lithosphere at greater depth. The relationship between the three distinct tectonic units of the region, and the potential for strain localisation along both the northern and southern branches of the NAFZ is critical to understanding the long term behaviour of the fault zone, and the seismic hazard that it poses.

Acknowledgments

The final S-wave velocity model derived from this study can be found as a separate file in the supplementary material. G. Taylor is supported by the Leeds-York Doctoral Training Partnership of the Natural Environment Research Council (NERC), UK. G. Hillers acknowledges support through a Heisenberg fellowship from the German Research Foundation (HI 1714/1-2). The DANA array was part of the Faultlab project, a collaborative effort by the University of Leeds, Kandilli Observatory and Earthquake Research Institute, and Sakarya University. Data for this study can be found at the IRIS Data Management Centre under network code YH (2012 – 2013). Major funding was provided by the UK NERC under grant NE/I028017/1. Equipment was provided and supported by the NERC Geophysical Equipment Facility (SEIS-UK) Loan 947. We thank the editor Martha Savage and two anonymous reviewers for their insightful comments that greatly improved this manuscript.

References

Akbayram, K., C. C. Sorlien, and A. L. Okay (2016), Evidence for a minimum 52 ± 1 km of total offset along the northern branch of the North Anatolian Fault in northwest Turkey, *Tectonophys.*, *668*, doi:10.1016/j.tecto.2015.11.026. 3.1, 3.4.1, 3.5

Allam, A. A., and Y. Ben-Zion (2012), Seismic velocity structures in the southern California plate-boundary environment from double-difference tomography, *Geophys. J. Int.*, *190*, doi:10.1111/j.1365-246X.2012.05544.x. 3.4.1

Allmendinger, R. W., R. Reilinger, and J. Loveless (2007), Strain and rotation rate from GPS in Tibet, Anatolia, and the Altiplano, *Tectonics*, *26*, doi:10.1029/2006TC002030. 3.4.2, 3.4.2

Altuncu Poyraz, S., M. U. Teoman, N. Türkelli, M. Kahraman, D. Cambaz, A. Mutlu, S. Rost, G. A. Houseman, D. A. Thompson, D. Cornwell, M. Utkucu, and L. Gülen (2015), New constraints on micro-seismicity and stress state in the western part of the North Anatolian Fault Zone: Observations from a dense seismic array, *Tectonophys.*, *656*, doi:10.1016/j.tecto.2014.03.015. 3.1, 3.3.2

Barka, A., H. S. Akyüz, E. Altunel, G. Sunel, Z. Çakir, A. Dikbas, B. Yerli, R. Armijo, B. Meyer, J. B. de Chabalier, T. Rockwell, J. Dolan, R. Hartleb, T. Dawson, S. Christofferson, A. Tucker, T. Fumal, R. Langridge, R. Stenner, W. Lettis, J. Bachhuber, and W. Page (2002), The Surface Rupture and Slip Distribution of the 17 August 1999 Izmit Earthquake (M 7.4), North Anatolian Fault, *Bull. Seismol. Soc. Am.*, *92*, doi:10.1785/0120000841. 3.1, 3.1

Bekler, T., and C. Gurbuz (2008), Insight into the crustal structure of the Eastern Marmara Region, NW Turkey, *Pure Appl. Geophys.*, *165*, doi:10.1007/s00024-008-0302-3. 3.3.1

Bensen, G. D., M. H. Ritzwoller, M. P. Barmin, A. L. Levshin, F. Lin, M. P. Moschetti, N. M. Shapiro, and Y. Yang (2007), Processing seismic ambient noise data to obtain reliable broadband surface wave dispersion measurements, *Geophys. J. Int.*, *169*, doi:10.1111/j.1365246X.2007.03374.x. 3.2.1, 3.2.2

Bercovici, D., and Y. Ricard (2014), Plate tectonics, damage and inheritance, *Nature*, *508*, doi:10.1038/nature13072. 3.1

Biryol, C. B., G. Zandt, S. L. Beck, A. A. Ozacar, H. E. Adiyaman, and C. R. Gans (2010), Shear wave splitting along a nascent plate boundary: the North Anatolian Fault Zone, *Geophys. J. Int.*, *181*, doi:10.1111/j.1365-246X.2010.04576.x. 3.1, 3.4.2

Bürgmann, R., and G. Dresen (2008), Rheology of the lower crust and upper mantle: Evidence from rock mechanics, geodesy, and field observations, *Annu. Rev. Earth Planet. Sci.*, *36*, doi:10.1146/annurev.earth.36.031207.124326. 3.1

Christensen, N. I., and R. S. Crosson (1968), Seismic anisotropy in the upper mantle, *Tectonophys.*, *6*, doi:10.1016/0040-1951(68)90013-9. 3.4.2

Şengör, A. M. C., and Y. Yılmaz (1981), Tethyan evolution of Turkey: A plate tectonic approach, *Tectonophys.*, *75*, doi:10.1016/0040-1951(81)90275-4. 3.1

Şengör, A. M. C., O. Tüysüz, C. İmren, M. Sakınç, H. Eyidoğan, N. Görür, X. L. Pichon, and C. Rangin (2005), The North Anatolian Fault: A New Look, *Annu. Rev. Earth Planet. Sci.*, *33*, doi:10.1146/annurev.earth.32.101802.120415. 3.1, 3.1, 3.3.1

DANA (2012), Dense Array for Northern Anatolia, *Int. Fed. of Digital Seismograph Networks, Other/Seismic Network, Seattle, Wash.*, doi:10.7914/SN/YH_2012. 3.1

Dayem, K. E., G. A. Houseman, and P. Molnar (2009), Localization of shear along a lithospheric strength discontinuity: Application of a continuous deformation model to the boundary between Tibet and the Tarim Basin, *Tectonics*, *28*, doi:10.1029/2008TC002264. 3.1

Doğan, B., O. Tüysüz, and F. B. Sanli (2014), Tectonostratigraphic evolution of the basins on the southern branch of the North Anatolian Fault System in the SE Marmara Region, Turkey, *Int. J. Earth Sci.*, *104*, doi:10.1007/s00531-014-1083-9. 3.1

Dziewonski, A. M., T. A. Chou, and J. H. Woodhouse (1981), Determination of earthquake source parameters from waveform data for studies of global and regional seismicity, *J. Geophys. Res.*, *86*, doi:10.1029/JB086iB04p02825. 3.1

Eberhart-Phillips, D., and S. Bannister (2002), Three-dimensional crustal structure in the Southern Alps region of New Zealand from inversion of local earthquake and active source data, *J. Geophys. Res. Solid Earth*, *107*, doi:10.1029/2001JB000567. 3.4.1

Eberhart-Phillips, D., and A. J. Michael (1993), Three-dimensional velocity structure, seismicity, and fault structure in the Parkfield Region, Central California, *J. Geophys. Res.*, *98*, doi:10.1029/93JB01029. 3.4.1

Ekström, G., M. Nettles, and A. M. Dziewonski (2012), The global CMT project 2004-2010: Centroid-moment tensors for 13,017 earthquakes, *Phys. Earth Planet. Inter.*, *200-201*, doi:10.1016/j.pepi.2012.04.002. 3.1

Emre, Ö., T. Y. Duman, S. Özalp, F. Şaroğlu, Ş. Olgun, H. Elmacı, and T. Çan (2016), Active fault database of Turkey, *Bull. Earthquake Eng.*, doi:10.1007/s10518-016-0041-2. 3.1

England, P., G. Houseman, and J.-M. Nocquet (2016), Constraints from GPS measurements on the dynamics of deformation in Anatolia and the Aegean, *J. Geophys. Res. Solid Earth*, *121*, doi:10.1002/2016JB013382. 3.1

Farrell, K. (2017), Characterising the deep structure and seismic signature of an exhumed ductile shear zone. doctoral thesis. retrieved from: http://etheses.whiterose.ac.uk/id/eprint/17687. 3.4.2

Fichtner, A., E. Saygin, T. Taymaz, P. Cupillard, Y. Capdeville, and J. Trampert (2013), The deep structure of the North Anatolian Fault Zone, *Earth Planet. Sci. Lett.*, *373*, doi:10.1016/j.epsl.2013.04.027. 3.4.1

Flerit, F., R. Armijo, G. King, and B. Meyer (2004), The mechanical interaction between the propagating North Anatolian Fault and the back-arc extension in the Aegean, *Earth Planet. Sci. Lett.*, *224*, doi:10.1016/j.epsl.2004.05.028. 3.1

Gerbi, C., S. E. Johnson, D. Shulan, and K. Klepseis (2016), Influence of microscale weak zones on bulk strength, *Geochem. Geophys. Geosys.*, *17*, doi:10.1002/2016GC006406. 3.1

Hardebeck, D. L., A. J. Michael, and T. M. Brocher (2007), Seismic velocity structure and seismotectonics of the eastern San Francisco Bay region, California, *Bull. Seismol. Soc. Am.*, *97*, doi:10.1785/0120060032. 3.4.1

Herrmann, R. B. (2013), Computer Programs in Seismology: An Evolving Tool for Instruction and Research, *Seis. Res. Lettr.*, *84*, doi:10.1785/0220110096. 3.2.2, 3.2.4, 3.3.3

Hillers, G., M. Campillo, Y. Ben-Zion, and M. Landès (2013), Interaction of microseisms with crustal heterogeneity: A case study from the San Jacinto fault zone area, *Geochem. Geophys. Geosys.*, *14*, doi:10.1002/ggge.20140. 3.2.2

Hillers, G., P. Roux, M. Campillo, and Y. Ben-Zion (2016), Focal spot imaging based on zero lag cross-correlation amplitude fields: Application to dense array data at the San Jacinto fault zone, *J. Geophys. Res. Solid Earth*, *121*, doi:10.1002/2016JB013014. 3.2.2

Hussain, E., T. J. Wright, R. J. Walters, D. Bekaert, A. Hooper, and G. A. Houseman (2016), Geodetic observations of postseismic creep in the decade after the 1999 Izmit earthquake, Turkey: Implications for a shallow slip decit, *J. Geophys. Res. Solid Earth*, *121*, doi:10.1002/2015JB012737. 3.4.1

Kahraman, M., D. G. Cornwell, D. A. Thompson, S. Rost, G. A. Houseman, N. Türkelli, U. Teoman, S. Altuncu Poyraz, M. Utkucu, and L. Gülen (2015), Crustal-scale shear zones and heterogeneous structure beneath the North Anatolian Fault Zone, Turkey, revealed by a high-density seismometer array, *Earth Planet. Sci. Lett.*, *430*, doi:10.1016/j.epsl.2015.08.014. 3.1, 3.4.1

Karahan, A. E., H. Berckhemer, and B. Baier (2001), Crustal structure at the western end of the North Anatolian Fault Zone from deep seismic sounding, *Annali. Di. Geofisica*, *44*. 3.2.2

Kennett, B. L. N., M. S. Sambridge, and P. R. Williamson (1988), Subspace methods for large inverse problems with multiple parameter classes, *Geophys. J. Int.*, *94*, doi:10.1111/j.1365-246X.1988.tb05898.x. 3.2.3

Kern, H., and H. R. Wenk (1990), Fabricrelated velocity anisotropy and shear wave splitting in rocks from the Santa Rosa Mylonite Zone, California, *J. Geophys. Res. Solid Earth*, *95*, doi:10.1029/JB095iB07p11213. 3.4.2

Komazawa, M., H. Morikawa, K. Nakamura, J. Akamatsu, K. Nishimura, S. Sawada, A. Erken, and A. Onalp (2002), Bedrock structure in Adapazari, Turkey: a possible cause of severe damage by the 1999 Kocaeli earthquake, *Soil Dyn. Earthquake Eng.*, *22*, doi:10.1016/S0267-7261(02)00105-7. 3.4.1

Levshin, A. L., and M. H. Ritzwoller (2001), Automated Detection, Extraction, and Measurement of Regional Surface Waves, *Pure Appl. Geophys.*, *158*, doi:10.1007/PL00001233. 3.2.2

Lin, F. C., D. Li, R. W. Clayton, and D. Hollis (2013), High-resolution 3D shallow crustal structure in Long Beach, California: Application of ambient noise tomography on a dense seismic array, *Geophysics*, *78*, doi:10.1190/geo2012-0453.1. 3.1

Lobkis, O. I., and R. L. Weaver (2001), On the emergence of the Greens function in the correlations of a diffuse field, *J. Acoust. Soc. Am.*, *110*, doi:10.1121/1.1417528. 3.2.1

Mainprice, D., and A. Nicolas (1989), Development of shape and lattice preferred orientations: application to the seismic anisotropy of the lower crust, *J. Struct. Geol.*, *11*, doi:10.1016/01918141(89)900424. 3.4.2

Okay, A. I., A. M. C. Şengör, and N. Görür (1994), Kinematic history of the opening of the Black Sea and its effect on the surrounding regions, *Geology*, *22*, doi:10.1130/0091-7613(1994)022¡0267:KHOTOO¿2.3.CO;2. 3.3.1

Okay, A. L. (2008), Geology of Turkey: A Synopsis, *Anschnitt*, *21*. 3.1

Okay, A. L., and O. Tüysüz (1999), Tethyan sutures of northern Turkey, *Geological Society, London, Special Publications*, *156*, doi:10.1144/GSL.SP.1999.156.01.22. 3.1, 3.4.1, 3.4.1

Papaleo, E., D. G. Cornwell, and N. Rawlinson (2017), Seismic tomography of the North Anatolian Fault: New insights into structural heterogeneity along a continental strikeslip fault, *Geophys. Res. Lett.*, *44*, doi:10.1002/2017GL072726. 3.4.1

Poli, P., H. A. Pedersen, M. Campillo, and the POLENET/LAPNET Working Group (2012), Emergence of body waves from crosscorrelation of short period seismic noise, *Geophys. J. Int.*, *188*, doi:10.1111/j.1365246X.2011.05271.x. 3.2.1, 3.2.2

Rawlinson, N., and M. Sambridge (2003), Seismic traveltime tomography of the crust and lithosphere, *Adv. Geophys.*, *46*, doi:10.1016/S00652687(03)460020. 3.2.3

Rawlinson, N., and M. Sambridge (2005), The fast marching method: an effective tool for tomographics imaging and tracking multiple phases in complex layered media, *Explor. Geophys.*, *36*. 3.2.3

Reilinger, R. E., S. R. McClusky, M. B. Oral, R. W. King, M. N. Tosoz, A. A. Barka, I. Kinit, O. Lenk, and I. Sanli (1997), Global Positioning System measurements in the Arabia-Africa-Eurasia plate collision zone, *J. Geophys. Res.*, *102*, doi:10.1029/96JB0373. 3.1

Sambridge, M. S. (1999), Geophysical inversion with a neighbourhood algorithm-I.Searching a parameter space, *Geophys. J. Int.*, *138*, doi:10.1046/j.1365-246x.1999.00900.x. 3.2.4, 3.2.4

Sethian, J. A., and A. M. Popovici (1999), 3D traveltime computation using the fast marching method, *Geophysics*, *64*, doi:10.1190/1.1444558. 3.2.3

Shapiro, N. M., M. Campillo, L. STehly, and M. H. Ritzwoller (2005), High resolution surface wave tomography from ambient seismic noise, *Science*, *307*, doi:10.1126/science.1108339. 3.2.1

Sherrington, H. F., G. Zandt, and A. Frederiksen (2004), Crustal fabric in the Tibetan Plateau based on waveform inversions for seismic anisotropy parameters, *J. Geophys. Res. Solid Earth*, *109*, doi:10.1029/2002JB002345. 3.4.2

Smith, M. L., and A. F. Dahlen (1973), The azimuthal dependence of Love and Rayleigh wave propagation in a slightly anisotropic medium, *J. Geophys. Res.*, *78*, doi:10.1029/JB078i017p03321. 3.2.5, 3.3.6

Stein, R. S., A. A. Barka, and J. H. Dieterich (1997), Progressive failure on the North Anatolian fault since 1939 by earthquake stress triggering, *Geophys. J. Int.*, *128*, doi:10.1111/j.1365-246X.1997.tb05321.x. 3.1

Tank, S. B., Y. Honkura, Y. Ogawa, M. Matsushima, N. Oshiman, and M. K. Tunçer and C. Çelik and E. Tolak and A. M. Işıkara (2005), Magnetotelluric imaging of the fault rupture area of the 1999 zmit (Turkey) earthquake, *Phys. Earth Planet. Int.*, *150*, doi:10.1016/j.pepi.2004.08.033. 3.4.1

Tapponier, P., G. Peltzer, A. Y. Le Dain, R. Armijo, and P. R. Cobbold (1982), Propagation extrusion tectonics in Asia: New insights from experiments with plasticine, *Geology*, *10*, doi:10.1130/0091-7613(1982)10¡611:PETIAN¿2.0.CO;2. 3.1

Taylor, G., S. Rost, and G. Houseman (2016), Crustal imaging across the North Anatolian Fault Zone from the autocorrelation of ambient seismic noise, *Geophys. Res. Lett.*, *43*, doi:10.1002/2016GL067715. 3.2.2, 3.4.1

Thurber, C. H., H. Zhang, F. Waldhauser, J. Hardebeck, A. Michael, and D. Eberhart-Phillips (2006), Three-dimensional compressional wavespeed model, earthquake relocations, and focal mechanisms for the Parkfield, California, region, *Bull. Seismol. Soc. Am.*, *96*, doi:10.1785/0120050825. 3.4.1

USGS (2006), Shuttle Radar Topography Mission, *Global Land Cover Facility, University of Maryland*. 3.1

Villaseñor, A., Y. Yang, M. H. Ritzwoller, and J. Gallart (2007), Ambient noise surface wave tomography of the Iberian Peninsula: Implications for shallow seismic structure, *Geophys. Res. Lett.*, *34*, doi:10.1029/2007GL030164. 3.2.2

Wapenaar, K. (2004), Retrieving the Elastodynamic Green's Function of an Arbitrary Inhomogeneous Medium by Cross Correlation, *Phys. Rev. Lett.*, *93*, doi:10.1103/PhysRevLett.93.254301. 3.2.1

Warren, L. M., S. L. B. amd C. Berk Biryol, G. Zandt, A. A. Ozacar, and Y. Yang (2013), Crustal velocity structure of Central and Eastern Turkey from ambient noise tomography, *Geophys. J. Int.*, *194*, doi:10.1093/gji/ggt210. 3.2.2

Wathelet, M. (2008), An improved neighborhood algorithm: Parameter conditions and dynamic scaling, *Geophys. Res. Lett.*, *35*, doi:10.1029/2008GL033256. 3.2.4

Yılmaz, Y., Ş. C. Genç, E. Yiğitbaş, M. Bozcu, and K. Yılmaz (1995), Geological evolution of the late Mesozoic continental margin of Northwestern Anatolia, *Tectonophys.*, *243*, doi:10.1016/0040-1951(94)00196-G. 3.1, 3.3.5, 3.4.1, 3.5

Zheng, Y., W. Shen, L. Zhou, Y. Yang, Z. Xie, and M. H. Ritzwoller (2011), Crust and uppermost mantle beneath the North China Craton, northeastern China, and the Sea of Japan from ambient noise tomography, *J. Geophys. Res. Solid Earth*, *116*, doi:10.1029/2011JB008637. 3.2.2

Zigone, D., Y. Ben-Zion, M. Campillo, and P. Roux (2015), Seismic tomography of the Southern California plate boundary region from noise-based Rayleigh and Love waves, *Pure Appl. Geophys.*, *172*, doi:10.1007/s00024-014-0872-1. 3.1, 3.4.1

Chapter 4

P-wave reflectivity structure of the North Anatolian Fault from the auto-correlation of teleseismic coda waves

G. Taylor[1], S. Rost[1] and G. Houseman[1,2]

[1] *School of Earth and Environment, University of Leeds, Leeds, United Kingdom*
[2] *Now also at School of Geosciences, University of Sydney, 2006, NSW, Australia*

Abstract

Vertically travelling waves from distant earthquakes that reverberate within the crust and upper mantle can be used for seismic imaging through the use of auto-correlation methods. In this study we apply auto-correlation techniques to the P-wave coda of teleseismic earthquakes recorded at a dense array of seismometers in north-western Turkey in order to produce reflection images of the North Anatolian Fault Zone. We observe a strong reflection from the Moho, and potentially other reflectors within the crust and upper mantle. Our results indicate that the Moho is vertically offset over a narrow region (< 7 km) beneath the North Anatolian Fault, indicating that the fault penetrates the upper mantle as a narrow shear zone. The vertical offsets in the Moho associated with the northern branch of the North Anatolian Fault are located ~ 16 km to the north of the surface expression, showing that the northern branch dips to the north at an angle of $\sim 60° - 70°$. In addition, we detect a reduction in the amplitude of the Moho reflection beneath both the northern and southern branches of the North Anatolian Fault, which we interpret as the presence of serpentinite within the upper mantle beneath the fault.

4.1 Introduction

The seismic structure of active fault zones provides important information that is required to understand the processes that govern the accumulation of strain in the crust, and the seismic hazard associated with the earthquake cycle (*Bürgmann and Dresen*, 2008). A wide range of seismic imaging techniques have been employed in fault zone environments to better understand fault zone structure and strain accumulation.

Seismic tomography is commonly used to construct 3-D models of seismic velocity (e.g., *Thurber et al.*, 2006, *Zigone et al.*, 2015, *Papaleo et al.*, 2017, *Eberhart-Phillips and Bannister*, 2002) which in turn provides information on physical properties of the fault zone such as lithology, material strength and the presence of potential fluids. However, seismic tomography often lacks resolution, particularly vertical resolution, and the ability to image narrow structures such as faults into the lower crust and upper mantle.

On the other hand, receiver function studies (e.g. *Zhu* (2000), *Zhang et al.* (2014), *Wilson et al.* (2004), *Kahraman et al.* (2015)) can provide information on the lateral continuity of crustal structures that may be cut by the fault. Specifically, receiver functions allow us to locate discontinuities in seismic properties by observing P-to-S conversions from interfaces within the Earth. Lateral discontinuities in these material interfaces can indicate the presence of a fault.

Recent advances in the field of seismic interferometry have opened up the possibility of obtaining information on P and/or S-wave reflectivity beneath a single seismometer. The principle of retrieving reflections by exploiting the interference of seismic waves is closely related to that of receiver functions (*Galetti and Curtis*, 2012). A study by *Claerbout* (1968) showed that it is possible to simulate the zero-offset reflection response of a 1-D layered medium by simply autocorrelating seismic records of an incident wave and the subsequent reverberations contained within the 'coda' that follows the first arrival. This theory has since been shown to hold true for 3-D media, whereby records of random fluctuations (such as the ambient seismic noise field) can be correlated and summed in order to retrieve the impulse response of a medium (*Wapenaar*, 2004, *Wapenaar and Fokkema*, 2006, *Snieder et al.*, 2007).

One advantage of the interferometric approach is that any seismic source can be used to excite the waves. The initial theoretical work of *Claerbout* (1968) has been put into practice to obtain the reflection response beneath seismometers through the autocorrelation of both ambient seismic noise (*Taylor et al.*, 2016, *Tibuleac and von Seggern*, 2012, *Gorbatov et al.*, 2013, *Kennett*, 2015, *Kennett et al.*, 2015, *Saygin et al.*, 2017, *Oren and Nowack*, 2017, *Becker and Knapmeyer-Endrun*, 2017, *Heath et al.*, 2018) and the P-wave coda of teleseismic earthquakes (*Ruigrok and Wapenaar*, 2012, *Sun and Kennett*, 2016, 2017, *Pham and Tkalčić*, 2017). In this paper, we will construct seismic reflection profiles of the crustal and upper mantle structure of the North

Anatolian Fault Zone in Turkey. These images will be constructed by autocorrelating the P-wave coda of teleseismic earthquakes recorded at a dense, temporary array deployed in north-west Turkey.

The North Anatolian Fault is a major right-lateral strike-slip fault located in northern Turkey that forms the boundary between the Anatolian region and the continent of Eurasia. Although northern Anatolia initially formed in a convergent environment during the subduction of the Neo-Tethys Ocean in the late Cretaceous (*Okay et al.*, 1994, *Okay*, 2008, *Yılmaz et al.*, 1995), the current motion along the North Anatolian Fault is sustained by a combination of the roll-back of the Hellenic trench at its south-western end, and the northwards motion of the Arabian Plateau to the east. This tectonic environment has formed a gradient of lithospheric gravitational potential energy across Anatolia, and the result is an anti-clockwise rotation and extension of the Anatolian region with respect to Eurasia (*England et al.*, 2016). Since the early Miocene, the majority of the relative motion between Anatolia and Eurasia has been accommodated along the North Anatolian Fault Zone (*Şengör et al.*, 2005).

The North Anatolian Fault shows a distinct westward propagating sequence of large earthquakes ($M_w > 7.0$) that began at Erzincan in 1939 (*Stein et al.*, 1997). The most recent large earthquakes in this sequence occurred on the western section of the fault in 1999 at İzmit ($M_w = 7.6$) and Düzce ($M_w = 7.2$) (*Barka et al.*, 2002). Such earthquake sequences are likely a recurring feature of the North Anatolian Fault (*Ambraseys*, 1970), and are characterised by progressive failure in which the Coulomb stress transfer following one earthquake increases the stress on an adjacent fault segment (*Stein et al.*, 1997).

The 1999 İzmit and Düzce earthquakes occurred in an area referred to as the Izmit-Adapazari region, located about 100 km east of Istanbul. In the Izmit-Adapazari region, the North Anatolian Fault splits into two main branches, a northern branch and a southern branch. The majority of the large earthquakes have occurred along these two segments. The İzmit earthquake ruptured the full length of the northern branch between İzmit and the town of Akyazi (*Barka et al.*, 2002). The southern branch also ruptured in at least two large earthquakes in the the 19th century (*Ambraseys and Finkel*, 1991). On the other hand, micro-seismicity in the region is quite diffuse, and not very well localised onto the major branches of the North Anatolian Fault (*Altuncu Poyraz et al.*, 2015).

The formation of the North Anatolian Fault in the Izmit-Adapazari region appears to have exploited pre-existing structural boundaries between three major tectonic units (Fig. 4.1). To the north of the fault zone lies the Istanbul Zone (*Okay*, 2008), a continental fragment of Eurasia that was likely rifted off of the Odessa Shelf by the opening of the Black Sea during the Cretaceous (*Akbayram et al.*, 2013). Following the closure of of the Neo-Tethys Ocean, the Istanbul Zone was sutured to the Sakarya Terrane, which lies to the south of the present day North Anatolian Fault. The Sakarya

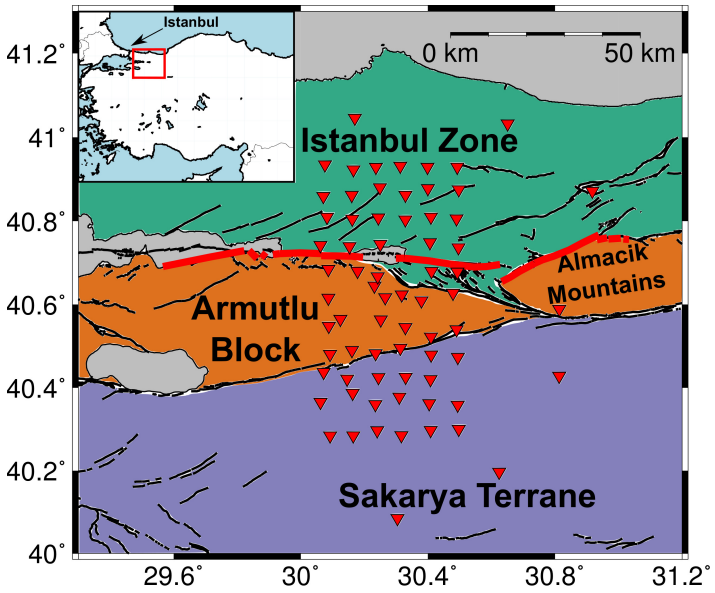

Figure 4.1: Overview of the Izmit-Adapazari region. Inverted red triangles are stations of the DANA array. Mapped faults are indicated by the thick black lines (*Emre et al.*, 2016). The major tectonic units separated by the fault zone are annotated in black and colour coded as: Istanbul Zone = Green, Armutlu-Almacik Block = Orange and Sakarya Terrane = Purple. The rupture zones of the 1999 İzmit and Düzce earthquakes are shown as a red line. Top left insert: map of Turkey, with the red box indicating the Izmit-Adapazari region shown in the main figure, and the location of the city of Istanbul.

Terrane is a sedimentary accretionary complex that overlies a paleozoic metamorphic basement (*Yılmaz et al.*, 1995). Between the two branches of the North Anatolian Fault is a region of high topography known as the Armutlu-Almacik Block. The Armutlu-Almacik Block is primarily composed of metamorphosed sediments, though their age and history are generally poorly understood (*Okay and Tüysüz*, 1999). The Armutlu-Almacik Block appears to be a relatively rigid, non-deforming, area. The rupture zones of all major historical earthquakes propagated around the edges of the block (*Barka et al.*, 2002). Despite this, the Armutlu section has been separated from the Almacik Block by motion along the North Anatolian Fault, and translated towards the west (*Karimi et al.*, 2014, *Koulakov et al.*, 2010, *Akbayram et al.*, 2016).

The University of Leeds and Turkish partners from Boğaziçi University Kandilli Observatory and Earthquake Research Institute and Sakarya University deployed a dense network of seismometers across the rupture zone of the 1999 İzmit earthquake between May 2012 and October 2013. This array, known as the Dense Array for Northern Anatolia (DANA) (*DANA*, 2012) consisted of a rectangular network of 66 three-component seismometers that covered an area of the Izmit-Adapazari region approximately 70 km by 35 km. The average station spacing was 7 km. This main array was supplemented by 7 stations, located in a semi-circular pattern surrounding the rectangular grid to the east. The locations of the stations of the DANA array are shown in Fig. 4.1.

In this study, we autocorrelate the P-wave coda of teleseismic earthquakes recorded

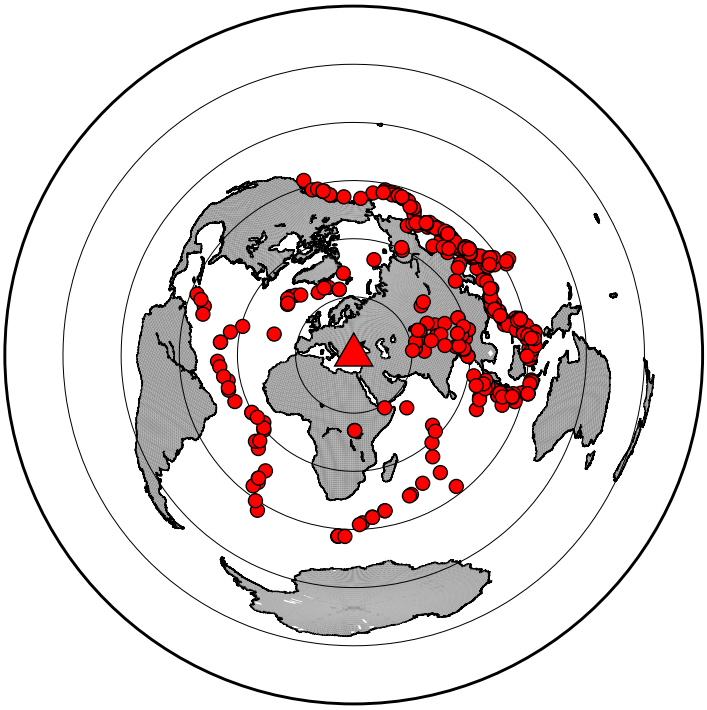

Figure 4.2: Locations of the 414 earthquakes used for the auto-correlation function data set. The location of the DANA network is the red triangle. The red circles represent the locations of earthquakes that produced at least one accepted auto-correlation function.

at the DANA array in order to construct a reflection image of the crustal and upper mantle structure of the Izmit-Adapazari region. We observe clear reflections from the Moho (*PPmp*) and other discontinuities in the crust and upper mantle and relate the resolved structure to the known geological structure and the North Anatolian Fault Zone. Vertical offsets in structures such as the Moho beneath fault zones have been interpreted as evidence for narrow shear zones that cut through the crust and penetrate the upper mantle (*Zhu*, 2000, *Zhang et al.*, 2014). We will compare our results to those of *Taylor et al.* (2016) and *Kahraman et al.* (2015) who found evidence for such vertical offsets and a reduced amplitude of the Moho reflected phase beneath the northern branch of the North Anatolian Fault.

4.2 Data and Methods

To produce a seismic reflection image of the structure beneath the Izmit-Adapazari region, we calculate auto-correlation functions from recordings of teleseismic earthquakes at the DANA array. We utilise seismograms of earthquakes that occurred between 5th May 2012 and 1st October 2015, with a minimum epicentral distance of 30° and a maximum distance of 95°. These epicentral distance constraints were used in order to avoid waveform complications that could arise from triplications, or the P-wave diffraction around the outer core. The minimum magnitude is set to $M_w = 5.0$ and the maximum

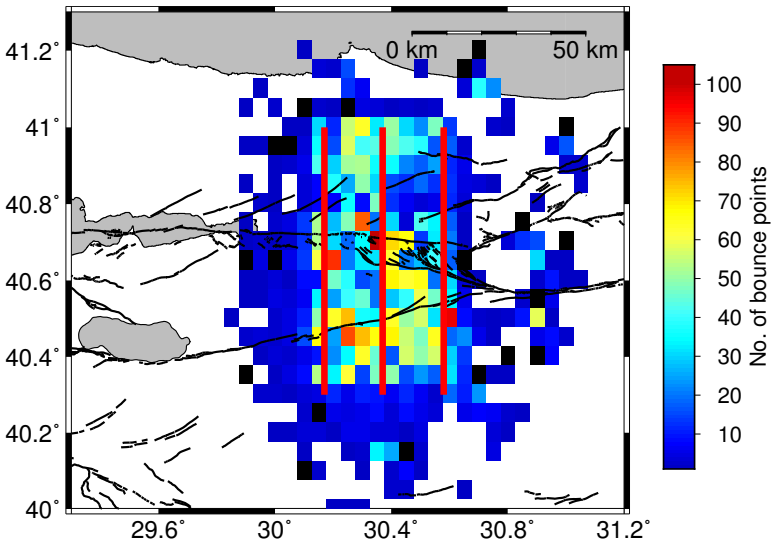

Figure 4.3: Common Moho reflection point bins for the auto-correlation functions calculated across the North Anatolian Fault Zone. The bins are colour coded according to the number of reflection points that fall within the bin. Red colours indicate more auto-correlation functions, blue colours indicate fewer. The thick red lines represent the location of the north-south reflection profiles shown in Fig. 4.5 and Fig. 4.6. Thick black lines show the mapped fault in the Izmit-Adapazari region (*Emre et al.*, 2016).

depth of the hypocentre is 600 km.

We resample the vertical component waveforms to 20 Hz, and apply an initial band-pass filter between 0.1 and 5.0 Hz. We then calculate the signal-to-noise ratio by comparing the root-mean-square (RMS) amplitude of a 40 s long time window centred on the theoretical arrival time of the direct P-wave (as calculated using the model iasp91 (*Kennett and Engdahl*, 1991)) to a 100 s long noise window that precedes the P-wave. Earthquake waveforms with signal-to-noise ratio > 2 are accepted. From an initial data set of 1112 earthquakes, we accept a total of 414. The locations of accepted earthquakes are shown in Fig. 4.2. In order to exclude the complex S-wave arrivals from our analysis, the accepted waveforms are cut to include only the P-wave coda, defined here as a time window from 10 s prior to the theoretical P-wave arrival time, to 590 s after.

Prior to correlation, we apply a band-pass filter between 0.1 and 0.5 Hz. This filter band was chosen as it represents the dominant frequencies of energy within teleseismic P-wave coda (*Paulssen et al.*, 1992). As we are only autocorrelating the records, no correction for the instrument response is required. The auto-correlation function of each record is calculated by multiplying the Fourier transform of the signal with itself, and transforming back to the time domain. Due to the inherent symmetry of the auto-correlation function, we analyse only the positive time lags. The central peak of the autocorrelation function is suppressed by a cosine taper that is applied to the first 5 s of the trace. The result of this process is 6221 auto-correlation functions which represents our dataset for this study.

We calculate the theoretical reflection point on the top of the Moho for the free surface reverberation leg for each accepted earthquake using iasp91 (*Kennett and Engdahl*, 1991). We then group the auto-correlation functions together into common reflection point bins 0f 0.05 x 0.05 deg in size. These bins and the corresponding number of auto-correlation functions in each bin are shown in Fig. 4.3. Due to the fact that the total move-out of the Moho reverberation *PPmp* is very small (<1 s) over the slowness range of teleseismic earthquakes (Fig. 4.4), no migration or move-out correction is applied. The reflection point on the Moho is typically located 0.1 – 0.2 degrees away from the receiver. We then stack all auto-correlation functions contained within each bin. For the stacking process, we employ the phase-weighted stacking technique of *Schimmel and Paulssen* (1997). The phase-weighted stack is defined as:

$$g(t) = \frac{1}{N}\sum_{j=1}^{N} s_j(t) \left| \frac{1}{N}\sum_{k=1}^{N} \exp[i\phi_k(t)] \right|^{\nu}, \tag{4.1}$$

where N is the number of auto-correlation functions, $s_j(t)$ is the time domain representation of the j^{th} auto-correlation function and $\phi_k(t)$ is the instantaneous phase of the kth record. i is the imaginary unit and ν is a weighting parameter that we set equal to 1. Increasing the parameter ν increases the weighting of in-phase signals in the final stack. The phase-weighted stack enhances low amplitude yet coherent energy contained within seismic records (*Schimmel and Paulssen*, 1997), and we employ it in this study in order to improve detection of potentially low amplitude arrivals in the P-wave coda such as *PPmp*.

We also calculate synthetic reflectivity images of the crust and upper mantle by computing the auto-correlation functions of the P-wave coda in synthetic earthquake waveforms. This allows us to compare our results to the theoretical prediction and aids in the identification and characterisation of the different seismic arrivals that may be present in the real data. To produce this image, synthetic vertical component earthquake waveforms with a maximum period of 2.0 s were calculated for each epicentral distance between 30° and 90°, with a separation of 1°. The 1D model used to produce the synthetics was iasp91 (*Kennett and Engdahl*, 1991). The synthetics were calculated using the IRIS Syngine resource for AxiSEM (*Nissen-Meyer et al.*, 2014, *Krischer et al.*, 2017, *IRIS DMC*, 2015). We then process the synthetic P-wave coda in exactly the same manner as described for the real data. The synthetic autocorrelations are shown as a function of the slowness of the incoming P-wave in the right panel of Fig. 4.4.

4.3 Results

The autocorrelations are plotted as a function of slowness of the direct P-wave in Fig. 4.4. The left hand panel in Fig. 4.4 shows our set of pre-stack auto-correlation functions

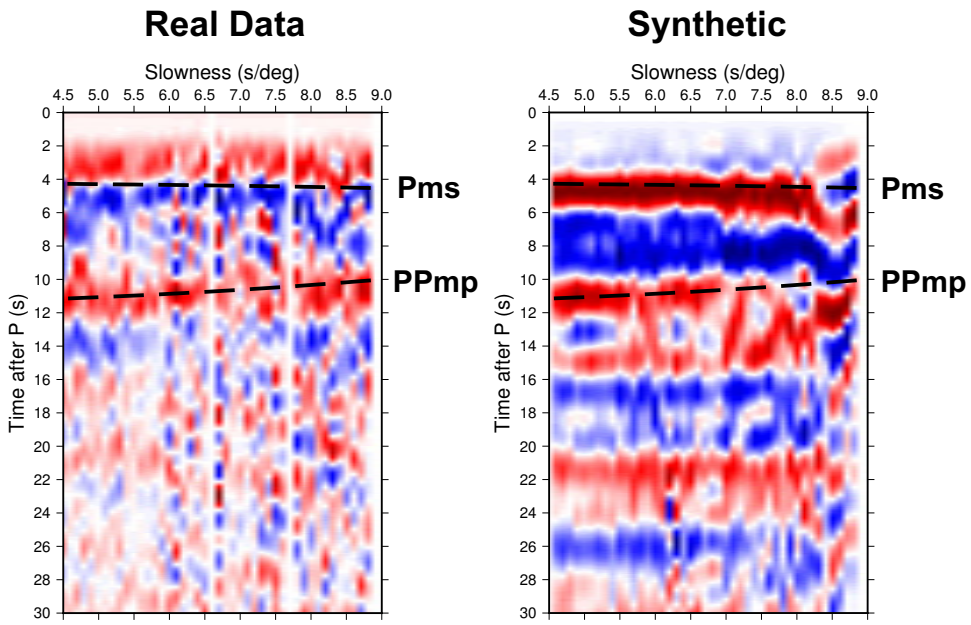

Figure 4.4: Left panel: Teleseismic autocorrelations as a function of slowness of the incoming direct P-wave. Red indicates positive P-wave reflectivity and blue indicates negative P-wave reflectivity. The theoretical move-out of a P-to-S conversion at the Moho, *Pms*, and the Moho free surface reverberation *PPmp* are shown as dashed black lines. Right panel: Synthetic auto-correlation functions with respect to slowness. The synthetic auto-correlation functions were calculated using the model iasp91 (*Kennett and Engdahl*, 1991)

displayed as a function of slowness of the direct P-wave, whilst the right hand panel shows the synthetic data set. In Fig. 4.4, red indicates positively polarised P-wave reflectivity. The P-to-S conversion from the Moho (*Pms*) is clear in the synthetic data, arriving at $\sim$ 4 s after the direct P-wave. The occurrence of *Pms* is not obvious in our data set, however. Both the real and synthetic data set contain a further arrival between 10 s and 12 s. This arrival has a move-out consistent with the free surface Moho reverberation *PPmp*. This *PPmp* arrival is coherent throughout the teleseismic slowness range in the real data set, but is more complex in the synthetics at slownesses higher than $\sim$ 7 s/deg. Above 8 s/deg ($<$ 45 degrees epicentral distance), the synthetic arrival times of both *Pms* and *PPmp* become highly variable, likely due to triplications occurring at these slownesses. The real data set does not contain this complexity, which may be attributable to variations in parameters such as Moho depth and seismic velocity that obscure the effect of triplications.

There is evidence of later arrivals in the observed data set, particularly at $\sim$ 16 s and $\sim$ 21 s. These arrival times are highly variable. The 21 s arrival is also prominent in the synthetic data set, and the lack of move-out as a function of slowness would suggest that it is likely to be a multiple of an earlier arrival (possibly *Pms*). There is positive energy present in the synthetic data at $\sim$ 18 s arrival time that could have a substantial move-out, but its presence is highly variable with slowness.

Fig. 4.5 show reflection profiles produced from the binned and stacked auto-correlation

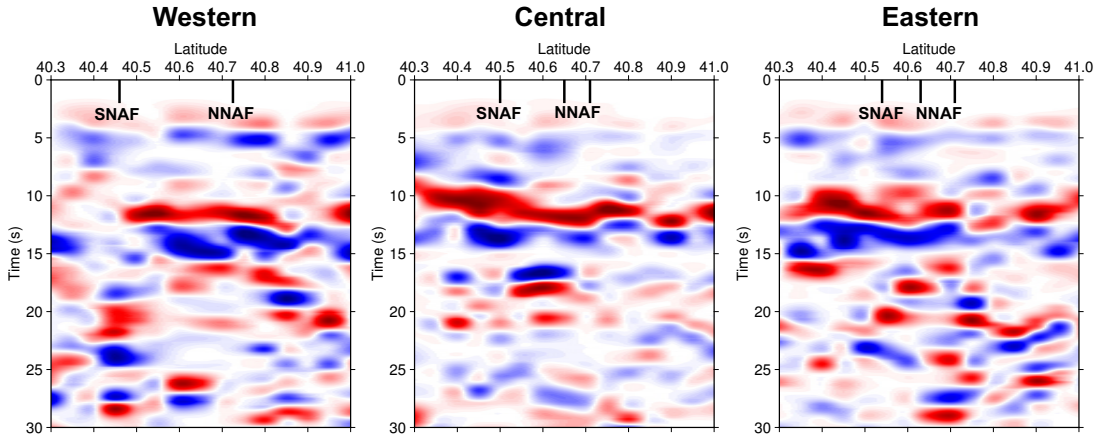

Figure 4.5: Reflection profiles across the North Anatolian Fault Zone constructed from the auto-correlation of teleseismic coda waves. The columns contain the profiles of the western, central and eastern profiles that are indicated as thick red lines in Fig. 4.3. Red colours indicate positive reflectivity, blue colours show negative reflectivity. The solid black lines indicate the position of the surface traces of the northern (NNAF) and southern (SNAF) branches of the North Anatolian Fault.

functions in the western, central and eastern parts of the Izmit-Adapazari region. The exact location of these profiles is shown in Fig. 4.3. The most prominent feature of the images is a coherent, positive reflection that arrives at $\sim$ 11 s. This arrival is clear in all of the panels and is almost certainly the reverberation from the Moho, *PPmp*. In the central and eastern profiles, the Moho reflection arrives $\sim$ 3 s earlier to the south of the southern branch of the North Anatolian Fault, possibly indicating a shallowing of the Moho beneath the Sakarya Terrane.

In the western profile, the Moho appears to terminate directly below the surface trace of the southern branch at roughly 40.45° latitude. The central and eastern profiles show two sharp vertical offsets in the Moho north of 40.7° latitude, which could be associated with the north branch of the North Anatolian Fault if it is dipping towards the north. The interpreted structure of the fault at depth is shown in Fig. 4.6. The amplitude of the Moho reflection appears to fade in areas where the North Anatolian Fault is interpreted to penetrate into the upper mantle (*Kahraman et al.*, 2015, *Taylor et al.*, 2016, *Papaleo et al.*, 2017, 2018), particularly in the western profile (Fig. 4.6).

There is a prominent negatively polarised (blue) arrival that appears beneath the Moho reflection in particular. Negative polarity in these reflection sections should represent a negative reflection coefficient, but it is also possible the negative arrival beneath the Moho is a side lobe of the main (positive) pulse generated by the autocorrelation process. The presence of the negative arrivals following the positive energy in the synthetic auto-correlation functions in Fig. 4.4 would support this interpretation. Wide-angle seismic reflection experiments targeting the S-to-P reverberations (*SsPmp*) from the Moho also observe a similar waveform (*Tseng et al.*, 2009, *Chen et al.*, 2013). There is a further negatively polarised arrival at 5 s in all of the profiles.

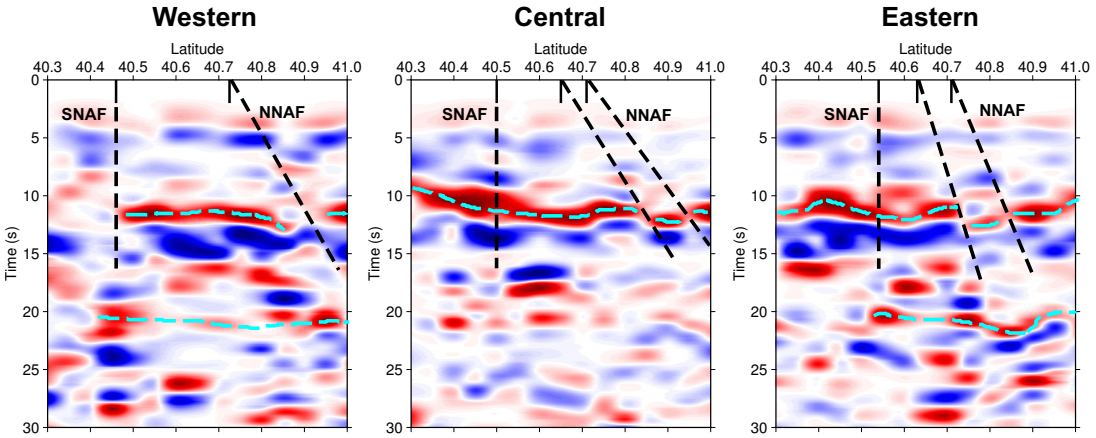

Figure 4.6: Interpreted reflection profiles from Fig. 4.5. The solid black lines indicate the position of the surface traces of the northern (NNAF) and southern (SNAF) branches of the North Anatolian Fault. The dashed black lines show the inferred depth extent of the fault traces of the northern and southern branches of the North Anatolian Fault. The dashed cyan lines are the locations of horizontal reflections, including the Moho (11 s) and the further energy arriving at $\sim$ 20 s.

There is more positively polarised energy arriving at approximately 20 s. This energy is smaller in amplitude than the Moho, but is present in all three profiles in Fig. 4.5. This reflected arrival could represent a deeper discontinuity within the upper mantle, though its arrival time is similar to a suspected multiple in the synthetic data set (Fig. 4.4).

4.4 Discussion

Our interpretations of the reflection profiles in Fig. 4.5 are shown in Fig. 4.6. We observe a clear reflection from the Moho in all profiles Fig. 4.5. In the central and eastern profile the Moho reflection arrives earlier towards the south. This could imply that the Moho dips towards the north, but could also be the result of lateral variations in seismic velocity in the crust that are not accounted for in the unmigrated images. If we assume a crustal P-wave velocity of 6.3 km/s for a Moho reflection that arrives at $\sim$ 12 s, a 33% increase in the average crustal P-wave velocity to 8.4 km/s would be required to explain the average travel time variation of $\sim$ 3 s that we observe between 40.3°N and 40.6°N in the central profile of Fig. 4.5. Receiver function analysis by *Kahraman et al.* (2015) observed a Moho that dipped in the opposite direction, towards the south. The Moho reflection generally arrives between 10 s and 12 s after the direct P-wave, which matches well with the observations of *Taylor et al.* (2016), who also observed the Moho reflection arriving at $\sim$ 12 s in their autocorrelations of ambient seismic noise using the DANA data set.

The Moho reflection is generally coherent throughout the Sakarya Terrane, Armutlu Block and Istanbul Zone. One exception to this is the reduced amplitude Moho reflec-

tion within the Sakarya Terrane in the western profile, where it appears to terminate directly beneath the southern branch of the North Anatolian Fault. This amplitude reduction could be due to a lack of data coverage, although this is unlikely as it is clear from Fig. 4.3 that the southern end of the western profile consists of common reflection point bins that contain 50+ auto-correlation functions which is generally sufficient to produce a visible Moho reflection elsewhere in the profile. North-south trending receiver function profiles calculated by *Kahraman et al.* (2015) through the Izmit-Adapazari region also noted a general reduction in the amplitude of the P-to-S conversion from the Moho towards the west, though the arrival is still visible.

Taylor et al. (2016) also observed that the Moho reflection terminated at the southern branch of the North Anatolian Fault using auto-correlation functions calculated from ambient seismic noise. These observations indicate that P-wave reflectivity of the Moho is greatly reduced within the Sakarya Terrane, whilst the amplitude of the P-to-S conversion is not drastically decreased. Previous studies have suggested that the serpentinisation of upper mantle peridotite due to the introduction of fluids that percolate down through the fault plane may be the cause of reduced Moho reflectivity in the vicinity of fault zones (*Hetényi et al.*, 2015, *Taylor et al.*, 2016). The serpentinisation of peridotite is known to significantly reduce both the P-wave velocity and density of the rock, even to the point where it is seismically indistinguishable from crustal rocks (*Birch*, 1960, *Christensen*, 1966, 2004).

Vertical offsets in the Moho beneath major continental faults are a common observation (*Weber et al.*, 2004, *Zhang et al.*, 2014, *Zhu*, 2000), and are particularly common beneath mature faults that have accumulated a large amount of offset, such as the San Andreas Fault and the Dead Sea Transform. The presence of these vertical offsets implies a degree of strain localisation in the lower crust and upper mantle, a region that is normally assumed to undergo diffuse deformation due to the presence of pervasive seismic anisotropy (*Bürgmann and Dresen*, 2008). Receiver function images of the Marlborough Fault Zone in New Zealand created by *Wilson et al.* (2004) show that whilst there is a change in depth beneath the fault, the Moho appears to dip gently and is not sharply offset. Vertical offsets in the Moho associated with the northern branch of the North Anatolian Fault were also observed by *Kahraman et al.* (2015) and *Taylor et al.* (2016).

The location of vertical offsets in the Moho in Fig. 4.5 suggests that the northern branch of the North Anatolian Fault is dipping $\sim 60^\circ - 70^\circ$ towards the north, whilst the southern branch appears to cut vertically through the crust. The dip of the northern branch seems to become steeper in the eastern profile (Fig. 4.5). *Kahraman et al.* (2015) also observed the fault plane of the northern branch dipping towards the north at $\sim 65^\circ$. A possible explanation of the northward dip of the northern branch of the North Anatolian Fault might be found in the fact that the formation of the fault in the Izmit-Adapazari region exploited the pre-existing Intra-Pontide Suture (*Okay*,

2008, *Fichtner et al.*, 2013, *Kahraman et al.*, 2015). The Intra-Pontide Suture marks the boundary between the Istanbul Zone and Sakarya Terrane, which collided during the Upper Cretaceous (66 – 100 Ma) (*Yılmaz et al.*, 1995). During this collision, the Istanbul Zone was thrust on top of the Sakarya Terrane (*Yılmaz et al.*, 1995). The present day North Anatolian Fault may have reactivated these ancient thrust faults with strike-slip motion since its formation in the middle Miocene ($\sim$ 13 Ma).

The fact that we observe coherent arrivals in our auto-correlation function contrasts with the observations of *Gorbatov et al.* (2013), *Kennett et al.* (2015) and *Kennett* (2015). In these studies the authors interpet a reduction in the amplitude of the auto-correlation functions as a proxy for the base of the crust, rather than searching for a coherent reflection from the Moho. This difference in the character of the reflectivity profiles may be the result of the frequency band employed. The auto-correlation functions in Fig. 4.5 contain a maximum frequency of 0.5 Hz, whereas *Gorbatov et al.* (2013), *Kennett et al.* (2015) and *Kennett* (2015) include frequencies up to 4 Hz. The phase-weighted stacking (*Schimmel and Paulssen*, 1997) employed in our study also likely enhances low amplitude yet coherent reflections contained within the P-wave coda.

The reflection profiles in Fig. 4.5 have higher resolution and contain less incoherent noise than the profiles produced by *Taylor et al.* (2016), who auto-correlated ambient noise recordings from the DANA array. The improvement is likely attributable to the higher amplitude of the *PPmp* phase in the coda of teleseismic earthquakes when compared to ambient noise.

4.5 Conclusions

We constructed P-wave reflectivity profiles of the crustal and upper mantle structure of the North Anatolian Fault Zone in the Izmit-Adapazari region by auto-correlating the coda of teleseismic earthquakes recorded at a dense array of seismometers. In our reflection images, we identify coherent reflections, particularly those from the Moho, which is produced by the correlation between the direct P-wave and the free surface reverberation to the Moho, *PPmp*. Our reflection profiles are comparable to previous crustal imaging studies by *Kahraman et al.* (2015) and *Taylor et al.* (2016), and show a reduction in the amplitude of the Moho reflection to the south of the North Anatolian Fault, and vertical offsets in the Moho likely associated with the northern branch of the fault zone. We interpret that these vertical offsets indicate that deformation associated with both branches of the North Anatolian Fault has penetrated to at least the Moho in the form of a narrow shear zone. These observations are similar to those of other continental fault zones, including the San Andreas Fault (*Zhu*, 2000), the Tibetan Plateau (*Zhang et al.*, 2014) and the Dead Sea Transform (*Weber et al.*, 2004). Additionally, our results indicate that the northern branch of the North Anatolian Fault

dips steeply towards the north in the Izmit-Adapazari region, and this may be the result of ancient thrust faults being reactivated by the more recent strike-slip motion that has characterised the North Anatolian Fault since the Miocene ($\sim$ 13 Ma). We have shown that it is possible to construct high resolution seismic images of the crust and upper mantle by auto-correlating the coda of teleseismic earthquakes recorded at an array of seismometers. Our approach gives an independent estimate of P-wave reflectivity that could be used to complement other seismic imaging techniques, such as seismic tomography and receiver functions.

Acknowledgments

G.T. is supported by the LeedsYork Doctoral Training Partnership of the Natural Environment Research Council (NERC), UK. The DANA array was part of the Faultlab project, a collaborative effort by the University of Leeds, Kandilli Observatory and Earthquake Research Institute, and Sakarya University. Major funding was provided by the UK NERC under grant NE/I028017/1. Equipment was provided and supported by the NERC Geophysical Equipment Facility (SEISUK) Loan 947. The DANA data set is freely available for download at the IRIS Data Management Centre under network code YH (2012 – 2013).

References

Akbayram, K., A. L. Okay, and M. Satır (2013), Early Cretaceous closure of the Intra-Pontide Ocean in western Pontides (northwestern Turkey), *J. Geodyn.*, *65*, doi:10.1016/j.jog.2012.05.003. 4.1

Akbayram, K., C. C. Sorlien, and A. L. Okay (2016), Evidence for a minimum 52 ± 1 km of total offset along the northern branch of the North Anatolian Fault in northwest Turkey, *Tectonophys.*, *668*, doi:10.1016/j.tecto.2015.11.026. 4.1

Altuncu Poyraz, S., M. U. Teoman, N. Türkelli, M. Kahraman, D. Cambaz, A. Mutlu, S. Rost, G. A. Houseman, D. A. Thompson, D. Cornwell, M. Utkucu, and L. Gülen (2015), New constraints on micro-seismicity and stress state in the western part of the North Anatolian Fault Zone: Observations from a dense seismic array, *Tectonophys.*, *656*, doi:10.1016/j.tecto.2014.03.015. 4.1

Ambraseys, N. N. (1970), Some characteristic features of the Anatolian fault zone, *Tectonophys.*, *9*, doi:10.1016/0040-1951(70)90014-4. 4.1

Ambraseys, N. N., and C. F. Finkel (1991), Long-term seismicity of Istanbul and of the Marmara Sea region, *Terra Nova*, *3*, doi:10.1111/j.1365-3121.1991.tb00188.x. 4.1

Barka, A., H. S. Akyüz, E. Altunel, G. Sunel, Z. Çakir, A. Dikbas, B. Yerli, R. Armijo, B. Meyer, J. B. de Chabalier, T. Rockwell, J. Dolan, R. Hartleb, T. Dawson, S. Christofferson, A. Tucker, T. Fumal, R. Langridge, R. Stenner, W. Lettis, J. Bachhuber, and W. Page (2002), The Surface Rupture and Slip Distribution of the 17 August 1999 Izmit Earthquake (M 7.4), North Anatolian Fault, *Bull. Seismol. Soc. Am.*, *92*, doi:10.1785/0120000841. 4.1

Becker, G., and B. Knapmeyer-Endrun (2017), Crustal thickness across the Trans-European Suture Zone from ambient noise autocorrelations, *Geophys. J. Int.*, *212*, doi:10.1093/gji/ggx485. 4.1

Birch, F. (1960), The velocity of compressional waves in rocks to 10 kilobars, *J. Geophys. Res*, *65*, doi:10.1029/JZ066i007p02199. 4.4

Bürgmann, R., and G. Dresen (2008), Rheology of the lower crust and upper mantle: Evidence from rock mechanics, geodesy, and field observations, *Annu. Rev. Earth Planet. Sci.*, *36*, doi:10.1146/annurev.earth.36.031207.124326. 4.1, 4.4

Chen, W. P., C. Q. Yu, T. L. Tseng, Z. Yang, C. Y. Wang, J. Ning, and T. Leonard (2013), Moho, seismogenesis, and rheology of the lithosphere, *Tectonophys.*, *609*, doi:10.1016/j.tecto.2012.12.019. 4.3

Christensen, N. I. (1966), Elasticity of ultrabasic rocks, *J. Geophys. Res*, *71*, doi:10.1029/JZ071i024p05921. 4.4

Christensen, N. I. (2004), Serpentinites, Peridotites, and Seismology, *Int. Geol. Rev.*, *46*, doi:10.2747/0020-6814.46.9.795. 4.4

Claerbout, J. F. (1968), Synthesis of a layered medium from its acoustic transmission response, *Geophysics*, *33*, doi:10.1190/1.1439927. 4.1

Şengör, A. M. C., O. Tüysüz, C. İmren, M. Sakınç, H. Eyidoğan, N. Görür, X. L. Pichon, and C. Rangin (2005), The North Anatolian Fault: A New Look, *Annu. Rev. Earth Planet. Sci.*, *33*, doi:10.1146/annurev.earth.32.101802.120415. 4.1

DANA (2012), Dense Array for Northern Anatolia, *Int. Fed. of Digital Seismograph Networks, Other/Seismic Network, Seattle, Wash.*, doi:10.7914/SN/YH_2012. 4.1

Eberhart-Phillips, D., and S. Bannister (2002), Three-dimensional crustal structure in the Southern Alps region of New Zealand from inversion of local earthquake and active source data, *J. Geophys. Res. Solid Earth*, *107*, doi:10.1029/2001JB000567. 4.1

Emre, Ö., T. Y. Duman, S. Özalp, F. Şaroğlu, Ş. Olgun, H. Elmacı, and T. Çan (2016), Active fault database of Turkey, *Bull. Earthquake Eng.*, doi:10.1007/s10518-016-0041-2. 4.1, 4.3

England, P., G. Houseman, and J.-M. Nocquet (2016), Constraints from GPS measurements on the dynamics of deformation in Anatolia and the Aegean, *J. Geophys. Res. Solid Earth*, *121*, doi:10.1002/2016JB013382. 4.1

Fichtner, A., E. Saygin, T. Taymaz, P. Cupillard, Y. Capdeville, and J. Trampert (2013), The deep structure of the North Anatolian Fault Zone, *Earth Planet. Sci. Lett.*, *373*, doi:10.1016/j.epsl.2013.04.027. 4.4

Galetti, E., and A. Curtis (2012), Generalised receiver functions and seismic interferometry, *Tectonophys.*, *532-535*, doi:10.1016/j.tecto.2011.12.004. 4.1

Gorbatov, A., E. Saygin, and B. L. N. Kennett (2013), Crustal properties from seismic station autocorrelograms, *Geophys. J. Int.*, *192*, doi:10.1093/gji/ggs064. 4.1, 4.4

Heath, B. A., E. E. E. Hooft, and D. R. Toomey (2018), Autocorrelation of the Seismic Wavefield at Newberry Volcano: Reflections From the Magmatic and Geothermal Systems, *Geophys. Res. Lett.*, *45*, doi:10.1002/2017GL076706. 4.1

Hetényi, G., Y. Ren, B. Dando, G. W. Stuart, E. Hegedüs, A. C. Kovács, and G. A. Houseman (2015), Crustal structure of the Pannonian Basin: The AlCaPa and Tisza Terrains and the Mid-Hungarian Zone, *Tectonophys.*, *646*, doi:10.1016/j.tecto.2015.02.004. 4.4

IRIS DMC (2015), Data Services Products: Synthetics Engine, doi:10.17611/DP/SYNGINE.1. 4.2

Kahraman, M., D. G. Cornwell, D. A. Thompson, S. Rost, G. A. Houseman, N. Türkelli, U. Teoman, S. Altuncu Poyraz, M. Utkucu, and L. Gülen (2015), Crustal-scale shear zones and heterogeneous structure beneath the North Anatolian Fault Zone, Turkey, revealed by a high-density seismometer array, *Earth Planet. Sci. Lett.*, *430*, doi:10.1016/j.epsl.2015.08.014. 4.1, 4.1, 4.3, 4.4, 4.4, 4.5

Karimi, B., N. McQuarrie, J.-S. Lin, and W. Harbert (2014), Determining the geometry of the North Anatolian Fault East of the Marmara Sea through integrated stress modeling and remote sensing techniques, *Tectonophys.*, *623*, doi:10.1016/j.tecto.2014.03.015. 4.1

Kennett, B. L. N. (2015), Lithosphereasthenosphere P-wave reflectivity across Australia, *Earth Planet. Sci. Lett.*, *431*, doi:10.1016/j.epsl.2015.09.039. 4.1, 4.4

Kennett, B. L. N., and E. R. Engdahl (1991), Travel times for global earthquake location and phase association., *Geophys. J. Int.*, *105*, doi:10.17611/DP/9991809. 4.2, 4.2, 4.2, 4.4

Kennett, B. L. N., E. Saygin, and M. Salmon (2015), Stacking autocorrelograms to map Moho depth with high spatial resolution in southeastern Australia, *Geophys. Res. Lett.*, *42*, doi:10.1002/2015GL065345. 4.1, 4.4

Koulakov, I., D. Bindi, S. Parolai, H. Grosser, and C. Milkereit (2010), Distribution of Seismic Velocities and Attenuation in the Crust beneath the North Anatolian Fault (Turkey) from Local Earthquake Tomography, *Bull. Seismol. Soc. Am.*, *100*, doi:10.1785/0120090105. 4.1

Krischer, L., A. Hutko, M. van Driel, M. Bahavar, C. Trabant, and T. Nissen-Meyer (2017), Ondemand custom broadband synthetic seismograms, *Seismol. Res. Lett.*, *88*, doi:10.1785/0220160210. 4.2

Nissen-Meyer, T., M. van Driel, S. C. Stähler, K. Hosseini, S. Hempel, L. Auer, A. Colombi, and A. Fournier (2014), AxiSEM: broadband 3-D seismic wavefields in axisymmetric media, *Solid Earth*, *5*, doi:10.5194/se-5-425-2014. 4.2

Okay, A. I., A. M. C. Şengör, and N. Görür (1994), Kinematic history of the opening of the Black Sea and its effect on the surrounding regions, *Geology*, *22*, doi:10.1130/0091-7613(1994)022¡0267:KHOTOO¿2.3.CO;2. 4.1

Okay, A. L. (2008), Geology of Turkey: A Synopsis, *Anschnitt*, *21*. 4.1, 4.4

Okay, A. L., and O. Tüysüz (1999), Tethyan sutures of northern Turkey, *Geological Society, London, Special Publications*, *156*, doi:10.1144/GSL.SP.1999.156.01.22. 4.1

Oren, C., and R. L. Nowack (2017), Seismic body-wave interferometry using noise autocorrelations for crustal structure, *Geophys. J. Int.*, *208*, doi:10.1093/gji/ggw394. 4.1

Papaleo, E., D. G. Cornwell, and N. Rawlinson (2017), Seismic tomography of the North Anatolian Fault: New insights into structural heterogeneity along a continental strikeslip fault, *Geophys. Res. Lett.*, *44*, doi:10.1002/2017GL072726. 4.1, 4.3

Papaleo, E., D. G. Cornwell, and N. Rawlinson (2018), Constraints on North Anatolian Fault zone width in the crust and upper mantle from Swave teleseismic tomography, *J. Geophys. Res. Solid Earth*, doi:10.1002/2017JB015386. 4.3

Paulssen, H., J. Visser, and G. Nolet (1992), The crustal structure from teleseismic P-wave coda-I. Method, *Geophys. J. Int.*, *112*, doi:10.1111/j.1365-246X.1993.tb01433.x. 4.2

Pham, T.-S., and H. Tkalčić (2017), On the feasibility and use of teleseismic P wave coda autocorrelation for mapping shallow seismic discontinuities, *J. Geophys. Res. Solid Earth*, *122*, doi:10.1002/2017JB013975. 4.1

Ruigrok, E., and K. Wapenaar (2012), Globalphase seismic interferometry unveils Pwave reflectivity below the Himalayas and Tibet, *Geophys. Res. Lett.*, *39*, doi:10.1029/2012GL051672. 4.1

Saygin, E., P. R. Cummins, and D. Lumley (2017), Retrieval of the P wave reflectivity response from autocorrelation of seismic noise: Jakarta Basin, Indonesia, *Geophys. Res. Lett.*, *44*, doi:10.1002/2016GL071363. 4.1

Schimmel, M., and H. Paulssen (1997), Noise reduction and detection of weak, coherent signals through phase-weighted stacks, *Geophys. J. Int.*, *130*, doi:10.1111/j.1365-246X.1997.tb05664.x. 4.2, 4.2, 4.4

Snieder, R., K. Wapenaar, and U. Wegler (2007), Unified Green's function retrieval by cross-correlation; connection with energy principles, *Phys. Rev. E*, *75*, doi:10.1103/PhysRevE.75.036103. 4.1

Stein, R. S., A. A. Barka, and J. H. Dieterich (1997), Progressive failure on the North Anatolian fault since 1939 by earthquake stress triggering, *Geophys. J. Int.*, *128*, doi:10.1111/j.1365-246X.1997.tb05321.x. 4.1

Sun, W., and B. Kennett (2017), Midlithosphere discontinuities beneath the western and central North China Craton, *Geophys. Res. Lett*, *44*, doi:10.1002/2016GL071840. 4.1

Sun, W., and B. L. N. Kennett (2016), Receiver structure from teleseisms: Autocorrelation and cross correlation, *Geophys. Res. Lett.*, *43*, doi:10.1002/2016GL069564. 4.1

Taylor, G., S. Rost, and G. Houseman (2016), Crustal imaging across the North Anatolian Fault Zone from the autocorrelation of ambient seismic noise, *Geophys. Res. Lett.*, *43*, doi:10.1002/2016GL067715. 4.1, 4.1, 4.3, 4.4, 4.4, 4.5

Thurber, C. H., H. Zhang, F. Waldhauser, J. Hardebeck, A. Michael, and D. Eberhart-Phillips (2006), Three-dimensional compressional wavespeed model, earthquake relocations, and focal mechanisms for the Parkfield, California, region, *Bull. Seismol. Soc. Am.*, *96*, doi:10.1785/0120050825. 4.1

Tibuleac, I. M., and D. von Seggern (2012), Crust-mantle boundary reflectors in Nevada from ambient seismic noise autocorrelations, *Geophys. J. Int.*, *189*, doi:10.1111/j.1365-246X.2011.05336.x. 4.1

Tseng, T. L., W. P. Chen, and R. L. Nowack (2009), Northward thinning of Tibetan crust revealed by virtual seismic profiles, *Geophys. Res. Lett.*, *36*, doi:10.1029/2009GL040457. 4.3

Wapenaar, K. (2004), Retrieving the Elastodynamic Green's Function of an Arbitrary Inhomogeneous Medium by Cross Correlation, *Phys. Rev. Lett.*, *93*, doi:10.1103/PhysRevLett.93.254301. 4.1

Wapenaar, K., and J. Fokkema (2006), Green's function representations for seismic interferometry, *Geophysics*, *71*, doi:10.1190/1.2213955. 4.1

Weber, M., K. Abu-Ayyash, A. Abueladas, A. Agnon, H. Al-Amoush, A. Babeyko, Y. Bartov, M. Baumann, Z. Ben-Avraham, G. Bock, J. Bribach, R. El-Kelani, A. Förster, H.-J. Förster, U. Frieslander, Z. Garfunkel, S. Grunewald, H. J. Götze, V. Haak, C. Haberland, M. Hassouneh, S. Helwig, A. Hofstetter, K.-H. Jäckel, D. Kesten, R. Kind, N. Maercklin, J. Mechie, A. Mohsen, F. M. Neubauer, R. Oberhänsli, I. Qabbani, O. Ritter, G. Rümpker, M. Rybakov, T. Ryberg, F. Scherbaum, J. Schmidt, A. Schulze, S. Sobolev, M. Stiller, H. Thoss, U. Weckmann, and K. Wylegalla (2004), The crustal structure of the Dead Sea Transform, *Geophys. J. Int.*, *156*, doi:10.1111/j.1365-246X.2004.02143.x. 4.4, 4.5

Wilson, C. K., C. H. Jones, P. Molnar, A. F. Sheehan, and O. S. Boyd (2004), Distributed deformation in the lower crust and upper mantle beneath a continental strike-slip fault zone: Marlborough fault system, South Island, New Zealand, *Geology*, *32*, doi:10.1130/G20657.1. 4.1, 4.4

Yılmaz, Y., Ş. C. Genç, E. Yiğitbaş, M. Bozcu, and K. Yılmaz (1995), Geological evolution of the late Mesozoic continental margin of Northwestern Anatolia, *Tectonophys.*, *243*, doi:10.1016/0040-1951(94)00196-G. 4.1, 4.4

Zhang, Z., Y. Wang, G. A. Houseman, T. Xu, Z. Wu, X. Yuan, Y. Chen, X. Tian, Z. Bai, and J. Teng (2014), The Moho beneath western Tibet: Shear zones and eclogitization in the lower crust, *Earth Planet. Sci. Lett.*, *408*, doi:10.1016/j.epsl.2014.10.022. 4.1, 4.1, 4.4, 4.5

Zhu, L. (2000), Crustal structure across the San Andreas Fault, southern California from teleseismic converted waves, *Earth Planet. Sci. Lett.*, *179*, doi:10.1016/S0012-821X(00)00101-1. 4.1, 4.1, 4.4, 4.5

Zigone, D., Y. Ben-Zion, M. Campillo, and P. Roux (2015), Seismic tomography of the Southern California plate boundary region from noise-based Rayleigh and Love waves, *Pure Appl. Geophys.*, *172*, doi:10.1007/s00024-014-0872-1. 4.1

Chapter 5

Discussion and conclusions

5.1 Comparison between the North Anatolian Fault and the San Andreas Fault

5.1.1 Crustal structure

There is a striking similarity between the North Anatolian Fault and the San Andreas Fault. Both are right-lateral continental transform faults with an overall length of approximately 1200 km, and an estimated age of 15 – 20 Ma (*Şengör and Yılmaz*, 1981, *Revenaugh and Reasoner*, 1997). The slip rate along both faults has been estimated to be between 20 – 35 mm/yr, although the San Andreas Fault may have a slightly faster average slip rate, closer to 30 mm/yr (*Weldon and Sieh*, 1985, *Fialko*, 2006, *Hussain et al.*, 2016a). Both the San Andreas and North Anatolian Faults exploit pre-existing suture zones along at least part of their length. The North Anatolian Fault exploits the Intra-Pontide Suture between the Istanbul Zone and Sakarya Terrane (Sections 1.1.2 and 1.1.3) (*Okay and Tüysüz*, 1999), whilst the central section of the San Andreas Fault separates the granitic Salinian Block from the Great Valley sedimentary sequence (*Dickinson*, 1966). Both the Intra-Pontide Suture and the suture separating the Salinian Block from the Great Valley are fossil subduction zones (*Okay and Tüysüz*, 1999, *Ernst*, 1970).

In Chapter 3 I created an S-wave velocity model for the upper crust of the Izmit-Adapazari region that showed that both the northern and southern branches of the North Anatolian Fault are located in areas where there is a large seismic velocity contrast at the northern and southern boundaries of the Armutlu Block (Fig. 3.6). *Thurber et al.* (2006) noted a similar sharp seismic velocity contrast across the San Andreas Fault at Parkfield (Fig. 1.4), which likely represents the boundary between the Salinian Block and the Great Valley sequence. *Catchings et al.* (2002) constructed a P-wave velocity image of the top 1 km of the San Andreas Fault near Parkfield from a refraction data set (Fig. 5.1). A $\sim$ 2 km wide low velocity zone associated with the San

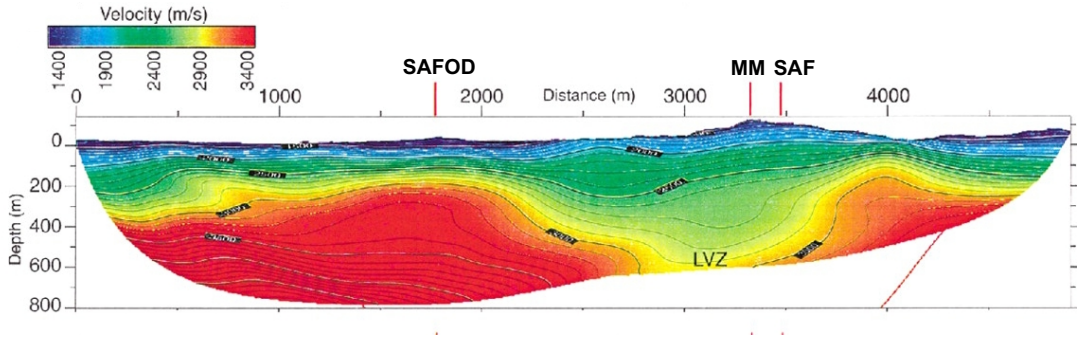

Figure 5.1: P-wave velocity model of the top 1 km of the San Andreas Fault Zone at Parkfield from *Catchings et al.* (2002). Red colours represent high P-wave velocity, blue colours are low P-wave velocity. The red dashes on the x-axis are labelled: SAFOD = Location of the SAFOD bore hole (35.97°N 120.55°W), MM = Middle Mountain (38.96°N 120.18°W) and SAF = surface trace of the San Andreas Fault. Figure modified from *Catchings et al.* (2002).

Andreas Fault trace is clearly visible, separating two regions of high P-wave velocity. The P-wave velocity profile across the San Andreas Fault of *Catchings et al.* (2002) (Fig. 5.1) bears a striking resemblance to the S-wave velocity profiles I show in Fig. 3.7, where the northern branch of the North Anatolian Fault is a zone of low S-wave velocity separating the Armutlu Block from the Istanbul Zone. Though there are discrepancies between the width of the low velocity zone of the San Andreas ($\sim$ 2 km, Fig. 5.1) and the North Anatolian Fault ($\sim$ 11 km, Fig. 3.7), the correspondence between Fig. 3.7 and Fig. 5.1 shows that the North Anatolian Fault in the Izmit-Adapazari region and the San Andreas Fault at Parkfield might have localised in comparable tectonic conditions that lead to a similar geological structure.

Eberhart-Phillips and Michael (1993) suggested that the strong contrast in seismic velocity across the San Andreas Fault at Parkfield, and corresponding change in lithology, might be relevant to the occurrence of aseismic creep along the Parkfield section. Aseismic creep along the Parkfield section of the San Andreas Fault has been measured at 15 to 25 mm/yr (*Lyons and Sandwell*, 2003). Most seismicity along the central section of the San Andreas Fault is $M_w < 4.0$, with M_w 5.0 – 6.0 events occurring every couple of decades (*Bakun and McEvilly*, 1984, *Bakun and Lindh*, 1985). The Izmit-Adapazari section of the North Anatolian Fault appears to experience larger magnitude seismicity than the Parkfield section of the San Andreas Fault, as evidenced by the $M_w > 7.0$ İzmit and Düzce earthquakes (*Barka et al.*, 2002). Measurements of interseismic creep rate along the Izmit-Adapazari section of the North Anatolian Fault are difficult due to the İzmit and Düzce earthquakes. *Hussain et al.* (2016b) reported that the slip rate of the North Anatolian Fault was 11 $\pm$ 2 mm/yr, though this measurement is likely the result of shallow postseismic after-slip following the İzmit and Düzce earthquakes, and does not represent the background aseismic creep rate.

5.1.2 Azimuthal anisotropy of the crust

Measurements of the fast propagation direction for Rayleigh waves in the Izmit-Adapazari region at 2, 4, 6 and 8 s period are shown in Fig. 3.8. In Fig. 3.9 I show the full variation of the magnitude of 2θ Rayleigh wave anisotropy and fast direction as a function of period. It is apparent from Fig. 3.9 that there is a smooth variation in the fast direction as the period of the waves increases. At short periods (2 – 3 s) the fast direction is aligned close to 90° from north, but changes smoothly to $\sim$ 70° from north above 5 s period. The 90° fast direction at 2 – 3 s period aligns approximately with the strike of the North Anatolian Fault through the region. There is also systematic variation in the magnitude of anisotropy. Below 2 s period, the anisotropy has a magnitude greater than 1%, but this magnitude decreases substantially between 2 and 4 s period, before increasing again at periods greater than 4.0 s to a value of $\sim$ 3%. The depth sensitivity of these Rayleigh wave observations is illustrated in Fig. A.8. The consistency and smooth variation of the measurements implies that they are a significant estimate of the anisotropy.

The $\sim$ 70° fast directions at longer periods are close to, though 25° out of line with, the 45° direction of maximum extension for the Izmit-Adapazari region calculated by *Allmendinger et al.* (2007). Shear wave splitting measurements of the central portion of the North Anatolian Fault by *Biryol et al.* (2010) found a fast polarisation direction that varied between 35° and 60°, although these measurements were mainly sensitive to the lithospheric mantle. Observations of crustal anisotropy from 12 – 24 s period Rayleigh waves from the San Andreas Fault Zone by *Lin et al.* (2009) show that the fast propagation direction is consistently aligned parallel to the strike of the San Andreas Fault. *Zhang and Schwartz* (1994) also noted that the fast polarisation direction of shear waves from local seismicity at Parkfield also consistently aligns parallel to the San Andreas Fault.

In the upper crust, aligned fractures are believed to make an important contribution to the anisotropy signal (*Crampin and Lovell*, 1991). It is generally expected that the fast propagation direction in the top $\sim$ 15 km of the crust will align with the direction of maximum compressive stress (*Lin and Schmandt*, 2014). This is due to the fact that fractures will be preferentially closed in the direction of maximum compressive stress. The direction of maximum compressive stress in the Izmit-Adapazari section of the North Anatolian Fault is $\sim$ 135° (*Allmendinger et al.*, 2007). The fact that our fast directions are close to 70° is an indication that another mechanism is responsible for the anisotropy in the region.

Mineral fabric and crystal preferred orientation is another likely explanation for the observed anisotropy. Upper crustal minerals such as micas and amphiboles are known to have cleavage planes and preferred orientations that align with the dominant strain direction (*Kern and Wenk*, 1990, *Mainprice and Nicolas*, 1989, *Sherrington et al.*,

2004). Analysis of samples of calcite and amphiboles taken from the Uludağ Massif ($\sim$ 100 km south-west of Izmit-Adapazari) by *Farrell* (2017) show that the fast propagation for both P and s waves aligns parallel to the foliation direction in these minerals. The fact that seismic fast directions at both the North Anatolian Fault and the San Andreas Fault are predominantly ($\sim 25^\circ$ misfit for the North Anatolian Fault) aligned in the direction of maximum strain indicates that mineral fabric may be an important contribution to anisotropy even within the top 10 km of the crust.

5.1.3 Strain localisation in the upper mantle

The seismic profiles (Figs. 2.2 and 4.5) in Chapters 2 and 4 show that there are vertical offsets in the Moho beneath the northern branch of the North Anatolian Fault. Vertical offsets in the Moho beneath the Izmit-Adapazari region were also observed in receiver function images by *Kahraman et al.* (2015). Offsets in Moho structure are widely regarded as evidence for localised ductile deformation that occurs in a narrow shear zone beneath the fault (*Bürgmann and Dresen*, 2008), and are typically observed to take place over lateral distances of < 10 km beneath strike-slip faults (*Stern and McBride*, 1998). Vertical offsets in the Moho over horizontal distances of < 10 km have also been observed in receiver function images along the length of the San Andreas Fault (*Zhu*, 2000, *Yan and Clayton*, 2007, *Ford et al.*, 2014). Beneath the central section, where the majority of the slip is confined to the main branch of the San Andreas Fault, receiver function images by *Ford et al.* (2014) also show offsets in the interpreted lithosphere-asthenosphere boundary. This offset occurs over a lateral distance of < 50 km, which indicates that whilst the deformation beneath the San Andreas Fault has broadened in the upper mantle, there is still some degree of strain localisation at the base of the lithosphere.

There is geological evidence for strain localisation in the upper mantle beneath the San Andreas Fault. Olivine crystals in spinel peridotite xenoliths collected from central California by *Titus et al.* (2007) show a strong crystallographic preferred orientation. *Titus et al.* (2007) estimate that the xenoliths were erupted from a depth of 38 – 40 km beneath the San Andreas Fault, indicating that the mantle shear zone extends to a depth of at least 40 km. In southern California slip along the San Andreas Fault system is distributed along many sub-parallel faults such as the East California Shear Zone. Despite the distributed nature of deformation in the upper crust in southern California, differential stresses of 13 – 17 MPa have been measured from $\sim$ 7 Ma old olivine crystals in mantle xenoliths that originate from 29 – 35 km depth beneath the East California Shear Zone by *Behr and Hirth* (2014). These differential stresses, when coupled with olivine flow laws, indicate that strain associated with faults in the East California Shear Zone persists through the seismogenic layer as a narrow ductile shear zone (*Behr and Hirth*, 2014). The similarity in the seismic observations of Moho offsets beneath both the San Andreas and North Anatolian Faults suggest comparable levels of

strain localisation in the upper mantle, and it may be possible to use geological evidence from the San Andreas Fault as a comparison for processes of strain localisation beneath the North Anatolian Fault.

5.1.4 Reduction in Moho reflection amplitude

In addition to a vertical offset in the Moho across the San Andreas Fault, *Zhu* (2000) also observed a reduction in the amplitude of the P-to-S conversion from the Moho beneath southern California. Receiver function images of the North Anatolian Fault by *Kahraman et al.* (2015) also show a reduction in amplitude of the Moho conversion, and the work I presented in Chapters 2 and 4 also show reduced P-wave reflectivity of the Moho beneath the Sakarya Terrane, and in the vicinity of the northern branch of the North Anatolian Fault.

Serpentinisation of upper mantle peridotite may be a mechanism to reduce both the seismic velocity and density of the upper mantle, and thus the amplitude of the Moho reflectivity (*Hetényi et al.*, 2015). Serpentinisation is a metamorphic process that requires the presence of water to hydrate olivine crystals. In Chapters 2 and 4 I suggested that the deformation associated with the North Anatolian Fault could allow fluid migration into the upper mantle and subsequent serpentinisation. Helium ratios in fluid inclusions along the San Andreas Fault measured by *Pili et al.* (2011) suggest a series of upper mantle and metamorphic sources for fluids that flow upwards through fractures in the San Andreas Fault Zone, with little evidence of this water having a meteoric source. The presence of upper mantle fluids in exhumed fault rocks along the San Andreas Fault indicates that there may be sufficient fluid at depth to serpentinise the upper mantle beneath the fault, and indicates the existence of high permeability pathways through the fault zone.

Fluid venting from the North Anatolian Fault Zone beneath the Marmara Sea, west of Izmit-Adapazari, has been inferred to have a mantle source from helium isotope ratios (*Burnard et al.*, 2012). In addition, magnetotelluric imaging by *Tank et al.* (2005) shows a broad area of low electrical resistivity in the crust and upper mantle beneath the Armutlu Block (Fig. 5.2), which *Tank et al.* (2005) interpreted as evidence for fluid generated by the metamorphic dehydration of minerals. Low electrical resistivity has also been interpreted to represent the presence of fluids in fractured rock beneath the San Andreas Fault at Parkfield by *Unsworth et al.* (1997). The evidence of deep fluids within both the North Anatolian Fault and the San Andreas Fault indicates that the reduced amplitude of the Moho in a $\sim$ 10 km wide zone beneath both fault zones is most simply explained by the serpentinisation of the upper mantle beneath continental transform faults.

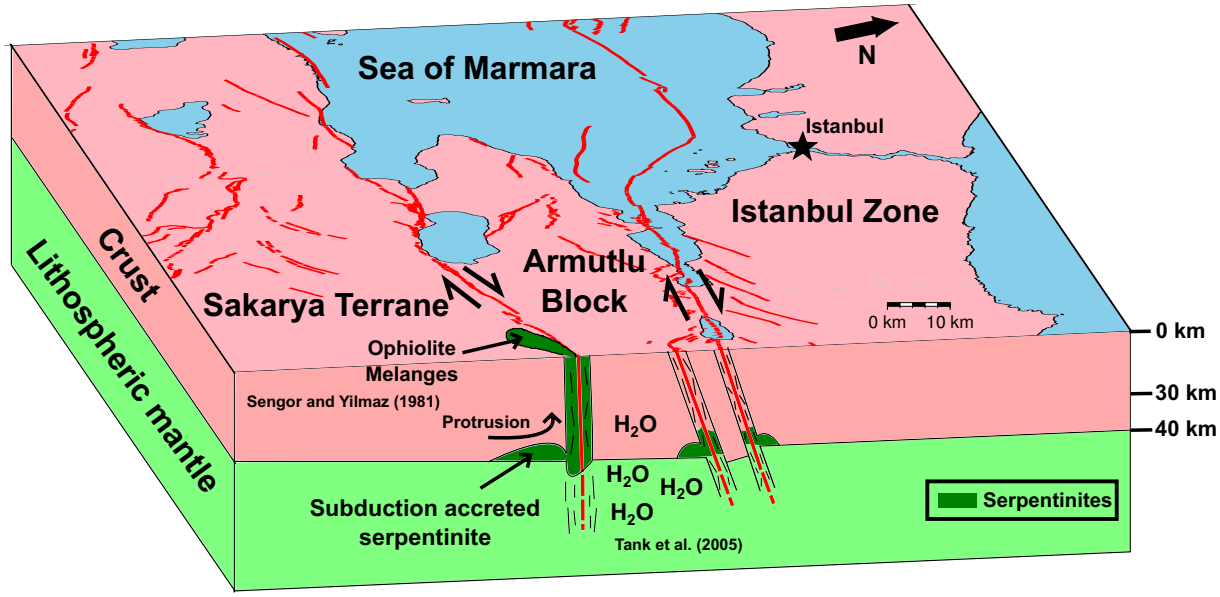

Figure 5.2: Sketch of the inferred deep structure of the North Anatolian Fault Zone in the Izmit-Adapazari. Mapped faults of the region are shown as thick red lines. The sense of motion along the northern and southern branches of the North Anatolian Fault are shown with arrows. The approximate position of ophiolite melanges along the southern branch mapped by *Şengör and Yılmaz* (1981) is annotated. Pink represents continental crust, light green lithospheric mantle, and dark green serpentinised mantle. The conductive region in the lower crust and upper mantle beneath the Armutlu interpreted by *Tank et al.* (2005) is labelled as H_2O. The dip of the faults through the crust and upper mantle, and the location of serpentinites, is inferred from reflection profiles in Fig. 4.4.

5.2 Presence of serpentinite in continental strike-slip faults

The presence of serpentinite at the base of continental fault zones would have a large impact upon the strength of the upper mantle, and the rheology of the fault zone. Serpentinite is usually much weaker than pure peridotite (*Moore et al.*, 1997). Serpentinite bodies likely promote strain localisation within a weakened region (*Guillot et al.*, 2015), and encourage the formation of narrow shear zones in the upper mantle beneath continental transform faults.

Serpentinite in the upper crust is sometimes associated with aseismic creep along continental strike-slip faults. The creeping section of the San Andreas Fault at Parkfield coincides with Coast Range ophiolite, a unit of serpentinised ultramafic rocks (*Hanna et al.*, 1972). The most extensive serpentinite body is located on the section with the highest creep rate (*McPhee et al.*, 2004). Aseismic creep along the North Anatolian Fault at Ismetpaşa also appears to be correlated with serpentinite bodies contained within Mesozoic ophiolitic mélange (*Cetin et al.*, 2014). Aseismic creep along a fault suggests low interseismic plate coupling and low frictional strength (*Manaker et al.*, 2008). Paradoxically, serpentinites have been found to have a frictional strength equivalent to most other silicate rocks (0.6 – 0.7) (*Reinen et al.*, 1994). It is likely that

other processes, such as fluids released during the dehydration of serpentine minerals (*Faulkner and Rutter*, 2001), or the presence of weaker minerals such as talc (*Moore and Rymer*, 2007), are responsible for weakening these sections of the fault zone.

In addition to the migration of fluids through deep fractures in fault zones (*Pili et al.*, 2011, *Burnard et al.*, 2012), serpentinites can be located in continental faults that reactivate ancient suture zones following subduction. Numerical modelling by *Kirby et al.* (2014) showed that following the cessation of subduction, as beneath California prior to the formation of the San Andreas Fault Zone, dehydration of the forearc mantle can drive the upward migration of serpentinite due to its positive buoyancy. In analogy with my findings in Chapters 2 and 4, seismic investigations of the forearc mantle throughout the Cascadia subduction zone show reduced Moho reflectivity (*Brocher et al.*, 2003), which could confirm the widespread presence of serpentinite in the mantle wedge beneath Cascadia.

Serpentinite mélanges are found along the length of the North Anatolian Fault (*Şengör et al.*, 2005), including within the Sakarya Terrane in the Izmit-Adapazari region (*Şengör and Yılmaz*, 1981). These serpentinites were likely emplaced during the final stages of the subduction of the Neo-Tethys Ocean (*Şengör and Yılmaz*, 1981). Whilst the creeping section of the North Anatolian Fault at Ismetpaşa is correlated with these serpentinite bodies, it is unclear whether the Izmit-Adapazari section creeps during the interseismic period. Measurements by *Hussain et al.* (2016b) suggest that current creep along the Izmit-Adapazari section is associated with shallow afterslip following the 1999 İzmit earthquake. As such, a lack of slip rate measurements during the interseismic period make it difficult to determine if the Izmit-Adapazari section undergoes aseismic creep, despite the fact that the geological and tectonic setting indicates that creep is possible.

Both geophysical and geological evidence suggest that fluids and metamorphic processes may be important controls on earthquake processes along the San Andreas and North Anatolian Faults, or indeed continental strike-slip faults in general. It is possible that the subduction and accretionary environment that dominated both California and Anatolia prior to the current strike-slip regime introduced fluids that favour the formation of serpentinite. The presence of serpentinite encourages strain localisation as a plane of weakness, which may be exploited by the fault zone, allowing deformation to remain narrow (< 10 km) into the upper mantle. The fracture zones produced by deformation along the fault, and pressure changes induced by earthquakes that occur, may increase the permeability of the fault zone, drawing fluids up through the crust. Fig. 5.2 is an interpretive sketch of the possible structure beneath the Izmit-Adapazari region.

5.3 Previous results from the DANA network

Previous results obtained using the DANA data set, such as receiver functions (*Kahraman et al.*, 2015) and observations of local seismicity (*Altuncu Poyraz et al.*, 2015), are readily comparable with the results I present in Chapters 2, 3 and 4. A comparison between the receiver function images of *Kahraman et al.* (2015) and the P-wave autocorrelation results I presented in Chapter 4 is shown in Fig. 5.3.

The profiles in each column are approximately co-located and have the same horizontal scale in the north–south direction. The observations from both methods are highly consistent, particularly in the vicinity of the two branches of the North Anatolian Fault. Both the receiver functions and autocorrelation profiles show a reduction in amplitude of the Moho arrival beneath the northern branch of the North Anatolian Fault. The apparent termination of the Moho arrival occurs at nearly identical latitude, particularly in the eastern profile (column b. in Fig. 5.3). In the western profile (column a. in Fig. 5.3), The location of the termination of the Moho arrivals against the southern branch of the North Anatolian Fault is also consistent between the two methods. This could be the result of the distribution of teleseismic earthquakes recorded at the DANA network that were used to create both sets of profiles, but could also be further evidence for some mechanism (Sec. 5.2) reducing the contrast in seismic properties across the Moho to the south of the North Anatolian Fault Zone. The receiver function profiles generally show a deepening of the Moho towards the south. In the eastern profile, the autocorrelation images show an earlier arriving Moho reflection south of the southern branch of the North Anatolian Fault, which could indicate a shallowing of the Moho. The receiver function profile lacks data in this region, but does also show that the Moho may be found at the shallower depth of $\sim$ 30 km within the Sakarya Terrane. The close correspondence between the major features of crustal structure that can be observed in both the receiver function and autocorrelation images provides greater certainty and confidence in both the seismic images produced by the two approaches, and in the efficacy of the autocorrelation method.

A comparison between the S-wave velocity model of the top 10 km of the crust presented in Chapter 3 and the locations of seismicity detected during the deployment of the DANA network by *Altuncu Poyraz et al.* (2015) is shown in Fig. 5.4. In the western profile, profile A–B, the majority of the local seismicity is highly localised to regions of reduced S-wave velocity. This observation is particularly clear in the vicinity of the northern and southern fault branches. Beneath the northern branch, the majority of the seismicity occurs in a region with S-wave velocity < 3.0 km s^{-1} that is clearly associated with the main fault. The seismicity associated with the southern branch is also confined to a narrow zone characterised by S-wave velocity lower than 3.2 km s^{-1}. Within the Armutlu Block (S-wave velocity > 3.2 km s^{-1}), there is only a small amount of seismicity on the northern edge of the Pamukova basin, and almost

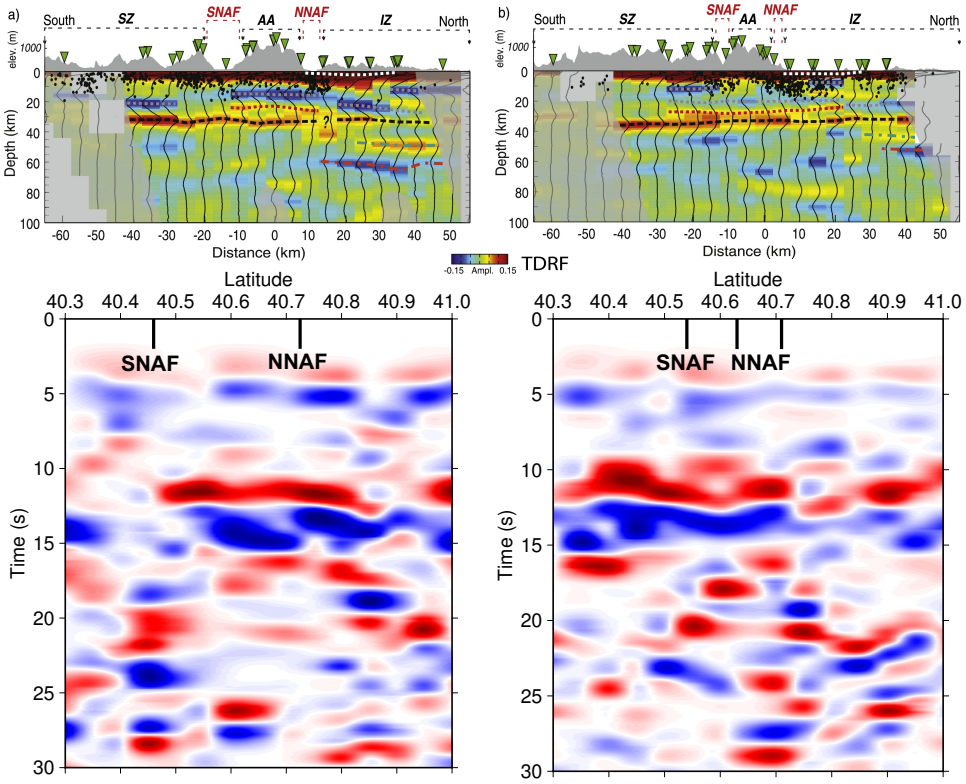

Figure 5.3: Comparison between the receiver function images of *Kahraman et al.* (2015) (top row), and the autocorrelation profiles shown in Chapter 4 (bottom row). The profiles in each column (a. for western profiles and b. for eastern profiles) are approximately co-located, with the autocorrelation profiles offset by ~ 7 km to the west of the corresponding receiver function profile. The north–south horizontal scales are comparable, but the autocorrelation profiles remain in the time domain and are not migrated to depth.

no large seismic events. The seismicity beneath the northern branch of the fault shows the possibility of dip towards the north, which is also observed in the autocorrelation profiles in Chapters 3 and 4.

In the eastern profile (A'–B' in Fig. 5.4), the pattern of seismicity is much more diffuse. There is some localisation of seismicity beneath the southern branch of the North Anatolian Fault, where there is reduced seismic velocities to approximately 4 km depth, but seismicity on the northern branch is much more scattered, and the largest events occur at depths > 5 km. Notably, the Armutlu Block contains much more seismicity than in the western profile, and this is accompanied by a reduction in S-wave velocity above 4 km between the two branches of the North Anatolian Fault.

Fig. 5.5 compares the S-wave velocity model and the local seismicity in map view. Whilst the majority of the seismicity is located in clusters to the west of the tomographic model, it is clear that the majority of seismicity that occurred within the DANA network occurred in areas of low S-wave velocity. This feature is particularly notable at 1.5 km and 5.5 km depth, where the seismicity is pre-dominantly located in low velocity zones associated with sedimentary basins and the northern branch of the

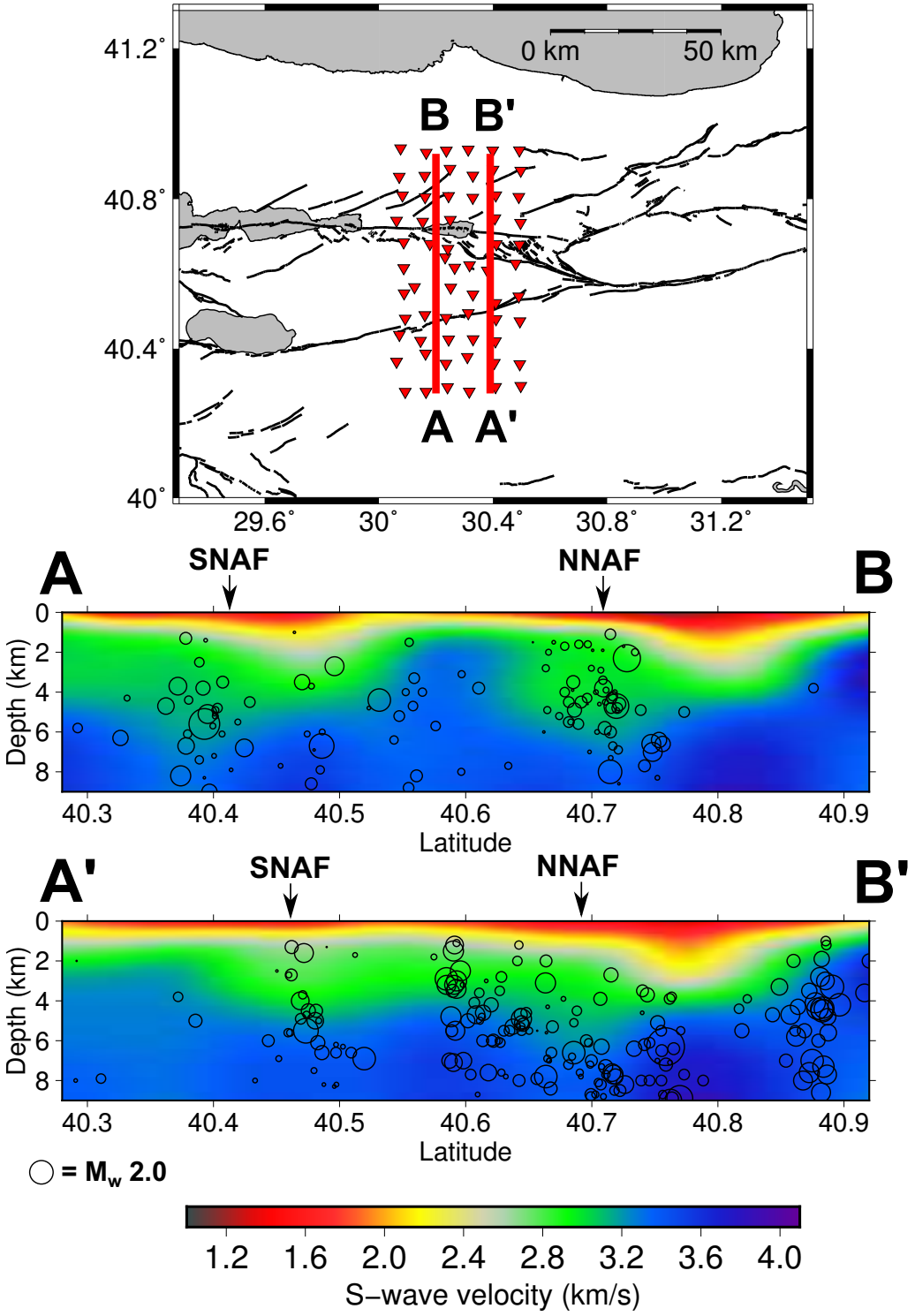

Figure 5.4: S-wave velocity vertical profiles from Chapter 3, overlain by the local seismicity detected during the deployment of the DANA network (hollow circles) (*Altuncu Poyraz et al.*, 2015). Seismicity located with 10 km of each velocity profile is projected onto the profile.

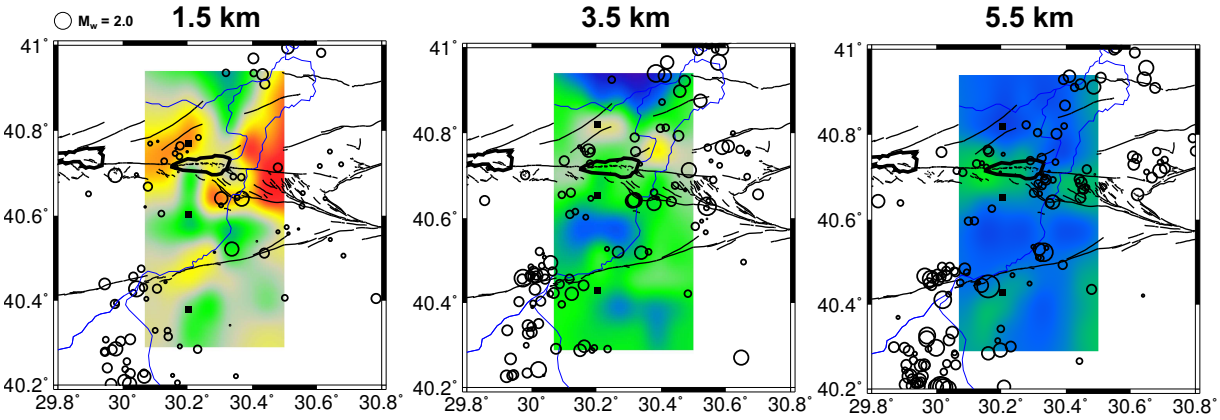

Figure 5.5: S-wave velocity maps from Chapter 3, overlain by the local seismicity detected during the deployment of the DANA network (hollow circles) (*Altuncu Poyraz et al.*, 2015). Seismicity located with 500 m depth of each velocity map is included in the image.

North Anatolian Fault. Seismicity also occurred at the boundaries of some of the high velocity zones, particularly the Armutlu Block and the northern part of the Istanbul Zone. Both the localisation of the main fault strands and the location of the bulk of the seismicity at the edges of the Armutlu Block is further evidence that this region has a strong rheology, and localises strain along its boundaries.

5.4 Implementing the autocorrelation method

Many different implementations of the autocorrelation method have featured in recent studies. Variations in methodology and processing parameters such as the seismic source and frequency band have a large impact on the quality and the interpretation of the results.

One characteristic of autocorrelation studies that utilise ambient noise as the source is the appearance of S-wave reflections on vertical component recordings. S-wave reflections from the Moho were observed by *Tibuleac and von Seggern* (2012), *Oren and Nowack* (2017). In Chapter 2 I suggested that the arrival in the reflection sections (Fig. 2.2) could be a P-wave reflection from an upper mantle discontinuity. However, s waves contained within ambient noise will arrive at a receiver with a wide range of incidence angles. In particular, vertically polarised s waves arriving from noise sources close to the receiver can be recorded on the vertical component. *Oren and Nowack* (2017) noted that whilst the P-wave reflection from the Moho can be retrieved using just one hour of noise data, the arrival interpreted as the S-wave reflection requires up to a month of data to become coherent. This property suggests the source of this arrival is lower amplitude than the P wave reflection, which could reflect the small s wave component of the noise field (*Koper et al.*, 2010). Thus, it is possible that the arrival at $\sim$ 20 s in Fig. 2.2 is indeed an S-wave reflection (*SmS* from the Moho. Auto-correlation functions constructed from the P-wave coda of teleseismic earthquakes will not contain direct S-

wave reflections due to the lack of S-wave reverberations that arrive in the P-wave coda, though it could be possible to detect P-to-S conversions and their respective multiple reflections.

The frequency band employed also has an impact on the character of the auto-correlation functions. *Gorbatov et al.* (2013), *Kennett* (2015), *Kennett et al.* (2015) and *Becker and Knapmeyer-Endrun* (2017) target waves at frequencies > 1 Hz, but do not obtain coherent reflections from any lithospheric discontinuities (Fig. 1.20). Instead, each of these studies advocates the interpretation of a sudden reduction in amplitude of the auto-correlation functions as the base of the crust, on account of the reduced reflectivity of the mantle. Other studies, such as *Tibuleac and von Seggern* (2012), *Taylor et al.* (2016) (Chapter 2), *Oren and Nowack* (2017) and *Heath et al.* (2018) show that it is possible to obtain coherent reflections from at least the Moho through the auto-correlation of either ambient noise or teleseismic P-wave coda. It may be that the lower frequency range employed by these studies (0.1 – 0.5 Hz) is better suited for producing coherent reflections. Energy in the ambient noise field is strongest between 0.1 and 0.5 Hz due to the presence of the ocean microseisms (*Peterson*, 1993). Whilst teleseismic P-wave coda energy can contain frequencies > 1 Hz (*Seriff et al.*, 1965, *Gupta*, 1965), much of the high frequency energy is attenuated prior to arriving at the receiver. It is possible that high frequency reflection images may only be possible in situations where there is a high frequency seismic source that generates vertically travelling waves directly beneath a receiver. Alternatively, a sufficiently long recording period may permit the exploitation of a greater number of teleseismic coda waveforms to improve the band-width of the auto-correlation functions and increase the signal-to-noise ratio of high frequency reverberations.

Some prior studies, such as *Oren and Nowack* (2017), *Pham and Tkalčić* (2017) and *Becker and Knapmeyer-Endrun* (2017) required the application of spectral balancing in order to improve the signal to noise ratio of their reflectivity profiles. I did not apply spectral balancing in the auto-correlation profiles in Chapters 2 and 4 (Figs. 2.2 and 4.5. The fact that we do not have to whiten the spectrum of the auto-correlation functions in Chapter 4 may indicate that the energy contained within the teleseismic P-wave coda is sufficiently well distributed across the frequency band 0.1 – 0.5 Hz (*Hennino et al.*, 2001). Spectral balancing may be required for noise studies that utilise a period range where the noise field is not sufficiently well partitioned (*Peterson*, 1993), or there are dominant, incoherent noise sources that are higher amplitude than the target reflections. *Schimmel et al.* (2011) show that if phase correlation methods are employed, then the application of spectral balancing will reduce the signal-to-noise ratio of the correlation functions.

Phase-weighted stacking techniques (*Schimmel and Paulssen*, 1997) appear to have an important impact on the quality of the results. The reflection profiles in Chapter 4 (Fig. 4.5) are higher signal-to-noise-ratio than the the profiles in Chapter 2 (Fig.

2.2). The improvement in the quality of the data is likely a function of the higher signal-to-noise ratio of the P-wave coda, and the phase-weighted stacking employed in Chapter 4. *Saygin et al.* (2017) also employed phase-weighted stacking to waveforms with frequencies between 2 – 4 Hz for imaging the thickness of the Jakarta Basin, and obtained coherent reflections from the sediment-basement interface. In contrast, studies by *Gorbatov et al.* (2013), *Kennett et al.* (2015), and *Kennett* (2015) also used 2 – 4 Hz waves but did not apply phase-weighted stacking and do not retrieve coherent reflections. The low amplitude of the free surface reverberations in both ambient noise and teleseismic coda likely requires the application of phase-based methods (*Schimmel and Paulssen*, 1997, *Schimmel*, 1999) in order to fully exploit the available data for seismic imaging.

5.5 Conclusions

My thesis has demonstrated the applicability of seismic interferometry to imaging lithospheric structure on a variety of spatial scales. By applying several interferometric methods, I have been able to produce precise images of the seismic structure of the North Anatolian Fault Zone from the upper crust to the lithospheric mantle. I have built upon the novel autocorrelation approach for extracting body wave reflections from ambient seismic noise and teleseismic earthquake coda. Additionally, I have employed phase correlation (*Schimmel*, 1999, *Schimmel et al.*, 2011) and stacking methods (*Schimmel and Paulssen*, 1997) in the autocorrelation approach to improve the quality of the seismic images.

My results are also important for understanding the tectonics of the Izmit-Adapazari region in Turkey, and the behaviour of earthquakes that occur in the region. I produced a tomographic image of the top 10 km of the crust which shows that the North Anatolian Fault likely exploits an ancient suture zone within the Armutlu Block that separates the tectonic units of the Istanbul Zone and Sakarya Terrane. I produced seismic reflection profiles across the fault zone which show that the amplitude of the Moho reflection is greatly reduced in a narrow (<10 km) zone beneath the North Anatolian Fault. The Moho also appears to be vertically offset ($\sim$ 3 s travel time) beneath the northern branch of the North Anatolian Fault, indicating that deformation associated with the fault may be localised until at least upper mantle depths. In this section, I will provide an overview of the key findings of my thesis, and propose further studies that might take advantage of my findings to further constrain fault structure and behaviour.

Key Finding 1: Autocorrelation methods can be used to isolate the reflectivity structure of the Earth beneath a single seismometer.

Chapters 2 and 4 of my thesis focused on using autocorrelation methods to extract P-wave reflections from ambient seismic noise and teleseismic earthquake coda. In

Chapter 2 (*Taylor et al.*, 2016) I built on the theoretical work of *Claerbout* (1968) and practical studies by *Tibuleac and von Seggern* (2012), *Gorbatov et al.* (2013), *Kennett et al.* (2015) and *Kennett* (2015) and auto-correlated vertical component records of ambient seismic noise recorded at the DANA network to produce a reflection image of the lithospheric structure of the North Anatolian Fault Zone. By implementing a phase correlation approach (*Schimmel*, 1999) I was able to improve the signal-to-noise ratio of P-wave reflections that were observed in the noise field, and observe coherent arrivals from seismic discontinuities within the Earth. The observation of coherent waves in the autocorrelation profiles is an improvement on the work of *Kennett et al.* (2015) and *Kennett* (2015), who instead interpret systematic reductions in the amplitude of the auto-correlation function as representing the base of the crust, on the ground of reduced reflectivity. In addition to observations of the Moho, we detect a deeper reflection at $\sim$ 17.5 s two way travel time that was also noted by *Tibuleac and von Seggern* (2012). This arrival could represent a discontinuity in the shallow upper mantle, or an S-wave reflection (*SmS*) from the Moho. Given the possible range of incidence angles for waves present in ambient noise, it is likely that S-wave reflections are common in images produced from auto-correlation functions of vertical component recordings (*Nakata et al.*, 2014).

In Chapter 4 I applied the autocorrelation method to the P-wave coda of teleseismic earthquakes, an approach that is analogous to receiver functions (*Galetti and Curtis*, 2012). I found that when utilising the P-wave coda, a phase correlation algorithm (*Schimmel*, 1999) was not necessary, and phase-weighted stacking (*Schimmel and Paulssen*, 1997) was sufficient to retrieve reflections. The combination of the more energetic source wavefield and amplitude independent stacking procedure produced reflection profiles that had a much higher signal-to-noise ratio than those created using ambient seismic noise. My results in Chapter 4 show that the autocorrelation approach could potentially be used in conjunction with other established seismic methods such as receiver functions, and provide an independent constraint on P or S-wave reflectivity beneath a seismometer.

Key Finding 2: Vertical offsets in the Moho beneath the Izmit-Adapazari region, indicating the presence of a narrow shear zone in the upper mantle beneath the North Anatolian Fault Zone.

The reflection images produced in Chapters 2 and 4 show apparent vertical offsets in the Moho beneath the northern branch of the North Anatolian Fault. In Chapter 2 I showed that at most 50% of this $\sim$ 3 s offset can be accounted for by reasonable seismic velocity variations within the the crust. Whilst the presence of pervasive seismic anisotropy in the lower crust and upper mantle suggests a diffuse deformation pattern, the presence of vertical offsets in the Moho beneath major faults is indicative of localised strain in the upper mantle. My observations in Chapters 2 and 4 show that, beneath

the North Anatolian Fault, the vertical offset in the Moho is sharp and occurs over a region <10 km wide. This observation contrasts with that of *Wilson et al.* (2004), who interpret a 60 km wide zone with a dipping Moho beneath the Marlborough Fault Zone, New Zealand. Vertical offsets in the Moho are a common observation beneath major continental faults with a high cumulative displacement such as the San Andreas Fault in California (*Zhu*, 2000), the Dead Sea Transform in the Middle East (*Weber et al.*, 2004) and a number of suture zones that cross the Tibetan Plateau (*Zhang et al.*, 2014).

The offset in the Moho may arise from variations in crustal structure across the Intra-Pontide Suture that separates the Istanbul Zone from the Sakarya Terrane. As described in sections 1.1.2 and 1.1.3, the Istanbul Zone and Sakarya Terrane have different tectonic histories, and likely different crustal thickness. My observations are consistent with earlier observations and interpretations which indicate that the North Anatolian Fault has exploited the Intra-Pontide Suture, and this observation is supported by seismic tomography (*Papaleo et al.*, 2017, 2018, *Fichtner et al.*, 2013) and receiver functions (*Kahraman et al.*, 2015).

Key Finding 3: The reflectivity of the Moho is reduced beneath the North Anatolian Fault Zone in the Izmit-Adapazari region, indicating possible serpentinisation of the upper mantle.

The P-wave reflection profiles in Chapters 2 and 4 show reduced amplitude of the Moho reflection in some regions beneath the North Anatolian Fault Zone. The reduction in amplitude is mostly localised to a region of the Moho beneath the northern branch of the North Anatolian Fault, but there is also a substantial reduction in reflection amplitude beneath the Sakarya Terrane. Reductions in the amplitude of the Moho reflection represent a reduction in reflectivity, which is a function of the seismic velocity and density contrast between the crust and mantle.

My observations in Chapters 2 and 4 suggest that a physical process has reduced the impedance contrast between crust and mantle beneath the North Anatolian Fault Zone. One potential mechanism for reducing the impedance contrast is the serpentinisation of the upper mantle peridotite. The serpentinisation of peridotite will significantly reduce both the P-wave velocity and density of the upper mantle (*Birch*, 1960, *Christensen*, 1966, 2004). Serpentinisation is a metamorphic process that requires the presence of water (*Moody*, 1976). Geological evidence from both the San Andreas and North Anatolian Faults suggests that fractures in the crust can increase the permeability of a fault zone and allow fluids from the mantle to migrate towards the surface (*Pili et al.*, 2011, *Burnard et al.*, 2012). The evidence that I have provided in Chapters 2 and 4 suggests the North Anatolian Fault cuts through the entire crust providing a possible high permeability channel for migration of fluids from the upper mantle.

Key Finding 4: The North Anatolian Fault exploited the pre-existing Intra-Pontide Suture during its formation. The northern branch of the North Anatolian Fault likely dips $\sim 60^\circ$ to the north, possibly along ancient thrust faults associated with the Intra-Pontide Suture.

The results that I presented in Chapters 2, 3 and 4 all suggest that the North Anatolian Fault exploited the Intra-Pontide Suture zone that separates the Istanbul Zone and the Sakarya Terrane. In the upper crust, the surface wave tomography model presented in Chapter 3 shows that the surface traces of both the northern and southern branches of the North Anatolian Fault are located at the edges of the Armutlu Block. At depths shallower than about 10 km, the Armutlu Block is a prominent region of high S-wave velocity in the tomography model, and is likely resistant to internal strain that is instead localised along the two fault strands located on its northern and southern boundaries. The Armutlu Block is also a region of high seismic velocity in the P and S-wave velocity models of *Papaleo et al.* (2017) and *Papaleo et al.* (2018). All large ($> M_w$ 6.7) earthquakes recorded in the Izmit-Adapazari region have occurred along the edges of the Armutlu Block (*Ambraseys and Finkel*, 1991, *Barka et al.*, 2002).

The reflection profiles of the North Anatolian Fault Zone in Chapter 4 show vertical offsets in the Moho that are located $\sim 10 - 20$ km north of the surface trace of the northern branch of the North Anatolian Fault. This horizontal separation suggests that the northern branch of the fault is likely dipping between 60° and 70° towards the north. This dip was estimated to be $\sim 80^\circ$ by *Kahraman et al.* (2015). The vertical S-wave velocity profiles in Chapter 3 appear to show both branches of the North Anatolian Fault as vertical structures within the top 5 km of the crust. This implies that the North Anatolian Fault cuts vertically through the upper crust, but then becomes listric in the middle and lower crust.

Key Finding 5: The fast direction for Rayleigh wave phase velocities is aligned 70° from north, with an average amplitude of $\sim 2.5\%$.

In Figs. 3.8 and 3.9 I showed that the fast direction for Rayleigh waves between 1.5 – 10.0 s consistently aligns $\sim 70^\circ$ from north, with an average magnitude of $\sim 2.5\%$. This fast direction is closely aligned to the 45° direction of maximum extension in the Izmit-Adapazari region (*Allmendinger et al.*, 2007), and agrees well with the $35^\circ - 60^\circ$ fast S-wave polarisation direction found by *Biryol et al.* (2010) for the central North Anatolian Fault. The fact that the fast direction aligns parallel to the direction of maximum extension and not the direction of maximum compression is an indication that mineral fabric is the dominant source of seismic anisotropy in the region (*Kern and Wenk*, 1990, *Mainprice and Nicolas*, 1989), rather than aligned micro-fractures (*Crampin and Lovell*, 1991).

5.6 Recommendations and Future work

5.6.1 Estimating S-wave reflectivity using the autocorrelation method

Chapters 2 and 4 of my thesis focused on estimating the P-wave reflectivity of the Earth by autocorrelating vertical component recordings of ambient seismic noise and the P-wave coda of teleseismic earthquakes. The same principle should apply to estimating S-wave reflectivity. To use the autocorrelation technique for the detection of S-wave reflections, it would be more convenient to use records of horizontal seismic motion generated by either noise or teleseismic earthquakes. Utilising the S-wave coda of teleseismic earthquakes would not be challenging, as the records can simply be rotated into the great circle path that aligns with the source earthquake to obtain radial and tangential components. In ambient noise studies there is no seismic source that can be used as a reference to rotate the recordings, though it may be possible to rotate into some direction that maximises the total energy recorded on one of the horizontal components. In this case the north and east components of a seismometer can be used, although *Tibuleac and von Seggern* (2012) also detected an S-wave reflection from the Moho on the vertical component of motion. The reflection profiles constructed from ambient seismic noise in Chapter 2 (Fig. 2.2) also might be interpreted as an S-wave Moho reflection.

Obtaining S-wave reflectivity is more difficult than P-wave reflectivity for a number of reasons. Firstly, the S-wave coda of teleseismic earthquakes is more complex than the P-wave coda. Due to the later arrival time of S-waves, the coda usually contains more seismic phases such as late P-wave reverberations and conversions between P and s waves. This abundance of seismic phases will lead to an increase in the number of spurious arrivals in the S-wave reflectivity series generated by the correlation between the direct S-wave and later arriving P-waves (*Pham et al.*, 2018). Furthermore, *Sun and Kennett* (2016) show that the high slowness (>8 s deg^{-1}) of teleseismic S-wave arrivals is problematic due to the fact that the autocorrelation method requires waves to be travelling vertically beneath a receiver (*Claerbout*, 1968). S-wave reflections also require significant moveout corrections to be applied prior to stacking the auto-correlation functions. *Sun and Kennett* (2016) suggest that using phases such as *SKS* or the direct S-wave from distant earthquakes may yield the best results. Vertical deep seismic sounding experiments that exploit total internal reflection of S-waves from earthquakes within the 30° – 50° degree distance range have also had success in producing S-wave reflection profiles of the Moho (*Tseng et al.*, 2009, *Chen et al.*, 2013).

5.6.2 Improving the retrieval of lithospheric reflections using the autocorrelation method

Whilst the autocorrelation method should in theory retrieve the full reflection response of a medium beneath a seismometer (*Claerbout*, 1968), the work I present in Chapters 2 and 4 shows that only reflections from strong contrasts in physical properties, such as the Moho, are reliably retrieved. The resolution in the crust may be limited by the frequency of the waves (0.1 – 0.5 Hz) that is used. Autocorrelation studies that have succeeded in imaging crustal structure in high resolution (e.g. *Saygin et al.* (2017)) utilised higher frequency waves (> 2 Hz). One of the reasons for this improvement is the fact that the zero lag peak of the auto-correlation function is wider in time for lower frequency waves, and reflections from shallow interfaces are obscured by this peak. Attenuation of high frequencies that travel long paths within the Earth may limit the potential of using teleseismic coda for the autocorrelation method, and short range, high frequency noise sources may perform better in this regard.

Another explanation for the poor retrieval of lithospheric reflections is that reverberations are typically low amplitude in the noise field and the teleseimic coda. It is likely that a large amount of data is required in order to increase the signal-to-noise ratio of the auto-correlation functions during the stacking process. Using a global dataset of all M_w 6.8 earthquakes contained in the global centroid moment tensor catalogue between 2010 – 2016, *Pham et al.* (2018) were able to construct a correlation wavefield that contained many low amplitude seismic phases. The work of *Pham et al.* (2018) shows that, with sufficient data, the full reflection response of a medium can be constructed, but it may not be possible to produce high resolution images from short recording periods (< 1 year). Combining phase correlation and phase-weighted stacking approaches (*Schimmel and Paulssen*, 1997, *Schimmel*, 1999, *Schimmel et al.*, 2011) may help to overcome the need for a long recording period by enhancing the detectability of low amplitude multiple reflections.

5.6.3 Crustal structure of continental fault zones

My work in Chapter 3 indicates that the physical properties of the crust within the Izmit-Adapazari region have had a large impact on the formation and structure of the North Anatolian Fault, and the behaviour of the earthquake cycle throughout the area. In the top 10 km of the crust, both branches of the North Anatolian Fault appear to be vertical zones of reduced seismic velocity <10 km wide. The Armutlu Block that separates the two fault branches is a prominent zone of high S-wave velocity that is likely resistant to strain and may localise deformation at its northern and southern edges. High resolution images of the upper crust for other continental fault zones, apart from the San Andreas Fault, are rare.

High resolution tomographic images of other continental transform faults such as

the Alpine and Marlborough Fault Zones in New Zealand, and the Altyn Tagh and Kunlun Faults in Tibet would be useful in order to build upon the results from the North Anatolian Fault presented in Chapter 3, and those of the San Andreas Fault. Further experiments along other sections of the North Anatolian Fault would also make for important comparisons. In particular, seismic images would help constrain the geometry and thickness of the fault zone in the upper crust, and the interaction between rheologically strong tectonic units and regional deformation. Both the San Andreas Fault at Parkfield and the North Anatolian Fault in the Izmit-Adapazari region appear to be less than 10 km wide in the top 15 km of the crust, and appear to have exploited a suture zone or boundary between two tectonic units during formation. It would be important to observe the behaviour of other fault zones in regions where no pre-existing suture zone is present. In addition, the extent to which regions of high seismic velocity affect fault zone localisation and seismicity is of great importance to the study of seismic hazard.

5.6.4 Reduction in amplitude of the Moho reflection

The reduction in the impedance and velocity contrast across the Moho has been noted for both the San Andreas Fault and the North Anatolian Fault. I posited in Chapters 2 and 4 that fractures in the crust generated by faulting may increase the permeability of the fault zone, and could encourage the migration of fluids through the crust, likely from upper mantle sources (*Pili et al.*, 2011, *Burnard et al.*, 2012). The process of serpentinisation reduces the impedance contrast between the upper mantle and lower crust, and thus reduces the amplitude of the Moho reflection.

More work is required in order to verify if this is a plausible mechanism. In particular, seismic images of other fault zones as described in section 5.6.3 are needed in order to assess whether the reduction in Moho amplitude is indeed widespread beneath continental faults, or whether this process could be unique to faults that are located within ancient suture zones following the cessation of subduction (*Kirby et al.*, 2014).

5.7 Concluding remarks

In this thesis I built on previous methods and developed enhanced techniques for retrieving reflections from both ambient seismic noise and the P-wave coda of teleseismic earthquakes using auto-correlation functions. I demonstrated the use of the autocorrelation method on a seismic data set collected in north-western Turkey in the vicinity of the North Anatolian Fault. I created high resolution reflection images of the lithospheric structure of the North Anatolian Fault and identified vertical offsets in the Moho that appear to be correlated with a fault trace that dips 60° to 70° towards the north. In addition, I detected a reduction in P-wave reflectivity of the Moho beneath the North Anatolian Fault Zone, and I proposed that this reduction could be due to

serpentinisation of the upper mantle. I also constructed an S-wave velocity model of the top 10 km of the Izmit-Adapazari region using ambient noise surface wave tomography. This S-wave velocity model allowed me to image the North Anatolian Fault as a narrow vertical structure that is less than 10 km wide in the upper crust. The S-wave velocity model also shows that the Armutlu Block, a region of high S-wave velocity, is resistant to strain, and appears to localise deformation associated with the North Anatolian Fault to its northern and southern boundaries. Other important structural parameters, such as the thickness of the sedimentary basins in the Izmit-Adapazari region, can also be retrieved from the S-wave velocity model. This thesis has contributed to understanding the structure and behaviour of continental fault zones, as well as the development of novel seismic imaging techniques that can be applied across the planet.

References

Allmendinger, R. W., R. Reilinger, and J. Loveless (2007), Strain and rotation rate from GPS in Tibet, Anatolia, and the Altiplano, *Tectonics*, *26*, doi:10.1029/2006TC002030. 5.1.2, 5.5

Altuncu Poyraz, S., M. U. Teoman, N. Türkelli, M. Kahraman, D. Cambaz, A. Mutlu, S. Rost, G. A. Houseman, D. A. Thompson, D. Cornwell, M. Utkucu, and L. Gülen (2015), New constraints on micro-seismicity and stress state in the western part of the North Anatolian Fault Zone: Observations from a dense seismic array, *Tectonophys.*, *656*, doi:10.1016/j.tecto.2014.03.015. 5.3, 5.4, 5.5

Ambraseys, N. N., and C. F. Finkel (1991), Long-term seismicity of Istanbul and of the Marmara Sea region, *Terra Nova*, *3*, doi:10.1111/j.1365-3121.1991.tb00188.x. 5.5

Bakun, W. H., and A. G. Lindh (1985), The Parkfield, California, earthquake prediction experiment, *Science*, *229*, doi:10.1126/science.229.4714.619. 5.1.1

Bakun, W. H., and T. V. McEvilly (1984), Recurrence models and Parkfield, California, earthquakes, *J. Geophys. Res.*, *89*, doi:10.1029/JB089iB05p03051. 5.1.1

Barka, A., H. S. Akyüz, E. Altunel, G. Sunel, Z. Çakir, A. Dikbas, B. Yerli, R. Armijo, B. Meyer, J. B. de Chabalier, T. Rockwell, J. Dolan, R. Hartleb, T. Dawson, S. Christofferson, A. Tucker, T. Fumal, R. Langridge, R. Stenner, W. Lettis, J. Bachhuber, and W. Page (2002), The Surface Rupture and Slip Distribution of the 17 August 1999 Izmit Earthquake (M 7.4), North Anatolian Fault, *Bull. Seismol. Soc. Am.*, *92*, doi:10.1785/0120000841. 5.1.1, 5.5

Becker, G., and B. Knapmeyer-Endrun (2017), Crustal thickness across the Trans-European Suture Zone from ambient noise autocorrelations, *Geophys. J. Int.*, *212*, doi:10.1093/gji/ggx485. 5.4

Behr, W. M., and G. Hirth (2014), Rheological properties of the mantle lid beneath the Mojave region in southern California, *Earth Planet. Sci. Lett.*, *393*, doi:10.1016/j.epsl.2014.02.039. 5.1.3

Birch, F. (1960), The velocity of compressional waves in rocks to 10 kilobars, *J. Geophys. Res*, *65*, doi:10.1029/JZ066i007p02199. 5.5

Biryol, C. B., G. Zandt, S. L. Beck, A. A. Ozacar, H. E. Adiyaman, and C. R. Gans (2010), Shear wave splitting along a nascent plate boundary: the North Anatolian Fault Zone, *Geophys. J. Int.*, *181*, doi:10.1111/j.1365-246X.2010.04576.x. 5.1.2, 5.5

Brocher, T. M., T. Parsons, A. M. Tréhu, C. M. Snelson, and M. A. Fisher (2003), Seismic evidence for widespread serpentinized forearc upper mantle along the Cascadia margin, *Geology*, *31*, doi:10.1130/0091-7613(2003)031¡0267:SEFWSF¿2.0.CO;2. 5.2

Bürgmann, R., and G. Dresen (2008), Rheology of the lower crust and upper mantle: Evidence from rock mechanics, geodesy, and field observations, *Annu. Rev. Earth Planet. Sci.*, *36*, doi:10.1146/annurev.earth.36.031207.124326. 5.1.3

Burnard, P., S. Bourlange, P. Henry, L. Geli, M. D. Tryon, B. Natal'in, A. M. C. Şengör, M. S. Özeren, and M. N. Çagatay (2012), Constraints on fluid origins and migration velocities along the Marmara Main Fault (Sea of Marmara, Turkey) using helium isotopes, *Earth Planet. Sci. Lett.*, *341-344*, doi:10.1016/j.epsl.2012.05.042. 5.1.4, 5.2, 5.5, 5.6.4

Catchings, R. D., M. J. Ryman, M. R. Goldman, J. A. Hole, R. Huggins, and C. Lippus (2002), High-Resolution Seismic Velocities and Shallow Structure of the San Andreas Fault Zone at Middle Mountain, Parkfield, California, *Bull. Seismol. Soc. Am.*, *92*, doi:10.1785/0120010263. 5.1.1, 5.1

Cetin, E., Z. Cakir, M. Meghraoui, S. Ergintav, and A. M. Akoglu (2014), Extent and distribution of aseismic slip on the Ismetpaşa segment of the North Anatolian Fault (Turkey) from Persistent Scatterer InSAR, *Geochem. Geophy. Geosy.*, *15*, doi:10.1002/2014GC005307. 5.2

Chen, W. P., C. Q. Yu, T. L. Tseng, Z. Yang, C. Y. Wang, J. Ning, and T. Leonard (2013), Moho, seismogenesis, and rheology of the lithosphere, *Tectonophys.*, *609*, doi:10.1016/j.tecto.2012.12.019. 5.6.1

Christensen, N. I. (1966), Elasticity of ultrabasic rocks, *J. Geophys. Res*, *71*, doi:10.1029/JZ071i024p05921. 5.5

Christensen, N. I. (2004), Serpentinites, Peridotites, and Seismology, *Int. Geol. Rev.*, *46*, doi:10.2747/0020-6814.46.9.795. 5.5

Claerbout, J. F. (1968), Synthesis of a layered medium from its acoustic transmission response, *Geophysics*, *33*, doi:10.1190/1.1439927. 5.5, 5.6.1, 5.6.2

Crampin, S., and J. H. Lovell (1991), A decade of shear-wave splitting in the Earth's crust: what does it mean? What use can we make of it? And what should we do next?, *J. Geophys. Int.*, *107*, doi:10.1111/j.1365-246X.1991.tb01401.x. 5.1.2, 5.5

Şengör, A. M. C., and Y. Yılmaz (1981), Tethyan evolution of Turkey: A plate tectonic approach, *Tectonophys.*, *75*, doi:10.1016/0040-1951(81)90275-4. 5.1.1, 5.2

Şengör, A. M. C., O. Tüysüz, C. İmren, M. Sakınç, H. Eyidoğan, N. Görür, X. L. Pichon, and C. Rangin (2005), The North Anatolian Fault: A New Look, *Annu. Rev. Earth Planet. Sci.*, *33*, doi:10.1146/annurev.earth.32.101802.120415. 5.2

Dickinson, W. R. (1966), Structural relationships of San Andreas fault system, Chalome Valley, and Castle Mountain Range, California, *Geol. Soc. Am. Bull.*, *77*, doi:10.1130/0016-7606(1966)77[707:SROSAF]2.0.CO;2. 5.1.1

Eberhart-Phillips, D., and A. J. Michael (1993), Three-dimensional velocity structure, seismicity, and fault structure in the Parkfield Region, Central California, *J. Geophys. Res.*, *98*, doi:10.1029/93JB01029. 5.1.1

Ernst, W. G. (1970), Tectonic contact between the Franciscan melange and the Great Valley sequence: Crustal expression of a late Mesozoic Benioff zone, *J. Geophys. Res.*, *75*, doi:10.1029/JB075i005p00886. 5.1.1

Farrell, K. (2017), Characterising the deep structure and seismic signature of an exhumed ductile shear zone. 5.1.2

Faulkner, D. R., and E. H. Rutter (2001), Can the maintenance of overpressured fluids in large strike-slip fault zones explain their apparent weakness?, *Geology*, *29*, doi:10.1130/0091-7613(2001)029¡0503:CTMOOF¿2.0.CO;2. 5.2

Fialko, Y. (2006), Interseismic strain accumulation and the earthquake potential on the southern San Andreas fault system, *Nature*, *441*, doi:10.1038/nature04797. 5.1.1

Fichtner, A., E. Saygin, T. Taymaz, P. Cupillard, Y. Capdeville, and J. Trampert (2013), The deep structure of the North Anatolian Fault Zone, *Earth Planet. Sci. Lett.*, *373*, doi:10.1016/j.epsl.2013.04.027. 5.5

Ford, H. A., K. M. Fischer, and V. Lekic (2014), Localized shear in the deep lithosphere beneath the San Andreas fault system, *Geology*, *42*, doi:10.1130/G35128.1. 5.1.3

Galetti, E., and A. Curtis (2012), Generalised receiver functions and seismic interferometry, *Tectonophys.*, *532-535*, doi:10.1016/j.tecto.2011.12.004. 5.5

Gorbatov, A., E. Saygin, and B. L. N. Kennett (2013), Crustal properties from seismic station autocorrelograms, *Geophys. J. Int.*, *192*, doi:10.1093/gji/ggs064. 5.4, 5.5

Guillot, S., S. Schwartz, B. Reynard, P. Agard, and C. Prigent (2015), Tectonic significance of serpentinites, *Tectonophys.*, *646*, doi:10.1016/j.tecto.2015.01.020. 5.2

Gupta, I. N. (1965), Standing-wave phenomena in short-period seismic noise, *Geophysics*, *30*, doi:10.1190/1.1439707. 5.4

Hanna, W. F., R. D. Brown, D. C. Ross, and A. Griscom (1972), Aeromagnetic reconnaissance and generalized geologic map of the San Andreas fault between San Francisco and San Bernardino, California, *US Geol. Surv. Geophys. Investig. Map GP-815*. 5.2

Heath, B. A., E. E. E. Hooft, and D. R. Toomey (2018), Autocorrelation of the Seismic Wavefield at Newberry Volcano: Reflections From the Magmatic and Geothermal Systems, *Geophys. Res. Lett.*, *45*, doi:10.1002/2017GL076706. 5.4

Hennino, R., N. Trégourès, N. M. Shapiro, L. Margerin, M. Campillo, B. A. van Tiggelen, and R. L. Weaver (2001), Observation of Equipartition of Seismic Waves, *Phys. Rev. Lett.*, *86*, doi:10.1103/PhysRevLett.86.3447. 5.4

Hetényi, G., Y. Ren, B. Dando, G. W. Stuart, E. Hegedüs, A. C. Kovács, and G. A. Houseman (2015), Crustal structure of the Pannonian Basin: The AlCaPa and Tisza Terrains and the Mid-Hungarian Zone, *Tectonophys.*, *646*, doi:10.1016/j.tecto.2015.02.004. 5.1.4

Hussain, E., A. Hooper, T. J. Wright, R. J. Walters, and D. Bekaert (2016a), Interseismic strain accumulation across the central North Anatolian Fault from iteratively unwrapped InSAR measurements, *J. Geophys. Res. Solid Earth*, *121*, doi:10.1002/2016JB013108. 5.1.1

Hussain, E., T. J. Wright, R. J. Walters, D. Bekaert, A. Hooper, and G. A. Houseman (2016b), Geodetic observations of postseismic creep in the decade after the 1999 Izmit earthquake, Turkey: Implications for a shallow slip decit, *J. Geophys. Res. Solid Earth*, *121*, doi:10.1002/2015JB012737. 5.1.1, 5.2

Kahraman, M., D. G. Cornwell, D. A. Thompson, S. Rost, G. A. Houseman, N. Türkelli, U. Teoman, S. Altuncu Poyraz, M. Utkucu, and L. Gülen (2015), Crustal-scale shear zones and heterogeneous structure beneath the North Anatolian Fault Zone, Turkey, revealed by a high-density seismometer array, *Earth Planet. Sci. Lett.*, *430*, doi:10.1016/j.epsl.2015.08.014. 5.1.3, 5.1.4, 5.3, 5.3, 5.5

Kennett, B. L. N. (2015), Lithosphereasthenosphere P-wave reflectivity across Australia, *Earth Planet. Sci. Lett.*, *431*, doi:10.1016/j.epsl.2015.09.039. 5.4, 5.5

Kennett, B. L. N., E. Saygin, and M. Salmon (2015), Stacking autocorrelograms to map Moho depth with high spatial resolution in southeastern Australia, *Geophys. Res. Lett.*, *42*, doi:10.1002/2015GL065345. 5.4, 5.5

Kern, H., and H. R. Wenk (1990), Fabricrelated velocity anisotropy and shear wave splitting in rocks from the Santa Rosa Mylonite Zone, California, *J. Geophys. Res. Solid Earth*, *95*, doi:10.1029/JB095iB07p11213. 5.1.2, 5.5

Kirby, S. H., K. Wang, and T. M. Brocher (2014), A large mantle water source for the northern San Andreas fault system: a ghost of subduction past, *Earth, Planets and Space*, *66*, doi:10.1186/1880-5981-66-67. 5.2, 5.6.4

Koper, K. D., K. Seats, and H. Benz (2010), On the Composition of Earths Short-Period Seismic Noise Field, *Bull. Seismol. Soc. Am.*, *100*, doi:10.1785/0120090120. 5.4

Lin, F. C., and B. Schmandt (2014), Upper crustal azimuthal anisotropy across the contiguous U.S. determined by Rayleigh wave ellipticity, *Geophys. Res. Lett.*, *41*, doi:10.1002/2014GL062362. 5.1.2

Lin, F. C., M. H. Ritzwoller, and R. Snieder (2009), Eikonal tomography: surface wave tomography by phase front tracking across a regional broad-band seismic array, *Geophys. J. Int.*, *177*, doi:10.1111/j.1365-246X.2009.04105.x. 5.1.2

Lyons, S., and D. Sandwell (2003), Fault creep along the southern San Andreas from interferometric synthetic aperture radar, permanent scatterers, and stacking, *J. Geophys. Res. Solid Earth*, *108*, doi:10.1029/2002JB001831. 5.1.1

Mainprice, D., and A. Nicolas (1989), Development of shape and lattice preferred orientations: application to the seismic anisotropy of the lower crust, *J. Struct. Geol.*, *11*, doi:10.1016/0191-8141(89)90042-4. 5.1.2, 5.5

Manaker, D. M., E. Calais, A. M. Freed, S. T. Ali, P. Przybylski, G. Mattioli, P. Jansma, C. de Prepetit, and J. B. Chabalier (2008), Interseismic plate coupling and strain partitioning in the northeastern Caribbean, *Geophys. J. Int.*, *174*, doi:10.1111/j.1365-246X.2008.03819.x. 5.2

McPhee, D. K., R. C. Jachens, and C. M. Wentworth (2004), Crustal structure across the San Andreas Fault at the SAFOD site from potential field and geologic studies, *Geophys. Res. Lett.*, *31*, doi:10.1029/2003GL019363. 5.2

Moody, J. B. (1976), Serpentinization: a review, *Lithos*, *9*, doi:10.1016/0024-4937(76)90030-X. 5.5

Moore, D. E., and M. J. Rymer (2007), Talc-bearing serpentinite and the creeping section of the San Andreas fault, *Nature*, *448*, doi:10.1038/nature06064. 5.2

Moore, D. E., D. A. Lockner, M. Shengli, R. Summers, and J. D. Byerlee (1997), Strengths of serpentinite gouges at elevated temperatures, *J. Geophys. Res.*, *102*, doi:10.1029/97JB00995. 5.2

Nakata, N., R. Snieder, and M. Behm (2014), Body-wave interferometry using regional earthquakes with multidimensional deconvolution after wavefield decomposition at the free surface, *Geophys. J. Int.*, *199*, doi:10.1093/gji/ggu316. 5.5

Okay, A. L., and O. Tüysüz (1999), Tethyan sutures of northern Turkey, *Geological Society, London, Special Publications*, *156*, doi:10.1144/GSL.SP.1999.156.01.22. 5.1.1

Oren, C., and R. L. Nowack (2017), Seismic body-wave interferometry using noise autocorrelations for crustal structure, *Geophys. J. Int.*, *208*, doi:10.1093/gji/ggw394. 5.4

Papaleo, E., D. G. Cornwell, and N. Rawlinson (2017), Seismic tomography of the North Anatolian Fault: New insights into structural heterogeneity along a continental strikeslip fault, *Geophys. Res. Lett.*, *44*, doi:10.1002/2017GL072726. 5.5

Papaleo, E., D. G. Cornwell, and N. Rawlinson (2018), Constraints on North Anatolian Fault zone width in the crust and upper mantle from Swave teleseismic tomography, *J. Geophys. Res. Solid Earth*, doi:10.1002/2017JB015386. 5.5

Peterson, J. (1993), Observations and modelling of background seismic noise., *Open-file report 93-322, US Geological Survey, Albuquerque, New Mexico.* 5.4

Pham, T., and H. Tkalčić (2017), On the feasibility and use of teleseismic P wave coda autocorrelation for mapping shallow seismic discontinuities, *J. Geophys. Res. Solid Earth*, *122*, doi:10.1002/2017JB013975. 5.4

Pham, T., H. Tkalčić, M. Sambridge, and B. L. N. Kennett (2018), Earth's Correlation Wavefield: Late Coda Correlation, *Geophys. Res. Lett.*, *45*, doi:10.1002/2018GL077244. 5.6.1, 5.6.2

Pili, É., B. M. Kennedy, M. E. Conrad, and J. P. Gratier (2011), Isotopic evidence for the infiltration of mantle and metamorphic CO_2H_2O fluids from below in faulted rocks from the San Andreas Fault system, *Chem. Geol.*, *281*, doi:10.1016/j.chemgeo.2010.12.011. 5.1.4, 5.2, 5.5, 5.6.4

Reinen, L. A., J. D. Weeks, and T. E. Tullis (1994), The frictional behavior of lizardite and antigorite serpentinites: experiments, constitutive models, and implications for natural faults, *Pure Appl. Geophys.*, *143*, doi:10.1007/BF00874334. 5.2

Revenaugh, J., and C. Reasoner (1997), Cumulative offset of the San Andreas fault in central California: A seismic approach, *Geology*, *25*, doi:10.1130/0091-7613(1997)025¡0123:COOTSA¿2.3.CO;2. 5.1.1

Saygin, E., P. R. Cummins, and D. Lumley (2017), Retrieval of the P wave reflectivity response from autocorrelation of seismic noise: Jakarta Basin, Indonesia, *Geophys. Res. Lett.*, *44*, doi:10.1002/2016GL071363. 5.4, 5.6.2

Schimmel, M. (1999), Phase cross-correlations: Design, comparisons, and applications, *Bull. Seismol. Soc. Am.*, *89*. 5.4, 5.5, 5.6.2

Schimmel, M., and H. Paulssen (1997), Noise reduction and detection of weak, coherent signals through phase-weighted stacks, *Geophys. J. Int.*, *130*, doi:10.1111/j.1365-246X.1997.tb05664.x. 5.4, 5.5, 5.6.2

Schimmel, M., E. Stutzmann, and J. Gallart (2011), Using instantaneous phase coherence for signal extraction from ambient noise data at a local to a global scale, *Geophys. J. Int.*, *184*, doi:10.1111/j.1365-246X.2010.04861.x. 5.4, 5.5, 5.6.2

Seriff, A. J., C. Velzeboer, and R. Haase (1965), Possible P-wave observations in short-period seismic noise, *Geophysics*, *30*, doi:10.1190/1.1439709. 5.4

Sherrington, H. F., G. Zandt, and A. Frederiksen (2004), Crustal fabric in the Tibetan Plateau based on waveform inversions for seismic anisotropy parameters, *J. Geophys. Res. Solid Earth*, *109*, doi:10.1029/2002JB002345. 5.1.2

Stern, T. A., and J. H. McBride (1998), Seismic exploration of continental strike-slip zones, *Tectonophys.*, *286*, doi:10.1016/S0040-1951(97)00255-2. 5.1.3

Sun, W., and B. L. N. Kennett (2016), Receiver structure from teleseisms: Autocorrelation and cross correlation, *Geophys. Res. Lett.*, *43*, doi:10.1002/2016GL069564. 5.6.1

Tank, S. B., Y. Honkura, Y. Ogawa, M. Matsushima, N. Oshiman, and M. K. Tunçer and C. Çelik and E. Tolak and A. M. Işıkara (2005), Magnetotelluric imaging of the fault rupture area of the 1999 zmit (Turkey) earthquake, *Phys. Earth Planet. Int.*, *150*, doi:10.1016/j.pepi.2004.08.033. 5.1.4, 5.2

Taylor, G., S. Rost, and G. Houseman (2016), Crustal imaging across the North Anatolian Fault Zone from the autocorrelation of ambient seismic noise, *Geophys. Res. Lett.*, *43*, doi:10.1002/2016GL067715. 5.4, 5.5

Thurber, C. H., H. Zhang, F. Waldhauser, J. Hardebeck, A. Michael, and D. Eberhart-Phillips (2006), Three-dimensional compressional wavespeed model, earthquake relocations, and focal mechanisms for the Parkfield, California, region, *Bull. Seismol. Soc. Am.*, *96*, doi:10.1785/0120050825. 5.1.1

Tibuleac, I. M., and D. von Seggern (2012), Crust-mantle boundary reflectors in Nevada from ambient seismic noise autocorrelations, *Geophys. J. Int.*, *189*, doi:10.1111/j.1365-246X.2011.05336.x. 5.4, 5.5, 5.6.1

Titus, S. J., L. G. Medaris, H. F. Wang, and B. Tikoff (2007), Continuation of the San Andreas fault system into the upper mantle: Evidence from spinel peridotite xenoliths in the Coyote Lake basalt, central California, *Tectonophys.*, *429*, doi:10.1016/j.tecto.2006.07.004. 5.1.3

Tseng, T. L., W. P. Chen, and R. L. Nowack (2009), Northward thinning of Tibetan crust revealed by virtual seismic profiles, *Geophys. Res. Lett.*, *36*, doi:10.1029/2009GL040457. 5.6.1

Unsworth, M. J., P. E. Malin, G. D. Egbert, and J. R. Booker (1997), Internal structure of the San Andreas fault at Parkfield, California, *Geology*, *25*, doi:10.1130/0091-7613(1997)025¡0359:ISOTSA¿2.3.CO;2. 5.1.4

Weber, M., K. Abu-Ayyash, A. Abueladas, A. Agnon, H. Al-Amoush, A. Babeyko, Y. Bartov, M. Baumann, Z. Ben-Avraham, G. Bock, J. Bribach, R. El-Kelani, A. Förster, H. Förster, U. Frieslander, Z. Garfunkel, S. Grunewald, H. J. Götze, V. Haak, C. Haberland, M. Hassouneh, S. Helwig, A. Hofstetter, K. Jäckel, D. Kesten, R. Kind, N. Maercklin, J. Mechie, A. Mohsen, F. M. Neubauer, R. Oberhänsli, I. Qabbani, O. Ritter, G. Rümpker, M. Rybakov, T. Ryberg, F. Scherbaum, J. Schmidt, A. Schulze, S. Sobolev, M. Stiller, H. Thoss, U. Weckmann, and K. Wylegalla (2004), The crustal structure of the Dead Sea Transform, *Geophys. J. Int.*, *156*, doi:10.1111/j.1365-246X.2004.02143.x. 5.5

Weldon, R. J., and K. E. Sieh (1985), Holocene rate of slip and tentative recurrence interval for large earthquakes on the San Andreas fault, Cajon Pass, southern California, *Geol. Soc. Am. Bull.*, *95*, doi:10.1130/0016-7606(1985)96¡793:HROSAT¿2.0.CO;2. 5.1.1

Wilson, C. K., C. H. Jones, P. Molnar, A. F. Sheehan, and O. S. Boyd (2004), Distributed deformation in the lower crust and upper mantle beneath a continental strike-slip fault zone: Marlborough fault system, South Island, New Zealand, *Geology*, *32*, doi:10.1130/G20657.1. 5.5

Yan, Z., and R. W. Clayton (2007), A notch structure on the Moho beneath the Eastern San Gabriel Mountains, *Earth Planet. Sci. Lett.*, *260*, doi:10.1016/j.epsl.2007.06.017. 5.1.3

Zhang, Z., and S. Y. Schwartz (1994), Seismic anisotropy in the shallow crust of the Loma Prieta segment of the San Andreas Fault System, *J. Geophys. Res. Solid Earth*, *99*, doi:10.1029/94JB00241. 5.1.2

Zhang, Z., Y. Wang, G. A. Houseman, T. Xu, Z. Wu, X. Yuan, Y. Chen, X. Tian, Z. Bai, and J. Teng (2014), The Moho beneath western Tibet: Shear zones and eclogitization in the lower crust, *Earth Planet. Sci. Lett.*, *408*, doi:10.1016/j.epsl.2014.10.022. 5.5

Zhu, L. (2000), Crustal structure across the San Andreas Fault, southern California from teleseismic converted waves, *Earth Planet. Sci. Lett.*, *179*, doi:10.1016/S0012-821X(00)00101-1. 5.1.3, 5.1.4, 5.5

Appendix A

Supplemental material Chapter 2

This supporting information provides figures related to the choice of pre-processing regime applied to our noise recording prior to the calculation of the cross correlation functions (Figs. A.1 and A.2). We show examples of the group velocity - period diagrams used when creating the phase velocity data set (Fig. A.3). We also include a figure illustrating our choice of damping parameter in the Rayleigh and Love wave phase velocity inversions (Fig. A.4). Fig. A.5 and A.6 show the data misfit information for our phase velocity tomography. Figs. A.8 – A.12 provide information on the vertical and horizontal resolution of our phase velocity tomography through sensitivity kernels and checkerboard tests. Fig. A.13 shows the azimuthal variation of our Love wave phase velocities.

A.1 Text A.1. Effect of noise pre-processing on the signal-to-noise ratio of the cross-correlation functions

Fig. A.1 shows the evolution of the signal-to-noise ratio of the cross correlation functions as a function of the amount of data stacked. The signal-to-noise ratio is defined as the ratio between the amplitude of the surface wave arrival, and a 20 s long window of coda energy that arrives late in the correlation function. We show examples for four different noise pre-processing schemes. We test the effects of the noise window duration (1-hour or 4-hours long), as well as different forms of amplitude normalization (1-bit normalization or amplitude clipping). It is clear that the choice of noise pre-processing has little effect on the final signal-to-noise ratios. All pre-processing approaches result in an average signal-to-noise ratio of $\sim$ 16 once all data have been stacked. This analysis was performed on a subset of the data that spanned a period of 3-months. The final tomography utilized data from the full 16-month long deployment of the DANA network.

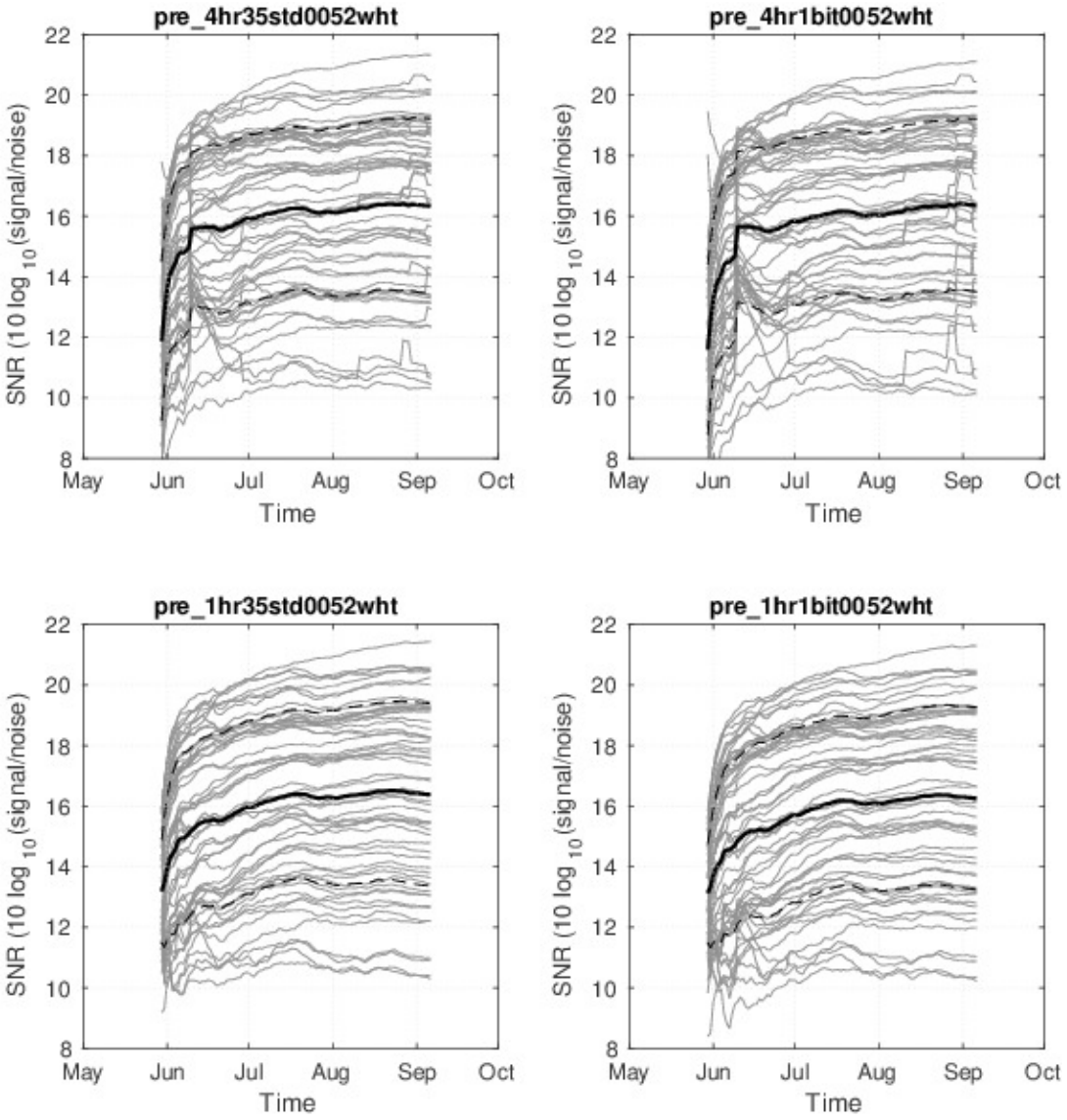

Figure A.1: Effect of noise pre-processing on the signal-to-noise ratio of the cross correlation functions as a function of the amount of data stacked. Each panel shows a different pre-processing scheme. Top left: 4-hour long noise windows with amplitude clipping. Top right: 4-hour long noise windows with 1-bit normalization. Bottom left: 1-hour long noise window with amplitude clipping. Bottom right: 1-hour long noise window with 1-bit normalization. Grey lines represent individual cross correlation functions, and the solid black line represents the mean of all correlation functions. The dashed blacked line indicates one standard deviation.

A.2 Text A.2. Effect of noise pre-processing on the coherency of the cross-correlation functions.

Fig. A.2 shows the power spectral densities of the cross correlation functions under the four different processing schemes (Text A.1.). As with signal-to-noise ratio, there is little variation in coherency between the different approaches. However, amplitude clipping does appear to have a slightly higher power spectral density than the 1-bit normalization approach. The 4-hour long windows are also slightly more coherent than the 1-hour long windows. Given this, we choose the pre-processing scheme that implements amplitude clipping on noise windows that are 4-hours long.

A.3 Text A.3. Examples of group velocity-period diagrams.

Fig. A.3 shows four examples of group velocity - period diagrams that were used in the study. We show examples of Rayleigh wave diagrams taken from the radial-radial cross-correlation functions between stations with inter-station distances of 17 km and 61 km. We also show transverse-transverse cross-correlation functions taken for stations separated by 22 km and 65 km. On the 17 km distance RR component, group and phase velocity values are not picked for periods longer than 4.0 s, as the measurements at long periods are deemed to be unreliable due to the wavelength criterion. On the 22 km TT component, velocity values are not picked above 5.0 s period for the same reason. The group velocity values begin to increase rapidly up to unrealistic values for periods greater than these cut-offs.

A.4 Text A.4. Effect of damping on the phase velocity inversion.

Fig. A.4 shows model variance vs. RMS travel time residual as a function of damping parameter for the final models produced by the Rayleigh and Love wave phase velocity inversions at 4.0 s period. We select the level of damping that gives us a substantial decrease in model variance for only a modest increase in data misfit. We trialled damping parameters with a range between 0 damping and $\epsilon = 500$.

A.5 Text A.5. Data misfit to the Rayleigh and Love wave phase velocity tomography.

Figs. A.5 and A.6 show the data misfit of the phase velocity tomography for Rayleigh and Love waves, respectively. We show the misfit of the initial, constant velocity model

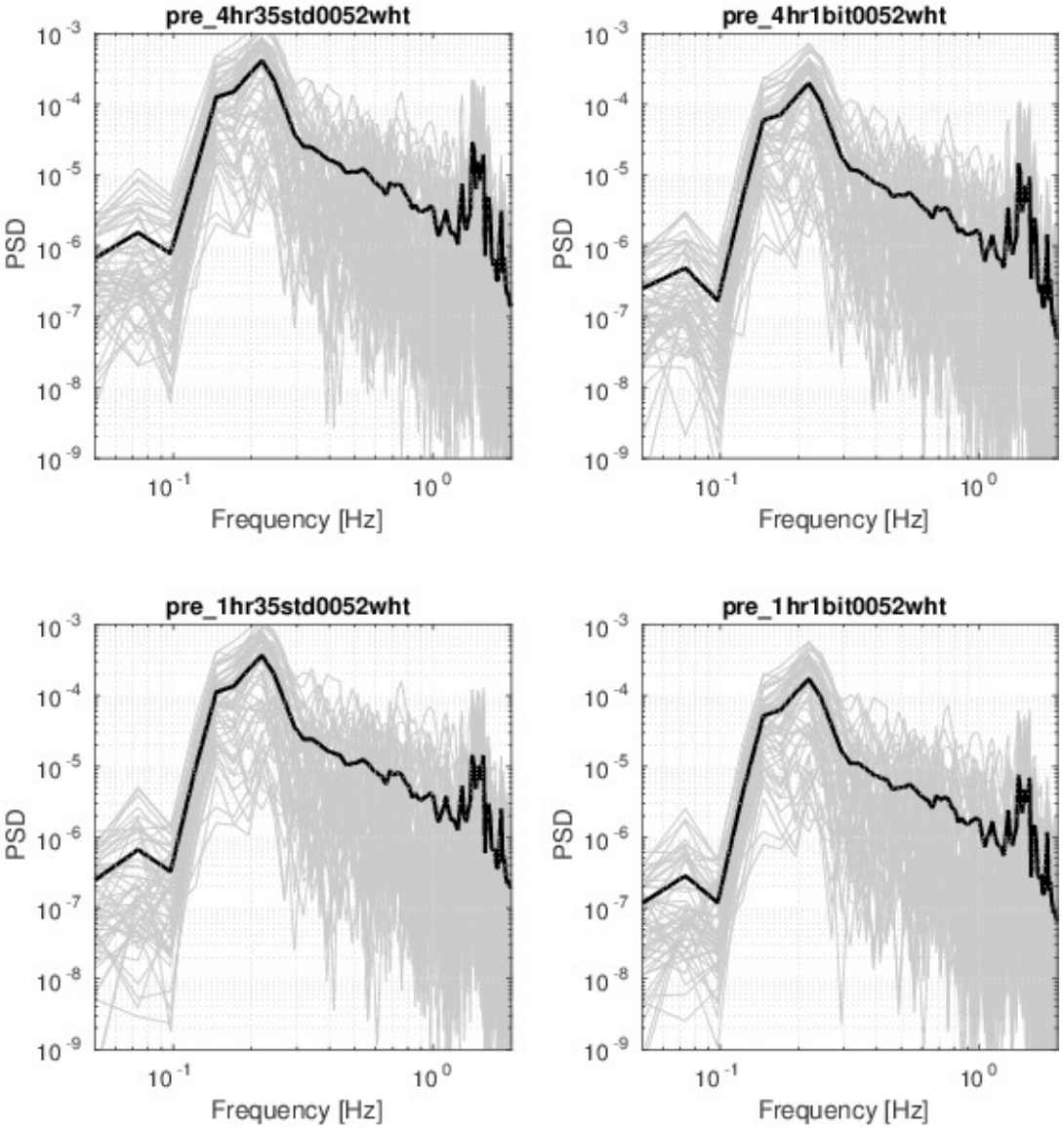

Figure A.2: Effect of noise pre-processing on the coherency of the cross correlation functions. Each panel shows a different pre-processing scheme. Top left: 4-hour long noise windows with amplitude clipping. Top right: 4-hour long noise windows with 1-bit normalization. Bottom left: 1-hour long noise window with amplitude clipping. Bottom right: 1-hour long noise window with 1-bit normalization. Grey lines represent individual cross correlation functions, and the solid black line represents the mean of all correlation functions.

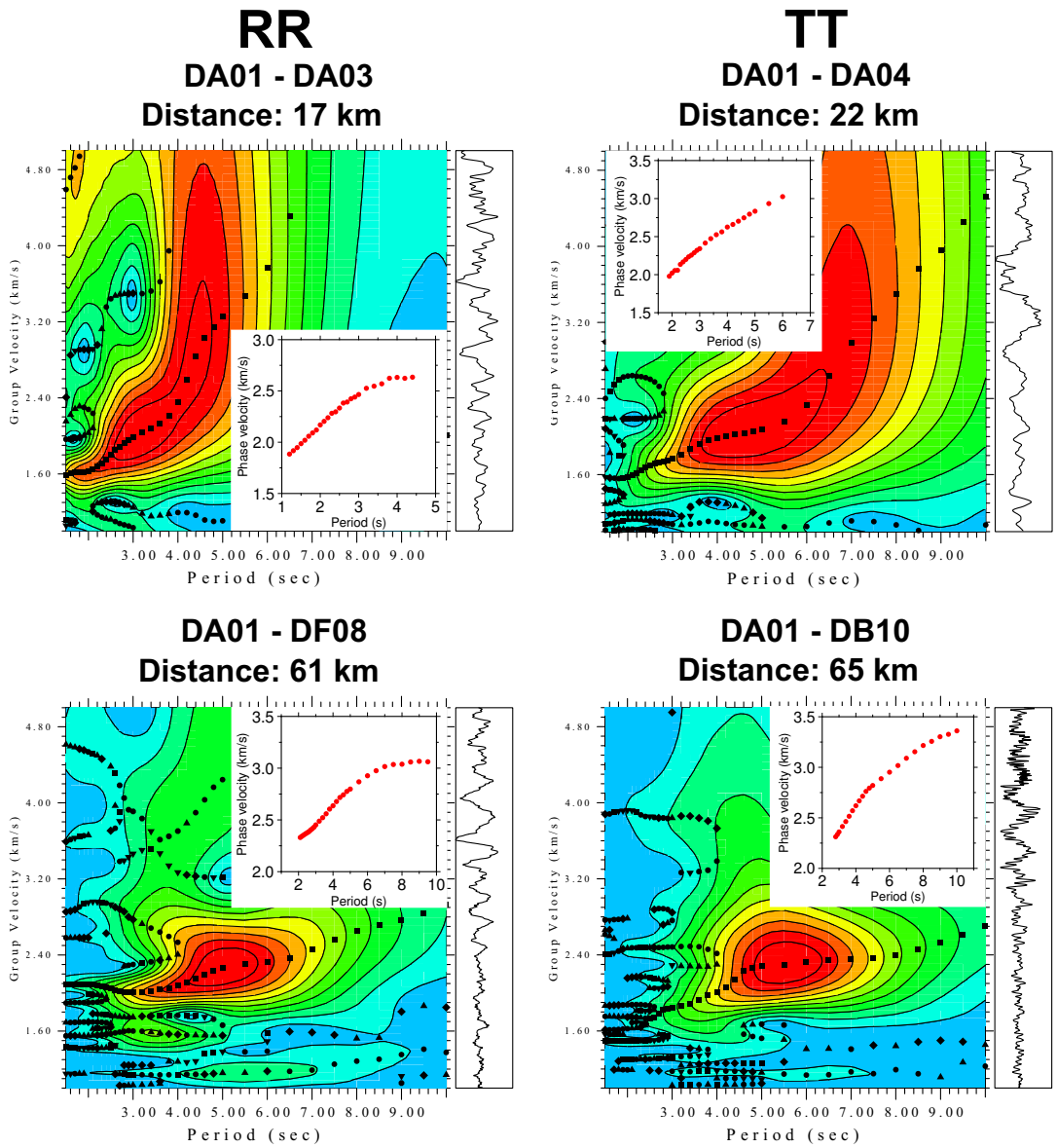

Figure A.3: Examples of period - group velocity maps for four inter-station pairs. The inset dispersion curves are the corresponding phase velocity curves that were picked, shown in red dots. Red colours indicate a larger amplitude for the envelope of the wave at the given period, for each velocity. The black squares indicate the likely group velocity values, which are picked manually. We show dispersion maps for both short and long distances (< 25 km and > 60 km) for both Rayleigh (left column) and Love (right column) waves. The bars of the right hand side of each period - group velocity map shows the cross correlation function.

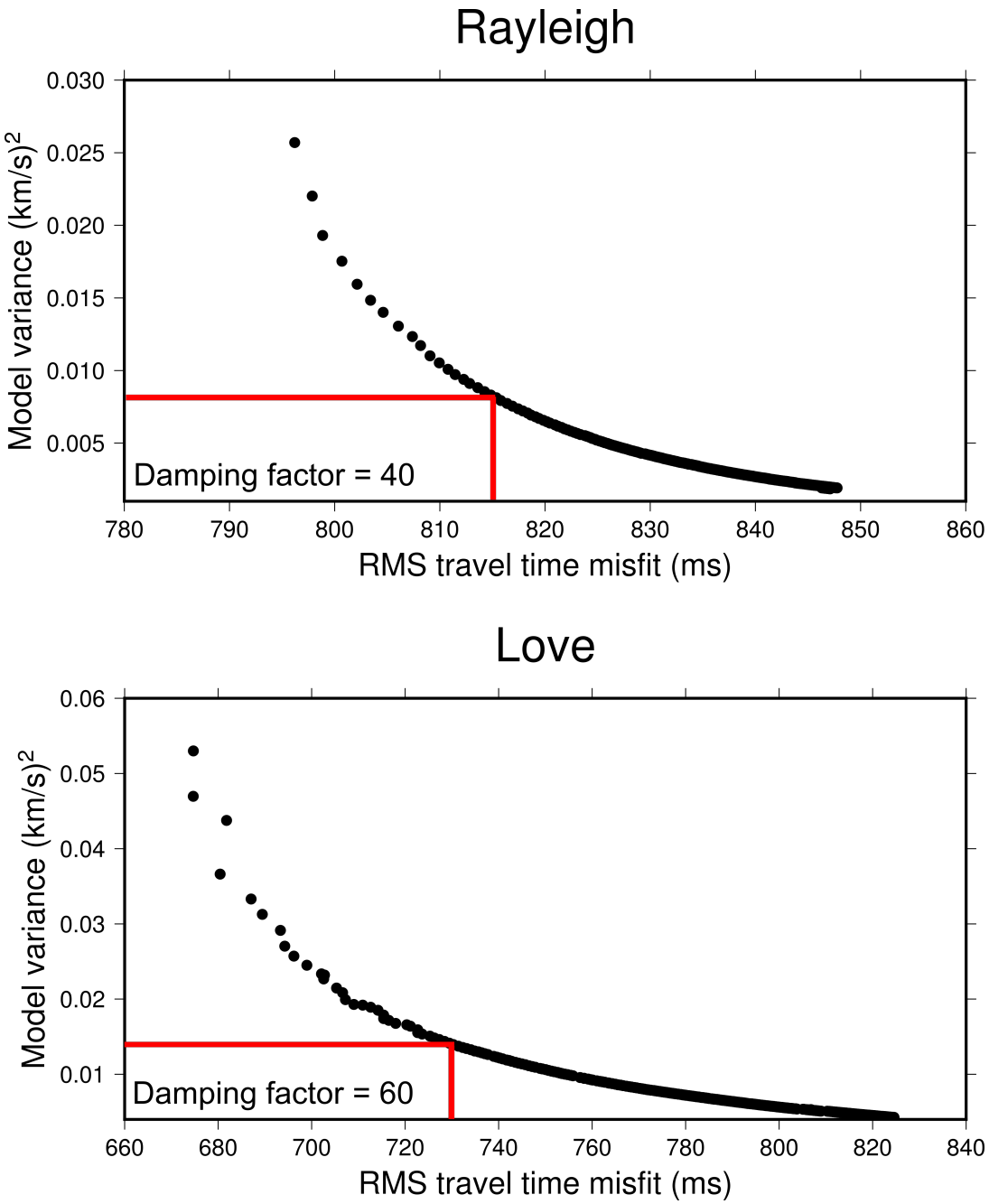

Figure A.4: Top: Effect of damping on the Rayleigh wave phase velocity inversion at 4.0 s period. Bottom: Effect of damping on the Love wave phase velocity inversion. Each black dot represents a trial of a different damping parameter between 0 and 500. The red lines indicate the model variance and data misfit of the chosen damping factor for the inversion, which is indicated on each figure.

prior to the tomographic inversion, and the data misfit of the final phase velocity model at 2.0, 4.0, 6.0 and 8.0 s period. The final phase velocity models are shown in Fig. 3.3 and 3.4 in the main text.

A.6 Text A.6. Data misfit of the S-wave velocity inversion.

Fig. A.7 shows the fit of the individual phase velocity dispersion curves at three nodes in the S-wave velocity model (Fig. 3.5 in the main text). We show the dispersion curves that are extracted from the phase velocity tomographies for both Rayleigh and Love waves, and the corresponding dispersion curves predicted by our final S-wave velocity model. The improvement of fit provided by the linearised inversion over the neighbourhood algorithm result is shown in each row.

A.7 Text A.7. Rayleigh and Love wave sensitivity kernels.

Fig. A.8 shows the partial derivatives of phase velocity with respect to S-wave velocity as a function of depth at each grid point is our final isotropic S-wave velocity model. We show period of 2.0 s, 5.0 s and 8.0 s. This illustrates the depth sensitivity of our phase velocity observations and constrains the depth resolution of our S-wave velocity model. Our long period Rayleigh wave observations maintain sensitivity up to 10.0 km depth, whilst our Love wave observations are sensitive to more shallow structure, mostly above 5.0 km depth.

A.8 Text A.8. Checkerboard tests for the Rayleigh and Love wave phase velocity.

Fig. A.9 shows checkerboard tests that illustrate the horizontal resolution of the Rayleigh wave phase velocity tomography between 3.0 and 9.0 s, Fig. A.10 shows the same image for the Love wave tomography. The maps were obtained by inverting for the original checkerboard pattern from a constant velocity starting model using a noisy synthetic data set with the same ray path distribution as our tomography. The standard deviation of the white noise is 1.5 s. We maintain good horizontal resolution at all periods, through there is some smearing down at long periods (9.0 s) for both Rayleigh and Love waves. In general, the checkerboard pattern is recovered better using the ray distribution of the Love wave tomography, rather than the Rayleigh wave tomography. The corresponding ray path distributions are shown in Figs. A.11 and A.12

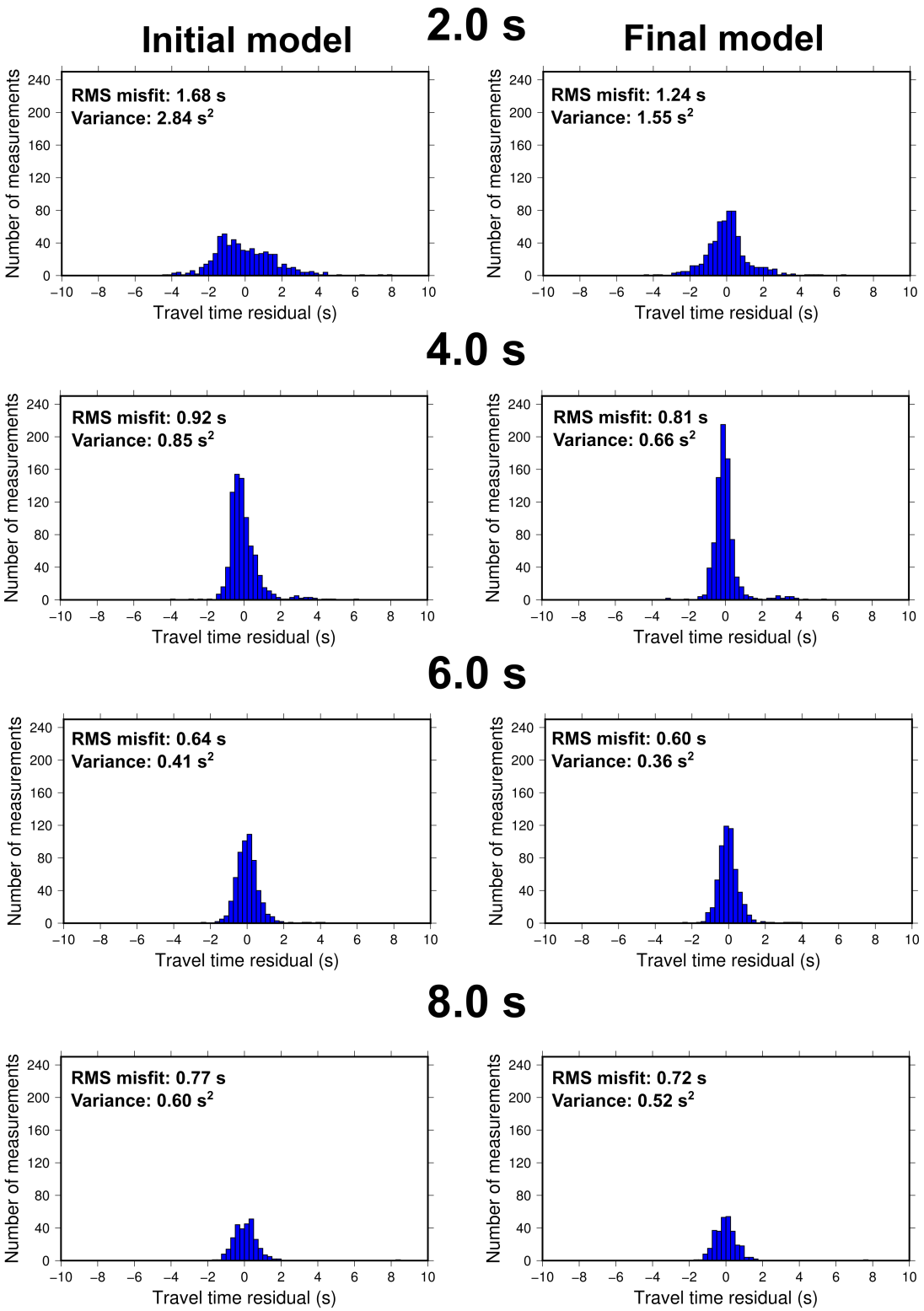

Figure A.5: Data misfit of the Rayleigh wave phase velocity tomography at periods 2.0, 4.0, 6.0 and 8.0 seconds. We show the travel time residual in 0.25 s bins, and the number of measurements that fall in each bin. The left hand column shows the misfit of the original, constant velocity inversion, and the right hand column shows the misfit of the final tomography model. Each histogram is labelled with the corresponding root mean square misfit and variance of the travel time residuals.

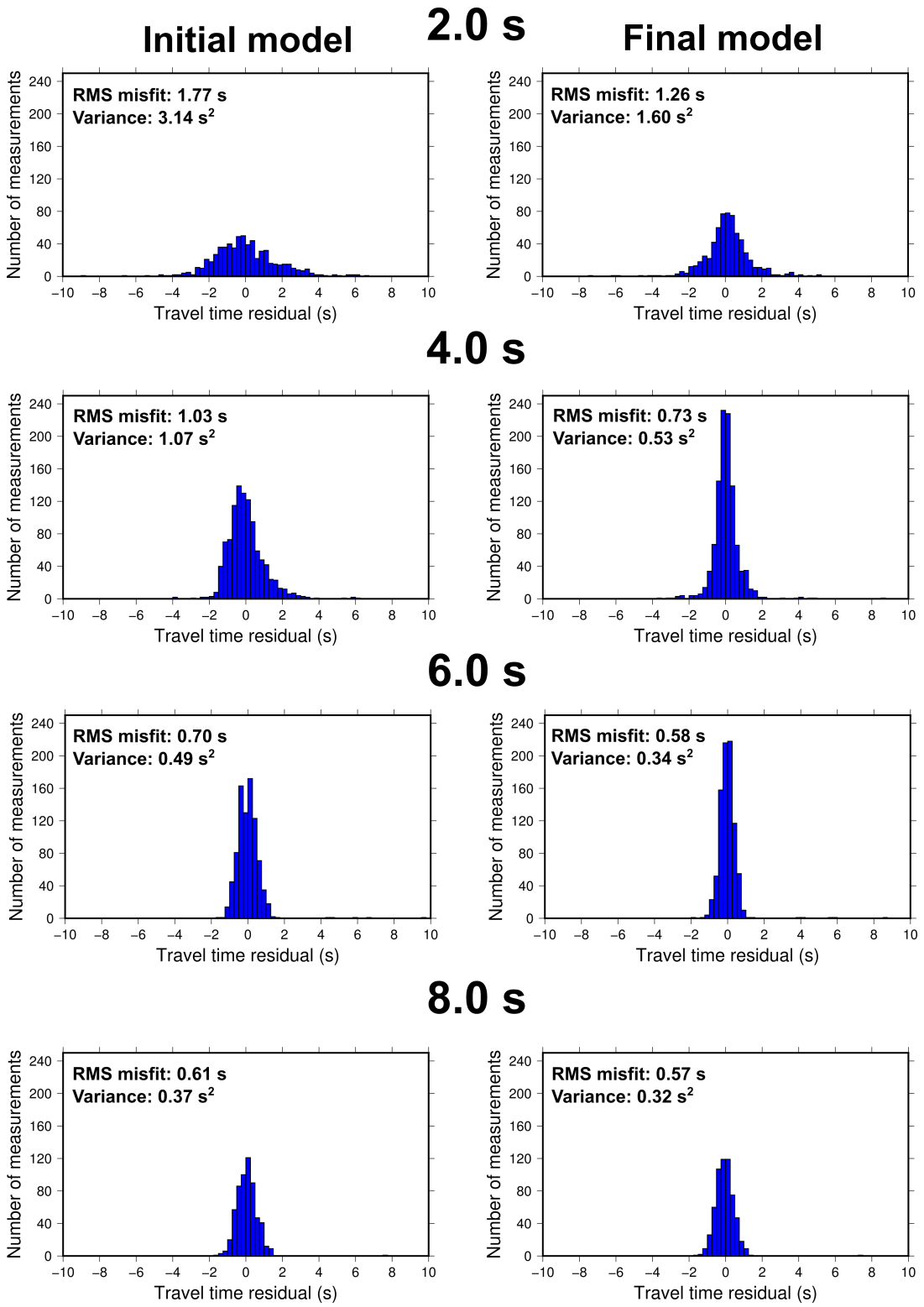

Figure A.6: Data misfit of the Love wave phase velocity tomography at periods 2.0, 4.0, 6.0 and 8.0 seconds. We show the travel time residual in 0.25 s bins, and the number of measurements that fall in each bin. The left hand column shows the misfit of the original, constant velocity inversion, and the right hand column shows the misfit of the final tomography model. Each histogram is labelled with the corresponding root mean square misfit and variance of the travel time residuals.

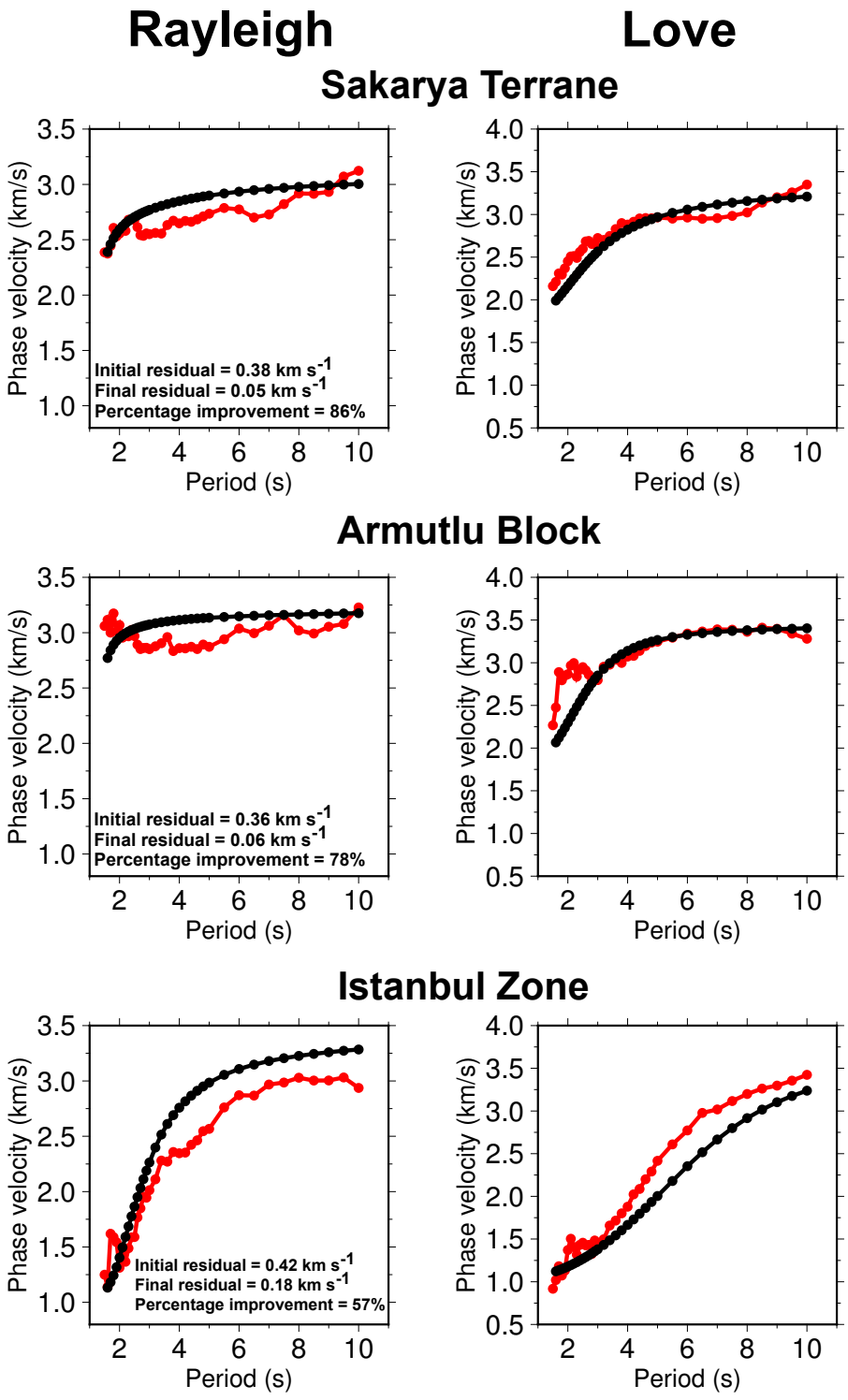

Figure A.7: Dispersion misfit of the S-wave velocity inversion at the three nodes shown in Fig. 3.5 (main text). The fit for Rayleigh wave phase velocities is shown in the left column, Love wave fits are shown on the right. The target dispersion curves from the phase velocity inversion is shown in black, and the red curves show the dispersion calculated from our final S-wave velocity model. The improvement in data fit at each node that results from applying the linearised inversion to the result of the neighbourhood algorithm is indicated on each row, including the final average data residual.

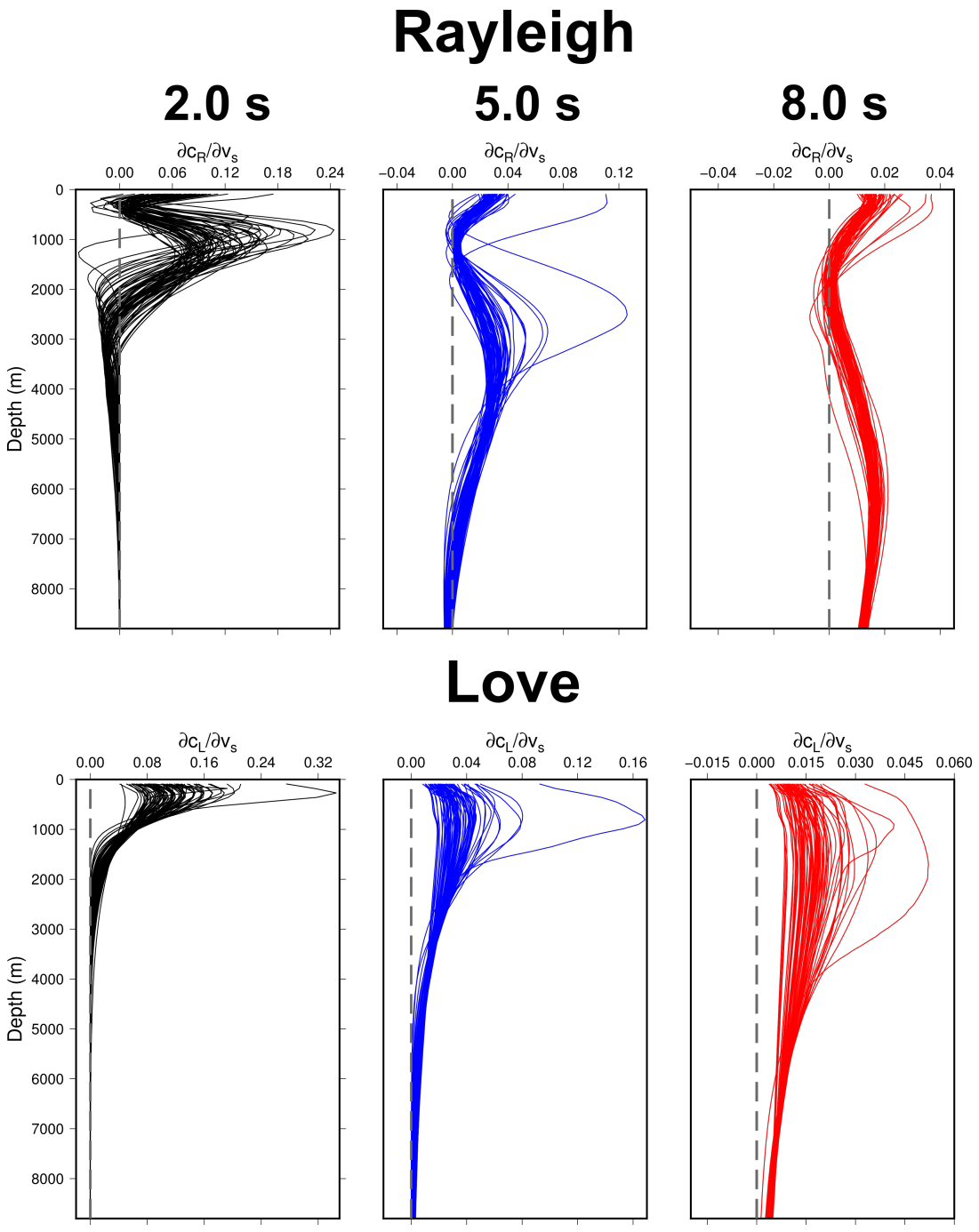

Figure A.8: Top: Partial derivatives of Rayleigh wave phase velocity with respect to S-wave velocity at each grid point in our final S-wave velocity model. Bottom: Partial derivatives of Love wave phase velocity with respect to S-wave velocity at each grid point in our final S-wave velocity model. Black lines show sensitivity at 2.0 s period, blue lines 5.0 s period and red lines 8.0 s period.

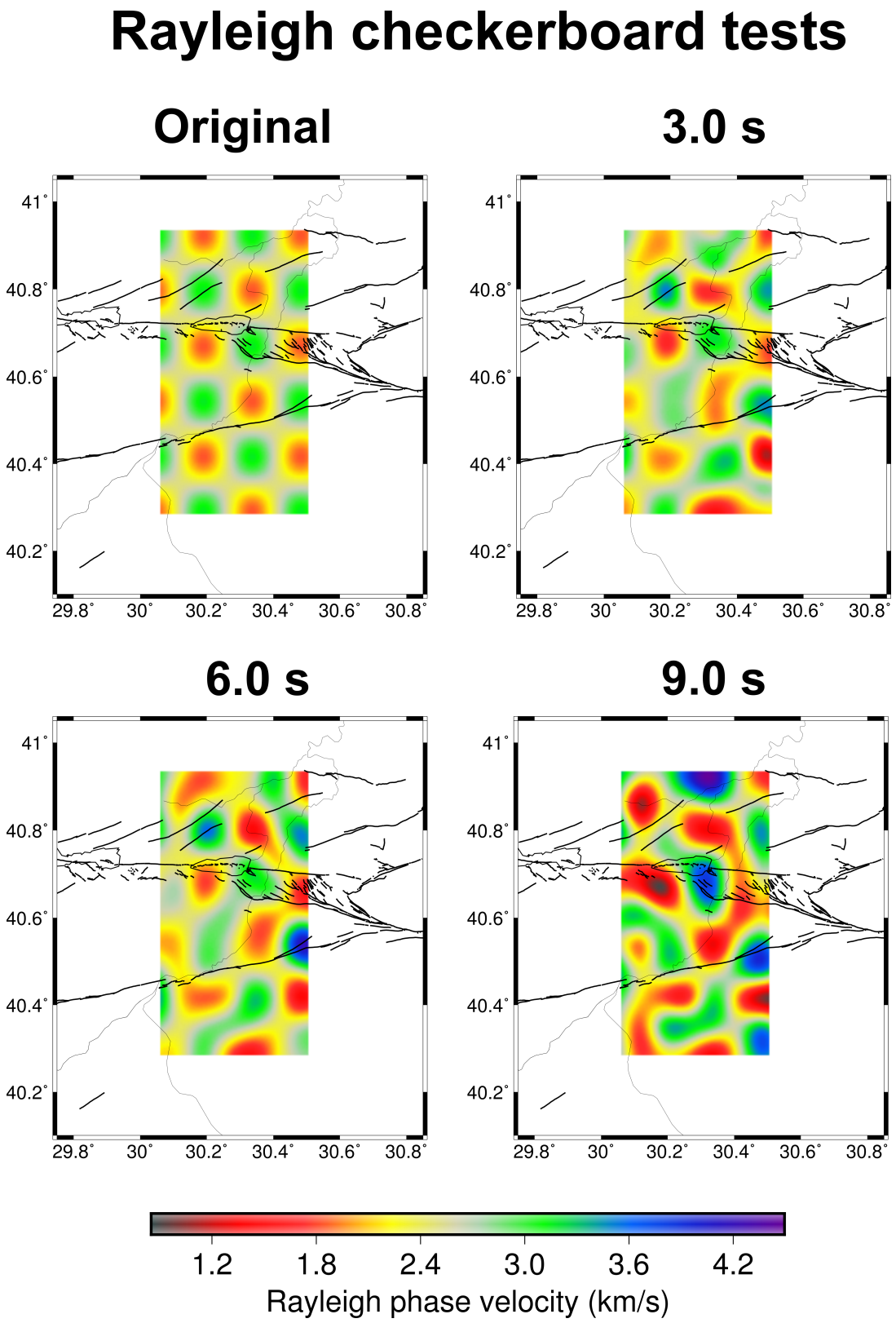

Figure A.9: Checkerboard tests for the Rayleigh wave phase velocity tomography between 3.0 s and 9.0 s. The top left panel shows the original checkerboard that we attempt to retrieve using a noisy synthetic data set with our ray path distribution at each period. Thick black lines represent the locations of the mapped faults. The thin black line represents the Sakarya River.

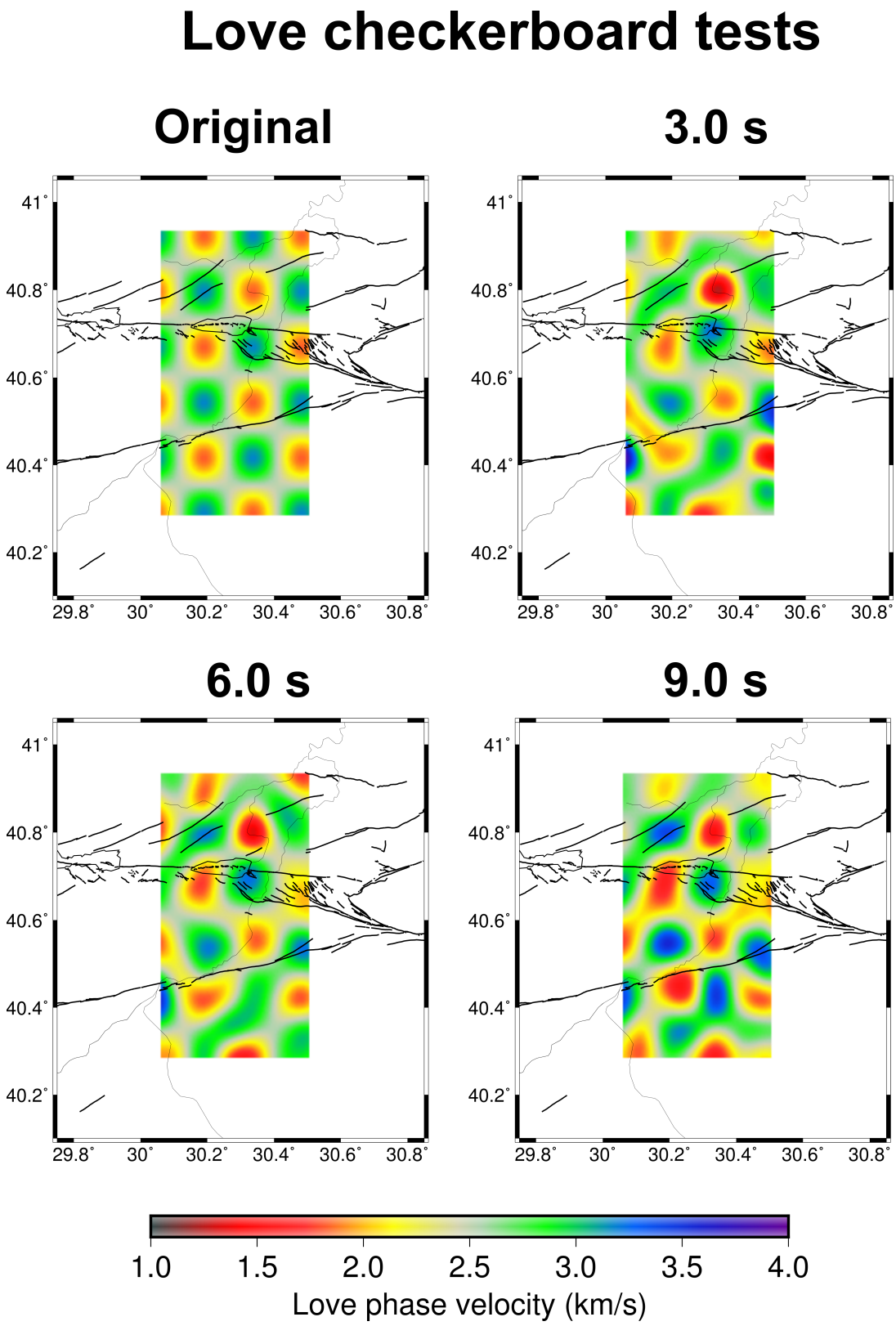

Figure A.10: Checkerboard tests for the Love wave phase velocity tomography between 3.0 s and 9.0 s. The top left panel shows the original checkerboard that we attempt to retrieve using a noisy synthetic data set with our ray path distribution at each period. Thick black lines represent the locations of the mapped faults. The thin black line represents the Sakarya River.

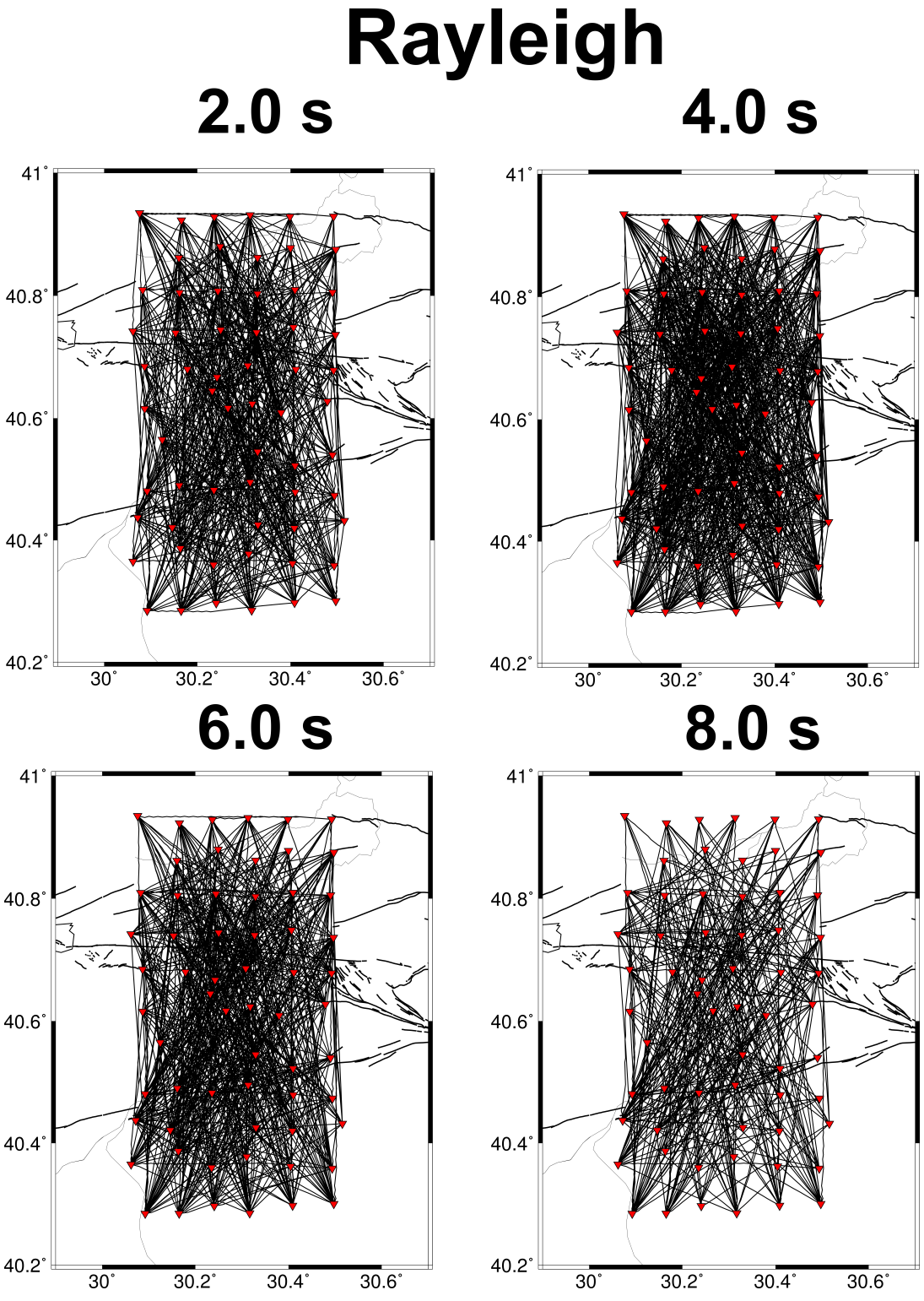

Figure A.11: Ray path distribution for the Rayleigh wave phase velocity tomography between 2.0 s and 8.0 s. Red triangles show stations of the DANA network. The black lines connecting them are the ray paths. Thick black lines represent the locations of the mapped faults. The thin black line represents the Sakarya River.

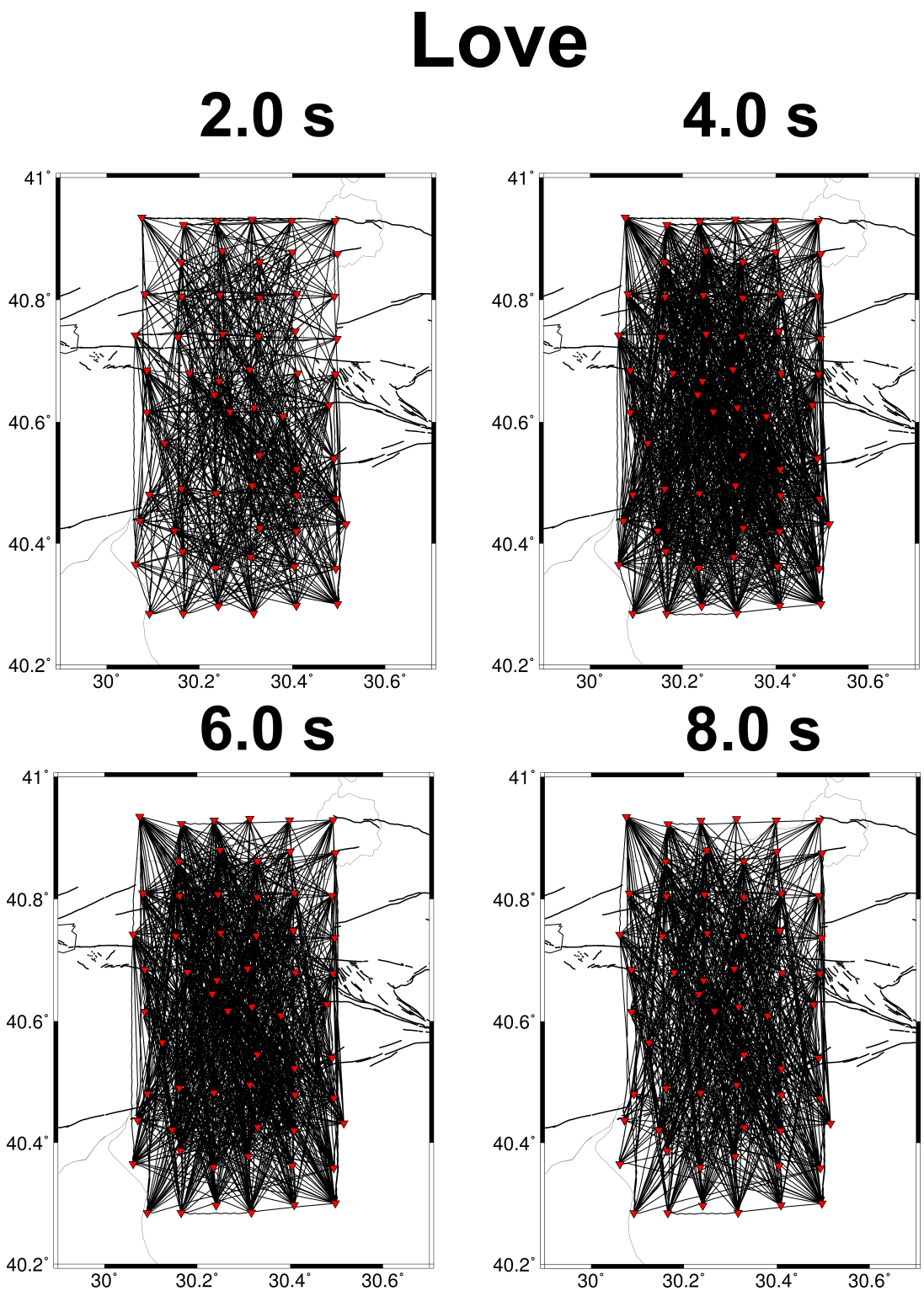

Figure A.12: Ray path distribution for the Love wave phase velocity tomography between 2.0 s and 8.0 s. Red triangles show stations of the DANA network. The black lines connecting them are the ray paths. Thick black lines represent the locations of the mapped faults. The thin black line represents the Sakarya River.

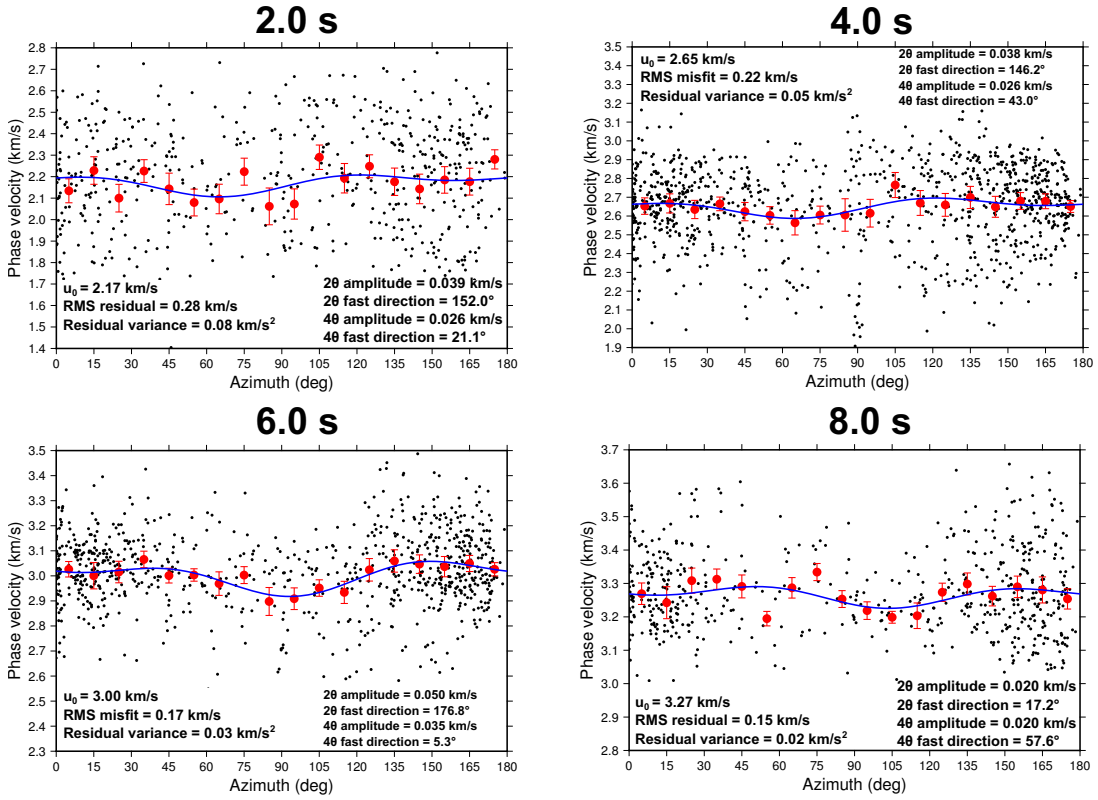

Figure A.13: Azimuthal variation of Love wave phase velocities with propagation azimuth (from north). Black dots indicate the raw phase velocity measurements, large red dots show the average of the phase velocities within 5 degree azimuth bins, and the corresponding standard deviation of the bin. The blue line is the best fitting curve (eq. 3.4) the raw data (black dots). u_0 is the average (isotropic) phase velocity. We show the root mean square misfit of the blue curve to the phase velocity measurements, as well as the variance of the residuals. We indicate the 2θ and 4θ amplitudes and fast directions that correspond to the blue curve.

A.9 Text A.9. Azimuthal anisotropy of Love wave phase velocities.

Fig. A.13 shows the azimuthal variation of the Love wave phase velocities between 0 and 180 degrees from north. The measurements have a higher variance than the Rayleigh wave counterparts, but the dominant fast direction varies between 25 and 40 degrees for the 2θ component. The 4θ component generally has a fast direction between 85 and 120 degrees. The average amplitude of the 2θ component is 0.036 km s^{-1} 1.3%), whilst the 4θ component has an average of 0.025 km s^{-1} (0.9%).

A.10 Text A.10. Rose diagrams of Rayleigh and Love wave propagation azimuths.

Figs. A.14 and A.15 shows the azimuthal distribution of ray coverage for both Rayleigh and Love waves. The azimuthal distribution of ray coverage shows a strong bias to

north-south oriented paths in both the Rayleigh and Love waves. The azimuthal distribution could be indicative of the dominant direction of noise propagation at the DANA network (oriented towards the Black Sea and Mediterranean Sea), but could also be the result of the rectangular array shape, and subsequent higher station density in the north-south direction.

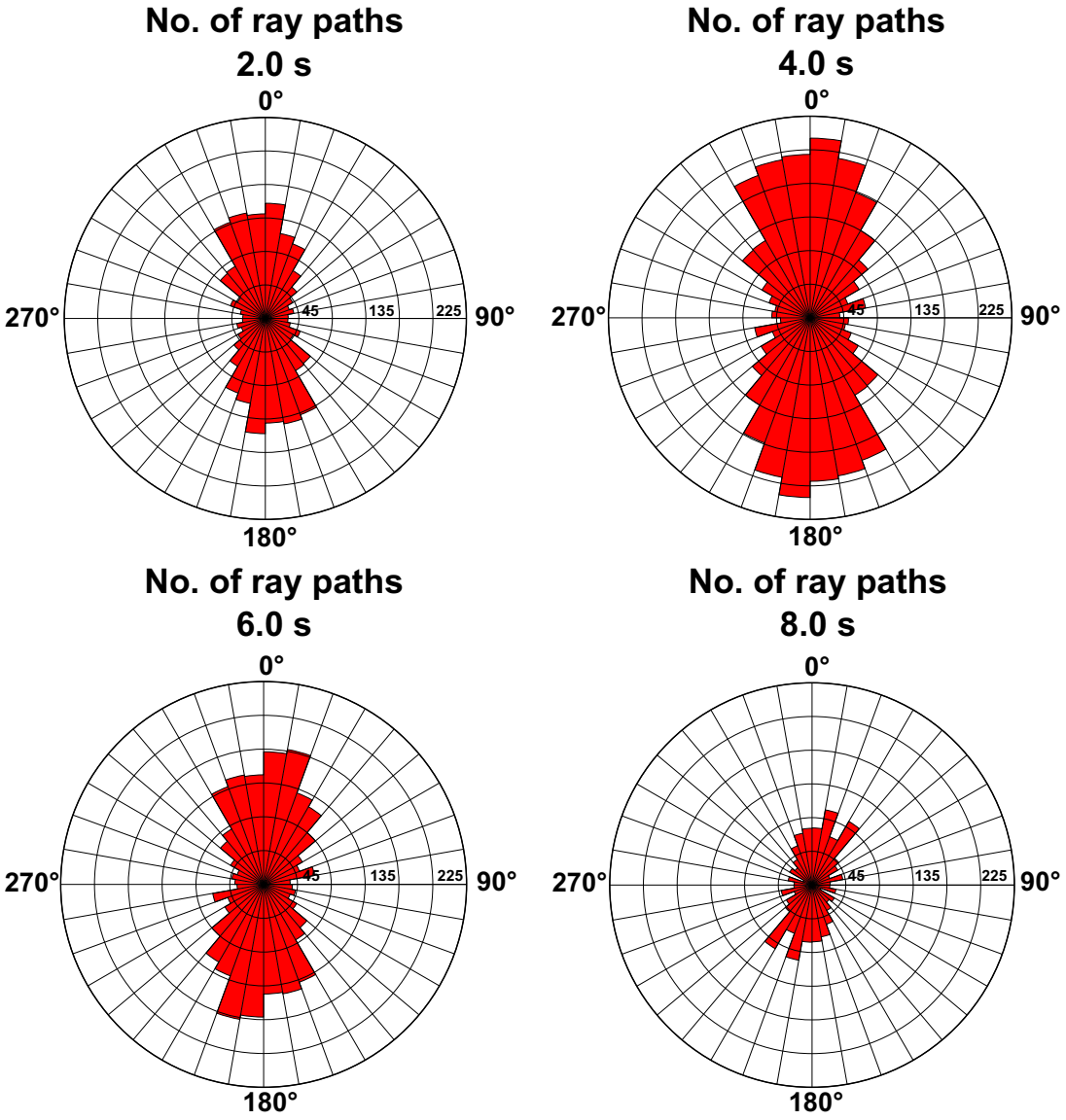

Figure A.14: Azimuthal distribution of Rayleigh wave ray coverage at 2 s, 4 s, 6 s and 8 s. The azimuth from north is indicated on the outside of the rose diagram. The data is split into 10 degree azimuth bins. The x-axis indicates the number of rays in the given azimuth bin.

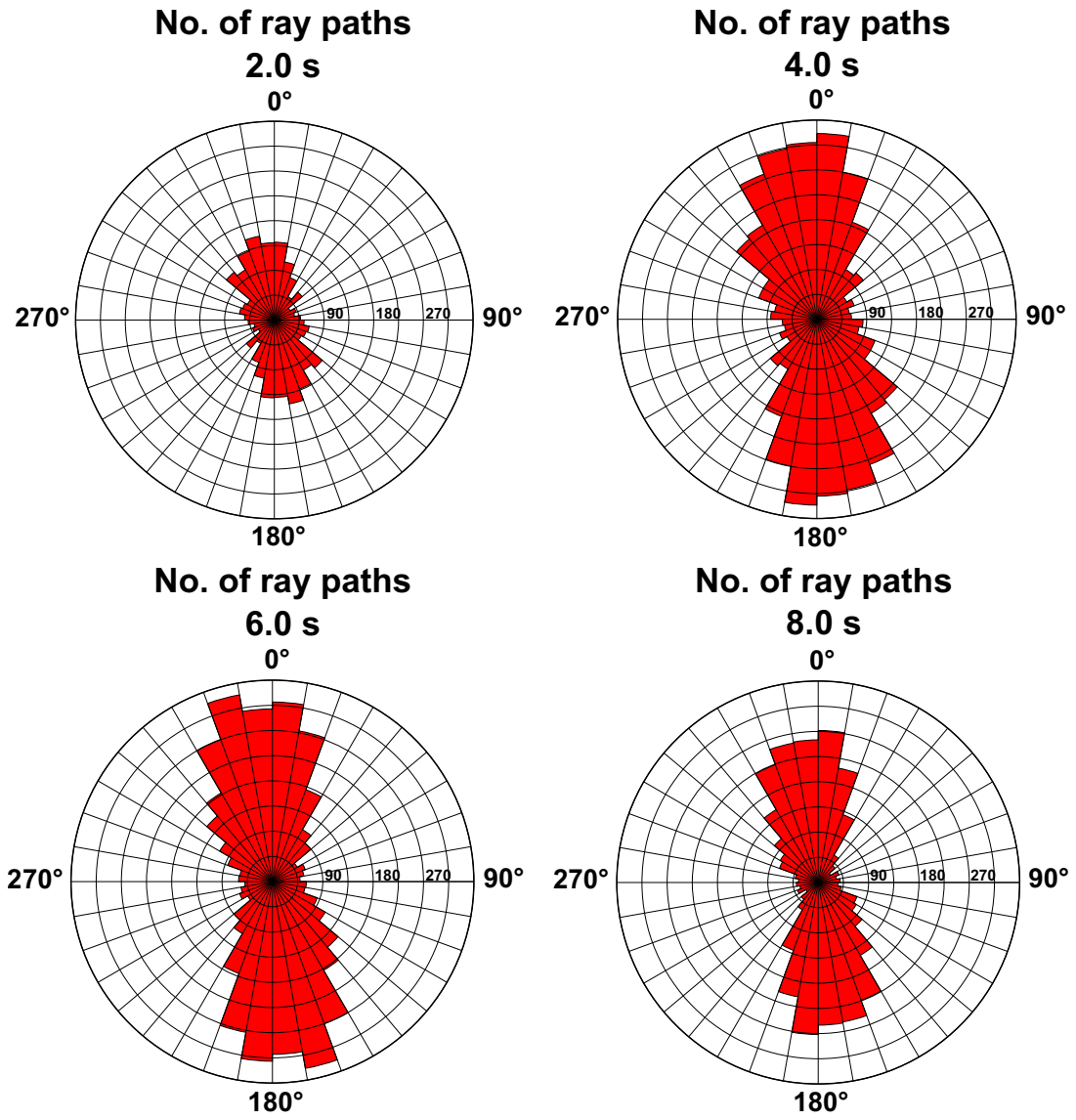

Figure A.15: Azimuthal distribution of Love wave ray coverage at 2 s, 4 s, 6 s and 8 s. The azimuth from north is indicated on the outside of the rose diagram. The data is split into 10 degree azimuth bins. The x-axis indicates the number of rays in the given azimuth bin.